Proceedings of the DINEST:

1st Conference on Structural Dynamics

Madrid , 20-21 June, 2018

1st Conference on Structural Dynamics (DinEst 2018)

Editors:

Iván Muñoz Díaz
José María Goicolea Ruigomez
Francisco Javier Cara Cañas
Jaime H. García Palacios
Gia Khanh Nguyen

Sponsors of the Conference:

Document designed and created by José Manuel Soria Herrera (jm.soria@upm.es)

Organization

Scientific committee

Guillermo Rus, ETSICCP – Universidad de Granada, España
Ignacio Romero Olleros, ETSII – UPM, España
Joaquín Martí Rodríguez, ETSIME – UPM, España
Orlando Maeso, ULPGC, España
Francisco López Almansa, UPC, España
Daniel García Vallejo, ETSI – US, España
Juan Carlos García Orden, ETSICCP – UPM, España
Salvador Ivorra-Chorro, UA, España
Felipe Gabaldón Castillo, ETSICCP – UPM, España
Antolín Lorenzana, EII – UVa, España
Pedro Museros Romero, UPV, España
Rena C. Yu, Universidad de Castilla-La Mancha, España
Rui Calçada, UP, Portugal
Guido de Roeck, KU Leuven, Bélgica
José Rodellar, UPC, España
Santiago Hernández, UDC, España
Alvaro Cunha, UP, Portugal
Francisco Martínez Cutillas, ETSICCP – UPM, España
Daniel Cantero, NTNU, Noruega
Amadeo Benavent Climent, ETSII – UPM, España
Alberto Fraile de Lerma, ETSII – UPM, España
Alejandro E. Martínez-Castro, ETSICCP – Universidad de Granada, España
Carlos Zanuy Sánchez, ETSICCP – UPM, España
Jaime Domínguez, ETSI – US, España
Juana Mayo, ETSI – US, España
María Jesús Elejabarrieta, Mondragón, España
Manuel López Aenlle, UNIOVI, España
Pedro Galvín, ETSI – US, España
Ricardo Perera Velamazán, ETSII – UPM, España
Mª Dolores Martínez Rodrigo, UJI, España
Jose Maria Goicolea, ETSICCP UPM, España
Iván M Díaz, ETSICCP – UPM, España
Jaime H. García-Palacios, ETSICCP – UPM, España
Javier Cara Cañas, ETSII – UPM, España
Dolores Gomez Pulido, IETCC, España
Gia Khanh Nguyen, ETSIA – UPM, España

Secretariat and management

Gia Khanh Nguyen, ETSIA - UPM, España
Jose Manuel Soria Herrera, ETSICCP - UPM, España
Carlos Velarde Ortega, ETSICCP - UPM, España

Preface

Madrid, 20 de Junio de 2018,

La dinámica estructural es un campo de interés común y de importancia creciente en diversas especialidades de la ingeniería y de la ciencia. Mientras que en algunos campos como las máquinas o los vehículos de transporte ha sido siempre un elemento básico, en otros como la ingeniería civil y la arquitectura, más preocupados tradicionalmente con la estática, se ha convertido en un aspecto muy relevante.

Esta primera conferencia a nivel nacional pretende ser un foro en el que tengan cabida los trabajos de investigación, desarrollo y aplicaciones, permitiendo la discusión, difusión, contacto con otros grupos y establecimiento de colaboraciones. Se organiza con proyección internacional y europea, contando con el apoyo de la European Association for Structural Dynamics (EASD) organizadora de los congresos EURODYN, así como con el apoyo de la Sociedad Española de Métodos Numéricos (SEMNI).

La participación incluye tanto trabajos basados en métodos teóricos y computacionales como experimentales. Por otra parte abarca todos los campos de la dinámica estructural, como son la ingeniería mecánica, el transporte, ingeniería civil y arquitectura, ingeniería sísmica e ingeniería de materiales. Aunque ubicados en especialidades de ingeniería distintas todos estos campos comparten conceptos y métodos comunes de dinámica.

Esta primera conferencia pretende iniciar una serie que se desarrolle de forma periódica. Asimismo se propone constituir una Asociación Española de Dinámica Estructural que articule las actividades de colaboración y difusión, y que sirva de interlocutora con otros órganos nacionales e internacionales como la EASD.

Desde el comité organizador queremos dar la bienvenida a todos los participantes y ponernos a disposición para el desarrollo de la conferencia.

José María Goicolea Ruigomez

Catedrático de Universidad,
ETS de Ingenieros de Caminos,
Universidad Politécnica de Madrid

Plenary keynote lecture

"Algunos problemas de vibraciones no lineales en ingeniería mecánica"

La dinámica vibratoria de sistemas mecánicos, ya sean máquinas o estructuras, se analiza normalmente haciendo la simplificación de linealidad en el comportamiento de dichos sistemas. La realidad nos dice que los sistemas se comportan normalmente de forma no lineal, en mayor o menor medida, dependiendo de diferentes parámetros, como son las características del sistema y las fuerzas excitadoras o la amplitud de la respuesta. Se presentan aquí brevemente algunos casos de comportamiento vibratorio no lineal de sistemas mecánicos, haciendo especial énfasis en los casos en que la excitación no es ideal debido a la interacción entre la excitación y el sistema vibrante, y cuya desviación de la linealidad suele ser mayor cuanto menor es la potencia del excitador en relación a la consumida en la respuesta del sistema.

About keynote speaker, Jaime Domínguez Abascal

Nacido en Sevilla en 1951. En la actualidad, Catedrático de Ingeniería Mecánica de la Universidad de Sevilla. Doctor Ingeniero Industrial por la Universidad de Sevilla (1978). Catedrático de Ingeniería Mecánica de la Escuela Superior de Ingenieros de la Universidad de Sevilla desde 1980. Profesor visitante en las Universidades de Stanford (1983) y Sheffield (1991), en el Southwest Research Institute (San Antonio, Texas) (1986-87) y en el Instituto Tecnológico de Massachussets (1996-98 y 2009).

Ha sido subdirector de la Escuela Superior de Ingenieros de Sevilla en dos ocasiones y director de departamento. Director de la Oficina de Gestión de la Investigación Científica y Técnica (1989–92) y de la Oficina de Transferencia de la Investigación (1994–2000) de la Universidad de Sevilla. Coordinador del Área de Tecnología Mecánica y Textil de la Agencia Nacional de Evaluación y Prospectiva (1992–95). Director del Centro Andaluz de Metrología (1998–). Miembro del Academic Council (1992–), del Administrative Council (1992–2010) y del Board of Governors (2011-) del International Center for Mechanical Sciences (CISM)

Ha trabajado en la Empresa Nacional de Autocamiones (1974) y en Abengoa (1974–78), en esta última como responsable del diseño y ensayo antisísmico de equipos electromecánicos para centrales nucleares. Ha trabajado principalmente en dinámica e integridad estructural de sistemas mecánicos. Los trabajos en dinámica se centran en vibraciones y dinámica de mecanismos con elementos flexibles sujetos a grandes y pequeñas deformaciones y en su comportamiento ante impactos. En integridad estructural ha trabajado principalmente en fatiga y fractura de componentes mecánicos, especialmente en fatiga y crecimiento de grietas ante cargas de variación irregular y aleatoria, el crecimiento de grietas originadas en concentradores de tensión y en fatiga bajo condiciones de fretting. Fruto de estos trabajos son unos 200 artículos publicados, más de la mitad de ellos internacionales. Conferenciante invitado en diversas universidades extranjeras y congresos y simposios nacionales e internacionales. Ha participado en más de 100 proyectos de I+D con financiación pública y privada, en la mayoría de ellos como responsable y ha colaborado en numerosos proyectos industriales, todos ellos relativos al análisis y diseño de sistemas mecánicos.

CONTENTS

Organization iii

Preface iv

Plenary keynote lecture v

SECTION 1: Structural dynamics 2

Sensitivity analysis in structural dynamics using statistical methods.
J. Cara, C. González, J.M. Mira . . . 2

First results of fragility curves of single story, double bay unreinforced masonry buildings in Lorca.
B. Orta, S. San Segundo, J. Cervera . . . 7

Tissue ultrasound mechanics and bioreactors.
J. Melchor, A. Callejas, I.H. Faris, and G. Rus . . . 12

Dynamic study of moderately thick plates by means of an efficient galerkin method.
J.M. Martínez-Valle . . . 16

Damage limits in the fades and partitions of buildings subject to the seismic action.
R. Álvarez Cabal, E. Díaz-Pavón, E. Díaz Heredia and E. Carricondo Sánchez . . . 20

Progressive structural collapse possible causes of implementation in the spanish regulations. ways to avoid it.
J. Tortosa del Carpio . . . 24

The effect of core thickness of viscoelastic sandwiches on the dynamic response of a lift.
J. Iriondo, L. Irazu, X. Hernández and M.J. Elejabarrieta . . . 28

SECTION 2: Tests and dynamic monitoring, damage detection, system identification, vibration control 32

Tuning a phase-controlled smart tmd for broad-band-frequency-varying vibration modes.
J.M. Soria, I.M. Díaz, J.H. García-Palacios, C. Zanuy and X. Wang . . . 32

Dynamic characterization and serviceability assessment of a timber footbridge.
Á. Magdaleno, N. Ibán, V. Infantino and A. Lorenzana . . . 38

On the search of multiple tuned mass damper configurations for a vibration mode with changing modal properties.
C.A. Barrera Vargas, J.M. Soria, X. Wang, I.M. Díaz and J.H. García Palacios . . . 42

Experimental analysis of the effect of rhythmic dynamic crowd loads on stadium grandstands.
J. Naranjo-Pérez, N. González-Gámez, J.F. Jiménez-Alonso, F. García-Sánchez and A. Sáez . . . 46

Modal analisys and finite element simulation of the tower of the laboral city of culture in Gijón.
M. López-Aenlle, R.P. Morales, G. Ismael, F. Pelayo and A. Martín . . . 50

Dynamic behavior of a footbridge in Gij subjected to pedestrian-induced vibrations.
G. Ismael, M. López-Aenlle and F. Pelayo 54

Motion-based design of multiple tuned mass dampers to mitigate pedestrians-induced vibrations on suspension footbridges.
M. Calero-Moraga, D. Jurado-Camacho, J.F. Jiménez-Alonso and A. Sáez 58

Measurement of the stress in tension bars using methods based on the image.
B. Ferrer and D. Mas 62

Foundation analysis for dynamic equipment: design strategies for vibration control.
D. Marco, J.A. Becerra, A.N. Fontán and L.E. Romera 66

Building information modeling (bim) and historical architecture: a proposal for the energy predictive performance assessment.
Ó. Cosido, R. Marmo, P.M. Rodríguez, A. Salcines, M. Tena and D. Basulto 70

Modal scaling of structures by operational and classical modal analysis.
F. Pelayo, M.L. Aenlle, R. Brincker and A. Fernández-Canteli 75

Enhancement of vibration pedestrian comfort of a footbridge via tuned mass damper.
M. Bukovics, J.M. Soria, I.M. Díaz, J.H. García-Palacios, J. Arroyo and J. Calvo 79

Dynamic analysis of a lively dinning hall floor: testing and modelling.
J.H. García-Palacios, I.M. Díaz, X. Wang, J.C. Deniz, J.M. Soria and C.M. de la Concha 83

Operating state identification of a high-speed train with analysis of the vibration signal.
A. Bustos, H. Rubio, C. Castejón and J.C. García-Prada 88

Dynamic test and vibration control of a two-story shear building model.
I. Embid, C.M. de la Concha, I.M. Díaz, J.H. García-Palacios and J.C. Mosquera 92

Active vibration control of human-induced vibrations: from siso to mimo.
I.M. Díaz, E. Pereira, X. Wang and J.H. García-Palacios 96

Step-by-step guide for mimo active vibration control: from the design to the implementation.
X. Wang, E. Pereira, I.M. Díaz and J.H. García-Palacios 101

Efficient sizing of isolated foundations for testing systems.
J. Ramírez-Senent, G. Marinas-Sanz, J.H. García-Palacios and I.M. Díaz 105

SECTION 3: Bridge dynamics **109**

Dynamic response of a short simply-supported girder bridge under railway excitation: effect of bracing beams on the transverse behaviour
E. Moliner, A. Romero P. Galvín and M.D. Martínez-Rodrigo 109

Resonance and cancellation in double-track simply supported railway bridges: theoretical predictions versus experimental measurements
M.D. Martínez-Rodrigo, E. Moliner, P. Galvín and A. Romero 114

Dynamic analysis of a skew i-beam railway bridge: experimental and numerical.
C. Velarde, J.M. Goicolea, K. Nguyen, J. García-Palacios, I. M. Díaz and J.M. Soria . . 118

Train-speed sensitivity analysis for maximum envelopes in dynamics of railway bridges.
A.E. Martínez-Castro and E. García-Macías 123

Assessment of lateral vibrations of footbridges using a frequency domain approach.
R.G. Cuevas, F. Martínez and I.M. Díaz 127

Dynamic analysis of a culvert-type structures in high speed lines.
A. Fraile, M.F. Báez, J. Fernández and L. Hermanns 132

Analysis of the lifting process of bridge segments.
L.M. Lacoma, J. Rodríguez, F. Martínez and J. Martí 136

Dynamic load models for new or existing railway bridges.
J.M. Goicolea, K. Nguyen, C. Velarde and E. Barrios 141

SECTION 4: Computational dynamics **142**

Meshfree modeling of dynamic fracture in fibre reinforced concrete.
R.C. Yu, P. Navas and G. Ruiz 142

Dynamic analysis performed by commercial software.
J. Pereiro-Barceló 147

General multi-region bem-fem model for fluid/soil and shell interaction problems.
J.D.R. Bordón, J.J. Aznárez and O.F. Maeso 151

SECTION 5: Dynamics of materials, vibroacoustics, wave propagation in solids **155**

Effect of magnetic field on the dynamic behaviour of the smart sandwich
L. Irazu and M.J. Elejabarrieta 155

Dynamic behaviour of viscoelastic laminated elements at different temperatures
F. Pelayo, M. López-Aenlle and G. Ismael 160

Scoping assesment of free-field vibrations due to railway traffic
D. López-Mendoza, P. Galvín, D.P. Connolly and A. Romero 164

A 2.5D spectral formulation to represent guided waves with acoustic and solid interaction
F.J. Cruz-Muñoz, A. Romero, A. Tadeu and P. Galvín 168

SECTION 6: Seismic engineering, soil-structure dynamic interaction **172**

Analisys of critical situation in the dynamic and seismic structural response of a cantilever bridge. ddbd and energy balance.
C. Iturregui, K. Nguyen, I.M. Díaz, J.H. García Palacios, J.M. Soria and A. Atorrasagasti-Villar 172

Kinematic bending moments in owt monopiles as a function of the ground type.
L.A. Padrón, J. Herrera, J.J. Aznárez and O. Maeso 178

Parapet wall fragility.
L. Navas-Sánchez, J. Cervera, J.M. Gaspar-Escribano and B. Benito 182

Direct model for the dynamic analysis of piled structures on non-homogeneous media.
G.M. Álamo, J.J. Aznárez, L.A. Padrón, A.E. Martínez-Castro, R. Gallego and O. Maeso 187

Definition of the seismic environment of the tokamak complex building of iter fusion facility.
F. Rueda, D. Combescure, L. Maqueda, J. Olalde, L. Moya and V. Domínguez 191

Looking for criteria to assess the relevance of structural flexibility on the response of large buried structures subject to seismic action.
A. Santana, J.J. Aznárez, L.A. Padrón and O. Maeso 195

Numerical model for the analysis of the dynamic response of the soria dam including soil?structure interaction.
J.C. Galván, L.A. Padrón, J.J. Aznárez and O. Maeso 199

Numerical simulation of shaking table tests on a reinforced concrete waffle-flat plate structure.
D. Galé-Lamuela, A. Benavent-Climent and G. Gonzalez-Sanz 203

Characterization of the behavior of seismic dampers with shape memory alloys.
G. González-Sanz, D. Galé-Lamuela and A. Benavent-Climent 207

Shaking table testing on seismic pounding of a rc building structure.
A. Kharazian, F. López Almansa, A. Benavent Climent and A. Gallego 211

Dynamic modeling of fluid-driven earthquakes in poroelastic media.
P. Pampillón, D. Santillán, J.C. Mosquera and L. Cueto-Felgueroso 215

Construction of elastic spectra for high damping.
J. Conde-Conde and A. Benavent-Climent 219

Dynamic soil-structure interaction in an offshore lattice tower.
A.E. Martínez-Castro, J.M. Terrés Nícoli and C. Mans 223

SECTION 7: Non-linear dynamics, dynamics of multibody systems, biomechanics, impact actions and explosions **227**

Symmetry-preserving formulation of nonlinear constraints in multibody dynamics.
J.C. García Orden 227

Simulation study of the influence of design parameters on a vibrocompaction process.
J. González-Carbajal, D. García-Vallejo and J. Domínguez 232

A new approach based on sparse matrices to efficiently solve the equations arising from the dynamic simulation of multibody systems.
Antón, J.A. and Cardenal, J. 236

Author index **240**

SECTION 1: Structural dynamics

SENSITIVITY ANALYSIS IN STRUCTURAL DYNAMICS USING STATISTICAL METHODS

Javier Cara*, **Camino González**†, **José Manuel Mira**†

*ETS Ingenieros Industriales
Universidad Politécnica de Madrid
28006 Madrid, Spain

e-mail: javier.cara@upm.es
ORCID: 0000-0002-1543-3066

† ETS Ingenieros Industriales
Universidad Politécnica de Madrid
28806 Madrid, Spain

Abstract. There are many applications of sensitivity analysis in structural mechanics: inverse analysis, numerical optimization, reliability analysis, modal identification,... Probably the most recent problem is the so-called Finite Element Model Updating, where researchers and engineers try to adjust certain parameters of a mathematical model of a real structure (bridges, buildings,...) taking into account the values recorded using sensors. These mathematical models (obtained using the finite element method) sometimes have thousands of variables, so it is very difficult to perform sensitivity analysis analytically, and many numerical methods have been used instead. In this sense, the performance of some statistical methods is analysed.

Key words: Sensitivity, Dynamics, Statistics.

1 INTRODUCTION

In this work, sensitivity is understood like how the response of a structural system changes with respect to a change in the model parameters. If the output of the system is called F and the parameters of the model are called $x = (x_1, x_2, \ldots, x_n)$, then for small change in the parameters, $\Delta x = (\Delta x_1, \Delta x_2, \ldots, \Delta x_n)$, sensitivity may be obtained through a first-order Taylor series expansion

$$F(x + \Delta x) = F(x) + \sum_{i=1}^{n} \frac{\partial F(x)}{\partial x_i} \Delta x_i + R(x)$$

where $R(x)$ is the remainder. The main difficulty of evaluating this equation is due to the presence of the derivative $\frac{\partial F(x)}{\partial x_i}$. Two different approaches can be found in technical literature [1, 2], analytical methods and numerical method. Traditionally, numerical methods try to compute derivatives in a deterministic way, using for example, the finite difference method. In this work we propose to use statistical methods like Analysis of Variance and Linear Regression.

2 SIMULATED EXAMPLE

2.1 The model

A simplistic model is used to demonstrate the efficiency of the proposed methods. The model has been taken from from in [2].

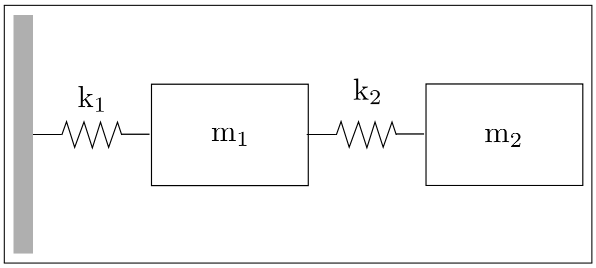

Figure 1: Simulated system.

The mass and stiffness matrices are:

$$K = \begin{bmatrix} k_1+k_2 & -k_2 \\ -k_2 & k_2 \end{bmatrix}, \quad M = \begin{bmatrix} m_1 & 0 \\ 0 & m_2 \end{bmatrix}.$$

We are interested in the sensitivity of the natural frequencies of vibration, ω_i^2, which are computed from the equation:

$$(K - M\omega_i^2)\phi_i = 0.$$

that is, ω_i^2 are the eigenvalues of $M^{-1}K$. For the model of Figure 1, these values can be computed analytically:

$$\omega_1^2 = \frac{k_1+k_2}{2m_1} + \frac{k_2}{2m_2} + \frac{R}{2},$$

$$\omega_2^2 = \frac{k_1+k_2}{2m_1} + \frac{k_2}{2m_2} - \frac{R}{2},$$

where

$$R = \sqrt{\frac{(k_1+k_2)^2}{m_1^2} + \frac{k_2^2}{m_2^2} - \frac{2k_1k_2}{m_1m_2} + \frac{2k_2^2}{m_1m_2}}.$$

The advantage of using a simplistic model is that we can compute partial derivatives by hand:

$$\frac{\partial\omega_1^2}{\partial k_1} = \frac{1}{2m_1} + \frac{k_1m_2 + k_2m_2 - k_2m_1}{2m_1^2m_2R}$$

$$\frac{\partial\omega_1^2}{\partial m_1} = -\frac{k_1+k_2}{2m_1^2} - \frac{(k_1+k_2)^2m_2 + 2k_1k_2m_1 - 2k_2^2m_1}{2m_1^3m_2R}$$

$$\frac{\partial\omega_2^2}{\partial k_1} = \frac{1}{2m_1} - \frac{k_1m_2 + k_2m_2 - k_2m_1}{2m_1^2m_2R}$$

$$\frac{\partial\omega_2^2}{\partial m_1} = -\frac{k_1+k_2}{2m_1^2} + \frac{(k_1+k_2)^2m_2 + 2k_1k_2m_1 - 2k_2^2m_1}{2m_1^3m_2R}$$

Using the numerival values $k_1 = 1,\ k_2 = 2,\ m_1 = 1,\ m_2 = 2$, the sensitivity of ω_1^2 and ω_2^2 with respect to k_1 and m_1 are shown in Table 1.

Table 1: Theoretical sensitivity

$\partial\omega_1^2/\partial k_1$	0.2113
$\partial\omega_1^2/\partial m_1$	-0.0566
ratio	-3.7320
$\partial\omega_2^2/\partial k_1$	0.7887
$\partial\omega_2^2/\partial m_1$	-2.9434
ratio	-0.2679

3 RESULTS

3.1 Methodology

In this section we will try to reproduce the values of Table 1 using the proposed methods. The procedure is:

- Generate a grid of values for k_1 and m_1. So, m values for k_1 and n values for m_1 are generated, called k_{1i} and m_{1j}.
- Form the mass and stiffness matrix for each $\{k_{1i}, m_{1j}\}$ pair.
- Compute the eigenvalues and eigenvectors numerically.
- Use statistical models to compute the sensitivity.

3.2 Analysis of variance

- Model

$$y_{ij} = \mu + \alpha_i + \beta_j + u_{ij}, \quad u_{ij} \to N(0, \sigma^2)$$

$$i = 1, 2, \ldots, m \quad j = 1, 2, \ldots, n$$

y_{ij} is the natural frequency for $\{k_{1i}, m_{1j}\}$.

- Parameter estimation

$$\hat{\mu} = \frac{1}{mn}\sum_{i=1}^{m}\sum_{j=1}^{n} y_{ij},$$

$$\hat{\alpha}_i = \frac{1}{n}\sum_{j=1}^{n} y_{ij} - \hat{\mu}$$

$$\hat{\beta}_j = \frac{1}{m}\sum_{i=1}^{m} y_{ij} - \hat{\mu}$$

- Taylor series

$$\begin{aligned} y(k_{1i}, m_{1j}) \approx\ & y(k_{10}, m_{10})+ \\ & + \frac{\partial y(k_{10}, m_{10})}{\partial k_1}(k_{1i} - k_{10})+ \\ & + \frac{\partial y(k_{10}, m_{10})}{\partial m_1}(m_{1j} - m_{10}) \\ & \approx y(k_{10}, m_{10})+ \\ & + \frac{\partial y(k_{10}, m_{10})}{\partial k_1}\Delta k_{1i}+ \\ & \frac{\partial y(k_{10}, m_{10})}{\partial m_1}\Delta m_{1j} \end{aligned}$$

where k_{10} and m_{1j} are the stiffness and mass at the center of the grid. These are the values where the sensitivity is computed.

- If Δk_{1i} and Δm_{1j} are constant:

$$\begin{aligned} \hat{\mu} &= y(k_{10}, m_{10}), \\ \hat{\alpha}_i &= \frac{\partial y(k_{10}, m_{10})}{\partial k_1}\Delta k_1, \\ \hat{\beta}_j &= \frac{\partial y(k_{10}, m_{10})}{\partial m_1}\Delta m_1 \end{aligned}$$

- We can use the variance explained

$$\begin{aligned} VE(\alpha) &= m\sum_{i=1}^{m}\hat{\alpha}_i^2 = \\ &= m\left(\frac{\partial y(k_{10}, m_{10})}{\partial k_1}\right)^2\sum_{i=1}^{m}(\Delta k_1)^2 \end{aligned}$$

$$\begin{aligned} VE(\beta) &= n\sum_{j=1}^{n}\hat{\beta}_j^2 = \\ &= n\left(\frac{\partial y(k_{10}, m_{10})}{\partial m_1}\right)^2\sum_{j=1}^{n}(\Delta m_1)^2 \end{aligned}$$

- Therefore, partial derivatives can be computed as:

$$\left|\frac{\partial y(k_{10}, m_{10})}{\partial k_1}\right| = \sqrt{\frac{VE(\alpha)}{m\sum_{i=1}^{m}(\Delta k_1)^2}}$$

$$\left|\frac{\partial y(k_{10}, m_{10})}{\partial m_1}\right| = \sqrt{\frac{VE(\beta)}{n\sum_{j=1}^{n}(\Delta m_1)^2}}$$

The results obtained with these equations are shown in Table 2.

3.3 Linear regression

- Model

$$y_i = \beta_0 + \beta_1 x_{1i} + \beta_2 x_{2i} + u_i, \quad u_i \to N(0, \sigma^2)$$

- Taylor series

$$\begin{aligned} y(k_{1i}, m_{1j}) \approx\ & y(k_{10}, m_{10})+ \\ & + \frac{\partial y(k_{10}, m_{10})}{\partial k_1}(k_{1i} - k_{10})+ \\ & + \frac{\partial y(k_{10}, m_{10})}{\partial m_1}(m_{1j} - m_{10}) \end{aligned}$$

- Taking $x_{1i} = (k_{1i} - k_{10})$ and $x_{2i} = (m_{1i} - m_{10})$

$$\begin{aligned} \hat{\beta}_0 &= y(k_{10}, m_{10}), \\ \hat{\beta}_1 &= \frac{\partial y(k_{10}, m_{10})}{\partial k_1} \\ \hat{\beta}_2 &= \frac{\partial y(k_{10}, m_{10})}{\partial m_1} \end{aligned}$$

Using this model, we can also compute the sign of the partial derivatives. The results obtained with these equations are shown in Table 2.

3.4 Linear regression and second order sensitivity

We can evaluate second order sensitivity easily with linear regression models:

- Model

$$y_i = \beta_0 + \beta_1 x_{1i} + \beta_2 x_{2i} + \beta_3 x_{3i} + \beta_4 x_{4i} + \beta_5 x_{5i} + u_i,$$
$$u_i \to N(0, \sigma^2).$$

- Taylor series:

$$\begin{aligned} y(k_{1i}, m_{1j}) \approx\ & y(k_{10}, m_{10})+ \\ & + \frac{\partial y(k_{10}, m_{10})}{\partial k_1}(k_{1i} - k_{10})+ \\ & + \frac{\partial y(k_{10}, m_{10})}{\partial m_1}(m_{1j} - m_{10})+ \\ & + \frac{\partial^2 y(k_{10}, m_{10})}{\partial k_1^2}(k_{1i} - k_{10})^2+ \\ & + \frac{\partial^2 y(k_{10}, m_{10})}{\partial m_1^2}(m_{1j} - m_{10})^2+ \\ & + \frac{\partial^2 y(k_{10}, m_{10})}{\partial k_1 \partial m_1}(k_{1i} - k_{10})(m_{1j} - m_{10}) \end{aligned}$$

- Taking $x_{1i} = (k_{1i} - k_{10})$ and $x_{2i} = (m_{1i} - m_{10})$

$$\hat{\beta}_0 = y(k_{10}, m_{10}),$$
$$\hat{\beta}_1 = \frac{\partial y(k_{10}, m_{10})}{\partial k_1}$$
$$\hat{\beta}_2 = \frac{\partial y(k_{10}, m_{10})}{\partial m_1}$$
$$\hat{\beta}_3 = \frac{\partial^2 y(k_{10}, m_{10})}{\partial k_1^2}$$
$$\hat{\beta}_4 = \frac{\partial^2 y(k_{10}, m_{10})}{\partial m_1^2}$$
$$\hat{\beta}_5 = \frac{\partial^2 y(k_{10}, m_{10})}{\partial k_1 \partial m_1}$$

3.5 Numerical results

Table 2: Sensitivity computed using the proposed models

	theory	ANOVA	LinReg	LinReg2
$\partial\omega_1^2/\partial k_1$	0.2113	0.1931	0.2115	0.2115
$\partial\omega_1^2/\partial m_1$	-0.0566	0.0513	-0.0562	-0.0562
ratio	-3.7320	3.7626	-3.7627	-3.7620
$\partial\omega_2^2/\partial k_1$	0.7887	0.7355	0.8056	0.8057
$\partial\omega_2^2/\partial m_1$	-2.9434	2.7899	-3.0354	-3.0355
ratio	-0.2679	0.2636	-0.2654	-0.2654

4 CONCLUSIONS

- ANOVA and Linear Regression models have been used to compute sensitivity of natural frequencies.
- Linear Regression gives better results than ANOVA.
- Non-linear effects are not important in this case.
- Both models can be applied to more complicated structures.

REFERENCES

[1] Andrea Saltelli et all. *Global Sensitivity Analysis: The Primer.* Wiley-Interscience, 2008.

[2] D. A. Tortorelli and P. Micharelis. Design sensitivity analysis: overview and review. *Inverse Problems in Engineering*, 1:71–105, 1994.

FIRST RESULTS OF FRAGILITY CURVES OF SINGLE STORY, DOUBLE BAY UNREINFORCED MASONRY BUILDINGS IN LORCA

Belén Orta*, Silvia San Segundo† and Jaime Cervera†

* Departamento de Estructuras y Física de la Edificación
ETS Arquitectura
Universidad Politécnica de Madrid
28040 Madrid, Spain
e-mail: belen.orta@upm.es
ORCID: 0000-0001-9290-1911

† ETS Arquitectura
Universidad Politécnica de Madrid
28040 Madrid, Spain

Abstract.

After the seism that took place in Lorca, there is a need to study the vulnerability and fragility of the built heritage in this town and other highly seismic towns in Spain.

This article aims to calculate the seismic performance and vulnerability of single story and double bay unreinforced masonry buildings (**URM buildings**), located in the town of Lorca, Murcia (Spain). This article focuses on the structural vulnerability of the building, excluding urbanistic factors.

The Capacity-Demand Diagram method will be applied in order to calculate the estimated damage due to seismic action. A non-linear static analysis is carried out, applying an increasing displacement in the upper part of the wall up until the structure collapses (pushover) in a three-dimensional model. The seism is considered in the two main directions, characterizing the uncertainty of the parameters of the structural model (geometry and resistance) through distribution functions that will be further explained in the main body of the article.

The capacity curves for the given typology are obtained. By crossing the obtained data with the seismic demand spectrum to deduce the behavior of the given typology in different kinds of earthquakes (from the lower intensity, most common ones to less frequent but more intense ones).

This capacity curve is compared to the demand spectrum of the seism that took place in Lorca on May 11th, 2011 to deduce the performance point of the chosen typology.

From the values of those curves, fragility curves are obtained. These curves are useful when evaluating the seismic risk of this structural typology, and afterwards, when proposing new restoration strategies that offer solutions to the deficiencies detected and specify actions that lessen the seismic risk.

Key words: Structures, Fragility curves, Seismic vulnerability, Masonry buildings, Nonlinear analysis, Lorca.

1 INTRODUCTION

The study of fragility has proven to be a useful tool for the assessment of seismic risk in structures. It can be used for evaluating the probable seismic loses. And allows to decide or propose different methods to reduce the seismic risk. This article uses a 3D model to represent the non-lineal behaviour of the given structural typology: single story, double bay URM building type of structures. Later on, the procedure is showed, the capacity and demand spectra are obtained and ultimately the fragility curves.

2 STRUCTURAL TYPOLOGY

Nowadays, in Lorca, the most common building typology is reinforced concrete buildings, it is studied in other publications [8]. However, URM buildings show higher vulnerability indexes both in Lorca [2] as well as in Europe [7]. This article focusses in the M3.1L (according to Risk-UE project's typology matrix): URM buildings (either stonework or brickwork), wooden slabs, low-rise, 1 or 2 stories, and height 6m and lower. M3.1 typology is the most commonly spread in Lorca up until 1945 [2], when there was no seismic normative in Spain. It is the most common building construction in the old town, and most of them got 0 to 2 degree damage [2]. The study and later layout of capacity and fragility curves for URM buildings are new.

3 STRUCTURAL MODEL

A building in Lorca is chosen, of those we have enough information of (**Figure 1**). It is a brickwork made, single story, double bay house, that did not suffer significative damage during 2011's earthquake.

To make this particular building representative of a whole typology, we consider the uncertainty of the parameters of its structural model: its geometry and the resistance of the masonry walls as showed.

3.1 Size of the model

Masonry buildings in Lorca are in the oldest neighbourhoods. The urban layout is closed blocks with housing between dividing walls. In order to bring light into the inner rooms there is a need for an inner courtyard.

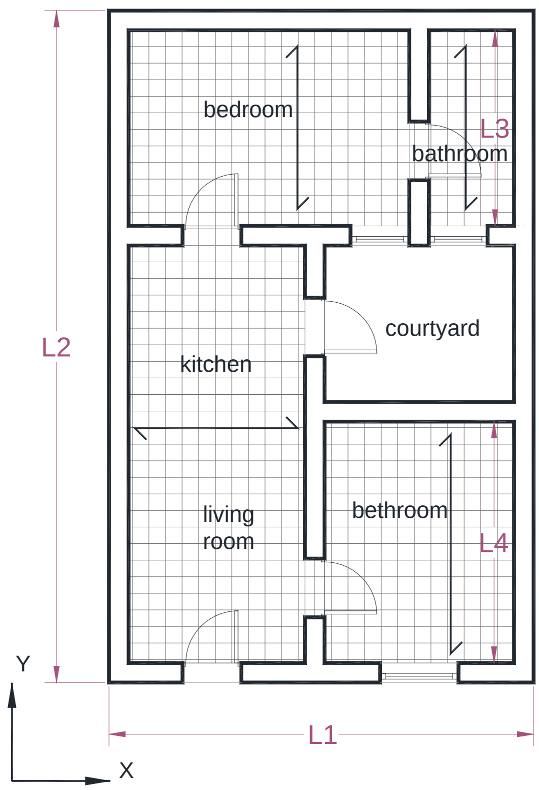

Figure 1: House plan.

We consult Lorca's cadastre in order to consider the uncertainty of the sizes of the given typology. Different housing dimensions are analysed in three different neighbourhoods in which the buildings are mainly masonry buildings **Figure 2**.

Figure 2: Partial plan of Lorca, with the case study buildings located [6].

A wide variety of measurements and façade width, construction length are obtained. They are represented with a blue line in **Figure 3** and **Figure 4**.

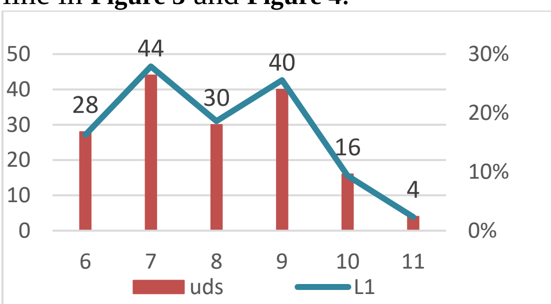

Figure 3: Façade width distribution.

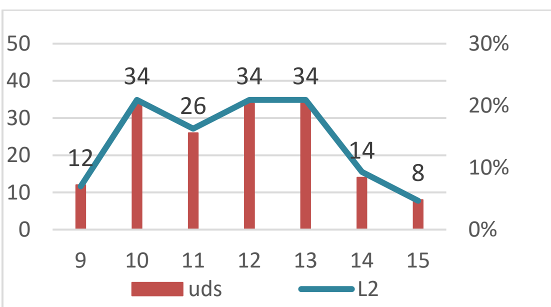

Figure 4: Building depth distribution.

The number of case study examples (140) is adapted to this distribution, represented in red columns in both in **Figure 3** and **Figure 4**.

3.2 Material

To characterize the variability of resistances, two representative values are taken (f_k = 2 y 4 N/mm^2) from the Spanish building code [4]. Currently the study is being conducted about 300 different examples with more materials that the ones used here.

Resistance to mechanical traction is considered to be a 10th of the resistance to compression. The elasticity module is stablished according to the resistance as $E=1000f_k$

3.3 Elements

A non-linear analysis is conducted, with an increase on the shifting in the top of the wall until total collapse of the structure (pushover). ANSYS version 18.2 is the software chosen to do the analysis.

The non-linear behaviour is modelled with SOLID65 elements. This element is used for the 3D modelling of walls of unreinforced masonry. The solid is capable of cracking in tension (in three orthogonal directions), crushing in compression. Also, it is capable of plastic deformation, and creep [1].

The studied typology has wooden horizontal structures that, due to the lack of a proper union, cannot be analysed as a stiff diaphragm. So, the model is done without a horizontal structure. Horizontal structures are considered to be done in non-aligned orientations in order to apply the gravity load in the roof.

4 CAPACITY CURVES

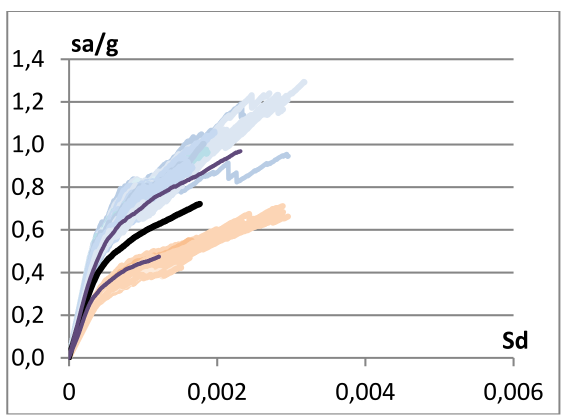

Figure 5: Capacity spectra along the x axis. In blue f_k=4N/mm^2 and in orange f_k=2N/mm^2.

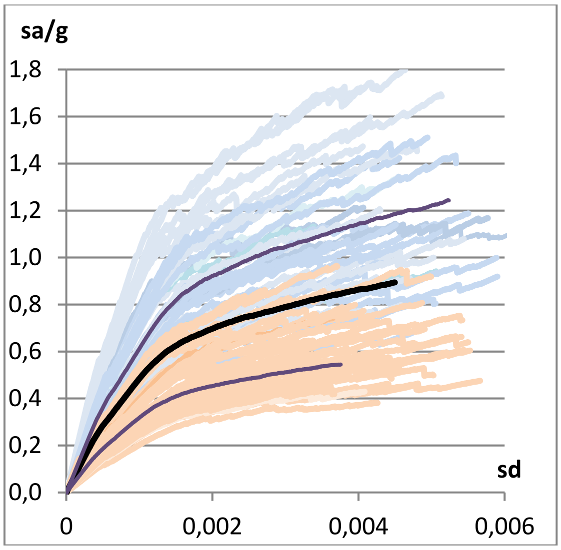

Figure 6: Capacity spectra along the Y axis. In blue f_k=4N/mm² and in orange f_k=2N/mm².

The LM2 RISK-UE's procedure was followed in order to do the analysis. Capacity curves are obtained for seismic action parallel to X and Y axis (Figure 6 and Figure 6).

From the medium capacity curve in both directions, we can draw the bilinear approximation of the same energy deformation (**Figure** 7). The following values are obtained: yield point: Sd_y= 9.63 E-04 [m], Sa_y = 0.58g; ultimate point: Sd_u = 3.13 E-03 [m], Sa_u = 0.79g.

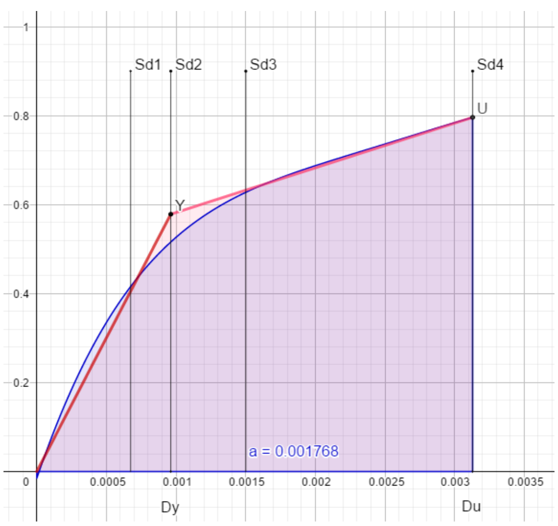

Figure 7: Bilinear approximation of the capacity curve.

4.1 Comparison with the demand spectrum

Capacity and demand spectrum are represented by the spectral pseudo-acceleration (relative to gravity) in the Y axis and pseudo spectral shifting in the X axis (**Figure 8** and **Figure 9**).

Demand spectra are obtained according to the Spanish legislation [5] with the map of seismic acceleration, last version by IGN, 2015 [3]. Four spectra are obtained, according to the earthquake's return period: 75, 225, 475 and 2475 years.

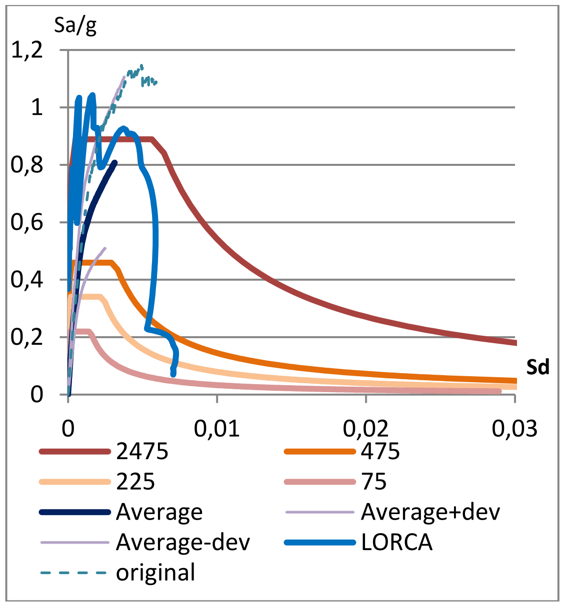

Figure 8: Demand spectra compared to the medium capacity curve of the typology.

5 FRAGILITY CURVES AS VULNERABILITY INDICATIVES

The fragility of the typology is a set of curves that are represented in the coordinate axes for that the Y axis represents spectral displacements (Sd) and the X axis the chance of finding (P[Ds=ds]) or exceeding (P[Ds>ds]) a particular damage stage.

Each curve is characterized by the average value of the spectral shifting, $S_{d,ds}$, and the lognormal deviation, β_{Sd}, determined by ductility (μ_u) as shown in

Table 1.

Damage State (ds)	$S_{d,ds}$	β_{Sd}
Slight	0.7 D_y	$\beta_{Sd1} = 0.25+0.07\ln(\mu_u)$
Moderate	D_y	$\beta_{Sd2} = 0.20+0.18\ln(\mu_u)$
Extensive	$D_y+0.25(D_u\text{-}D_y)$.	$\beta_{Sd3} = 0.10+0.040\ln(\mu_u)$
Complete	D_u.	$\beta_{Sd4} = 0.15+0.50\ln(\mu_u)$

Table 1: Damage stages according to Risk-UE, shifting in the head and beta value.

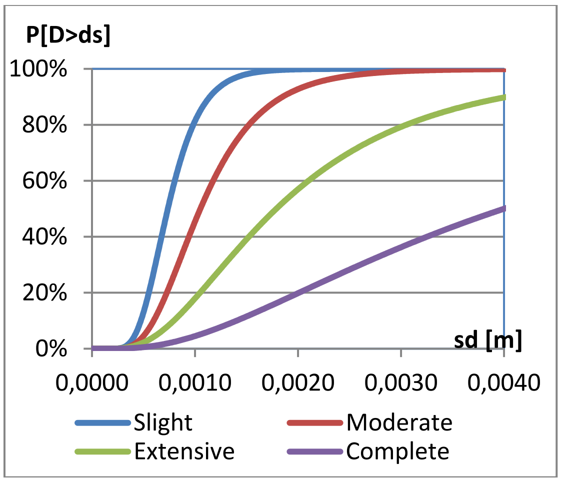

Figure 9: Fragility curves

6 CONCLUSIONS

The obtained results may differ from the real response due to the imperfections or flaws of the construction that have not been taken into account.

Seismic behaviour of URM buildings is quite sensible to the wall's out-of-plane stiffness.

Parameters published by RISK-UE for fragility curves do not include the studied typology. The obtained results when this investigation comes to an end can be used to complete the ones published within the Risk-UE project for URM buildings.

The structural modelling method introduced in this study can be efficiently applied for the development of fragility curves of URM buildings.

REFERENCES

[1] Ansys inc. *ANSYS User's Manual*, 2018.

[2] M. Feriche, M. Navarro, C. Aranda. "Vulnerabilidad y daño en el terremoto de Lorca de 2011". *7th asamblea hispano-portuguesa de geodesia y geofísica;* 2012.

[3] Instituto Geográfico Nacional www.ign.es/web/ign/porta/mapas-sismicidad, 2015.

[4] Ministerio de Fomento. *Código Técnico de la Edificación. Documento Básico, Seguridad Estructural: Fábrica*. Ministerio de Fomento, 2004.

[5] Ministerio de fomento. *Norma de Construcción Sismorresistente: Parte general y edificación (NCSE-02).* Ministerio de Fomento, 2002.

[6] Sede Electrónica del Catastro https://www1.sedecatastro.gob.es/

[7] Zoran V. Milutinovic & Goran S. Trendafiloski. *Risk-UE, An advanced approach to earthquake risk scenarios with applications to different European towns: WP4: Vulnerability of current buildings*. 2003.

[8] Navas-Sánchez L. Parapet Wall Fragility. *1st Conference on Structural Dynamics*, 2018.

1st. Conference on Structural Dynamics (DinEst 2018)
Madrid, 20–21 June

TISSUE ULTRASOUND MECHANICS AND BIOREACTORS

J. Melchor[*,†,+], **A. Callejas**[*], **I. H. Faris**[*], **and G. Rus**[*,†,+]

[*]Ultrasonics Group, NDE Lab, Dpt. Structural Mechanics
[†] MNat Excellence Research Unit "Modelling Nature" (MNat)
Universidad de Granada
[+] Biomechanics Group, Biosanitary Research Institute IBS
Granada, Spain

e-mail: jmelchor@ugr.es
ORCID: 0000-0002-5542-1588

Abstract. The use of the rational principles of the mechanics of solids is proposed to understand and control the characterization and interaction of tissues through ultrasonic propagation to generate diagnostic techniques of pathological processes that manifest themselves in changes of tissue consistency. Addressing tissue biomechanics requires a collaborative effort among engineers, physicists, and physicians. This multidisciplinary work will allow a better understanding of the structural and mechanical functioning of the tissues.

To quantify the variations of the mechanical properties, the inverse problem based on models is proposed to reconstruct the linear and nonlinear mechanical properties from the measurement of the ultrasonic waves as it propagates through the tissue and interacts with it. Ultrasounds are physical waves of a mechanical nature, and therefore ideally sensitive to mechanical properties.

The ultrasonic group's application areas focus on (1) computationally modeling the ultrasound-tissue interaction, focusing on the constitutive models, (2) designing and testing transducers and measurement devices, (3) designing and applying a robust algorithm to reconstruct the relevant mechanical parameters from the measured signals, (4) explore the physiological, histological and biochemical variables to provide a rational view of the clinical processes and (5) designing of bioreactors to monitor the biological processes and contribute to the approach of biomedical aims and challenges.

The scientific and strategic power of this area lies in covering for the first time in a unified way from basic research on the physics of ultrasound-tissue interaction to applied engineering in clinical devices.

Key words: Ultrasonics, Mechanical Characterization, Bioreactors, Soft Tissue Mechanics

1 INTRODUCTION

The use of ultrasound, as a type of mechanical wave opens a range of potential applications on pathologies that manifest themselves in changes of tissue consistency, such as breast cancer, prostate tumor or liver disorders. These changes will allow understanding the internal process and quality of tissue engineering [6, 5, 7]. Our research on ultrasound focused on the analysis and real-time characterization of the mechanical properties of different cell cultures through the design of two types of ultrasonic bioreactors with different types for fibroblasts, cornea and cartilage, and an ultrasound monitoring Petri dish [1], with the aim of exploring their application in the Field of Tissue Engineering. The readings from the ultrasonic sensors need a detailed analysis, based on numerical models of the ultrasound-tissue interaction, and a stochastic treatment, in order to extract the relevant information and its evolution with sufficient sensitivity. In order to rank the proposed interaction models that are more plausible the authors used a formulation of a stochastic model-class selection[2].

Recent works relate advances in organ replacement therapy, based on the development of so-called bioarticular organs. An example of a singularly challenging organ is the bioengineered nanostructured cornea, due to the mechanical, transparency and vascularization requirements [3, 4]. Bioreactors are a promised tool to enhance this procedure. So, to optimize the process, it is necessary to control the parameters that may vary its effectiveness. Among those, mechanical parameters are relevant and critical.

2 METHODOLOGY

The proposed methodology consists of four elements: (1) A setup based on ultrasound-tissue interactions. (2) A selection simulating the transfer matrix formalism. (3) A stochastic model-class selection to evaluate the plausibility. (4) The reconstruction of the mechanical parameters.

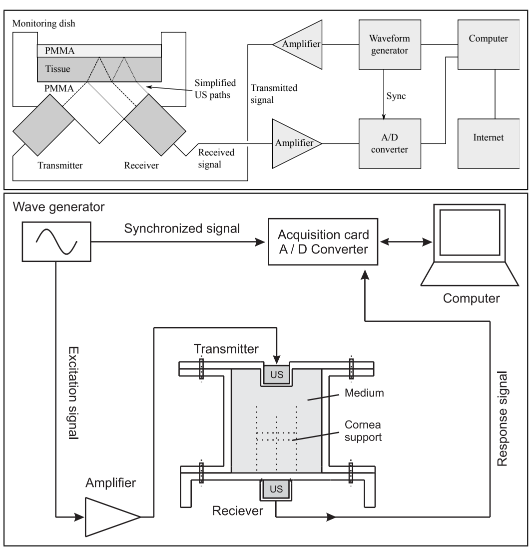

Figure 1: Bioreactor setups

2.1 Experimental configuration

The preparation of the cell culture carried a bioprinted or gel scaffolds were sterilized by being immersed in 70 wt.% ethanol aqueous solution for 1 hour, washed several times in phosphate buffered saline (PBS) and then subjected to ultraviolet light for 20 minutes each size in order to ensure the sterile conditions of the construct. Then, scaffolds were introduced into the bioreactor and monitored by an ultrasonic sine-burst at a central frequency of 1 MHz and 10 V amplitude during 4 weeks. Figure 1(top) illustrates the employed electronic setup to conduct the experiment, while Figure 1(bottom) shows the framework before launching the experiment.

Figure 2 shows two different cultures of fibroblasts and chondrocytes into a bioreactors designed for different requirements.

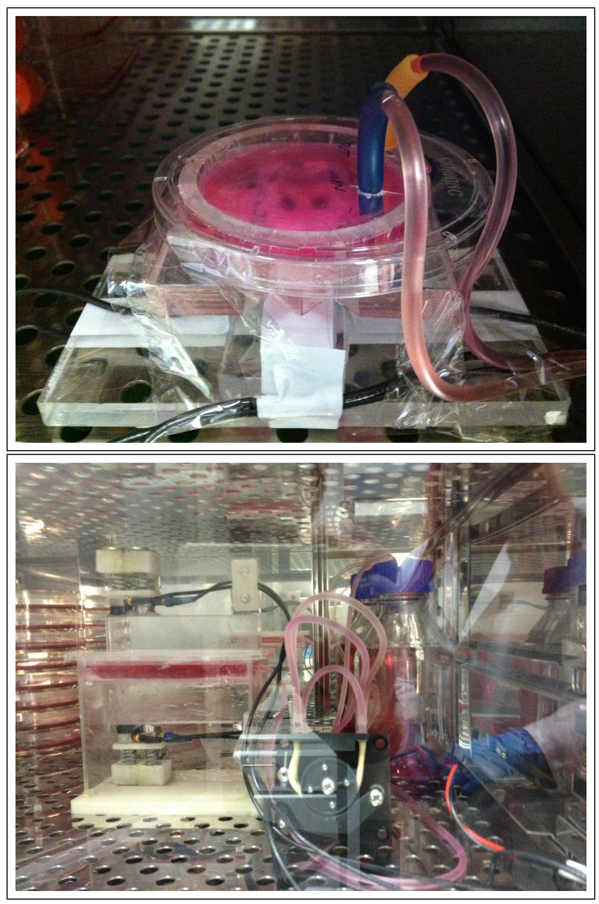

Figure 2: Bioreactor designed for cultures of fibroblasts and chondrocytes

2.2 Theory

The velocity of wave equation employed for ultrasonic propagation is described as monochromatic 1D in terms of mechanical parameters,

$$c_p = \sqrt{\frac{E(1-\nu)}{\rho(1+\nu)(1-2\nu)}} = \sqrt{\frac{M}{\rho}} \tag{1}$$

The energy dissipation is derived from three different viscoelastic models detailed below,

- Viscous:
$$M^*(\omega) = M^0 \left(1 - i\omega d^{\text{vis}}\right) \tag{2}$$
- Hysteretic:
$$M^*(\omega) = M^0 \left(1 - i d^{\text{hys}}\right) \tag{3}$$
- Fractional time derivative:
$$M^*(\omega) = M^0 \frac{1+b(i\omega)^\beta}{1+a(i\omega)^\alpha} \tag{4}$$

The physical mechanisms taken into account are: thermal flow (nm + mm scale), the multiple transmission, multiple reflections, Snell's law and the correction of excitation by temperature and amplitude are considered. The propagation matrix, discontinuity matrix, transfer matrix (sequence of material transitions) and detected wave are described int he next equations.

The dispersion and propagation as,

$$\tilde{U}_m(d_m,\omega) = P_m(a_m,k_m)\tilde{U}_m(d_{m-1},\omega) \tag{5}$$

The compatibility and equilibrium as,

$$\tilde{U}_{m+1}(d_m,\omega) = D_{m,m+1}(Z_m,Z_{m+1})\tilde{U}_m(d_m,\omega) \tag{6}$$

The transference as,

$$\tilde{U}_3(h,\omega) = \underbrace{D_{2,3}P_2D_{1,2}}_{T}\tilde{U}_1(0,\omega) \tag{7}$$

And the received displacement as,

$$\tilde{u}_1^b(0,\omega) = -\frac{T_{[2,1]}}{T_{[2,2]}}\tilde{u}_1^f(0,\omega) \tag{8}$$

To evaluate and decide in terms of plausibility of the model viscoelasticy the probabilistic inverse problem procedure is studied based on probability density := plausibility of being true = certainty. A prior information about the measured observations $\mathcal{O}$, $p^0(\mathcal{O},\mathcal{M},\mathcal{C})$, model parameters $\mathcal{M}$ and model class v. $p^m(\mathcal{O},\mathcal{M},\mathcal{C})$ is the information about their relationship, as provided by the model. Statistical inference theory incorporates both by conjuntion preferred over the Bayesian formulation of statistical inference for being more general [8]. *A posteriori* probability:

$$p(\mathcal{O},\mathcal{M},\mathcal{C}) = k_1\frac{p^0(\mathcal{O},\mathcal{M},\mathcal{C})p^m(\mathcal{O},\mathcal{M},\mathcal{C})}{\mu(\mathcal{O},\mathcal{M},\mathcal{C})} \tag{9}$$

where k_1 is the normalization constant and $\mu(\mathcal{O},\mathcal{M},\mathcal{C})$ uniform distribution.

3 RESULTS

To reconstruct the velocity modulus and compressibility in Figure 3 from the recorded signals in different cases of fibroblast culture and chondrocytes culture, a genetic-algorithm and BFGS based inverse problem is combined with an iterative computational propagation is used.

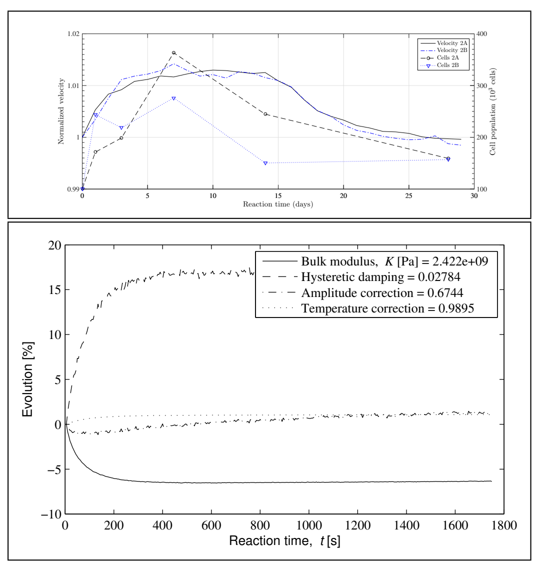

Figure 3: Biomechanics and time of culture for proliferating culture in a bioreactor

A set of three attenuation models (viscous, hysteretic and fractional time derivative damping) that simulate the ultrasound-tissue interaction were evaluated using a model-class selection formulation and the viscous is usually the more plausible.

4 CONCLUSIONS

Wave velocity and attenuation are some of the parameters that results from this process, they indirectly determine histological parameters non-invasively in real time. There is an obvious correlation among velocity, attenuation and the development of the culture. So, as a conclusion, authors can affirm that ultrasound is sensitive to the evolution and quality of the tissue under test. In addition, in the case of ultrasound monitoring of the real-time evolution of the mechanical parameters of the tissue during the decellularization process in the cornea, it is feasible with high sensitivity, but this must be deeply tested. Thus, the usefulness of this technology in the field of regenerative medicine appears promising. Ongoing works will propose a biologically plausible explanation of the changes in the culture taking into account more medical information such as a genetic profile analysis.

5 ACKNOWLEDGMENTS

The authors acknowledge the financial support provided by P11-CTS-8089, PI16/00339, CTS-6568 and PI-0107-2017, the Ministerio de Economía, Industria y Competitividad (MINECO), FEDER funds, DPI2014-51870-R, DTS15/00093, UNGR15-CE-3664 and UGR PP2017-PIP09.

REFERENCES

[1] Nicolas Bochud and Guillermo Rus. Probabilistic inverse problem to characterize tissue-equivalent material mechanical properties. *IEEE transactions on ultrasonics, ferroelectrics, and frequency control*, 59(7), 2012.

[2] Juan Chiachío, Manuel Chiachío, Guillermo Rus, Nicolas Bochud, Laura Maria Peralta, and Juan M Melchor. A stochastic model for tissue consistence evolution based on the inverse problem. *Journal of Biomechanics*, 45:S652, 2012.

[3] Jessica A DeQuach, Shauna H Yuan, Lawrence SB Goldstein, and Karen L Christman. Decellularized porcine brain matrix for cell culture and tissue engineering scaffolds. *Tissue Engineering Part A*, 17(21-22):2583–2592, 2011.

[4] Miguel Gonzalez-Andrades, Juan de la Cruz Cardona, Ana Maria Ionescu, Antonio Campos, Maria del Mar Perez, and Miguel Alaminos. Generation of bioengineered corneas with decellularized xenografts and human keratocytes. *Investigative ophthalmology & visual science*, 52(1):215–222, 2011.

[5] J Melchor, E López-Ruiz, J Soto, G Jiménez, C Antich, M Perán, JM Baena, JA Marchal, and G Rus. In-bioreactor ultrasonic monitoring of 3d culture human engineered cartilage. *Sensors and Actuators B: Chemical*, 2018.

[6] Mark A Rice, Kendall R Waters, and Kristi S Anseth. Ultrasound monitoring of cartilaginous matrix evolution in degradable peg hydrogels. *Acta biomaterialia*, 5(1):152–161, 2009.

[7] Guillermo Rus, Nicolas Bochud, Juan Melchor, Miguel Alaminos, and Antonio Campos. Dispersive model selection and reconstruction for tissue culture ultrasonic monitoring. In *AIP Conference Proceedings*, volume 1433, pages 375–378. AIP, 2012.

[8] Albert Tarantola. *Inverse problem theory and methods for model parameter estimation*, volume 89. siam, 2005.

1st Conference on Structural Dynamics (DinEst 2018)
Madrid, 20-21 June

DYNAMIC STUDY OF MODERATELY THICK PLATES BY MEANS OF AN EFFICIENT GALERKIN METHOD

J.M. Martínez-Valle*

* Escuela Politécnica Superior
University of Cordoba
14071 Cordoba, Spain
e-mail: jmvalle@uco.es
ORCID: 0000-0002-4660- 8770

Abstract. The vibrations of plates are a topic of undoubted interest in the field of civil engineering and aeronautics. Today, we find many examples where this type of phenomena occur, and there are structural elements that we can study as plates or shells. The analytical solutions for the governing equations for the dynamics of higher order plates are very difficult or impossible to obtain so we have to resort to numerical methods. The Finite Element Method (FEM) has been and is a very powerful tool to solve differential or integral equations.

The method of Galerkin is another interesting possibility that can be applied without difficulty and that has not been given as much interest as the FEM. As with the FEM, there are different techniques to relieve numerical instabilities (shear locking of the stiffness matrix) for the solutions of thin plates.

In this communication, we studied this phenomenon by making use of a higher order shear deformation plate theory deduced by the author. We made use of D'Alembert's principle and used a modified method of Galerkin. The results obtained are in very good agreement with those present in the literature.

Key words: Plates, Vibrations, Structures, Galerkin Method.

1 INTRODUCTION

The first studies on free vibration in structural elements date back to at least 1800s. Kirchhoff introduced the famous biharmonic equation that relates the vertical displacements of the plate with the transverse loads applied. However, this theory is only valid for thin plates. It was Reissner [1] who introduced the shear deformation in plates and who even proposed including the dynamic formulation of the problem. From there, numerous higher order plate theories have emerged with infinity of variants that analysed both the dynamic and the static problem [2]. The analytical solutions for these equations are very difficult or impossible to obtain so we have to resort to numerical methods. The Finite Element Method (FEM) has been and is a very powerful tool to solve differential or integral equations [3].

The method of Galerkin is another interesting possibility that can be applied without difficulty and that has not been given as much interest as the MEF. One of the advantages of this method with regard to the FEM is that it does not need to operate with any functional and that the discretization is performed over the whole domain of the problem. As with the FEM, there are different techniques to relieve shear locking [4].

In this communication, we studied this

phenomenon by making use of a higher order shear deformation plate theory [2].

2 1 DEFINITION OF THE STUDY PROBLEM OF TRANSVERSAL OSCILLATIONS OF MODERATELY THICK PLATES

The equations of calculation of the classical theory of plates including shear deformation in dynamic regime without applied external forces are, [5],

$$-\frac{\partial M_x}{\partial x}-\frac{\partial M_{xy}}{\partial y}+Q_x-\gamma I\,\frac{\partial^2\theta_x}{\partial t^2}=0\,,$$
$$-\frac{\partial M_{xy}}{\partial x}-\frac{\partial M_y}{\partial y}+Q_y-\gamma I\,\frac{\partial^2\theta_y}{\partial t^2}=0\,, \quad (1)$$
$$\frac{\partial Q_x}{\partial x}+\frac{\partial Q_y}{\partial y}-\gamma h\,\frac{\partial^2 w}{\partial t^2}=0\,,$$

Where M_x , M_{xy} and M_y are the generalized moments, Q_x and Q_y are the generalized shear forces, γ is the density, I is the moment of inertia, h is the thickness of the plate, θ_x the angle rotated by the rectilinear segment normal to middle surface around the Ox-axis, θ_y the angle rotated around the Oy-axis and w is the vertical displacement. We have to notice that in the classic theories of plates with shear deformation and in the higuer order shear deformation plate theories, the rotations are decoupled from the shifts, resulting in a system of 3 partial differential equations that, in general, do not have analytical solutions. The first two equations take into account the rotational inertia or, what is equivalent, the influence of shear deformation on the phenomenon of vibration.

We can express these equations in terms of the displacements, rotations and the geometric characteristics of the plate as well as its material properties,

$$\Delta w+\frac{\partial\vartheta_y}{\partial x}-\frac{\partial\vartheta_x}{\partial y}-\gamma h\,\frac{\partial^2 w}{\partial t^2}=-\frac{12(1+\mu)}{5Eh}P$$

$$\Delta\vartheta_x-\frac{5(1-\mu)}{h^2}(\vartheta_x-\frac{\partial\widehat{w}}{\partial y})-\gamma I\,\frac{\partial^2\theta_x}{\partial t^2}=\frac{(1+\mu)}{2}\frac{\partial}{\partial x}(\frac{\partial\vartheta_y}{\partial y}+\frac{\partial\vartheta_x}{\partial x}) \quad (2)$$
$$\Delta\vartheta_y-\frac{5(1-\mu)}{h^2}(\vartheta_y+\frac{\partial\widehat{w}}{\partial x})-\gamma I\,\frac{\partial^2\theta_y}{\partial t^2}=\frac{(1+\mu)}{2}\frac{\partial}{\partial y}(\frac{\partial\vartheta_y}{\partial y}+\frac{\partial\vartheta_x}{\partial x})$$

These equations are known as Bolle Reissner equations and can be expressed in a more compact form as a function of the moment sum, the displacements and the applied loads.

We also take into account another important condition; that is, the rotation w_{xy} of a differential element around the z-axis is null for all points of the plate, [2],

$$w_{xy}=\frac{1}{2}\left(\frac{\partial v}{\partial y}-\frac{\partial u}{\partial x}\right)=0, \quad (3)$$

Which is equivalent to,

$$\frac{\partial\vartheta_y}{\partial y}+\frac{\partial\vartheta_x}{\partial x}=0. \quad (4)$$

Doing so, the transformed Bolle Reissner equations are,

$$\frac{\partial\vartheta_y}{\partial x}-\frac{\partial\vartheta_x}{\partial y}+\Delta w-\gamma h\,\frac{\partial^2 w}{\partial t^2}=-\frac{12(1+\mu)}{5Eh}P$$
$$\Delta\vartheta_y-\gamma I\,\frac{\partial^2\theta_y}{\partial t^2}=\frac{5(1-\mu)}{h^2}\left(\vartheta_y+\frac{\partial\widehat{w}}{\partial x}\right), \quad (5)$$

$$\Delta\vartheta_x-\gamma I\,\frac{\partial^2\theta_x}{\partial t^2}=\frac{5(1-\mu)}{h^2}\left(\vartheta_x-\frac{\partial\widehat{w}}{\partial y}\right).$$

Or also expressed in a more compact form,

$$\Delta M=-P$$
$$\Delta w=-\frac{M}{D}-\frac{6P}{5GH} \quad (6)$$

Where M, Marcus Moment, [5], is

$$\frac{M_x+M_y}{(1+\mu)}=M \quad (7)$$

4 NUMERICAL RESOLUTION OF THE PROBLEM BY THE GALERKIN METHOD

4.1 Approach to the weak integral formulation by the Galerkin method

The system formed by equations (6) and (7) is a variant of the typical Dirichlet problem (resolution of the Poisson equation with Dirichlet-type boundary conditions), in which the uniqueness of the solution is ensured and is known as Green function, [6]. It admits its resolution by numerical methods like finite elements and it is strongly convergent even for not very dense meshes, approaching the weak integral formulation by the Galerkin method.

Taking $V = V(x,y)$, with $V = 0$ at the boundary, we form the integral equation:

$$\iint_\Omega \left(\Delta M - \gamma h \ddot{w} + \frac{\mu\gamma h^3}{10(1+\mu)}\Delta\ddot{w}\right) V dA = 0 \quad (8)$$

Transforming the first and the second summing term of this equation, according to the 2nd and 1st Green´s Identity,

$$\iint_\Omega \Delta M V dA = \int_\Gamma \frac{\partial M}{\partial n} V ds - \iint_\Omega \nabla M \cdot \nabla V dA = -\iint_\Omega \nabla M \cdot \nabla V dA \quad (9)$$

or

$$\iint_\Omega \Delta\ddot{w} V dA = \int_\Gamma \frac{\partial \ddot{w}}{\partial n} V ds - \iint_\Omega \nabla\ddot{w} \cdot \nabla V dA = -\iint_\Omega \nabla\ddot{w} \cdot \nabla V dA \quad (10)$$

for choosing V = 0 at the border.

So, we obtain,

$$-\iint_\Omega \nabla M \cdot \nabla V dA = \iint_\Omega \gamma h \ddot{w}\, V dA + \frac{\mu\gamma h^3}{10(1+\mu)} \iint_\Omega \nabla\ddot{w} \cdot \nabla V dA \quad (11)$$

Following the Ritz-Galerkin method we adopted,

$$M = \textstyle\sum_\Gamma \alpha_f \phi_f(x,y) + \sum_\Omega \alpha_i \phi_i(x,y) \quad (12)$$

being α_f constants and $\phi_f(x,y)$ shape functions or interpolation functions, for example piece-wise continuous functions, with unit value in the node in which they are defined and null in the rest of the nodes of the domain, even in the border (Kronecker delta property: the shape function at any node has value of 1 at that node and a value of zero at all other nodes)). With the subscript *"f"* we denote the possible nodes that we could place at the edges of the domain. In the case of simply supported plates, where M is null in the border *(M = 0)*, we would have for the previous expression,

$$M = \textstyle\sum_\Omega \alpha_i \phi_i(x,y) \quad (13)$$

Or also,

$$M = \textstyle\sum_\Omega M_i \phi_i(x,y) \quad (14)$$

Being M_i the value of M in node *i*.

In the same way we adopt for the displacements w,

$$w = \textstyle\sum_\Omega w_i \phi_i(x,y) \quad (15)$$

We can express the displacements w_i as,

$$\hat{w}_i = \textstyle\sum_i w_i \phi_i(x,y) sen\,(ft+\beta) \quad (16)$$

Operating with the previous equations, (9),(10) and (11), we have,

$$\begin{aligned} &-\sum M_i^0 \iint_\Omega \nabla\phi_i \cdot \nabla V dA \\ &= -\Bigg[\sum \gamma h f^2 w_i^0 \iint_\Omega \phi_i(x,y)\, V dA \\ &- \sum \frac{\mu\gamma h^3}{10(1+\mu)} f^2 w_i^0 \iint_\Omega \nabla\phi_i \\ &\cdot \nabla V dA\Bigg] sen(ft+\beta) \end{aligned} \quad (17)$$

And also,

$$\begin{aligned} &\left[-\sum w_i^0 \iint_\Omega \nabla\phi_i \nabla\phi_j\, dA\right] sen(ft+\beta) \\ &= -\sum \frac{1}{D} M_i^0 \iint_\Omega \phi_i \cdot \phi_j dA \\ &- \frac{6\gamma}{5G(1+\mu)} f^2 \left[\sum w_i^0 \iint_\Omega \phi_i\phi_j\, dA\right] sen(ft \\ &+ \beta) \end{aligned} \quad (18)$$

If we take $\lambda = \frac{1}{f^2}$, we obtain a typical eigenvalue problem in the form,

$$\lambda I\{w_i^0\} = \left[\frac{\gamma h}{D}\psi^{-1}\Phi\psi^{-1}\Phi + \frac{(12+6\mu-6\mu^2)}{5E}\psi^{-1}\Phi\right]\{w_i^0\} \quad (19)$$

Where $\psi = \iint_\Omega \nabla\phi_i \nabla\phi_j\, dA$ and $\Phi = \iint_\Omega \phi_i\phi_j\, dA$.

We must bear in mind that the system of equations to be solved is very similar to the one which is formulated by the finite element method (MEF) by means of the stiffness matrix K and the mass matrix M.

10 RESULTS

In order to compare the results, we consider a simple supported isotropic rectangular plate with $\frac{a}{b} = 0.4$, [7], in which the pb-2 Rayleigh-Ritz method was adopted. These results are referred to the nondimensional frequency parameter ϖ given by,

$$\varpi = \frac{f^2 a^2}{\pi^2} \sqrt{\frac{\rho h}{D}} \tag{20}$$

Results are shown for different ratios thickness/length (0.01, 0.1 and 0.2) in the following Table 1.

Mode	h/a=0.01	h/a=0.1	h/a=0.2
1	7.250	6.4769	5.1831
4	22.231	16.847	11.489
8	33.999	23.400	15.036
Sol.1(Liew)	7.250	6.4773	5.1831
Sol.4(Liew)	22.233	16.845	11.487
Sol.8(Liew)	33.998	23.399	15.034

For the present results we have chosen linear interpolation functions (shape functions) corresponding to a linear triangle. The definition of the interpolation functions and the vector $\nabla\phi_i$ on each triangle is the one corresponding to a flat triangle

11 CONCLUSIONS

- In the present work we have shown a methodology for the numerical obtaining of the natural frequencies and modes of vibration of the transverse oscillations of moderately thick plates. We have based on a refined shear deformation plate theory.
- The comparison with other competitive numerical methods has allowed us to establish the goodness of the obtained solutions.

REFERENCES

[1] E. Reissner, *The effect of transverse shear deformation on the bending of elastic plates.* ASME Journal of Applied Mechanics, 12: 69-77,1945.

[2] J.M. Martinez Valle. *Equations transformed and expanded for a general study of isotropic plates with the Bolle-Reissner theory as a starting point*. 10th World Congress Computational Mechanics, Sao Paulo Brasil, 2012.

[3] K.J. Bathe. Finite Element Procedures. Prentice Hall of India Pvt. Ltd., New Delhi, 1996.

[4] M.S. Cheung and M.Y. Chan. *Static and dynamics analysis of thin and thick sectorial plates by the finite strip method.* Computers and Structures, 14(1):79-88, 1981.

[5] J. N. Reddy. *Theory and analysis of elastic plates and shells*. CRC Press, Taylor and Francis, 2007.

[6] R. Haberman. *Ecuaciones en derivadas parciales con Series de Fourier y problemas de contorno.* Prentice Hall, 2003.

[7] K.M. Liew and C.M Wang. *Pb-2 Rayleigh Ritz method for general plate analysis*. Engineering Structures, 15(1):55-60, 1993.

DAMAGE LIMITS IN THE FAÇADES AND PARTITIONS OF BUILDINGS SUBJECT TO THE SEISMIC ACTION

R. Álvarez Cabal†, E. Díaz-Pavón †, E. Díaz Heredia* and E. Carricondo Sánchez

* INTEMAC.
ETS Ingenieros de Caminos, Canales y Puertos
Universidad Politécnica de Madrid
28040 Madrid, Spain
e-mail: ediaz@intemac.es

†INTEMAC

Olave earthquake, on March 10, 2017, registered an acceleration of around 16% of the acceleration of gravity and a magnitude of 4.2. Despite the high value of the accelerations reached, no damage occurred so that the maximum intensity assigned in the municipalities in which it was felt was V. From the data provided by the IGN, we have had the opportunity to numerically simulate the spectrum, accelerogram and velocity of the seismic action of Olave earthquake. From the analysis of the spectrum, it is observed how the energy of the shock is concentrated in the components of greater frequency and fails to deliver important values in the own frequencies of buildings. This would justify that, in spite of the high accelerations recorded, the intensity assigned has been low. However, from the comparison of the velocity of the solicitation with the specifications established in DIN 4150-3, it can be deduced that this velocity was higher than the lower limit that the aforementioned standard sets as likely to cause cracks in covering and partitions of buildings. This last aspect, therefore, would justify some of the cracking patterns identified in partition walls of buildings after earthquakes of low magnitude and intensity but in which high accelerations are reached

Key words: seismic, damage, code, masonry, response

1 INTRODUCTION

Despite the high value of the accelerations reached in several of the earthquakes that have occurred in Spain, no damage was identified. According to the absence of damage maximum intensity assigned in the municipalities in which the earthquakes were felt was V.

We have had the opportunity to numerically simulate the spectrum, accelerogram and velocity of the seismic action of the Olave and Torreperogil earthquakes, and from the analysis of the spectra it has been possible to observe the velocity and the frequencies in which the shock energy is concentrated.

The values obtained have been compared with the limits of damage specified in different standards in an attempt to justify the few damages identified, limited to cracks in covering and partitions.

2 REPRESENTATIVENESS OF ACCELERATION

Existing historical acceleration records show certain pecularIarities. For example, it is not difficult to find records in which the maximum recorded acceleration corresponds to the vertical component.

Therefore, an important factor to consider in the seismic design is the representativeness of the maximum acceleration. Thus, the adoption of this as a base parameter should consider, among other aspects, the epicentral distance, since it determines the appearance of accelerograms.

[1] indicate that impulsive type accelerograms, very close to the epicenter, show a series of acceleration pulses of great magnitude, high frequency and small duration, which do not correspond at all to the effective acceleration experienced by the ground.

This would be in accordance with some of the earthquakes that occurred in the Peninsula in which very high accelerations have been recorded in relation to the magnitude and intensity assigned to the event.

This is the case of one of the earthquakes of the Torreperogil series (Jaén), an area of limited seismicity (a_b = 0.05g according to NCSE-02 and a_b = 0.08g according to the 2012 map update) where they were recorded accelerations of almost 0.2g, comparable to those of earthquakes as destructive as the one in Mexico in 1985.

In the same sense, in the Olave earthquake, in March 2017, the recorded acceleration reached values around 0.16 g. These are values not much lower than those registered in Lorca during the May 2011 event (0.36 g) and much higher than those registered in Melilla (0.1 g).

Both the values of Torreperogil and Olave are not consistent with the damage recorded or correlated with the intensity assigned or the magnitude of the event. In fact, and according to the correlation used in the standard itself, an acceleration of 0.2g registered would correspond to an intensity greater than VIII.

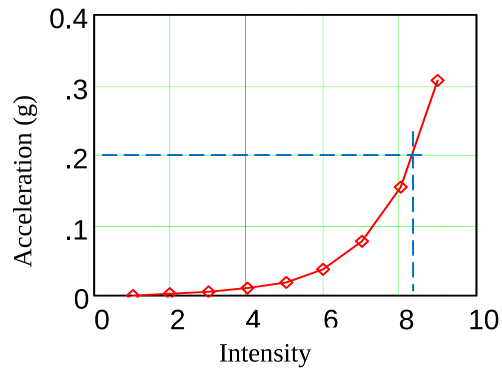

Figure 1: Intensity - Acceleration

3 SPECTRUMS OF OLAVE AND TORREPEROGIL EARTHQUAKES

From the data provided by the IGN, we have had the opportunity to numerically simulate the spectrum of the seismic action of Olave and Torreperogil earthquakes.

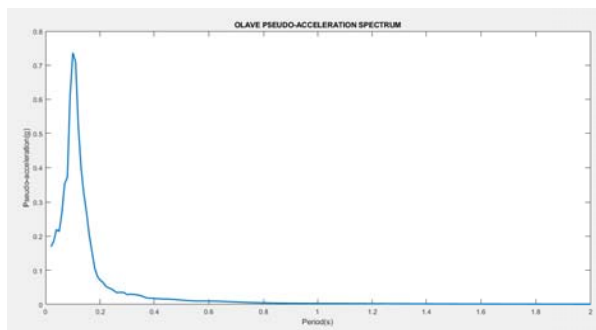

Figure 2: Olave pseudo-acceleration spectrum

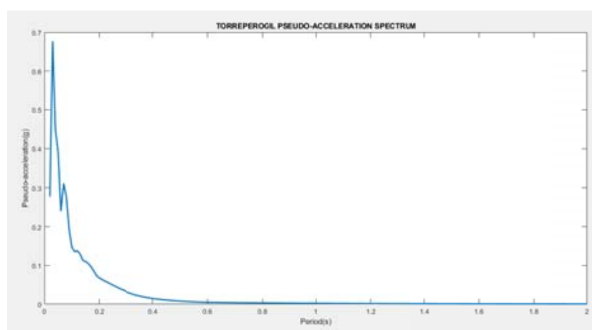

Figure 3: Torreperogil pseudo-acceleration spectrum

From the analysis of the spectrum, it is observed how the energy of the shock is concentrated in the components of greater frequency and fails to deliver important values in the own frequencies of buildings. This would justify that, in spite of the high accelerations recorded, the intensity assigned has been low.

4 BUILDING RESPONSE

From the displacement and acceleration spectra, a model is formulated for the evaluation of the displacements of the building.

Specifically, it is intended to estimate the maximum distortion between plants, defined as the difference between the horizontal displacements of each plant and the consecutive one. The model is formulated for a housing block, of five floors, which has been considered representative of residential construction in the area.

From the values of modal displacement the values in each plant of the relative distortion between plants have been determined, producing the maximum horizontal displacement in the ground floor, figure 4.

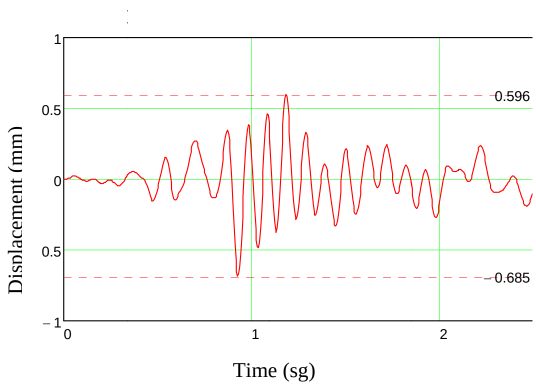

Figure 4. Distortion first floor

It is verified how the maximum value of the distortion reaches 0.23 ‰.

Compared to the maximum value obtained, the regulatory limit prescribed by the current UNE-EN 1998-1 is 5 ‰, clearly higher.

The values of distortion between plants obtained have been compared with the model of behavior of the masonry of Fardis [3] particularized for a typical wall of 2.5 m of height and 5 m of span.

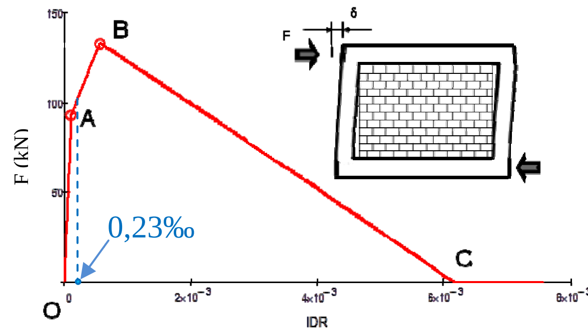

Figure 5. Behavior model of walls

According to the above, a distortion of 0,23 ‰ is enough to justify some damage to the masonry.

5 AFFECTION TO OTHER ELEMENTS

From the acceleration values, considering the component in which the maximum value was registered, we have expressed the record of the earthquakes in terms of velocity.

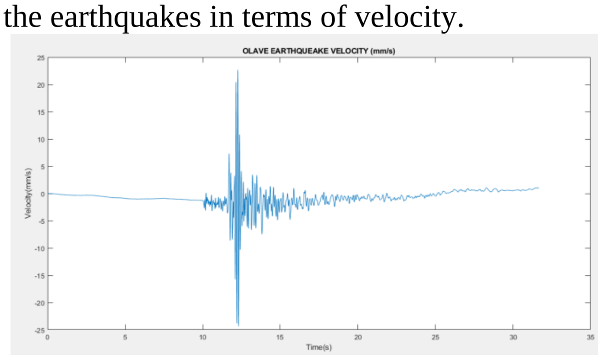

Figure 6: Olave earthquake velocity

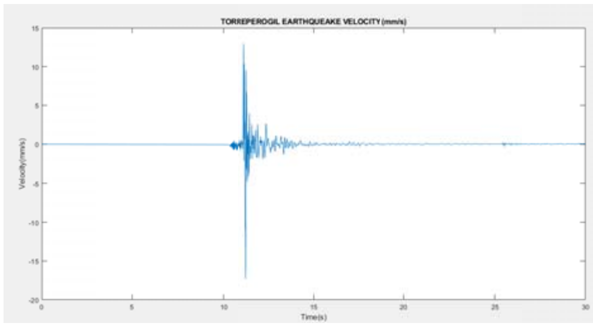

Figure 7: Torreperogil earthquake velocity

The transformation to the frequency range has been made following the indications included in Appendix D of DIN 4150-3, multiplying a Hanning type window by another one of the same extension in which the main amplitude of the temporal history of velocities is shown, attenuated at the extremes and in whose center the highest speed record reached was placed.

DIN 4150-3 does not specify the window size to be used. In the calculations a window of size 3 seconds has been considered to make the transformation of both registers, previously it has been tested with windows of different sizes, even with a window of a size in which the Aria Intensity of the vibration is collected, without significant variations in the final results.

Next we show the periodograms obtained where it is observed that in Olave for a frequency of 9.33 Hz the value of the associated velocity is 24.3692 mm/sg and in Torreperogil for a frequency of 6.331 Hz the value of the associated velocity is 17.3093 mm/sg.

From the comparison of the velocity of the solicitation with the specifications established in DIN 4150-3, it can be deduced that in both earthquakes the velocity was higher than the lower limit that the aforementioned standard sets as likely to cause cracks in covering and partitions of buildings. This last aspect, therefore, would justify some of the cracking patterns identified in partition walls of buildings after earthquakes of low magnitude and intensity but in which high accelerations are reached.

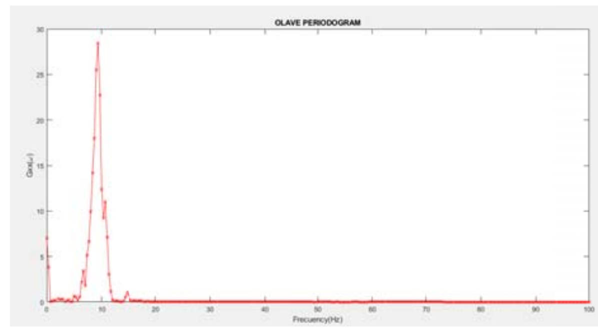

Figure 8: Olave periodogram

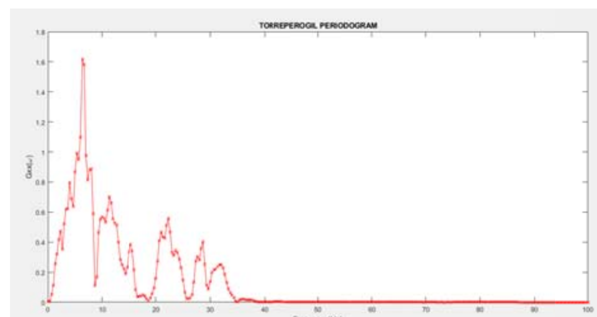

Figure 9: Torreperogil periodogram

REFERENCES

[1] Walter W. Hays *Procedures for Estimating Earthquake Ground Motions*. Geological Survey Professional paper 114, 1980.

[2] Blázquez, R. Suárez, A. Carreño, E. Martín, A.J. *Análisis de los acelerogramas de la serie de Adra (Almería) Diciembre de 1993 a Enero de 1994*.

[3] Fardis, Michael N. *Seismic design, assessment and retrofitting of concrete buildings based on EN-Eurocode 8*". Springer. 2009.

[4] DIN 4150-3. *Structural Vibration. Part 3: Effects of vibration on structures.* Deutsche Norm. February 1999.

PROGRESSIVE STRUCTURAL COLLAPSE POSSIBLE CAUSES OF IMPLEMENTATION IN THE SPANISH REGULATIONS. WAYS TO AVOID IT

Author: Julio Tortosa del Carpio

Doctor of Construction Engineering.

Civil Engineer.

Armaments and Construction Engineer.

NATIONAL INSTITUTE OF AEROSPACE TECHNOLOGY
(INTA)
Madrid, Spain

e-mail: *tortosacjr@inta.es*

Abstract: A building may undergo progressive structural collapse for various reasons: earthquake, accidental explosion or terrorist attack. In certain cases, it is required to carry out a study of progressive structural collapse and how to prevent it.

Key words: Progressive structural collapse, earthquake, explosions

----

1 INTRODUCTION

A building can suffer a progressive structural collapse due to various causes, earthquakes, accidental explosions or terrorist attacks. In certain cases, the study of progressive structural collapse and how to avoid it is mandatory.

Progressive collapse of a structure means the propagation of a local failure of the structure initially. This failure is transferred from element to element, resulting in the collapse of the entire structure, or a disproportionately large part of it, as the end result.

There are a number of conditions that can cause a structural failure of this nature, a number of possible causes of the non-exhaustive failure will be listed:

- Abnormal charges such as an accidental explosion.
- Explosion due to a terrorist act.
- Event of (Earthquake or Wind).
- Construction defect , design error.
- Unforeseen overload.
- Misuse of the building.

2 STATUS OF REGULATIONS ON PROGRESSIVE COLLAPSE TODAY.

The ASCE/SEI 7 standard defines progressive collapse as:

"The propagation of a localized initial failure, from element to element, eventually resulting in the total collapse of the structure or a disproportionately large part of it."

A more complete definition would be the following:

Progressive collapse of a structure means the propagation of an initial local structural failure. This failure is transferred from element to element, resulting in the collapse of the entire structure, or a disproportionately large part of it, as the end result.

One of the first regulations that contemplated the progressive collapse in its design was the Building Regulations in England, due to an event that took place in London. Specifically in the Ronan Point Tower building in London in 1968. A small-scale explosion occurred due to a gas leak on the 18th floor, which resulted in partial collapse, extending to a progressive collapse. In response, England adopted the design against progressive collapse in its regulations in 1970.

Figure. 1 Ronan Point Tower. Source Newhan.com

Measures were also introduced to protect buildings in the event of an explosion. This new Standard stipulated that all new buildings constructed and more than 5 stories high must be capable of withstanding an explosive force of 34 kPa (4.9 psi).

In the USA, since the attack on the A. P. Murrah Federal Building in Oklahoma in 1995, with an explosive charge, and especially since the 11 M attack on the Twin Towers, the development of regulations to prevent progressive structural collapse has been promoted through the UFC (Unified Facilities Criteria). And also the protection of buildings against terrorist attacks, by means of explosives.

In the EN Eurocode[2], in the building design, permanent actions, variable actions, and accidental actions must be taken into account. In the Eurocode, two actions are cited as accidental: impacts and explosions. It also proposes detailed models to estimate the calculation values of accidental (exceptional) load caused by impacts or explosions. It does not cover actions for explosions attributable to sabotage or war.

The reference standard in Spain for building is the Technical Code[3], this standard is the mandatory standard for building. For the structural calculation of a building in Spain at present, it is compulsory to follow these rules for the structural calculation, although the calculations would have to be carried out according to the Eurocodes.

The Technical Code, in section 3.3.2.1 Classification of Shares. Accidental actions:

These are those whose probability of occurrence is small but of great importance, such as earthquakes, fires, impacts or explosions. The imposed deformations will be considered as permanent or variable actions.

Specifically in the T.C., it does not specify how the effect produced by the explosions is calculated. The T.C. does not specify how to model this type of effect on a structure. It would be necessary to incorporate in the T.C., the way of valuing this type of actions.

The C.T. I'd have to consider, two aspects. First, how to model the effects of an explosion on a structure, and second, how to design a structure to prevent progressive collapse.

3 EXTERNAL EXPLOSIONS.

Due to the globalisation of terrorism throughout the world, it would also be necessary to have an equality regulation that exists in the USA, for example, "Unified Facilities Criteria (UFC)". This Regulation contemplates the calculation of buildings subjected to external explosions, in particular the following Regulation within the series of UFC "Structures To Resist The Effects Of Accidental Explosions", which contemplates the whole process for the protection of a building against accidental actions produced by explosions, also derived from terrorist attacks in the form of explosives (for example, car bombs, or any other type of explosive device).

These regulations basically provide for the protection of the constructive elements of a building, and the stand-off (safety distance).

Among the basic building elements of a building that must be protected against such threats are the following:

- Structure of the building, reinforcement against the loads caused by the shock wave and above all to prevent progressive structural collapse.
- Enclosures, facades.
- Cover - Cover
- Doors and windows

4 CALCULATION METHODS.

Among the different calculation methods that exist to avoid progressive collapse is the so-called. "Alternate Path Metodh (APM)", this method explained in a succinct way, is that if a pillar fails structurally, the structure would not enter into progressive structural collapse. By reticularity, the load is distributed to the adjacent abutments, thus avoiding progressive structural collapse. It is important to point out that on the pillars that transport the load, the total load is notably increased, finally all this load is transported to the foundation, and it is transferred to the ground, suffering an important increase in its solicitations, adding also dynamic effects in the case of structural failure due to accidental explosions, earthquakes, etc.

5 GROUND FAILURE DUE TO PROGRESSIVE STRUCTURAL COLLAPSE:

It is important to note that in no rule (not even in the U.S. CFU), is there any action on the ground or foundation, which supports the building designed and calculated so that it does not have a progressive structural collapse.

If a pillar fails, for example due to an explosion, and the building is designed so that it does not collapse, the load of that pillar will be distributed to the adjacent pillars by the effect of the reticularity, these in turn will channel them to the foundation and finally this load will transfer it to the ground, there will be an increase in the loads on it. Failure to take this into account may result in a building prepared and calculated to avoid progressive collapse, which could collapse due to a local failure of the ground on which it rests, due to a sudden increase in load in certain areas where the foundations of this building are laid.

A possible way to avoid this ground failure would be to treat the ground itself, choosing the most suitable of the different treatments that exist, taking into account the type of ground and loads that it will receive.

REFERENCES

[1] U.F.C. Unifies Facilities Criteria (2005). Design build technical requirements. UFC 1-300-07A. Washington, DC. US Army Corps of Engineers.

[2] IN 1990 - IN 1999, EN Eurocodes are a series of 10 European standards.

[3] Spain. Royal Decree 314/2006, of March 17, which approves the Technical Building Code. B.O.E. of March 28, 2006. No. 74. P. 11816-11831.

1st Conference on Structural Dynamics (DinEst 2018)
Madrid, 20-21 June

THE EFFECT OF CORE THICKNESS OF VISCOELASTIC SANDWICHES ON THE DYNAMIC RESPONSE OF A LIFT

J. Iriondo*, L. Irazu*, X. Hernández and M. J. Elejabarrieta***

* Mechanical & Manufacturing Department
Mondragon Unibertsitatea
20500 Arrasate-Mondragon, Spain
e-mail: jiriondo@mondragon.edu
ORCID: 0000-0002-3321-6460

** Orona
20120 Hernani, Spain
e-mail: xhernandez@orona-group.com

Abstract. The use of thin viscoelastic sandwiches in terms of vibration attenuation has been widely validated. Sandwich structures composed of viscoelastic adhesive films and metallic constraining layers result in thin composite structures with improved dynamic capabilities. Due to the viscoelastic core, the damping capacity of the sandwich is considerably increased compared to metallic panels. In addition, the small thickness of these sandwich structures enables them to be processed in conventional metal sheet transformation techniques to obtain damped components of complex geometries. In this work, a numeric model of a lift using viscoelastic sandwiches is presented in order to evaluate the influence of the viscoelastic film thickness on the dynamic response of a lift. A fractional derivative viscoelastic model is proposed to determine the shear complex modulus of the adhesive film and a numerical model of the lift is developed. Different control points have been selected for the evaluation of the dynamic response. The results show that the thickness of the viscoelastic film determines the vibrational response of the lift.

Key words: Viscoelastic sandwich; Complex modulus; Numerical model; Lift

1 INTRODUCTION

Passive damping techniques by means of viscoelastic materials are cost-effective ways to control structural vibrations and dissipate acoustic energies. The viscoelastic material can be confined between two rigid layers to form a sandwich structure in which the viscoelastic material deforms in shear mode dissipating energy. These structures are of special interest for applications in which the mass of components is critical, and high strength-to-weight and stiffness-to-weight ratios are desired, such as in aeronautical, automotive, railroad and marine industries [1].

Currently, the conventional viscoelastic materials used to form sandwich structures are being replaced by micron-size viscoelastic adhesive films [2][3][4]. The use of these adhesives and metallic constraining layers result in sandwich structures with high stiffness-to-weight and damping-to-weight ratios. In addition, the total thickness of the sandwich is similar to that of the metal sheets, which makes possible to use them on classic sheet metal forming processes. This feature is of special interest because damped pieces of complex geometries can be obtained with less manufacturing steps, saving time and costs.

Considering that the noise and vibration levels are increasingly imposed by the legislator with strict regulations, the importance of the NVH behavior is no longer negligible and it has become a fundamental differentiator. Therefore, the use of sandwich structures formed by viscoelastic films could be an interesting alternative to conventional materials in vertical transport applications such as lifts.

The main aim of this work is to study the effect of core thickness of viscoelastic sandwiches on the dynamic response of a lift. Three thin sandwich structures composed of different thickness of viscoelastic films are analysed. The experimental characterisation by means of a forced vibration test with resonance carried in a previous work [2] is used. Then, the numerical modelling of the specimens is presented and validated using the software ABAQUS 6.14 where the dynamic response of the lift built of sandwich structures is calculated. Finally, the dynamic response of the tree different sandwiches is compared in order to determine the influence of the thickness of the core in the attenuation of the vibrations into the passenger cabin.

2 MATERIAL

2.1 Geometrical properties

The sandwich structure analysed is symmetric and composed of thin viscoelastic films and metallic skins. A polyester-based adhesive is used as a viscoelastic core, and a stainless steel AISI 316 as metallic skins. The geometrical and physical properties of the sandwich structure and the constituent materials, used for the validation, are summarized in Table 1 and Table 2 respectively. Note that $(\cdot_e)$ and $(\cdot_v)$ refer to the elastic and viscoelastic layers.

Sandwich		
H (±0.002 mm)	b (±0.1 mm)	ρ (±0.05 g/cm^3)
0.472	9.9	7.37

Table 1: Geometrical and physical properties of the sandwich

Metallic skin		Viscoelastic layer	
H_e (±0.002 mm)	ρ_e (g/cm^3)	H_v (±2 μm)	ρ_v (g/cm^3)
0.216	7.96	41	1.13

Table 2: Geometrical and physical properties of the constituent materials

2.2 Material characterization

Both the metallic skins and the viscoelastic core were characterised by means of a forced vibration test with resonance. The whole experimental procedure carried out is described in a previous work [2]. The metallic skins showed an elastic behavior, where a elastic modulus of 205.7 GPa was calculated, while the frequency dependence is specially significant in the case of the viscoelastic core. A four-parameter fractional derivative model was used to describe the dynamic behavior of the adhesive. The complex shear modulus of the viscoelastic core obtained by the mentioned model is showed in Figure 1.

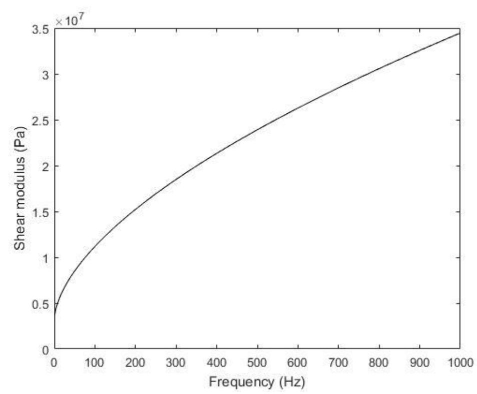

(a)

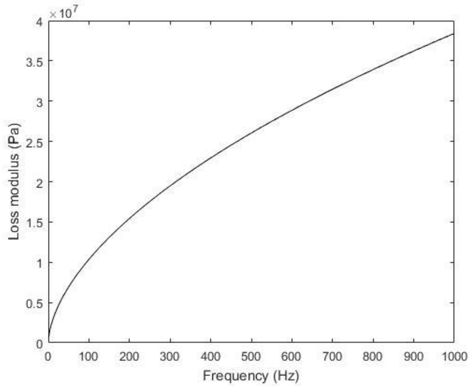

(b)

Figure 1: The fitted shear complex modulus (a) shear modulus and (b) loss modulus

The strong frequency dependence of the adhesive involves a significant increase of both the stiffness and the damping as the frequency increases. The use of a viscoelastic adhesive in a sandwich configuration, allows an important improvement in the attenuation of the vibrations, with practically no variation in the stiffness. In Figure 2, a comparison between a sandwich beam and a metal beam, with the same thickness of that of the sandwich is shown.

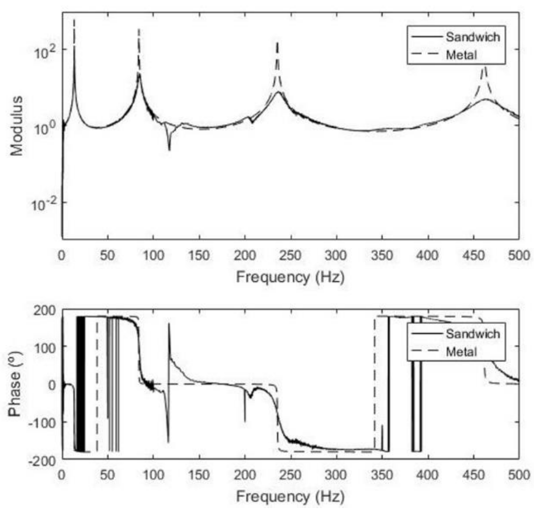

Figure 2: The transmissibility functions of the metal and sandwich beam

3 NUMERICAL MODEL

The numerical model was developed by the software Abaqus. Both the two metallic skins and the viscoelastic core were discretised using solid elements C3D20R. In general, the standard dimensions of the passenger cabin of lift are about 2.2m x 1.5m x 1m. Consiering symmetry and in order to reduce the model, a quarter of the lift was modeled.

In a common configuration, a passenger cabin is guided along rails. The contact between the rails and the cabin occurs at the lateral panels. Therefore, the model was built using the sandwich structure in the lateral panel and steel panels in the rest of the cabin. A base motion of a 10 mm displacement in a frequency range up to 100 Hz was considered as an excitation source and the transmissibility function between the lateral face and front face was calculated.

Three different sandwich structures were studied with three different core thicknesses: 25 µm, 100 µm and 250 µm. The validation of the model was performed using a sandwich structure with a viscoelastic core of 41 µm, a length of 170 mm and a width of 10 mm due to the experimental measurement available. It should be noted that linear vibrations were considered in the analysis and the attenuation was considered in terms of the direct transmissibility function.

4 RESULTS AND DISCUSSION

The validation of the model was performed using a sandwich of a 41µm thickness core. In Figure 3 a correlation between the transmissibility function of the sandwich beam obtained by ABAQUS and the transmissibility function obtained experimentally by means of the forced vibration test with resonance, are shown. A frequency range up to 200 Hz was studied.

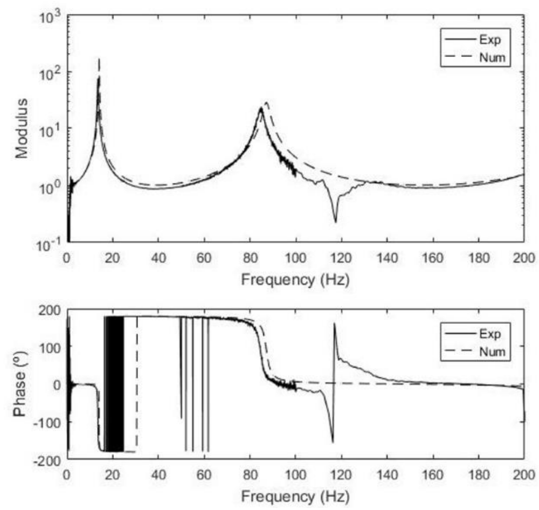

Figure 3: Experimental and numerical transmissibility functions

A good correlation was observed between both transmissibility functions and the model was validated.

In Figure 4, the comparison between the three transmissibility functions obtained using different core thicknesses are shown.

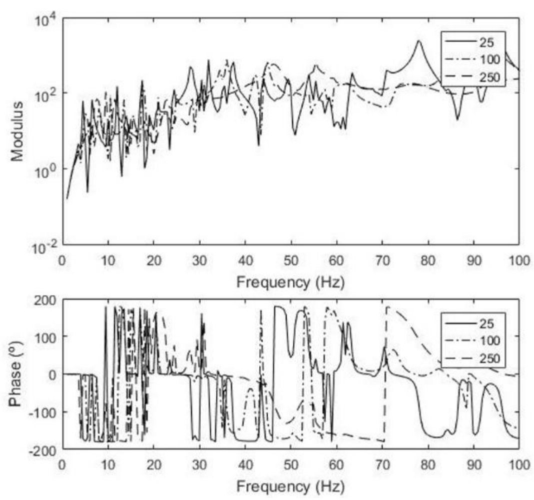

Figure 4: Transmissibility functions of the sandwiches of 25 µm, 100 µm and 250-µm thickness

The thicker sandwich exhibited the greatest attenuation. As the thickness of the core decreases, the damping capacity of the sandwich decreases. Therefore, at frequencies up to 100 Hz, where the main vibrations are located, the increment in the attenuation becomes significant as the thickness of the core increases.

5 ACKNOWLEDGEMENT

The present study has been partially supported by AVISANI (DPI2015-71198-R, Spanish Government) and AVISANI (PI_2016_1_0026, Basque Government) projects and Replasa S.A.

6 CONCLUSIONS

- The attenuation of vibrations of a sandwich with a viscoelastic core was demonstrated.
- The numerical model of a lift was validated based on the correlation carried out between the numerical and experimental transmissibility functions of a beam.
- The attenuation of the vibrations of the lift increases as the thickness of the core increases.

7 REFERENCES

[1] M. Rao, “Recent applications of viscoelastic damping for noise control in automobiles and commercial airplanes,” *J. Sound Vib.*, vol. 262, no. 3, pp. 457–474, May 2003.

[2] L. Irazu and M. J. Elejabarrieta, “The influence of viscoelastic film thickness on the dynamic characteristics of thin sandwich structures,” *Compos. Struct.*, vol. 134, pp. 421–428, Dec. 2015.

[3] M. Martinez-Agirre and M. J. Elejabarrieta, “Characterisation and modelling of viscoelastically damped sandwich structures,” *Int. J. Mech. Sci.*, vol. 52, no. 9, pp. 1225–1233, 2010.

[4] M. Martinez-Agirre and M. J. Elejabarrieta, “Dynamic characterization of high damping viscoelastic materials from vibration test data,” *J. Sound Vib.*, vol. 330, no. 16, pp. 3930–3943, 2011.

SECTION 2: Tests and dynamic monitoring, damage detection, system identification, vibration control

1st. Conference on Structural Dynamics (DinEst 2018)
Madrid, 20–21 June

TUNING A PHASE-CONTROLLED SMART TMD FOR BROAD-BAND-FREQUENCY-VARYING VIBRATION MODES

José M. Soria*, **Iván M. Díaz***, **Jaime H. García-Palacios***, **Carlos Zanuy*** and **Xidong Wang***

*Department of Continuum Mechanics and Theory of Structures
ETS Ingenieros de Caminos, Canales y Puertos
Universidad Politécnica de Madrid
28040 Madrid, Spain

e-mail: jm.soria@upm.es

Abstract. Lightweight and high-span pedestrian structures are usually prone to vibrate excessively. Although current codes may be fulfilled, these structures are not usually comfortable in any way. Control devices can mitigate vibration and improve significantly the comfortability as well as increase the structure life span. This paper describes a semi-active vibration control strategy based on a Semi-active Tuned Mass Dampers implements through the use of a Magneto-Rheological damper (MR-STMD) for lightweight slender structures. It is important to include the Magneto-Rheological damper model in the simulation in order to be aware of the loss of effectiveness respect to the perfect linear-viscous damping model in a STMD. The STMD increases significantly the controller robustness but the enhancement for MR-damper models are smaller than the one predicted by the perfect viscous case.

Key words: Semi-active vibration control; Smart Tuned Mass Damper; Magneto-Rheological damper.

1 INTRODUCTION

Control devices can mitigate vibration and improve significantly the vibration comfortability as well as increase the structure life span of flexible structure. Vibration control techniques are classified into passive, active, hybrid and semi-active strategies. In the last two decades, considerable research efforts have been devoted to semi-active vibration control strategies, mainly due to their inherent advantages. When structures show modal properties changing over time, and/or several vibration modes [4] must be canceled by the same device, passive devices (Tuned Mass Dampers, TMD, are the most popular ones) may detune and experience a significant loss of efficiency. Under these circumstances, the use of semi-active devices may be an alternative [6, 5]. Thus, semi-active TMD (STMD) through the use of controllable magneto-rheological damper (MR-STMD) as dissipation device has been developed. However, several issues have to be tackled carefully when broad-band frequency vibrations are to be canceled: i) the frequency tuning, ii) the control law (an on-off phase control is adopted) and iii) MR properties.

This paper studies the above mentioned issues. That is, the performance of TMD and STMD assuming ideal viscous damping as well as MR-TMD and MR-STMD are studied, including the Magneto-Rheological damper (MR-damper) model in the simulation obtaining, under a time-varying modal-property targeted mode.

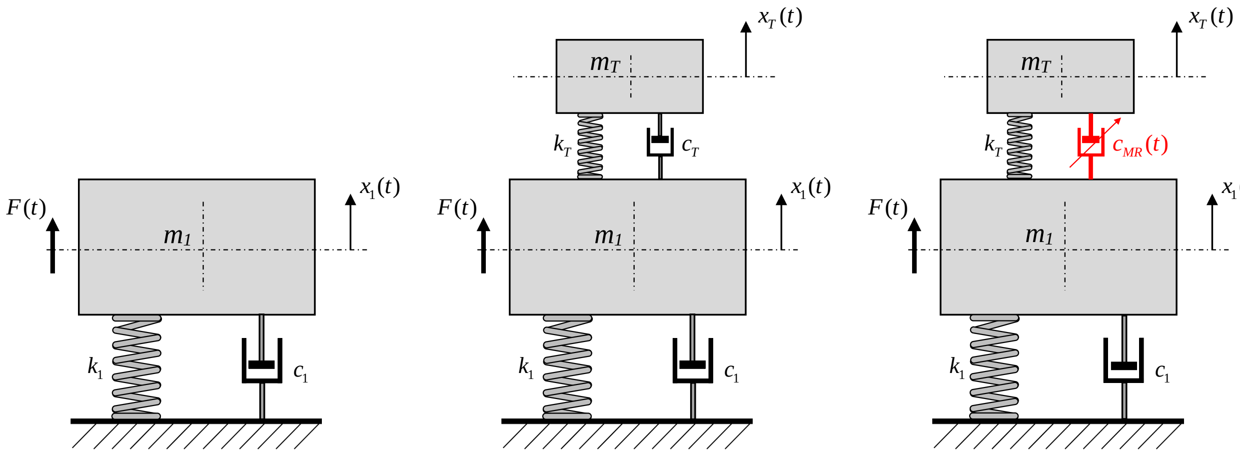

(a) Uncontrol SDOF model. (b) Passive control, 2-DOF. (c) STMD control, 2-DOF.

Figure 1: Model of the different systems studied. The second box is the control device installed on a primary structure. Red symbol (↗) means changing over time.

2 PASSIVE CONTROL, TUNED MASS DAMPER

A TMD consists of a secondary mass attached to the structure by means of springs and dampers. Figure 1a shows the model of a classical TMD composed of an inertial mass m_T attached to a primary system by means of a spring of constant k_T and a viscous damper of constant c_T. The primary system is the structure modeled as a SDOF system, which is composed of a mass m_1, a spring of constant k_1 and a viscous damper of constant c_1. The TMD properties are obtained from the Den Hartog [2] formulaes,

$$\eta = \frac{1}{1+\mu} \tag{1}$$

$$\zeta_{\mathrm{T}} = \sqrt{\frac{3\mu}{8(1+\mu)^3}}, \tag{2}$$

in which $\mu = m_T/m_1$ is the mass ratio and $\eta = \omega_T/\omega_1$ is the frequency ratio and the stiffness and damping ratio for the TMD are obtained from

$$k_T = \omega_T^2 m_T \tag{3}$$

$$c_T = 2\zeta_T m_T \omega_T, \tag{4}$$

respectively.

3 SEMI-ACTIVE TUNED MASS DAMPER

3.1 Phase control

Figure 1c shows a STMD in which the TMD damper is supposed to be a MR-damper ($c_{\mathrm{MR}}(t)$), whose damping can be changed continuously through a control feedback. A phase control strategy proposed by Moutinho [3] for the TMD damping has been adopted. The control law achieves a phase lag between the control force (the force coming from the TMD) and structure displacement close to 90° even in situation of significant detuning. The control law adopted is of ON/OFF type due to its simplicity. Thus, the adopted control law is defined as:

$$\begin{cases} \ddot{x}_1 \cdot \dot{x}_T \leq 0, & c_{\mathrm{MR}} = c_{min}\,(\text{normal}) \\ \ddot{x}_1 \cdot \dot{x}_T > 0, & c_{\mathrm{MR}} = c_{max}\,(\text{blocking}), \end{cases} \tag{5}$$

in which c_{max} is the maximum damping achieved by the MR-damper, c_{min} is the optimal damping obtained from passive TMD tuning, $\ddot{x}_1$ is the structure acceleration (obtain by an accelerometer) and $\dot{x}_T$ is the absolute velocity of the TMD mass (which might be obtained from the integration of an accelerometer signal installed on the TMD mass).

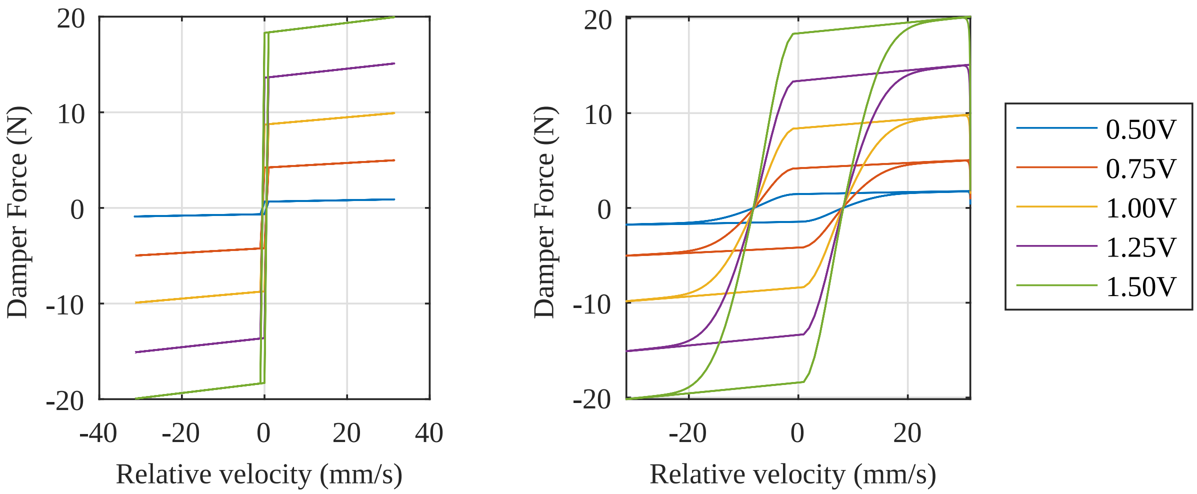

(a) Bingham MR-damper model. (b) Bouc-Wen MR-damper model.

Figure 2: Response of Bingham and Bouc-Wen MR-damper models for 1.00 Hz sinusoidal excitation with 5mm amplitude and different input voltages.

Figure 3: Sponge RD-1097-1 MR-damper from Lord Corporation company.

4 DAMPER TUNING: BINGHAM AND BOUC-WEN MR-DAMPER MODELS

The phenomenological model are considered here for the MR-damper: Bingham and Bouc-Wen models. The objective is to study how the TMD and STMD performaces degrade when MR-damper models are considered as compared to ideal linear-viscous damping.

Figure 2 shows the response of Bingham and Bouc-Wen MR-damper models using the parameter's model proposed by Braz and Carneiro [1] for sponge RD-1097-1 MR-damper (see Figure 3) for a load excitation of 1.00 Hz sinusoidal with 5 mm amplitude and different input voltages. Figure 2 shows the damper force against the relative velocity of the MR-damper.

4.1 Simulated results

The simulations carried out have the following variables and parameters:

- As an excitation, it has been applied a chirp signal of constant amplitude of 50 N and lived frequency varying from 0.1 and 6 Hz with a sampling frequency of $f_s = 500$ Hz.
- The structure parameters are: mass of $m_1 = 500$ kg, frequency of $f_1 = 1$ Hz and damping ratio of $\zeta_1 = 0.5\%$.
- The TMDs parameters are changing and different for each case (f_t from 0.1 up to 2 f_1 and ζ_t from 0 to 0.2 in the linear case and from 0 up to 0.5 A with the magneto-rheological models), only the mass ratio has a constant value of $\mu = 2\%$ ($m_T = 10$ kg). The results are shown for a normalized frequency f_n instead of f_t.

Different tuning cases, varying the normalized frequency of tuning f_n and the damping of the

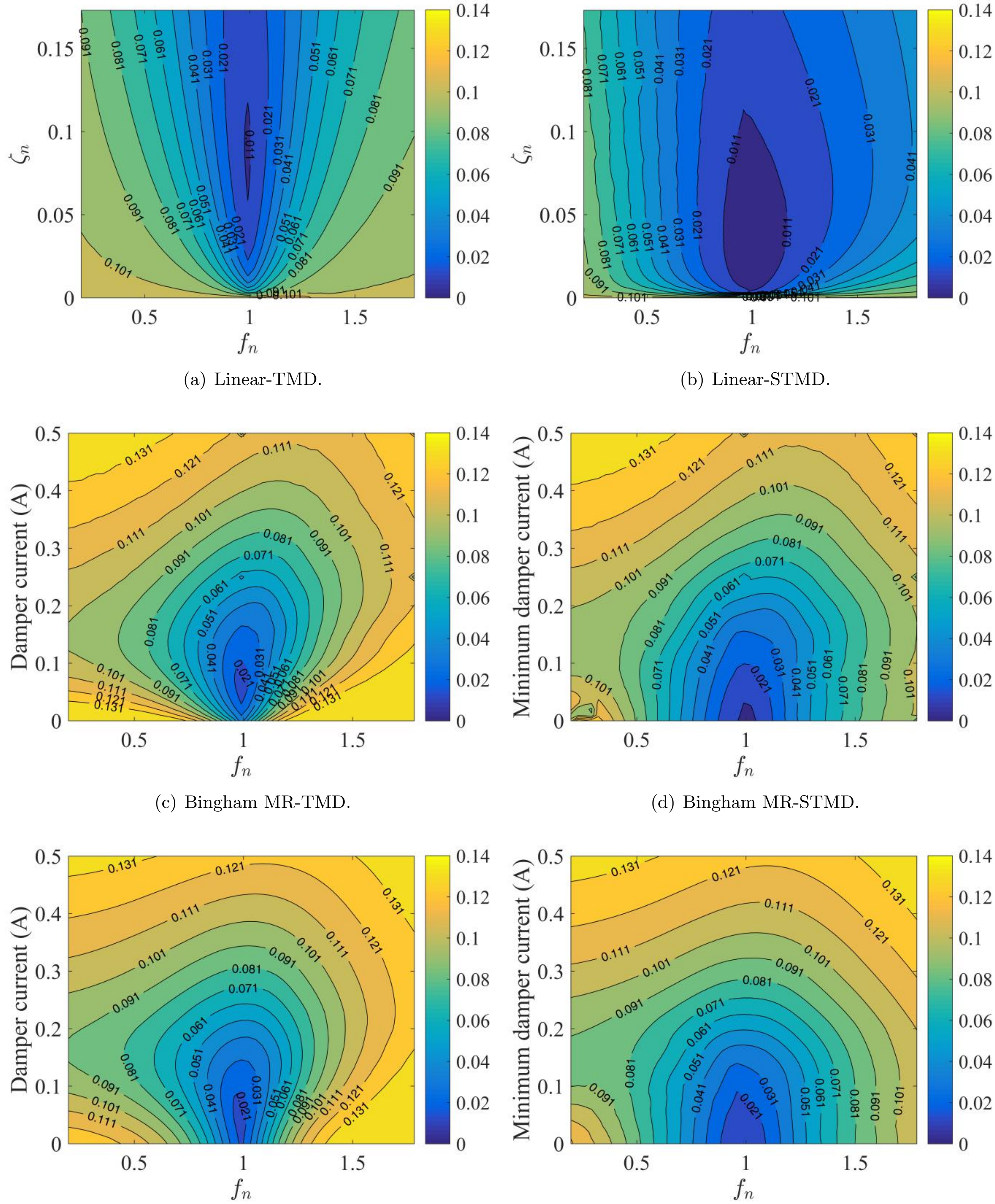

(a) Linear-TMD.

(b) Linear-STMD.

(c) Bingham MR-TMD.

(d) Bingham MR-STMD.

(e) Bouc-Wen MR-TMD.

(f) Bouc-Wen MR-STMD.

Figure 4: Maximum frequency spectrum of the different systems studied (abs) for different damping models.

TMD ζ_n (current for MR-damper models), have been calculated for the different models (linear TMD, linear STMD, Bingham MR-TMD, Bingham MR-STMD, Bouc-Wen MR-TMD and Bouc-Wen MR-STMD). In the semi-active cases, only the minimum damping value is tuning because the blocking value is the maximum (current for MR-damper model).

For each case, the the maximum value of spectrum response is obtaining from the frequency domain response. Contour plots are obtained for each case study indicating constant isolines (Figure 4). Theses surfaces are an useful tool to compare the different cases: TMD and STMD behavior (viscous-lineal damping) and also to compare these results including MR-damper models, MR-TMD and MR-STMD.

5 DISCUSSION

From Figure 4, the following conclusions can be drawn:

- From (a) and (b) (linear damping cases), the STMD increases significantly the controller robustness, 266% of enhancement. Also, it is seem the STMD works better for smaller c_{min} than TMD.
- Similar conclusion as before are achieve from (c) and (e) and (d) and (f). However, the enhancement is now much smaller than the one predicted by the perfect viscous case. Thus, this shows as that the MR model should be considered into the control law design. This control law should considered the highly non-linear behavior.
- For quantifying the enhancement of the performance, Table 5 shows the normalized area inside of a reference isoline (0.021):

Damping	TMD	STMD
Linear-viscous	21.13	77.26
Bingham model	1.000	5.592
Bouc-Wen model	1.299	3.826

- The optimum tuning frequency f_n in semi-active remains similar to the passive cases but in a non-symmetrical area. This issue is important to take into account if there are uncertainties for the modal parameters of structure.

ACKNOWLEDGMENTS

The authors acknowledge the support provided by the *Department of Continuum Mechanics and Theory of Structures* of ETSICCP at UPM and by the Research Net VIBRASTRUNET (BIA2015-71942-REDT).

REFERENCES

[1] M Braz Cesar and R Carneiro De Barros. Properties and Numerical Modeling of MR Dampers. In *15th International Conference on Experimental Mechanics*, Porto, Portugal, 2012.

[2] J.P. Den Hartog. *Mechanical vibrations*. Courier Corporation, 1985.

[3] C. Moutinho. Testing a simple control law to reduce broadband frequency harmonic vibrations using semi-active tuned mass dampers. *Smart Materials and Structures*, 24(5):964–1726, 2015.

[4] José M Soria, I.M. Iván M Díaz, Jaime H García-Palacios, and Norberto Ibán. Vibration Monitoring of a Steel-Plated Stress-Ribbon Footbridge: Uncertainties in the Modal Estimation. *Journal of Bridge Engineering*, 21(8):1–13, 2016.

[5] José M. Soria, Iván M. Díaz, and Jaime H García-Palacios. Vibration control of a time-varying modal-parameter footbridge: study of semi-active implementable strategies. *Smart Structures and Systems*, 20(5):525–537, 2017.

[6] José M Soria, Iván M Díaz, Emiliano Pereira, Jaime H García-Palacios, and Xidong Wang. Exploring vibration control strategies for a footbridge with time-varying modal parameters. In *MOVIC & RASD 2016*, Southampton, 2016.

DYNAMIC CHARACTERIZATION AND SERVICEABILITY ASSESSMENT OF A TIMBER FOOTBRIDGE

Á. Magdaleno[1*], N. Ibán[2], V. Infantino[3] and A. Lorenzana[1]

[1]ITAP. Escuela de Ingenierías Industriales
Universidad de Valladolid
47011 Valladolid, Spain

[2]Centro Tecnológico CARTIF
Parque Tecnológico de Boecillo
47151 Boecillo, Spain

[3]DICEAM
Università degli Studi Meditteranea di Reggio Calabria
89124 Reggio Calabria, Italy

Abstract. This paper shows the experimental and numerical methodology used for the modal characterization and serviceability assessment applied to a timber pedestrian walkway. The footbridge is a 103 meters long and 2 meters wide structure consisting on 4 prefabricated modules designed by Media Madera, mounted between the two abutments at the ends and three intermediate supports. It crosses the Duero River at Pesquera, Valladolid, with, from right to left, four spans of 12, 50, 18 and 23 m. It is part of the Senda del Duero, a natural trail (GR14) of 37.5 km concluded in 2013. With applied research motivation, an experimental campaign was carried out in January 2018. Useful data has been collected to calibrate the computational model of the structure. Also serviceability dynamic tests were carried out to quantify the vibrations induced by pedestrian crossing.

Key words: Timber footbridge, Model updating, Serviceability assessment

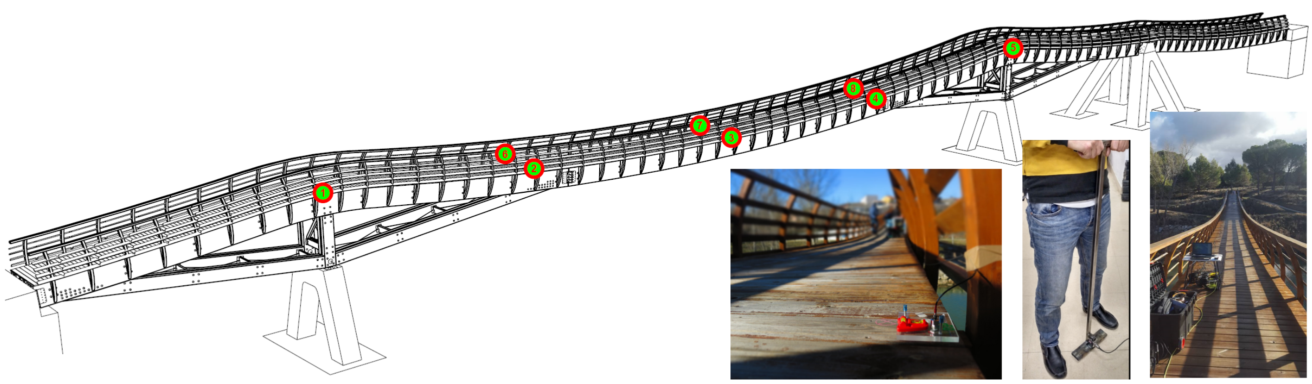

Figure 1: Experimental layout and details of datalogger, accelerometer and pogo

*Corresponding Author. E-mail: alvaro.magdaleno@uva.es ; ORCID: 0000-0002-5606-1545

1 INTRODUCTION

Some well-known structural dynamic drawbacks can take place in low damped slender footbridges when they are crossed by pedestrians. Depending on the pace, either walking or running, semiperiodic ground reaction forces are applied and, in case of resonance, mechanical response may exceed some desirable limits, both regarding to the ultimate stress behaviour and serviceability points of view. In the first case, structural integrity can be compromised and in the second, users can experience uncomfortable sensations that could affect their own pace and even give rise to certain interaction phenomena [1].

From the assessment point of view, in the design stage, the comfortability of a footbridge can be estimated following some procedures described in standards and design guides. Thus, for example, the EAE 2011 in its article 38.3.2 establishes, for vertical movements, the convenience of carrying out additional dynamic checks when the span exceeds 50 m and the natural frequencies lay in the rank between 1.25 Hz and 4.6 Hz. It is desirable that the acceleration (in some points of the structure) under the intended use will not exceed 2.5 m/s^2. For the case study, preliminary estimate for the first vertical bending mode is 3.13 Hz. As the structure is longer than 50 m, additional dynamic studies are convenient, as described below.

2 EXPERIMENTAL SET-UP

In order to register the response of the structure and to identify its vibration modes, natural frequencies and modal damping ratios, eight uniaxial accelerometers (MMF-KS76C, 100 mV/g) are placed in the vertical direction at points 1 to 8 of the central span shown in Figure 1. The eight locations have been distributed along the span so the first and second bending and torsional modes can be properly identified. All the recordings are synchronously registered at 1024 S/s by means of a data logger (SIRIUS-HD 16xSTGS) located at the position 4. In this place there is also a pogo instrumented with a load cell at its lower end whose force signal has been recorded synchronously along with the accelerometer signals. Details in Figure 1 show part of the described layout: the data logger, one accelerometer and the pogo. The intention is to excite the structure in a controlled way by jumping on the pogo. As the point of excitation does not match to any node of vibration for the predicted (by simulation) 1st and 2nd bending and torsional modes, a good modal identification is expected. Note that one average person jumping on the pogo has a significant body weigh in comparison with the mass of the lightweight footbridge and therefore the structure can be effectively excited. Figure 2 shows, for one test, the recordings of the accelerometers located at points 3 and 4 and also the pogo force.

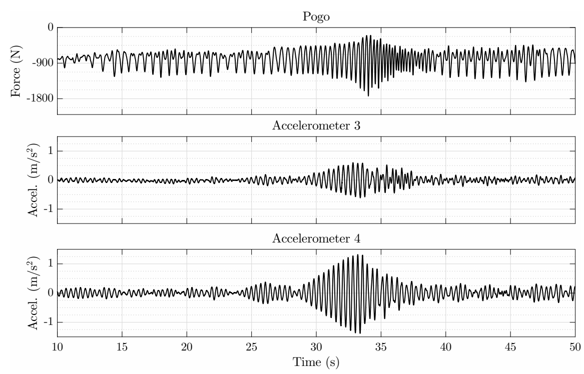

Figure 2: Recorded signals from the pogo and the accelerometers 2 and 3

3 MODAL IDENTIFICATION

Taking the pogo force at point 4 as input and the response at the 8 monitorized points as outputs, eight frequency response functions (FRF) can be evaluated. The Dewesoft software [https://www.dewesoft.com/] allows, for each peak, to visualize the corresponding modal shape. After the interpretation of these shapes, it is concluded that the peak at 2.67 Hz accounts for the first bending mode, the peak at 3.55 Hz corresponds to the first torsion mode and the peaks at 4.28 Hz and 5.7 Hz are for the second bending and torsion modes, respectively. According to the EAE 2011 standard, only the first three ones are under 4.6 Hz and, thus, they are likely to be excited by pedestrian activities. However, from the point of view of the statistical distribution of human steps and the intended use of the pedestrian walkway (occasional trekking), the mode of greatest interest is the first one and the following sections will focus on it. For an accurate identification of this mode of interest, several tests were carried out jumping on the pogo in point 3. Figure 3 shows the auto FRF where up to 4 peaks are clearly identified in the displayed range (1.5 Hz to 8.0 Hz).

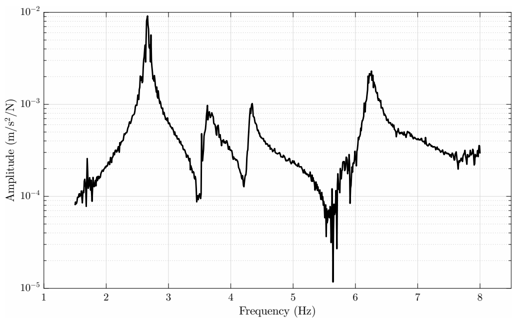

Figure 3: Auto-FRF at point 3

4 FIRST MODE PARAMETERS

From the dynamic point of view, it is desirable to know the mass M, the stiffness K and the damping C of an equivalent one-degree-of-freedom (1DOF) system, whose equation of motion is stated in Eq. 1. From the auto FRF shown in Figure 3, a least-square adjustment procedure can be carried out in the neighbourhood of the first peak in order to fit the accelerance expression of the simplified model (Eq. 2 [2]). In doing that, the simplified one-degree-of-freedom system should respond close to the original structure when excited by forces with frequencies in that range. This statement is usually right when the modes of the structure are apart enough, as in the footbridge under study (see Figure 3). Figure 4(a) shows the best adjustment (R = 0.992) in the range 2.2 Hz to 3.2 Hz, resulting in a mass, a stiffness and a damping values of $M = 7890$ Kg, $K = 2.21$ MN/m and $C = 2261$ Ns/m respectively. With these values, the resulting modal damping ratio of $\xi = 0.86\%$.

$$M\ddot{x} + C\dot{x} + Kq = F \tag{1}$$

$$A(\omega) = \frac{\omega^2}{\sqrt{(K - M\omega)^2 + (C\omega)^2}} \tag{2}$$

Figure 4(b) shows the experimental response at point 3 (blue) and the numerical response of the equivalent 1DOF (red) system when undergoing the same excitation. As blue and red curves are almost identical, in fact both systems are equivalent.

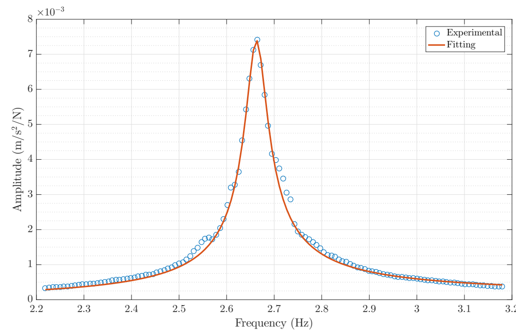

(a)

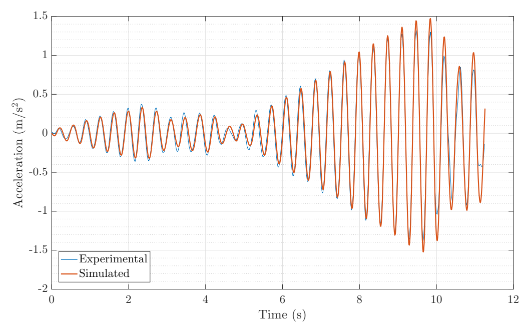

(b)

Figure 4: First mode identification

5 SIMULATED RESPONSE UNDER STANDARD PEDESTRIAN LOADING MODEL

The former results can be used, among other applications, to calibrate the preliminary computational model (FEM) and to estimate the dynamic response when some loading pattern is applied to the structure.

Following the Eurocode 1 (Annex A), for a pedestrian of 70 kg of mass the force to be considered would be simplified as $F(t) = 280\sin(2\pi f \alpha t)$ [N], with f the pace rate of the pedestrian which, in the worst case, equals to the natural frequency ($f = 2.67\ Hz$). The parameter α accounts for the physical impossibility for the pace to be exactly the natural frequency of the structure. Considering this loading case (with $\alpha = 1$) during the transit time considered (15 seconds, assuming 12 m/s speed) Figure 5(a) shows the estimated response for a round trip in which it is assumed a first crossing starting at 5 s and ending at 20 s, followed by a second crossing starting at 30 s and ending at 45 s.

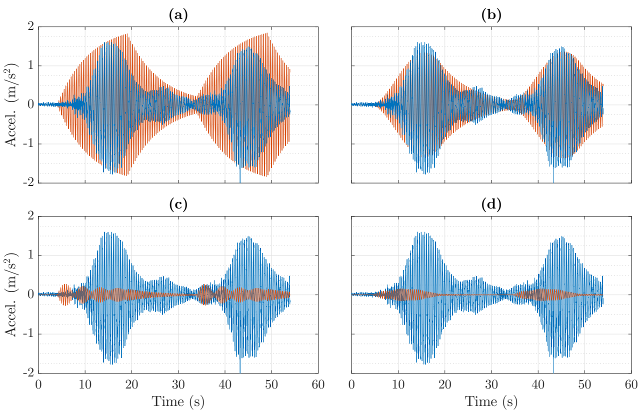

Figure 5: Comparison between experimental data (blue) and different simulation results (red)

This response could over-estimate the real response for two reasons. On one hand, by taking $\alpha = 1$, a total coordination between the pedestrian and the structure is assumed. On the other hand, from the very first moment it is assumed that all the force acts in the centre of the span. Bearing in mind this, some authors [3] recommend to modulate the amplitude of the force by the modal shape, to take into account the effect of the moving force. Assuming, for the first bending mode, a sinusoidal modal shape, the force to be considered would be $F(t) = 280\sin(\pi t/T)\sin(2\pi f\alpha t)$ [N], where T is the transit time. In this case, the corresponding response ($\alpha = 1$) is shown in Figure 5(b).

For comparison reasons, the best registered experimental test has been selected. It corresponds to a single 70 kg runner (at 160 bpm, guided by a metronome). The experimental response at point 3 is the one shown in blue in Figures 5(a) to (d). A good matching with Figure 5(b) is noticeable.

To take into account the impossibility of coordination, the EC 1 recommends $\alpha = 0.9$. In this case, for a not modulated force, the response is shown in Figure 5(c) and, for the modulated one, in Figure 5(d). Clearly $\alpha = 0.9$ under-estimate the real response. This consideration must be taken into account in the case of vandalism loading.

6 CONCLUSIONS

Through the studies presented, it is remarkable that with a portable equipment and simple dynamic tests, valuable data can be obtained for a good dynamic characterization of lightweight infrastructures. The 1DOF model reduction may be adequate for estimating the response to pedestrian crossings, provided that the loading model is realistic enough. With this aim, it is always convenient to compare the numerical models with real cases so that the parameters can be adjusted in the best possible way. The adjustments can depend on the structure under study. Once the model is calibrated, simulations can provide good estimations regarding serviceability.

7 ACKNOWLEDGMENTS

Authors wish to acknowledge the financial support of the MINECO (Spanish Government, Project BIA2014-59321) and the MECD (Spanish Government, FPU Grant). Also the technical support provided by Media Madera Ingenieros Consultores S.L. is acknowledged.

REFERENCES

[1] E. Shahabpoor, A. Pavic, V. Racic, and S. Zivanovic. Effect of group walking traffic on dynamic properties of pedestrian structures. *Journal of Sound and Vibration*, 387:207–225, jan 2017.

[2] N.M.M. Maia and J.M.M. Silva. *Theoretical and Experimental Modal Analysis*. Engineering dynamics series. Research Studies Press, 1997.

[3] J. Sebastián, I. M. Díaz, C. M. Casado, A. V. Poncela, and A. Lorenzana. Evaluación de la predicción de aceleraciones debidas al tránsito peatonal en una pasarela en servicio. *Informes de la Construcción*, 65(531):335–348, sep 2013.

ON THE SEARCH OF MULTIPLE TUNED MASS DAMPER CONFIGURATIONS FOR A VIBRATION MODE WITH CHANGING MODAL PROPERTIES

Christian A. Barrera Vargas[†], José M. Soria[†], Xidong Wang[†], Iván M. Díaz[†], Jaime H. García Palacios[†],

[†]ETS Ingenieros de Caminos, Canales y Puertos
Universidad Politécnica de Madrid
28040 Madrid, Spain

e-mail: christian.barrera.vargas@alumnos.upm.es

Abstract. The design and installation of a Tuned Mass Damper (TMD) to reduce the vibration response level of a structure has been widely studied. This type of passive control system loses efficacy and performance due to its detuning when the modal parameters of the structure change due to external factors or model uncertainties. Under these circumstances, the use of several TMD, also known as multi-tuned mass dampers (MTMD), could be a solution to be explored. However, the design of these TMDs is not obvious: i) configuration to be adopted (several TMDs in parallel or in serie), ii) number of devices to be considered, and iii) tuning of each single TMD parameters. Thus, this paper studies the tuning parameters and MTMD configurations as well as their performance compared with the classical TMD approach with the same mass ratio, in order to compare TMD configurations with the same total inertial mass.

Key words: Vibration control; Tuned mass damper; Multiple tuned mass dampers

1 INTRODUCTION

Tuned Mass Dampers (TMD) are devices used to control and cancel vibrations in structures, which is achieved through the dissipation of energy that provides the damping of that device when is connected to a structure or primary system. A lot of researches have been carried out about the design and optimization of TMDs [1]. However, as it is well-know, TMDs suffer from detuning when modal parameters of the structure change over time and their performance degrade drastically. Multi-TMDs (MTMD) and semi-active TMDs are designed to reduce such detuning issue.

Zuo and Nayfeh [2] studied the use of MTMD, substituting the original idea of a simple degree of freedom system with a multiple degree of freedom system. Under this new concept, Yamaguchi and Harnpornchai [3] studied the response of this Multiple Degree of Freedom system under Harmonically Forced Oscillations, adjusting each TMD to a close frequency for each vibration mode of the main structure; this feature was also studied by Xu and Igusa in [4]. MTMDs have two presents two configurations, *in Parallel and in Serie* and some of these investigations were carried out by Hong and Xiang in [5] and Zuo in [6], respectively.

In this paper, the tunning frequency necessary for a system of MTMDs is evaluated in parallel and in serie, and compared with a single TMD with the same inertial.

2 Multiple Tuned Mass Dampers - Parallel and Serie

A structure that has a TMD attached, can be considered as a system of two degrees of freedom (figure 1), where each DOF has modal parameters of mass (m), damping (c) and stiffness (k), while the MTMDs are considered as a system of multiple degree of freedom, where the mathematical problem is more complex to solve, and their behavior over the main structure depends directly of the configuration adopted, Parallel (figure 2) or Serie (figure 3).

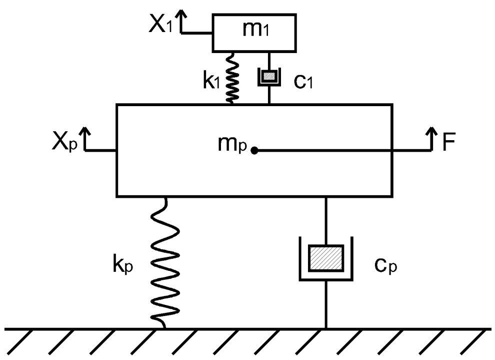

Figure 1: Classical TMD

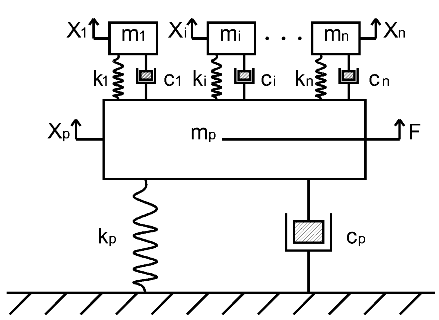

Figure 2: Parallel MTMD.

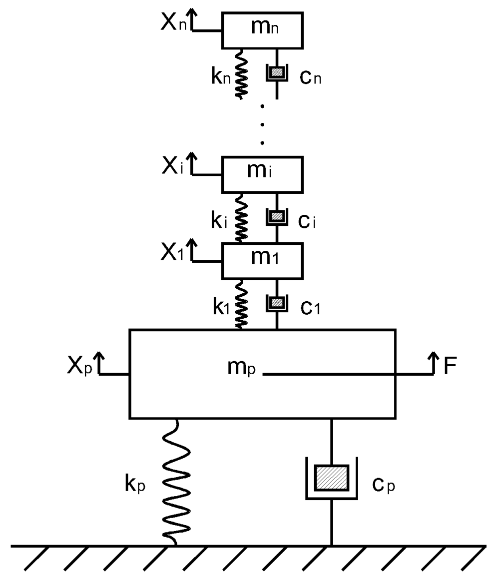

Figure 3: Series MTMD.

2.1 Mathematical solution

The dynamic of system with N-DOF, is defined by the equation of motion.

$$M\ddot{\mathbf{x}} + C\dot{\mathbf{x}} + K\mathbf{x} = F \tag{1}$$

where:

$$N = n + 1$$

and n = number of TMDs

The TMDs generate inertial forces that are exerted on the structure to reduce its vibration. The Laplace domain is used here for dynamic analysis in such a way that transfer function (TF) between relevant magnitude are derived and analysed.

2.2 Transfer Function MTMD Parallel

The equations of motion for this configuration (figure 2) are:

$$m_p\ddot{x}_p + c_p\dot{x}_p + k_p x_p - \sum_{i=1}^{n} ft_i = f \tag{2}$$

$$with = 1, ..., n$$

$$m_i \ddot{x}_i + \sum_{i=1}^{n} ft_i = 0 \tag{3}$$

Where ft_i is the force transmitted to the primary mass by TMD i:

$$ft_i = c_i(\dot{x}_i - \dot{x}_p) + k_i(x_i - x_p) \tag{4}$$

The Laplace transform of (2) is as follows:

$$X_p(s)(s^2 m_p + s c_p + k_p) + \sum_{i=1}^{n} (s^2 m_i T_i(s) X_p(s)) = F(s) \tag{5}$$

In which $T_i(s)$ is the TF between TMD displacement and structure displacement:

$$T_i(s) = \frac{X_i(s)}{X_p(s)} = \frac{(sc_i + k_i)}{(s^2 m_i + sc_i + k_i)}$$

The TF between the primary mass movement and the external force is derived from (s) as follows:

$$\frac{X_p(s)}{F(s)} = \frac{1}{(s^2 m_p + sc_p + k_p) + \sum_{i=1}^{n} s^2 m_i T_i(s)} \tag{6}$$

2.3 Transfer Function MTMD Series

The equations of motion for this configuration (figure 3) are :

$$m_n \ddot{x}_n + F_{t_n} = 0 \tag{7}$$

$$m_i \ddot{x}_i + F_{t_i} - F_{t_{i+1}} = 0 \tag{8}$$

Where the force transmitted by each TMD is:

$$F_{t_r} = c_r(\dot{x}_r - \dot{x}_{r-1}) + k_r(x_r - x_{r-1})$$

and r is (i) or $(i+1)$, with $1 \leq i \leq n$

The force balance for primary mass is:

$$m_p \ddot{x}_p + c_p \dot{x}_p + k_p x_p - F_{t_1} = f \tag{9}$$

The Laplace transform of (9) is as follows:

$$X_p(s)(s^2 m_p + sc_p + k_p + sc_1 + k_1) - X_1(s)(sc_1 + k_1) = F(s) \tag{10}$$

Where the Laplace transform for each TMD is:

$$X_i(s) = \frac{X_{i+1}(s)(sc_{i+1} + k_{i+1}) + X_{i-1}(s)(sc_i + k_i)}{(s^2 m_i + sc_i + k_i + sc_{i+1} + k_{i+1})}$$

The TF between the primary mass movement and the external force is obtained from (10):

$$\frac{X_p(s)}{F(s)} = \frac{1}{(s^2 m_p + sc_p + k_p + sc_1 + k_1) - X_1(s)(sc_1 + k_1)} \tag{11}$$

Note that TFs (6) and (11) are the objetive TFs in which $X_p(s)$ should be minimized. Note also that (11) should be derived recursively from TFs of all coupled series TMDs.

3 Efects in Variation of Frequency Tuning

Using the Den Hartog formulation to derive TMD parameters, it is obtained a mass ratio $(m) = 0.01 \cdot m_p$, frequency $(f) = 0.995 \cdot f_p$, damping ratio $(\zeta) = 0.061$ for a single TMD (figure 1). The frequency tuning for parallel and serie MTMD is studied. Two parallel TMDs and two serie TMDs are considered (n=2), with the same total mass of the single TMD: $m_1 = m_2 = \frac{m_t}{2}$, so that the effect of f_1 and f_2 is studied (figure 4) and (figure 5). The same damping ratio as the single TMD is assumed $\zeta_1 = \zeta_2 = 0.061$.

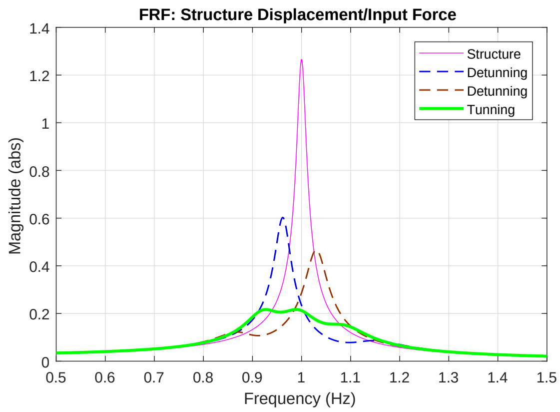

Figure 4: **Parallel Two MTMDs ($f_1 < f_p < f_2$)(solid),($f_1 = f_2 > f_p$)(dash),($f_1 = f_2 < f_p$)(dash-dot)**

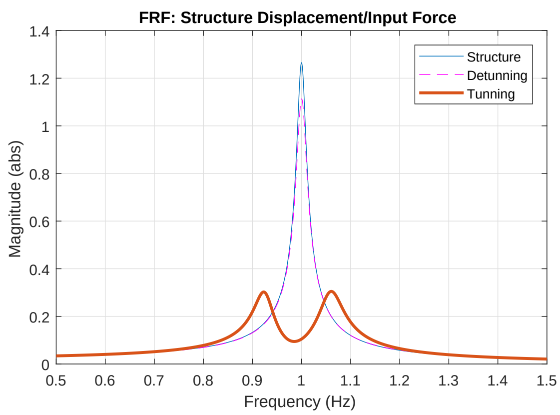

Figure 5: **Series Two MTMDs ($f_1 = f_2 > f_p$)(solid),($f_1 = f_2 < f_p$)(dash)**

After obtaining the criteria to tune the frequency, it is observed the behavior compared with a classical TMD

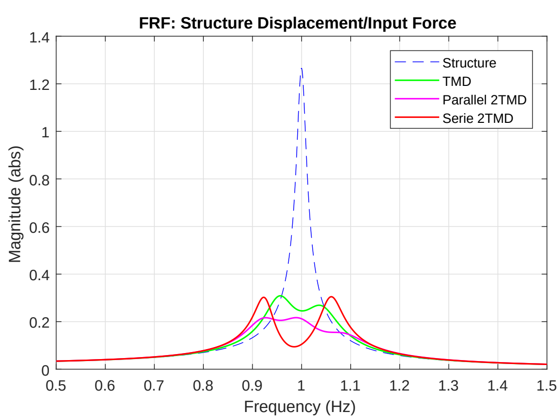

Figure 6: **Classical TMD, Parallel Two MTMDs and Serie Two MTMDs**

4 CONCLUSIONS

- The parallel system requires for the tuning frequencies and upper and a lower value than the main frequency of the structure
- If we increase the mass ratio, it is possible to separate the frequency of TMDs from the frequency of the main structure, increasing the wide-band.
- The serie system for a mass ratio of 1% kg and $\zeta = 0.06$ in each TMD, requires a frequency tuned at $1.6 \cdot f_p$ in each TMD, but if the damping value change drastically, it is necessary change the tunning frequency.

REFERENCES

[1] SAMCO "*Final Report 2006 F05 Guidelines for Structural Control* "

[2] Zuo Lei and Nayfeh 2002 "*Design of Mult - Degree -of - Freedom Tuned - Mass Dampers: A Minmax Aprroach* "43td AIAA/ASME/ASCE/AHS/ASC Structures, Structural Dynamics and Materials Conference, AIAA Paper No 2002-1283

[3] Yamaguchi, H., and Harpornchai, N., 1993, "*Fundamental Characteristics of Multiple Tuned Mass Dampers for suppressing Harmonically Forced Oscillations,* "Earthquake Eng. Struct Dyn., 22,pp 51-62.

[4] Xu, K., and Igusa, T., 1992, "*Dynamic Characteristics of Multiple Substructures With Closely Spaced Frequencies,* "Earthquake Eng. Struct Dyn., 21,pp 1059-1070.

[5] Hong-Nan and Xiang-Lei 2007, "*Optimization of non-uniformly distributed multiple tuned mass damper* "Journal of Sound and Vibration 308 (2007) 80-97.

[6] Zuo, Lei., 2009, "*Effective and Robust Vibration Control Using Series Multiple Tuned Mass Dampers,* "Journal of Vibration and acoustics.

1st. Conference on Structural Dynamics (DinEst 2018)
Madrid, 20–21 June

EXPERIMENTAL ANALYSIS OF THE EFFECT OF RHYTHMIC DYNAMIC CROWD LOADS ON STADIUM GRANDSTANDS

Javier Naranjo-Pérez[†], Nicolás González-Gómez[◇], Javier F. Jiménez-Alonso[*], Felipe García-Sánchez[◇] and Andrés Sáez[†]

[†]Escuela Técnica Superior de Ingeniería
Universidad de Sevilla
41092 Sevilla, Spain

[◇]Escuela de Ingenierías Industriales
Universidad de Málaga
29071 Málaga, Spain

[*] Escuela Técnica Superior de Ingeniería de Edificación
Universidad de Sevilla
41012 Sevilla, Spain

e-mail: jfjimenez@us.es
ORCID: 0000-0002-4592-0375

Abstract. Assembly structures, as stadium grandstands, must be designed to put up with extreme dynamic crowd loads. The effect of the crowd is firmly influenced by the human activity performed by the spectators, which can be classified into two extreme situations: (i) passive spectators, which are seated quietly during all the event and (ii) active spectators, which are performing rhythmic activities continuously. The present study is intended to analyse the transition between these two situations. For this purpose, the modal parameters of a real grandstand have been identified experimentally by using the Operational Modal Analysis (OMA) techniques under different load scenarios. First, the modal parameters of the unoccupied structure have been estimated experimentally measuring the accelerations produced in an ambient vibration test. Second, 100 spectators are seated quietly on the structure (passive spectators) and subsequently the modal parameters of the occupied structure have been identified experimentally. Finally, the modal parameters of the structure have been determined experimentally while the mentioned crowd performs different human activities (bouncing, jumping, dancing and waving). As results of this study, relationships between the change of the modal properties of the grandstand and the human activity performed by the crowd are obtained.

Key words: Modal Analysis, Rhythmic Loads, Human-structure Interaction, Stadium Grandstands.

1 INTRODUCTION

Dynamics forces generated by pedestrian crowd through rhythmic activities can significantly modify the dynamic properties of the structure over which it moves. Many authors have studied this influence under the action of active spectators. Jumping loads are considered the most significant and several parameters such as jump height or repetition speed have been taken into account to model this type of load and prove how it affects the structure [1, 2, 3]. Another load scenarios with active spectators, such as running and bouncing, have been the focus of recent works though the generated loads by these activities are low in comparison to loads from jumping [4, 5]. Passive spectators are supposed to have a higher natural frequency, and although they do not transmit dynamic forces, they especially contribute to the damping of the structure [6].

This study analyses the variation of a grandstand modal parameters. For this purpose, first of all, an experimental identification will be performed by an ambient vibration test and the analysis of the measured signal using the operational modal analysis (OMA) techniques. Subsequently, several tests will be conducted on the occupied structure under different crowd loads and the modified modal parameters will be obtained.

2 EXPERIMENTAL TEST

In order to know the influence of the crowd on the modal parameters, an ambient vibration test was first performed to obtain the modal parameters of the empty grandstand. The grandstand (Figure 1) is a reinforced concrete structure, formed by a waffle slab supported by 12 pillars. The length of the grandstand is 19.2 m and the width is 12.6 m.

Figure 1: The stadium grandstand with the crowd of people.

The measurements were taken along five longitudinal lines. The grandstand was divided into 7 sections, therefore a total of 5×7 points were instrumented. Three high-sensitivity triaxial force-balanced accelerometers were used, moving two of these devices to the instrumentation locations and using the other accelerometer as reference. The recordings of the acceleration were taken during 10 minutes and sampled at 100 Hz. The UPC-Merge (Unweighted Principal Component Merged Test Setups) algorithm, based on the stochastic subspace identification (SSI) method [7], as implemented in the software program ARTeMIS (2014), is considered to perform the experimental identification of the modal parameters. In this algorithm, the signal is pre-treated to merge the results of the different setups [8]. The natural frequencies obtained for the first three experimental vibration modes are shown in Table 1. The damping ratios are also estimated for each vibration mode [9].

Table 1: First three experimental vibration modes of the grandstand.

Mode	f_{EXP} [Hz]	ξ [%]	Description
1	4.231	3.863	First transversal
2	11.117	3.110	First vertical
3	13.580	2.242	Second vertical

To characterize the behaviour of the structure under the action of passive/active spectators, several tests were performed under different load scenarios. A group of 100 people equally distributed with a mean mass of 75 kg was selected. A brief description of the tests is given below.

Passive: Crowd remains still, therefore there is not dynamic excitation due to the crowd.

Waving: People sit down and get up repeatedly at a frequency of 2 Hz.

Dancing: People move randomly without following any rhythmic pattern.

Jumping: People jump at a fixed frequency controlled by a metronome. Two different tests were conducted: 2 Hz and 4 Hz.

Bouncing: People bounce at a fixed frequency controlled by a metronome. Two different tests were performed: 2 Hz and 4 Hz.

The accelerations were measured in three instrumented points with the same three accelerometers mentioned above. Each test had a duration of 3 minutes and a sampling frequency of 100 Hz, except for the passive test which had a duration of 5 minutes. This difference is due to the difficulty of performing an activity for more than 3 minutes synchronously. Due to the short duration of the measurements, a frequency domain OMA method was used. In order to obtain the damping ratios, the EFDD (Enhanced Frequency Domain Decomposition) algorithm [10] is selected to experimentally identify the modal parameters of the occupied grandstand. The values of the first, second and third vibration modes for each test are compared in Figures 2a, 2b and 2c, respectively.

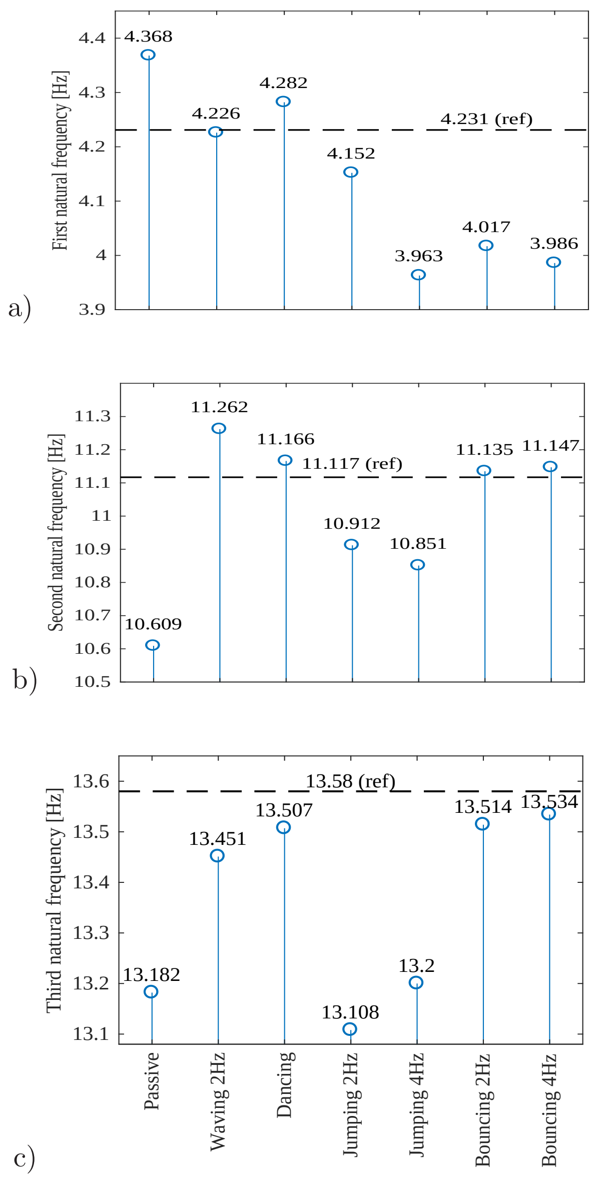

Figure 2: Variation with respect to the reference value (empty grandstand) of the: a) first, b) second and c) third natural frequencies under crowd loads.

According to the results in Figure 2a, some trends could be observed: when the crowd of people was still (passive test; the spectator is modeled as a SDOF system with a natural frequency $f_p = 5\,\text{Hz}$ [11]), the natural frequency of the occupied grandstand, f_{gp}, is greater than the natural frequency of the empty grandstand, f_g. On the other hand, when people were doing rhythmic activities with a frequency below f_g, the natural frequency of the occupied grandstand, f_{gp}, is below f_g. In the jumping and bouncing tests at 4 Hz, the difference is more significant than in the same tests at 2 Hz due to the higher stiffness of the people, according with the relation $k_p = m_p(2\pi f_p)^2$. Despite the frequency in the dancing test was also below f_g, the natural frequency of the occupied grandstand f_{gp} is above f_g.

In Figure 2b, the relationship between the reference natural frequency and the natural frequency of the dancing and jumping tests is similar. Nevertheless, the bouncing tests tends to increase the frequency. In case of passive spectators the natural frequency is the lowest, as opposed to the first vibration mode. The third vibration mode (Figure 2c) shows a different behaviour of the occupied grandstand natural frequency, f_{gp}, as this is less than f_g for all the tests. In this case, the natural frequency of the occupied grandstand is below the natural frequency of the empty grandstand, so that the people presence tends to decrease the natural frequency of the third vibration mode.

3 CONCLUSIONS

The change of modal parameters of a stadium grandstand has been obtained when the structure was occupied by a crowd of people performing several activities. The main concluding remarks are as follows. First, it has been observed that the change in the natural frequencies of the structure under the action of a crowd carrying out an activity depends on the type of activity. Secondly, it has been noted that the frequency of the activity also has an influence on the modification of the modal parameters of the occupied structure, i.e., the same activity performed with different frequencies generates different changes in the natural frequencies of the structure. Therefore, modelling spectators as SDOF systems with different properties for the different activities is justified. Finally, several further studies should be carried out with the aim of validating the results, such as conducting a test with a different crowd of people in the same grandstand or the same crowd in another similar structure.

4 ACKNOWLEDGEMENTS

This work was supported by the Ministerio de Economía y Competitividad of Spain and the European Regional Development Fund under project DPI2014-53947-R. J. Naranjo-Pérez was also supported by a research contract from the Universidad de Sevilla (Ref: USE-17047-G). The financial support is gratefully acknowledged. In addition, the students of the Departamento de Ingeniería Civil de Materiales y Fabricación are acknowledged for their participation in the experimental tests.

REFERENCES

[1] S.O. Hansen and J.D. Sørensen. Dynamic loads due to synchronized movements of people. In *Proceedings of the 4th International Conference on Structural Dynamics, Eurodyn*, pages 1217–1222, 2002.

[2] Y. Tuan. Loads due to human movements on assembly structures. 1984.

[3] H.N. Özgüven and N. Berme. An experimental and analytical study of impact forces during human jumping. *Journal of Biomechanics*, 21(12):1061–1066, 1988.

[4] S. Yao, J.R. Wright, A. Pavic, and P. Reynolds. Experimental study of human-induced dynamic forces due to bouncing on a perceptibly moving structure. *Canadian Journal of civil engineering*, 31(6):1109–1118, 2004.

[5] E. Agu and M. Kasperski. A statistical approach to loads induced by bobbing. In *Structural Dynamics EURODYN*, 2008.

[6] C.A. Jones, P. Reynolds, and A. Pavic. Vibration serviceability of stadia structures subjected to dynamic crowd loads: A literature review. *Journal of Sound and Vibration*, 330(8):1531–1566, 2011.

[7] F. Magalhães and A. Cunha. Explaining operational modal analysis with data from an arch bridge. *Mechanical systems and signal processing*, 25(5):1431–1450, 2011.

[8] M.l. Döhler, P. Andersen, and L.T. Mevel. Data merging for multi setup operational modal analysis with data driven ssi. In *28th International Modal Analysis Conference*, 2010.

[9] F. Magalhães, A. Cunha, E. Caetano, and R. Brincker. Damping estimation using free decays and ambient vibration tests. *Mechanical Systems and Signal Processing*, 24(5):1274–1290, 2010.

[10] R. Brincker, C. Ventura, and P. Andersen. Damping estimation by frequency domain decomposition. In *19th International Modal Analysis Conference*, pages 698–703, 2001.

[11] IStructE/DCLG/DCMS Joint Working Group, IStructE/DCLG/DCMS Joint Working Group, et al. Dynamic performance requirements for permanent grandstands: recommendations for management design and assessment. *Institution of Structural Engineers, London*, 2008.

MODAL ANALISYS AND FINITE ELEMENT SIMULATION OF THE TOWER OF THE LABORAL CITY OF CULTURE IN GIJON

M. López-Aenlle, R.P. Morales, G. Ismael, F. Pelayo and A. Martín.
Department of Construction and Manufacturing Engineering,
University of Oviedo, Gijón, Spain
Corresponding author: aenlle@uniovi.es
ORCID : 0000-0002-7538-2758

Abstract. The building of the Laboral City of Culture is located in the city of Gijón (Spain) and it was built in the 1950s. This tower is a significant part of the main building from which all the city of Gijón and the shoreline can be seen. The tower has a square shape 12 x 12 m and a height of 130 m. Operational Modal Analysis (OMA) was applied to the tower in order to study its dynamic behaviour. Two modal tests were carried out: the first in 2015 and the second in 2017. Bending and torsional modes in the frequency range 0-6 Hz were identified using OMA software.

Additionally, a detailed 3D finite element model, was assembled in ABAQUS. The experimental modal parameters (natural frequencies and mode shapes) were used to validate and update the FE model.

Key words: Operational Modal Analysis, modal updating, civil engineering.

1 INTRODUCTION

The “Universidad Laboral” of Gijón, since 2007 known as Laboral city of culture with an area of around 270,000 m^2 is the largest building in Spain. With a height of 130 m, the tower is currently the highest building in Asturias. The tower is a 3D concrete frame structure and it has 21 floors (Figure 1). A Steel cross structure 25 meters long is located on the top of the tower. On the 12th floor there are four clocks with a diameter of 4m. On the 17th floor (height of 108.1 m,) there is a balcony which provides tourists and visitors with magnificent views of the surroundings

In March 2014, an operational modal test was performed on the tower measuring the ambient response with sensors placed in 4 floors. The same test was repeated in March 2017 using a slightly different setup. Twelve modes were identified in the frequency range 0-6 Hz using the frequency domain decomposition technique.

In this paper, the results of the modal tests performed in 2017 are presented and compared with those carried out in 2014.

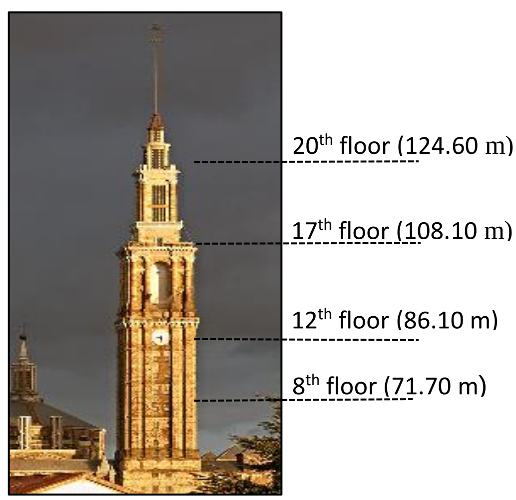

Figure 1- Tower of the "Universidad Laboral".

2 TEST SETUP

In March 2014, operational modal tests were carried out in the structure, measuring the responses in floors 12,17,18 and 20. The sampling rate was 50 Hz and the responses were recorded for approximately 8 hours. An anemometer was situated at the height of the 17th floor. Wind gusts of 9 m/s were recorded and the average temperature was 13.1ºC (Figs. 2 and 3).

With respect to the experimental tests carried out in March 2017, the experimental responses were measured in floors 8, 12, 17 and 20, respectively (Fig. 1). Wind gusts of 13 m/s were recorded and the average temperature was 14.36ºC (Figs. 2 and 3).

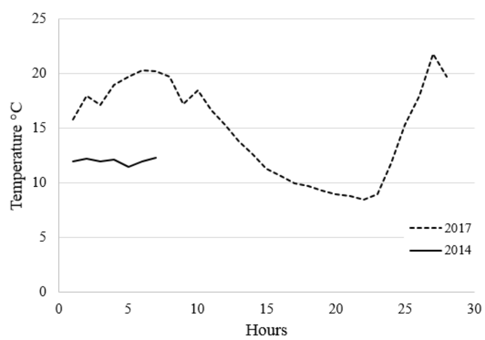

Figure 2- Mearured temperature.

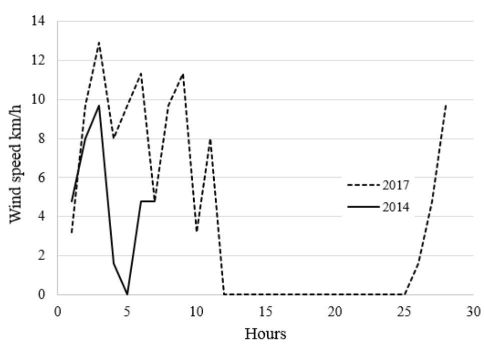

Figure 3- Measured wind speed.

The following data acquisition systems and sensors (by Güralp Systems) were used to record the experimental responses under ambient excitation:

- A 12 channels Monitoring Equipment CMG-DM24S12EAM.
- An Extension module CMG-DM24S6EAM with 6 channels and synchronized with the Monitoring Equipment.
- 9 force-balance uniaxial sensors CMG-5U/12V/8mA.
- 2 force-balance triaxial sensors CMG-5TC/12V/ 38mA

The uniaxial (U) sensors were place at floors 8, 12 and 21 whereas the triaxial (TR) sensors were located at floor 17. Figure 4 shows the location and orientation of the sensors. Figure 5 shows the connection scheme of sensors and data acquisition systems.

The experimental responses were recorded for 25 hours with a sampling frequency of 50 Hz.

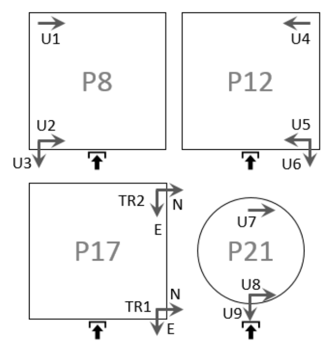

Figure 4. Location of sensors.

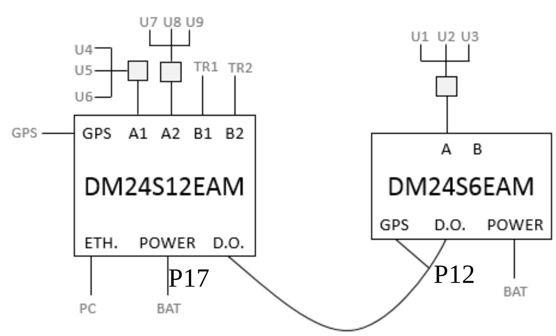

Figure 5. Connection scheme.

3 MODAL IDENTIFICATION

The modal parameters were identified with the frequency domain decomposition technique (FDD) using the Artemis Modal software. The signals were decimated with order 4 and the spectral densities were calculated using 1024 frequency lines. The singular value decomposition of the responses in the frequency range 0 < f < 6 Hz is presented in Fig. 6.

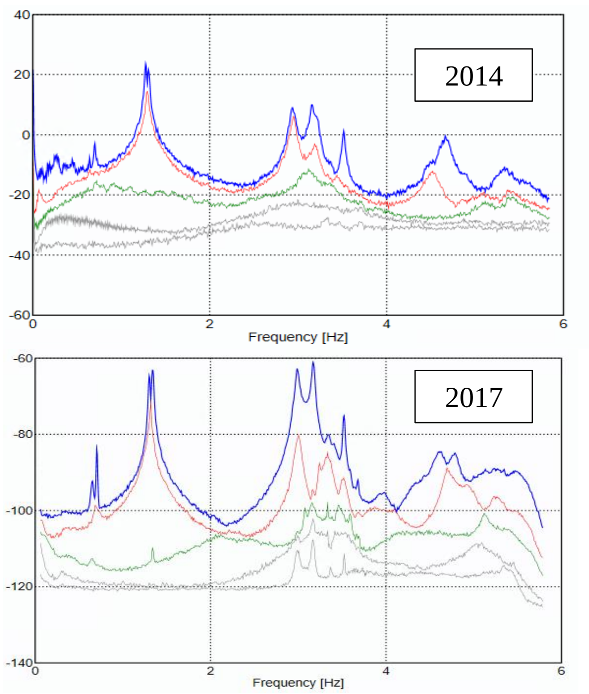

Figure 2- Singular value decomposition of the experimental responses.

The natural frequencies and damping ratios, corresponding to the tests carried out in 2014 and 2017 are presented in Tables 1 and 2, respectively.

It can be observed that the natural frequencies estimated in 2017 are slightly higher than those estimated in 2014. This can be explained by the different weather conditions existing in 2014 (maximum 14ºC) and in 2017 (maximum 21ºC).

This structure has local modes of the steel cross (located at the top of the tower) but with a small motion of the tower. Although the steel cross was not measured, the corresponding modes can be captured by the sensors placed in the tower, which explain the small amplitude of the singular values at 0.64 and 0.7 Hz with respect to the first global models (1.277 and 1.307 Hz).

Moreover, due to the symmetry of the structure, the bending modes are repeated or closely spaced. The experimental mode shapes are shown in Figure 7.

N	Mode	2014	2017	Error (%)
1	1st steel cross Bending Y	0.642	0.651	+1.43
2	1st steel cross Bending X	0.701	0.703	+0.29
3	1st Tower Bending X	1.277	1.302	+1.96
4	1st Tower Bending Y	1.307	1.341	+2.60
5	2nd Tower Bending Y	2.942	2.991	+1.67
6	2nd steel cross X	2.943	3.001	+1.97
7	2nd steel cross Y	3.158	3.172	+0.44
8	1st Torsion	3.206	3.340	+4.18
9	2nd Tower Bending X	3.515	3.520	+0.14
10	3rd Tower Bending Y	4.492	4.621	+2.80
11	3rd Tower Bending X	4.663	4.777	+2.42
12	2nd Torsion	5.365	5.542	+3.22

Table 1. Frequency [Hz] comparison 2014-2017.

4 CONCLUSIONS

- Operational modal analysis has been applied to the tower of "Laboral City of Culture" in March 2014 and March 2017.

- The natural frequencies estimated in 2017 are slightly higher than those estimated in 2017, which can be explained by the different temperature conditions existing in both tests.

N	Mode	2014	2017	Error Rate
1	1st steel cross Bending Y	ND	1.842	-
2	1st steel cross Bending X	ND	0.493	-
3	1st Tower Bending X	0.628	0.449	28.503
4	1st Tower Bending Y	0.752	0.497	33.910
5	2nd Tower Bending Y	0.443	0.593	-33.860
6	2nd steel cross X	0.830	0.818	1.446
7	2nd steel cross Y	0.479	0.442	7.724
8	1st Torsion	0.533	0.491	7.880
9	2nd Tower Bending X	0.484	0.297	38.636
10	3rd Tower Bending Y	1.16	0.883	23.879
11	3rd Tower Bending X	0.965	1.26	-30.570
12	2nd Torsion	1.227	1.354	-10.350

Table 2. Damping ratio [%] comparison 2014-2017.

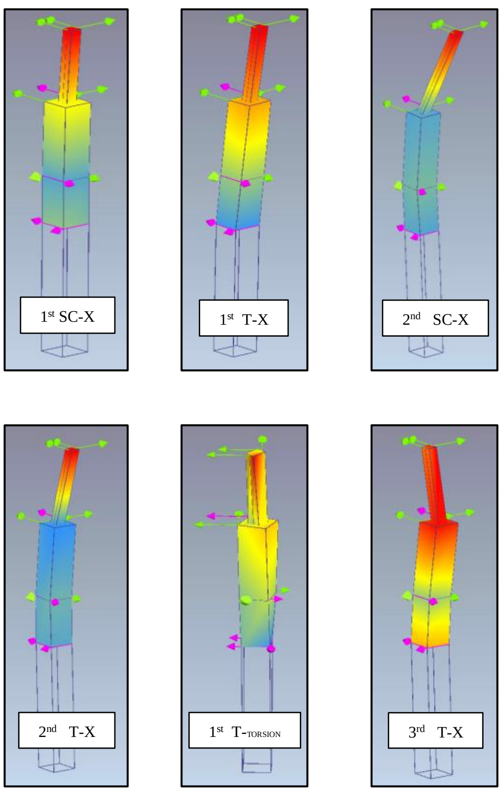

Figure 3- Experimental mode shapes of the structure (SC : steel cross, T : Tower)

ACKNOWLEDGMENTS

The authors wish to thank to Laboral City of Culture/Government of the Principality of Asturias for having allowed us to perform the experimental testing.

The economic support given by the Spanish Ministry of Science and Innovation through the project BIA 2011-28380-C02-01 and by the Asturias Institute for Industrial Technology (IUTA) through the project SV-14-GIJÓN-1.12 is gratefully appreciated.

REFERENCES

[1] R. Brincker, C. Ventura. *Introduction to Operational Modal Analysis.* Wiley, 2015

[2] J. Zatón, J.C. Alvárez (1993). *Guía Histórico Artística del C.E.I. de Gijón Antigua Universidad Laboral.* Ediciones Júcar.

[3] *Structural Vibrations Solutions*, SVIBS Artemis Modal, 2017.

[4] G. Ismael, A. Pardo et al, Modal Analysis of the Tower of the Laboral City of Culture, IOMAC Conference, May 2015, Gijón

1st Conference on Structural Dynamics (DinEst 2018)
Madrid, 20-21 June

DYNAMIC BEHAVIOR OF A FOOTBRIDGE IN GIJON SUBJECTED TO PEDESTRIAN-INDUCED VIBRATIONS

G. Ismael*, M. López-Aenlle and F. Pelayo

Department of Construction and Manufacturing Engineering
University of Oviedo,
33209 Gijón, Spain
*e-mail: garciaismael@uniovi.es

Abstract. Footbridges are slender structures and consequently susceptible to human-induced vibrations. For this reason, structural design codes establish frequency bands to be avoided in order to prevent resonances that could cause structural damages or affect the users comfort level. The specifications established by the codes also include a safety threshold in the acceleration amplitudes for the vertical and transversal directions. In this work, the dynamic behavior of the "Moreda" pedestrian footbridge, located in the city of Gijón (Spain), is studied. A finite element model of the structure was assembled in ABAQUS in order to predict the natural frequencies and the corresponding mode shapes. This information was used to define the test setup configuration. Then the structure was tested under service conditions (pedestrians, runners and bikers) during approximately 1 hour using acceleration sensors. The experimental responses were used to estimate the experimental modal parameters using Operational Modal Analysis (OMA). The results show that the natural frequencies of the structure are in the pedestrian-induced vibration range. Moreover, from the experimental responses is also inferred that the vibration amplitudes are out of the acceptable levels.

Key words: Footbridge, Human-induced, Modal Analysis, Structural vibrations.

1 INTRODUCTION

The vibration serviceability assessment is one of the criteria that must be taken into account in the design of footbridges [1]. Footbridges are slender structures and often highly susceptible to human induced vibrations, due to their low mass and low damping.

In this paper, the vibrations of a pedestrian footbridge (see Figure 1) located at the Moreda park (Gijón) are studied. Since the coming into service of the footbridge (1995), the users reported some discomfort during the use of the structure. This discomfort is manifested by both vertical and transversal vibrations. In 2014, the Gijón council executed a structural reinforcement in order to improve its dynamic behavior. Before this reinforcement, the structure was tested under service conditions. The information obtained will be useful to check the dynamic behavior of the reinforcement undertaken in 2013.

Figure 1: The Pumarin-Moreda footbridge

2 SERVICIABILITY AGAINST VIBRATIONS

Pedestrians running or walking on footbridges can affect to the dynamic response of these structures. For this reason, structural design codes establish frequency bands to be avoided in order to prevent resonances.

The walking behavior of a pedestrian can be affected by the interaction with the structure. The running and walking frequencies are usually provided in the codes (see Table 1). The simplest method for preventing the risk of resonance consists of avoiding the natural frequencies in the same range of pedestrian walking frequency (Table 2).

People…	**Estimated frequency range [Hz]**		
	CPA	ISO 10137	SETRA
Walking	1.25 -2.40	1.20-2.40	1.60-2.40
Running	2.00-3.50	2.00-4.00	2.00-3.50
Walking (2nd mode)	2.50-4.60	2.40-4.80	-

Table 1: Pedestrian range of frequencies

CODE		**FREQUENCY RANGES [Hz]**			
		TRANSVERSAL		**VERTICAL**	
		Min	**Max**	**Min**	**Max**
EAE and IAP (Spain)		0.50	1.20	1.25	4.60
EHE (Spain)		< 5			
Eurocode 0- A.2		0	2.50	0	5
SETRA (France)	maximum risk	0.5	1.1	1.7	2.1
	medium risk	0.3	0.5	1	1.7
		1.1	1.3	2.1	2.6
	low risk	1.3	2.5	2.6	5
	negligible risk	0	0.3	0	1
		2.5	Inf	5	Inf

Table 2: Critical Frequencies in Pedestrian Bridges

The codes [2, 3, 4, 5, 6] also provide values for the critical acceleration for vertical and transversal accelerations with the aim of classifying the comfort of the structure (see Table 3).

CODE	**COMFORT**	**ACCELERATION RANGES [m/s^2]**	
		VERTICAL	**HORIZONTAL**
IAP/EAE	maximum	<0.5	<0.1
	medium	0.5 to 1	0.1 to 0.3
	low	1 to 2.5	0.3 to 0.8
	Not acceptable	>2.5	>0.8
SETRA	maximum	<0.5	<0.1
	medium	0.5 to 1	0.1 to 0.3
	low	1 to 2.5	0.3 to 0.8
	Not acceptable	>2.5	>0.8
E0-A.2	acceptable (normal condition)	<0.7	<0.2
	acceptable (exceptional)		<0.4

Table 3: Acceleration ranges for vertical and horizontal vibrations

3 TEST SETUP

The footbridge, constructed in 1995, has a total length of 160 m, the central span being 60 m long. The structure is made of steel with a concrete deck 2.5 m wide. Modal analysis was performed under service conditions: pedestrians, runners and cyclists crossed the structure. Ten PCB393B31 accelerometers (10V/g) were used to measure the acceleration response using a TEAC-LX120 data acquisition system. The register time was approximately 60 minutes and the sampling frequency 50 Hz.

A total of 15 DOFs were measured through two data sets using five reference sensors and five roving sensors. The measured DOFs are shown in Figure 2.

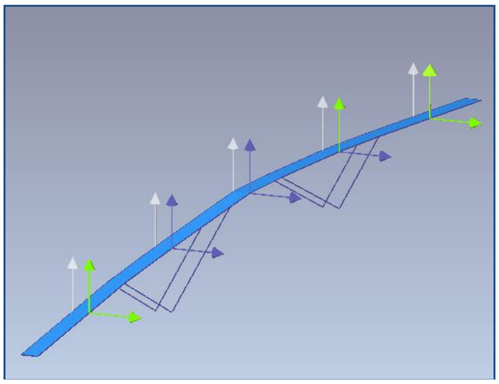

Figure 2: Test setup.

In order to compare the experimental results, a finite element model of the footbridge was assembled in ABAQUS.

All the parts of the structure were modeled using Shell elements (S4R). The concrete of the deck was modelled as linear elastic ($E = 25\,GPa$, ν=0.22), whereas a linear-elastic structural steel S275 was used for the rest of the structure.

4 EXPERIMENTAL AND NUMERCIAL RESULTS

The Singular Value Decomposition (SVD) of the experimental responses are shown in Figure 3.

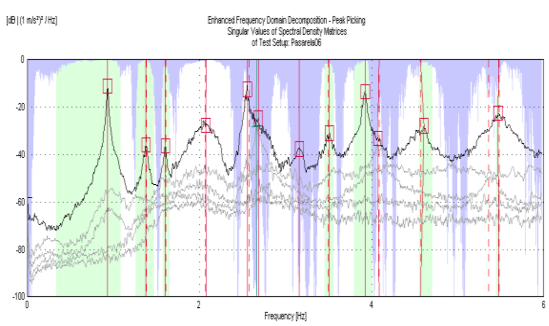

Figure 3: Singular Value Decomposition of the measured signals.

The modal parameters were estimated using the Frequency Domain Decomposition (EFDD) technique [7] implemented in the ARTEMIS MODAL software and 8 modes were identified in the range $0 - 4$ Hz The estimated natural frequencies and damping ratios are shown in the Table 1. The natural frequencies predicted with the FE model are also presented in Table 1.

The first four numerical mode shapes of the footbridge are presented in Figure 4

Mode	DIR.	f_{exp} [Hz]	ζ_{exp} [%]	f_{num} [Hz]	Error [%]
1	L	0.93	0.612	0.82	11.8
2	L	1.38	0.907	1.37	0.72
3	L	1.60	0.759	1.68	5.00
4	V	2.08	4.083	2.12	1.92
5	L	2.67	0.404	2.68	0.34
6	V	3.16	0.399	3.25	3.01
7	V	3.51	0.990	3.28	6.29
8	L	4.08	0.212	4.04	0.25

Table 4: Natural frequencies and damping ratios (L: lateral direction, V: vertical direction).

5 DISCUSSION OF THE RESULTS

It can be observed in Table 4 that the damping ratio corresponding to the fourth mode (f_4=2.08 Hz) is much higher than the damping of the rest of the modes. This can also be seen in figure 3 where the peak corresponding to the fourth mode is wider than the rest of the modes. This effect was due to the pedestrian-structure interaction (see Table 1) [8].

From the experimental responses, the maximum acceleration values in the horizontal and vertical directions were 0.553 m/s^2 and 1.047 m/s^2, respectively. According to Table 3, the structure is classified of minimum comfort attending to IAP/EAE and SETRA, whereas these acceleration values are not acceptable for the Eurocode 0 (A2).

With respect to the natural frequencies of the structure, they are in the range of critical values (see Table 2) for practically all the identified modes of the structure.

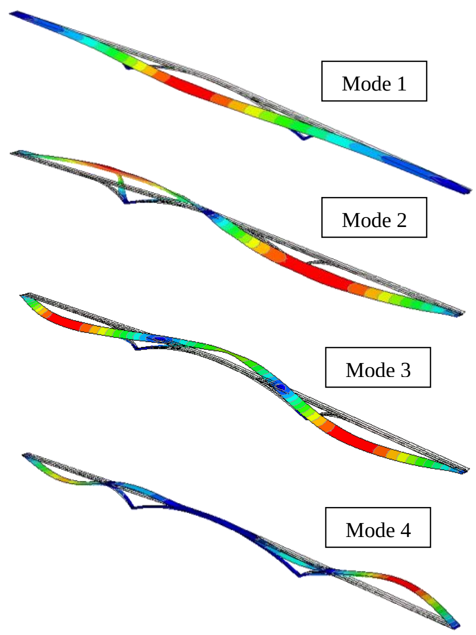

Figure 4: First mode shapes of the footbridge.

6 CONCLUSIONS

The results show that there are natural frequencies of the structure in the same range of pedestrian (walking and running) frequencies. As a consequence, the interactions between the pedestrians and the structure can cause high vibration levels.

According to the measured acceleration levels, the structure is classified in the range of minimum comfort as reported by the EAE and IAP codes. On the other hand, the vibration levels are not acceptable attending to Eurocode 0 (A2).

Finally, a new modal analysis with the reinforced structure should be carried out in order to check the improvement provided by the reinforcement.

ACKNOWLEDGMENT

The economic support given by the University Institute of Industrial Technology of Asturias (IUTA) through the Project SV-14-GIJÓN-1.12 is gratefully appreciated.

REFERENCES

[1] J. de Sebastián, I.M. Díaz, C.M. Casado, A.V. Poncela and A. Lorenzana. *Evaluación de la predicción de aceleraciones debidas al tránsito peatona en una pasarela en servicio*. Informes de la Construcción, 65, 531, 335-348, 2013.

[2] ISO 10137. *Bases for Design of Structures Serviceability of Buildings and Walkways against Vibrations*, International organization for standardization edition, 2007.

[3] Setra/AFGC. *Footbridges - Assessment of vibrational behaviour of footbridges under pedestrian loading*, Paris. 2006.

[4] IAP 11. *Instrucción sobre acciones a considerar en el proyecto de puentes de carretera. Centro de Publicaciones Secretaría General Técnica Ministerio de Fomento*, Madrid. 2011.

[5] EHE-08. *Instrucción de hormigón estructural. Centro de Publicaciones Secretaría General Técnica Ministerio de Fomento*, Madrid. 2008.

[6] UNE-EN 1995-2:2010. *Eurocódigo 5: Proyecto de estructuras de madera. Parte 2: Puentes*. AENOR, 2010.

[7] R. Brincker, L-M. Zhang and P. Anderson. *Modal Identification from Ambient Response Using Frequency Domain Decomposition*, in:18th IMAC, 625-630. 2000.

[8] S. Živanović1, Diciembre, *Influence of walking and Standing Crowds on Structural Dynamic Properties*, Proceedings of the IMAC XXVII, 2009.

MOTION-BASED DESIGN OF MULTIPLE TUNED MASS DAMPERS TO MITIGATE PEDESTRIANS-INDUCED VIBRATIONS ON SUSPENSION FOOTBRIDGES

M. Calero-Moraga[†], D. Jurado-Camacho[†], J.F. Jiménez-Alonso[*] and A. Sáez[†]

[†]Escuela Técnica Superior de Ingeniería
Universidad de Sevilla
41092 Sevilla, Spain

[*] Escuela Técnica Superior de Ingeniería de Edificación
Universidad de Sevilla
41012 Sevilla, Spain
Corresponding author e-mail: jfjimenez@us.es
ORCID: 0000-0002-4592-0375

Abstract. Suspension footbridges are usually slender structures, which are prone to vibrate under pedestrian action. In order to guarantee an adequate comfort level, while maintaining the slenderness of the structure, their damping ratios may be usually increased via the implementation of multiple tuned mass dampers (MTMDs). In this case, the design of the damping devices must tackle two main issues: (i) the complexity of the affected vibration modes; and (ii) the variability of the natural frequencies of the footbridge associated with its inherent non-linear geometrical behavior. Herein, a motion-based design method is implemented on a real suspension footbridge in order to design a passive control system based on the use of MTMDs. The motion-based design method transforms the design problem into a constrained minimization problem, where the objective function is defined in terms of the TMD masses, the constraints are established based on the required comfort levels and design criteria and the design variables are the MTMDs parameters. Two conventional design criteria have been considered here: (i) the H_∞ criterion and (ii) the H_2 criterion. Finally, two main conclusions are obtained from this study: (i) the H_∞ criterion allows obtaining more reduced MTMDs parameters and (ii) the inclusion of the MTMDs reduce the variability of the natural frequencies of the footbridge related to its non-linear behavior.

Key words: Motion-based design, MTMDs, Pedestrian-induced vibrations, Suspension footbridges.

1 INTRODUCTION

Suspension footbridges are prone to vibrate due to pedestrian-induced vibrations [1]. In order to guarantee the compliance of an adequate comfort level of the footbridge, while maintaining its aesthetics and slenderness, it is often necessary to increase its damping ratio via the implementation of an external passive control system [2]. Due to the complexity of the vibration modes associated with these structures, the passive control system is usually materialized by multiple tuned mass dampers (MTMDs). The design of the MTMDs system must be robust enough to meet the serviceability vibration requirements under the uncertainty associated with the inherent non-linear behavior of the structure [3]. Herein, two conventional TMD design criteria are compared [4]. Both design criteria have been considered for the design of a MTMDs system in order to mitigate the pedestrian-induced vibrations on a real suspension footbridge under walking pedestrian action. The design problem has been formulated as a constrained minimization problem where the objective function is the sum of the MTMDS masses; the constraints are the comfort requirements and design criteria established by the designer; and the design variables are the parameters of the MTMDs [5].

2 PROBLEM FORMULATION

2.1 Pedestrian Load

In order to define the walking pedestrian load, the relationship provided by the SYNPEX guidelines [2] is considered. The equivalent walking pedestrian force [N/m] in vertical direction may be defined as:

$$p(t) = 280 \cdot \cos(2\pi \cdot f_s \cdot t) \cdot n' \cdot \psi / L_f \qquad (1)$$

where L_f is the length of the footbridge [m], f_s the step frequency (it is assumed that it equals the natural frequency of the footbridge, f_f,); n' is the equivalent number of pedestrians on the footbridge and ψ is the reduction coefficient, which takes into account the probability that the footfall frequency approaches the natural frequency under consideration.

2.2 Comfort Requirements

Pedestrian comfort levels depend on accelerations produced across the footbridge [2]. The acceleration serviceability limit of footbridges is thus a suitable performance criterion for design. Table 1 illustrates the comfort classes established by the SYPENX guidelines [2] in terms of the vertical accelerations obtained at the footbridge.

Table 1. Comfort classes according to SYNPEX guidelines [2] in vertical direction.

Comfort Classes	Comfort Level	Vertical Accelerations
CL1	Maximum	<0.5 m/s^2
CL2	Medium	0.5-1.0 m/s^2
CL3	Minimum	1.0-2.5 m/s^2
CL4	Uncomfortable	>2.5 m/s^2

2.3 Design Criteria

Two conventional design criteria have been considered herein [4]: (i) the H_∞ criterion, where the form of the frequency response function of the footbridge is modified in order to minimize the dynamic response of the structure under a harmonic excitation; and the H_2 criterion, where the frequency response function is adapted to reduce the dynamic response of the structure under a random excitation.

2.4 Problem Formulation

In this way, the formulation of the design problem (constrained single-objective minimization problem) may be written as [5]:

$$\text{Minimize } f(\theta_i) \qquad (2)$$

$$\text{Subject to } \begin{array}{ll} g_{eq,j}(\theta_i) = g^*_{eq,j} & j = 1,2,\dots,s \\ g_j(\theta_i) \le g^*_j & j = 1,2,\dots,k \end{array} \qquad (3)$$

$$\theta_i^l \le \theta_i \le \theta_i^u \; i = 1,2,\dots,n_d \qquad (4)$$

where $f(\theta_i)$ is the objective function, $g_{eq,j}(\theta_i)$ is the *jth* equality constraint (design criteria), $g^*_{eq,j}$ is the threshold of the *jth* equality constraint, *s* is the number of equality constraints, $g_j(\theta)$ is the *jth* inequality constraint (comfort requirements), g^*_j is the threshold for the *jth* inequality constraint, *k* is the number of inequality constraints, θ_i^l are the lower and θ_i^u the upper bounds of the design variables, θ_i (MTMDs parameters), and n_d is the total number of design variables. As global optimization method, genetic algorithms have been taken into account herein.

3 NUMERICAL APPLICATION

3.1 Description of Zuheros suspension footbridge

In order to assess the performance of the two mentioned design criteria, the motion-based design method has been implemented to reduce the vertical walking pedestrian-induced vibrations of a lively suspension footbridge (Zuheros footbridge which is illustrated in Figure 1).

Figure 1: Suspension footbridge at Zuheros (Cordoba, Spain).

The first four vertical natural frequencies of the structure are shown in Table 2. They have been obtained from a finite element model of the footbridge which has been previously updated based on the modal parameters estimated by an operational modal analysis.

Table 2. Updated numerical vibration modes of the footbridge in vertical direction.

Mode	f_{upd} [Hz]	Description
1	1.219	1st vertical bending
2	1.659	2nd vertical bending
3	2.467	3rd vertical bending
4	3.148	4th vertical bending

The second vertical vibration modes is inside the range that characterizes the walking action in vertical direction [2]. Due to the location of the footbridge, a minimum comfort class has been considered [2]. As the vibration level of the footbridge does not meet the comfort requirements (Table 3), a passive control system has been designed to mitigate the walking pedestrian-induced vibrations. As the affected vibration mode presents three sinusoidal peaks, three TMDs have been considered (MTMDs system). The parameters of the MTMDs have been determined implementing the proposed motion-based design method under the two mentioned conventional design criteria. The results of this study are compared in order to find the most cost-effective solution for this particular case.

Table 3 illustrates the maximum acceleration at mid-span of the footbridge in terms of the pedestrian density considering three situations: (i) without MTMDs.: (ii) with MTMDS under H_∞ criterion, $a_{w\_MTMDs\_H_\infty}$; and (iii) with MTMDS under H_2 criterion, $a_{w\_MTMDs\_H_2}$.

Table 3. Maximum acceleration at mid-span of the footbridge under walking pedestrian action for different traffic scenarios (pedestrian density d=Person/m^2).

d [P/m^2]	a_{wo_MTMDs} [m/s^2]	$a_{w\_MTMDs\_H_\infty}$ [m/s^2]	$a_{w\_MTMDs\_H_2}$ [m/s^2]
0.2	14.06	2.19	2.30
0.5	11.97	2.47	2.49
0.8	9.13	0.92	0.82
1.0	19.67	0.91	0.87

Additionally Table 4 shows the MTMDs parameters (TMD mass, m_d, TMD damping, c_d, and TMD stiffness, k_d) for each considered design criterion. Herein, the same parameters are considered for the three TMDs.

Table 4. TMD parameters for the two considered design criteria.

	m_d [kg]	c_d [Ns/m]	k_d [N/m]
H_∞	72	106	6157
H_2	80	102	6881

4 DISCUSSION OF RESULTS

As Table 3 illustrates, the implementation of the MTMDs system improves clearly the dynamic behavior of the structure.

Notwithstanding, as Table 4 reflects, the H_∞ criterion is slightly more cost-effective than the H_2 criterion since it reduces the mass of the passive control system.

A key aspect, for the performance of this control system, is the reduction of the range of variation of the second natural frequency of the structure associated with its inherent non-linear geometrical behavior. This fact is shown in Figure 2 (where $f_{upd,2\_wo\_MTMDs}$ and $f_{upd,2\_w\_MTMDs}$ are the second natural frequency of the footbridge without and with MTMDs designed according to the H_∞ criterion).

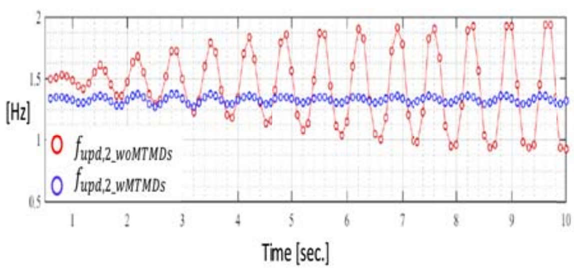

Figure 2: Variation of the second updated natural frequency of the footbridge.

5 CONCLUSIONS

Two main conclusions are obtained from this study:

- Although both design criteria allow controlling successfully the vibration problem, the H_∞ criterion achieves a large reduction of the MTMDs parameters when compared to the H_2 criterion.
- The implementation of the MTMDs system reduces the range of variation of the affected natural frequency associated with its inherent non-linear geometrical behavior.

ACKNOWLEDGMENTS

This work was partially funded by the Spanish Ministry for Science under the research projects DPI2014-53947-R and BIA2015-71942-REDT. The authors also acknowledge the construction company, Metalhergos S.L., for its collaboration and support during the development of the experimental test.

REFERENCES

[1] Y. Daniel, O. Lavan and R. Levy, (2012). *Multiple-Tuned Mass Dampers for Multimodal Control of Pedestrian Bridges*. Journal of Structural Engineering ASCE, 138(9): 1173-1178.

[2] CH Butz, CH Heinemeyer, A. Goldack, A. Keil, M. Lukic, E. Caetano, A. Cunha, (2007), "Advanced Load Models for Synchronous Pedestrian Excitation and Optimised Design Guidelines for Steel Footbridges (SYNPEX)". *RFCS-Research Project RFS-CR-03019*.

[3] J.Connor (2003), Introduction to Structural Motion Control, *Prentice Hall, Pearson Education*, Inc., New Jersey, United States.

[4] T. Asami, O. Nishihara, A.M. Baz (2002), *Analytical solutions to H_∞ and H_2 optimization of dynamic vibration absorbers attached to damped linear systems*, Journal of Vibration and Acoustics; 124(2), 284-295.

[5] J.F: Jiménez-Alonso, A. Sáez (2017), *Motion-based design of a slender steel footbridge and assessment of its dynamic behavior*, International Journal of Steel Structures, 17(4): 1459–1470.

MEASUREMENT OF THE STRESS IN TENSION BARS USING METHODS BASED ON THE IMAGE

B. Ferrer*, D. Mas†

* Escuela Politécnica Superior
Universidad de Alicante
03690 Alicante, Spain
e-mail: belen.ferrer@ua.es
ORCID: 0000-0002-8455-5534

† Instituto Universitario de Física Aplicada a las Ciencias y las Tecnologías
Universidad de Alicante
03690 Alicante, Spain

Abstract. This paper shows one interesting application of a new developed method to measure the vibration frequency of a moving body through image processing and without the use of any particular target on the body. It allows data acquisition without the need of physically reaching the measured point, which results in a big improvement of procedure safety and cost. The procedure was used to measure the actual tension in some tension bars that were affected by an earthquake. The measurement was checked by comparison with some accelerometers glued to the bars. The good results obtained and the simplicity of the new method compared to standard one makes this technique appealing in frequency of vibration measuring tasks.

Key words: Frequency measurement, Image processing, Vibrating bars, Structural health monitoring.

1 INTRODUCTION

Image processing is a well-known discipline that has been recently introduced to structural analysis. It has evident advantages in the inspection and monitoring of structures, such as being a non-invasive technique, long distance measurement capability and the possibility of its use with not expensive devices, among others. Most of them are based in target location and tracking through digital image correlation [1], which can be further refined in order to improve their accuracy [2, 3]. However, these methods need a recognizable shape in the point to measure. This shape can be part of the existing pattern of the object surface or, when this surface is too uniform, it is needed to add (by gluing or painting) a particular target to the surface. On this last case, it is mandatory the access to the point to measure of, at least, one worker. This can be a safety problem when this point is not easy to reach, such as mid spam of bridges and cables, top of slender towers or unreachable areas of singular structures. In this communication we present an application of a new procedure in order to measure the vibration frequency of a body without the need to reach the point.

2 METHODS

The method is based on the binarization in different threshold levels of a sequence of the vibrating body. The result obtained after binarization is connected with the object geometry and the illumination structure in such a way that a subtle change in the object location slightly modifies its brightness and therefore the appearance of the object in the image. The complete description of this method can be found in [4].

3 A CASE STUDY

In 2011 an earthquake of moderate magnitude hit the city of Lorca, located in the Region of Murcia (Spain) and it lead some damaged buildings in the city, as well as some injured and even three dead people. In some cases, despite the building had not perceptible damage, it was appealing to check the health of some public buildings. In particular, the town hall has several cantilever slabs that are hanged to one wall in its free end by using some tension bars (figure 1). After the earthquake, the actual tension in the bars was questioned, as it may affect the safety of both workers and users. To find the tension, the easiest way is to measure the main frequency for each bar. However, the building should remain opened during the testing procedures and the bars were located just over the main entrance and over the windows to public attendance.

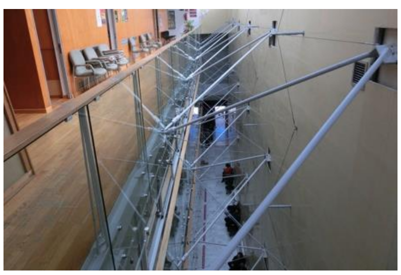

Figure 1: View of some of the bars under study.

The bars are Gewi type with a diameter of 25 mm and length of 2.9 m. The design values are unknown, but the manufacturer gives a yield load of 245 kN for this bar and an elastic modulus of $205000 \cdot 10^6$ N/m^2. [5] Density of steel was taken as 7850 kg/m^3.

3.1 Data acquisition procedure

To record the images the camera was located in a stable point in the slab, in which all the bars were recorded simultaneously (Figure 2, right). Additionally, an accelerometer was glued to the middle spam of the bar, in order to check the results given through image processing. This added complexity to the works as a lifting platform had to be located among the public, with a risk of a falling devices or tools (Figure 2, left).

Figure 2: Comparison between the two different setups needed for the acquisition procedures. Left : Opperation of accelerometers glue. Right : Camera located in a slab ready to record.

Once all devices were ready to record, the bar was softly hit with a rubber hummer in order to induce a vibration. The experiment was repeated several times for each bar and vibration frequency data were collected with the accelerometer glued to the considered bar and the camera.

3.2 Image processing

On the recorded sequences some regions of interest (ROIs) were selected in order to analyze only the local information given at that regions (Figure 3). It is advisable to have some dark and light areas inside this ROIs in order to maximize the intensity changes due to the movement of the bar. On each one of these regions a multiple binarization in different threshold levels was done and then the number of pixel that changes for each considered threshold level was considered as a signal. Fourier transform of that signal gives the frequency of the movement. Combination of the signal obtained with the different threshold may enhance the main peak of the frequency while canceling the noise. Therefore, we obtain a more accurate signal. [4]. Notice that the procedure was used here only for some ROIs but it can be extended to the whole image thus giving a map of frequencies of the whole scene [6].

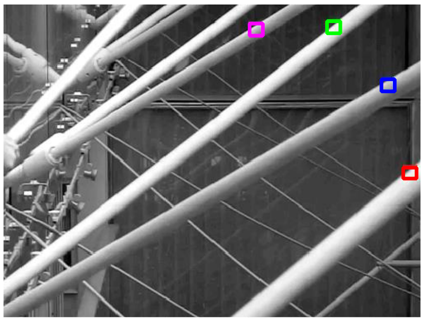

Figure 3: ROIs (colored rectangles) selected for image processing

3.4 Results

The frequencies obtained through image processing were compared to those obtained from the Fourier transform of the signal given by the accelerometers. Notice also that this method allows obtaining the frequency from the movement itself, and not from the acceleration, so the results are not weighted by the squared of the frequency, like it happens in the accelerometer. Therefore, the comparison is done only for the frequency value and not for its relative weight. That comparison is showed in table 1. Frequencies from both devices are very close, having a maximum divergence of 1,2 Hz. It should be noted that in the third floor, due the high of the bars, it was not possible to locate accelerometers and only the results from camera were recorded.

From this comparison, we can validate the values obtained from image processing.

From the frequency values, we can determine the force supported by each bar through classic vibrating cable theory. According to their properties, we found the values of the loads on the bars, and we obtained that all studied bars are under its yield limit, with a safety factor between 3.4 and 5.1, therefore without any risk of use.

Frequencies (Hz)			
		Accelerom.	Camera
1^{st} floor	Barra 1	20,6	21,8
	Barra 2	22,4	23,5
	Barra 3	22,8	22,8
2^{nd} floor	Barra 4	23,1	23,3
	Barra 5	23,3	23,5
	Barra 6	22,1	22,8
3^{rd} floor	Barra 7	-----	24,48
	Barra 8	-----	20,23
	Barra 9	-----	23,6

Table 1 : Comparison between measurements done with accelerometers and image processing

4 CONCLUSIONS

- The procedure based in image processing gives good results compared to those obtained by accelerometers.
- The experimental setup needed to obtain the movement frequency from images gives a huge advantage compared to the setup needed to record the same information using accelerometers.
- Additionally, the acquisition data needed for the image processing used in this paper also gives an important advantage with respect to other image processing techniques in which an additional target is needed in the measured point. In these last cases, the setup safety is close to that given by using accelerometers, because in both cases the point to measure has to be reached.

REFERENCES

[1] F Hild and S Roux, 'Digital Image Correlation: from displacement Measurement to identification of elastic properties – a review', Strain Vol 42, No 2, pp 69–80, 2006.

[2] Xiujun Lei, Yi Jin, Jie Guo, Chang'an Zhu "Vibration extraction based on fast NCC algorithm and high-speed camera" Applied Optics, 54 (27) pp. 8198-8206, 2015.

[3] Chris A. Murray, Neil A. Hoult, W. Andy Take "Dynamic measurement using digital image correlation" International Journal of Physical Modelling in Geothecnics", 17 (1) pp. 41-52, 2016.

[4] Ferrer B, Espinosa J, Roig AB, Perez J, Mas D "Vibration frequency measurement using a local multithreshold technique" Opt. Express, 21 (22) pp 26198–26208, 2013.

[5] https://www.dywidag-sistemas.com/fileadmin/downloads/dywidag-sistemas.com/dsi-dywidag-gama-de-productos-geotecnicos-es.pdf, last accessed on April of 2018.

[6] Mas, D.; Ferrer, B.; Acevedo, P.; Espinosa, J. "Methods and algorithms for video-based multi-point frequency measuring and mapping" Measurement, 85 pp 164-174, 2016.

FOUNDATION ANALYSIS FOR DYNAMIC EQUIPMENT: DESIGN STRATEGIES FOR VIBRATION CONTROL

David Marcos [(1)], José A. Becerra [(1)] Arturo N. Fontán [(2)] and Luis E. Romera [(2)]

[(1)] Ingeniero de Caminos, Canales y Puertos.
NETO Ingeniería S.L. A Coruña, España.
e-mail: dmarcos@netoingenieria.com

[(2)] Grupo de Mecánica de Estructuras.
ETSI Caminos, Canales y Puertos. Universidad de A Coruña.
Campus de Elviña. A Coruña, España.

Abstract. The structural design of a foundation system supporting dynamic equipment is very complex by the need to model the load transmitted (frequently a Dynamic Load) jointly with the supporting foundation and the soil response. The analysis, based on classical theories derived from Soil Dynamics may be supplemented by the Finite Element Method (FEM), bringing more reliability to the calculations. Nevertheless, the FEM may have its results strongly influenced by the parameter values adopted in the simulation hence, when the design engineer is faced to the uncertainties, fundamentally the dynamic soil properties, the values adopted need to be conservative and must be assessed with critical sense. The final goal of the dynamic analysis is to obtain a proper design for the foundation system ensuring an acceptable structural behavior, avoiding resonance with the supported machine, limiting vibrations (therefore internal loads and stresses) within equipment and surrounding areas and ensuring minimal human perception of vibrations.

Key words: Equipment-Foundation-Soil System, Dynamic Load, Impedance, FEM, Vibration Amplitude, Human Perception, Vibration Control.

1 INTRODUCTION

In this article we summarize one possible methodology to be carried out to guarantee a proper design of the Machine - Foundation - Soil System subjected to dynamic loads. Two main criteria are checked (structural behaviour as well as functional response of the whole System) to validate the results obtained in the analysis assuring a good machine operability, feasible human perception of vibrations and also minimum transmission of vibrations to the surrounding environment. Emphasis is placed on the dynamic soil parameters adopted in calculations, since they are usually a source of uncertainty and greatly influence the results of the analysis as well as the resulting final design. It is essential to ensure, during the design stage, a fluent partnership between the equipment manufacturer and the engineering team responsible for the definition of the foundation to make sure an "optimum" final design.

2 PROBLEM STATEMENT

The industrial equipment (rotating, reciprocating, impulsive or impact machines, ...) generate dynamic unbalanced forces that it is necessary to control, resist and transmit adequately to the soil foundation. The problem includes the complete definition of the dynamic characteristics of the Equipment - Foundation - Soil System as we mention in the following paragraphs.

2.1 Equipment Data

It is necessary to know: the weight (mass) and centre of gravity of the machine and all the auxiliary equipment supported by the foundation, as well as type, position and dimensions of support points and also values of static and dynamic loads (Forces and Moments) transmitted by the Equipment and auxiliary elements, and finally the machine's working speed.

2.2 Foundation Definition

The definition of the initial size of the foundation depends on several aspects: configuration and arrangement of the equipment and auxiliary elements to be supported, maintenance requirements and accessibility to the equipment, geometric constraints existing in situ,... As design initial rules to set the foundation overall dimensions we highlight the following: 1) Match the centre of gravity of the equipment and auxiliary elements to the foundation one; 2) Increase, as far as possible, the horizontal dimensions of the foundation (B, L) to adequately resist the maximum amplitudes for "Rocking" vibration type modes; 3) Adopt a minimum depth of 60cm for the supporting block, in order to guarantee a "rigid" behavior of the foundation; 4) Under static loads, the pressure transmitted to the ground will be less than or equal to 50% of the admissible value; and under total loads (Static and Dynamic) 75% of these value must not be exceeded. These assumptions make possible to consider the soil behaviour accurately as linearly elastic.

2.3 Soil Definition

It is necessary to know, before start the analysis, different dynamic properties of the soil. Generally, these parameters will be obtained from both in situ and laboratory soil testing arising from an intensive on site geological and geotechnical survey. The main parameters to take into consideration are the following: soil specific weight (ρ), Poisson's ratio (ν), Shear modulus (G) and critical damping coefficient (ξ) taking into account both the "Radiation" and the "Hysteretic" component; for the latter parameter and for practical purposes, we can accept an average value equal to 5%. For initial design purposes, there are numerous expressions and correlations in the technical literature [5, 6, 7] with the aim of obtain an order of magnitude of these soil parameters.

3 SOIL DYNAMIC PARAMETERS

3.1 Uncertainty of Values

The Soil Shear Modulus (G) is the most important parameter related with determining the dynamic behaviour of the Equipment - Foundation - Soil System. Since we are trying to evaluate inherent mechanical properties of an heterogeneous and anisotropic medium, the values obtained directly from tests or from the technical literature must be considered as average values subject to some measurement uncertainty and variability. So it is recommended, for design purposes, to consider a range of "probable" values into the analysis as described below:

$$Gmin = \frac{Gmed}{\gamma} \qquad (1a)$$

$$Gmax = \gamma \, Gmed \qquad (1b)$$

$$\gamma \in [1.35\,,\ 1.50] \qquad (1c)$$

3.2 Calculation of Dynamic Impedances

The fundamental equation that governs the dynamic problem [1] results:

$$M\ddot{u}(t) + C\dot{u}(t) + Ku(t) = F(t) \qquad (2)$$

The term F (t) is determined by the equipment, generally a harmonic load, but in order to solve the problem moreover it is necessary to obtain the values of Dynamic Stiffness (K) and Damping (C) of the Foundation - Soil System. This couple of values (K, C), by analogy, is named as Dynamic Impedance of the Foundation - Soil System. Generally the foundation block resting on the ground, for design and practical purposes, behaves like a rigid body resting on an elastic medium. To determine the parameters (K, C) there are several formulations available in the technical literature, in this case we have adopted the formulation by Gazetas et al (1991) [5], assuming the behaviour of the Foundation - Soil System for each one of the six degrees of freedom in space, as an equivalent Mass - Spring - Dashpot System and calculating for everyone of them (Figure 1) an equivalent Stiffness and Viscous Damping coefficient, to be used in order to solve the dynamic problem stated according to equation (2).

4 SOLVING THE PROBLEM - A DESIGN EXAMPLE

Once the problem has been stated (see Sections 2 and 3) it will be necessary to carry out a dynamic time history analysis to obtain results, generally frequencies and fundamental vibration modes of the whole System, as well as amplitudes of vibration, speeds and maximum accelerations in several control points, previously selected, situated into the Equipment / Foundation and compare these results with acceptable limit values established by the Equipment Manufacturer and / or collected in the specialized technical literature [8].

Following are summarized the main results derived from a dynamic analysis carried out for a foundation designed to support an industrial equipment. Furthermore we emphasize the verification criteria finally adopted to validate the design and ensure adequate vibration control for the whole system.

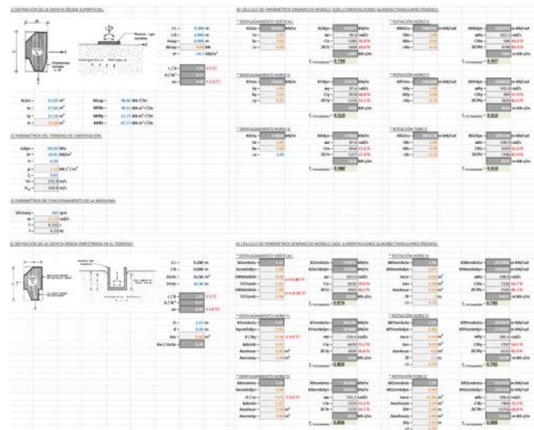

Figure 1: Problem Data and Dynamic Impedance calculations (K, C)

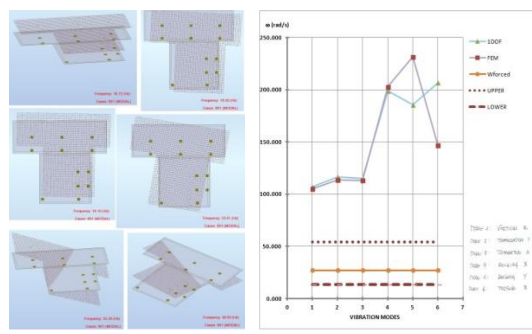

Figure 2: Fundamental Vibration Modes: comparison between FEM and 1 DOF equivalent system.

One of the fundamental goals of the dynamic analysis is avoiding resonance, these can be done (Figure 2) computing the ratio between the frequency of operation of the machine and the frequency of different natural modes of vibration of the System, verifying that it is sufficiently far away from unity (Resonance effect) The margin to adopt varies according to several authors [5, 6, 8] and depending on the machine type although it may be necessary to adopt more conservative limits when we have uncertainty in the values of one or several parameters that govern the problem.

The final purpose of the design of the Equipment - Foundation - Soil System consists in ascertain that the vibrations resulting from the operation of the Equipment are kept within acceptable limits (Figure 3), in order to guarantee an adequate operational behaviour (avoiding damage or premature wear to the equipment or its components) as well as ensuring the comfort of operators working in the vicinity of the equipment and avoid transmitting vibrations to other structures or nearby facilities.

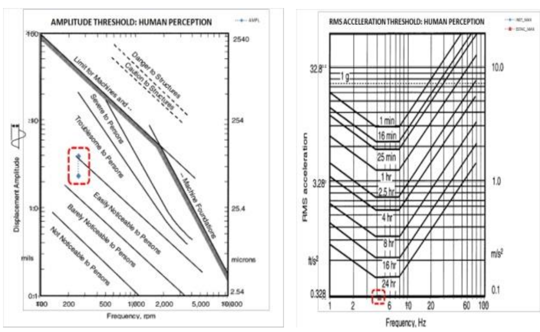

Figure 3a: Analysis Results Check: foundation maximum amplitude vibration and acceleration [8]

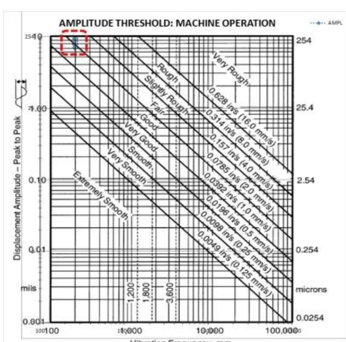

Figure 3b: Analysis Results Check: machine supports maximum amplitude vibration [8]

5 CONCLUSIONS

The structural design of a foundation system supporting dynamic equipment is a very complex problem greatly influenced by the dynamic parameters of the soil adopted in the analysis. This article summarizes a methodology for analyzing the problem taking into account, in a simplified manner, the uncertainty of the parameters involved in the analysis and providing several criteria for checking and validate the results obtained from the analysis in order to achieve an effective vibration control and also avoid damages to the own equipment as well as to reduce the transmission of vibrations to the other workers and machines located in the immediate vicinity.

REFERENCES

[1] Anil K. Chopra. *Dynamics of Structures.* Prentice Hall International. 3rd Ed., 2007.

[2] Singiresu S. Rao. *Mechanical Vibrations.* Addison-Wesley. 3rd Ed., 1995.

[3] George Gazetas. *Analysis of machine foundations: State of the art*. Soil Dynamics and Earthquake Engineering, 1983, Vol. 2, No. 1.

[4] George Gazetas. *Formulas and Charts for Impedance of Surface and Embedded Foundations*. Journal of Geotechnical Engineering, Soil Dynamics and Earthquake Engineering, 1991, Vol. 117, No. 9.

[5] H.Y. Fang. *Foundation Engineering Handbook.* Chapman & Hall. 2nd Ed., 1991.

[6] Joseph E. Bowles. *Foundation Analysis and Design.* McGraw-Hill. 5th Ed., 1996.

[7] Braja M. Das. *Principles of Soil Dynamics.* Cengage Learning. 3rd Ed., 2016.

[8] ACI 351.3R-04. *Foundations for Dynamic Equipment.* ACI Comittee 351. 2004.

BUILDING INFORMATION MODELING (BIM) AND HISTORICAL ARCHITECTURE: A PROPOSAL FOR THE ENERGY PREDICTIVE PERFORMANCE ASSESSMENT

Óscar Cosido*[1,2,3], †[2] Rossella Marmo, †[2]Pedro M. Rodríguez, †[2]Alberto Salcines, †[3]Mario Tena, †[3]Daniel Basulto

*[1] Departamento de Matemática Aplicada y Ciencias de la Computación
E.T.S de Ingenieros Industriales y de Telecomunicación.
Universidad de Cantabria
39005 Santander (Cantabria)
oscar.cosido@unican.es

†[2] UPINTELLIGENCE
E.T.S de Ingenieros Industriales y de Telecomunicación.
Universidad de Cantabria
39005 Santander (Cantabria)

†[3]Fundación Santa María la Real del Patrimonio Histórico
Aguilar de Campoo
34800 Aguilar de Campoo (Palencia)

Abstract. The use of Building Information Modelling (BIM) technology is commonly used in the new construction field and has been used for several years for the existing buildings too. This provides the opportunity to have architectural models continuously updatable and investigable in any components, in order to have a unique hub of knowledge as a support for enhancement, restoration or maintenance interventions. Anyway the difficulties linked to the realization of historic architecture digital models are not few, including modelling the wealth of not geometric information, as the environmental conditions of a place. This paper aims to investigate the challenge of integrating in BIM platforms the data from environmental conditions monitoring with the purpose of improve the preventive maintenance, the energy efficiency and the temperature and humidity conditions control. In this sense, the heritage monitoring project promoted by the Santa María la Real of Historical Heritage Foundation represents an interesting opportunity to further explore limits and potentialities that BIM arises in such context. Starting from the environment and construction analysis of some historic buildings, forming parts of the aforementioned project, have been made energy models of significant parts of them, containing environmental monitoring data and capable of providing a predictive assessment of both temperature and humidity conditions and energy consumption over the time. The proposed methodology provides for the use of several computer interoperable tools, which allows achieving a 3D model and a database uniquely linked. The model thus remains upgradeable in real time in accordance with data from building monitoring and control systems.

Keywords: Building Information Modeling, HBIM, Preventive Maintenance, Energy Efficiency, Predictive Assessment

1 INTRODUCTION

Building Information Model (BIM) is defined by international standards as '*shared digital representation of physical and functional characteristics of any built object* […]*which forms a reliable basis for decisions'* [1]. In the past decades, the use of Building Information Modeling (BIM) within the new buildings sector has led to many benefits and recourse savings during the planning, design, and construction phases [2]. More recently the BIM was applied to the entire life cycle of a building and to the built heritage, led to the theorization of Historic Building Information Modeling (HBIM) [3]. In this paper it is advanced a methodology through which join in a unique upgradeable model the monitoring data and the physical information about the environmental condition of an architectural heritage example.

2 INTEGRATION OF BUILDING CONDITIONS MONITORING IN BIM PLATFORM

A crucial activity is the integration, in BIM platform, of a variety of information, as the one comes from historically archived documentation, analytical investigations, surveys, diagnostics and monitoring. Furthermore you'd expect to real-time update models by installing monitoring systems linked to them [4]. These kinds of activities are useful in energy retrofitting and preventive maintenance project.

The common approach at present consists of simulating the current building energy performance referring to standardized thermal parameters and with no link to the current environmental situation. This approach provides two phases: the analysis of energy performance and the control and monitoring of energy demand. In literature there's no applications evidence about the integration of thermal data capture in HBIM platform, meanwhile are available some case studies concerning the environmental condition monitoring of existing buildings. Some contributions [5, 6] in order to optimize the energy simulation, propose to use measured parameters of humidity and temperature and evaluated transmittance properties, such as with thermo-graphic surveys. In this way, current thermal conditions and actual heat transfer capacity are captured and inserted into BIM as properties influenced by the deterioration of the materials [4]. Another approach provides a Virtual Retrofit Model, integrating building-related data from a virtual building model based on BIM platform, energy related data from a wireless sensor network, environmental data from weather station and occupants perceptions from a stakeholders survey [7].

Anyway, some gaps in knowledge in integrating BIM applications with diagnostic and monitoring system are still present. Some challenges regard the need for methods and strategies to collect diagnostic data for accurate and complete results; need for BIM tools allowing modeling any geometry exportable in .gbXML schema [6]; time-consuming approaches for mapping properties and building components; required real-time updating of energy performances and involved parameters for adaptive solutions [4].

3 CURRENT METHODS AND APPROCHES FOR BUILDING CONDITIONS ESTIMATION

Building energy estimation could be achieve with different software (among the building simulation programs we could remind DOE-

2, ESP-r, Energy Plus) and modeling methods. Models could be divided in three major categories: *statistical*, *hybrid* or *gray-box*, and *engineering* [8]. The first one involves simple linear or multiple linear regressions and learning or training algorithms, it needs a large amount of registered data. The third one is a method that use physical principles to estimate energy performance at the building or component level, it includes a zone or multi-zone approach considering that the thermodynamic state of each building g thermal zone are homogeneous over the entire volume. The models that come out from the engineering approach could also been calibrated with measured data for validation. The hybrid model combines elements of physical and statistical approaches, trying to overcome the limitations linked to the required knowledge of detailed information on building characteristics, and the limitations linked to the need of considerable amount of monitored data. In this sense, the hybrid model is a physical model representing the structure or physical configuration of the building or HVAC system, that provides for the identification of important building parameters and characteristics by statistical analysis. For the question of what approach is the best the answer depends on what type of information is available and its magnitude [8]. For building energy consumption analysis, Artificial Intelligent methods are widely implemented due to their accuracy result and the ability of analyzing nonlinear problems. In fact they are able to cope with the complexity of buildings system that is influenced by many buildings parameters.[9]. But they could present the disadvantage of not considering the effect of input parameters on output parameters.

4 PROPOSAL OF A MONITORING-AIDED HBIM FOR ENERGY PERFORMANCE ASSESSMENT

A historic buildings model requires a huge amount of information with evidence of the building conditions by diagnostics and monitoring systems. It could be better manage linking the physical model to Artificial Intelligent systems, which could improve the diagnosis and the evaluation phases. An interesting occasion to explore the potentiality of integrating such amount of data in a BIM platform is offered by the Monitoring Heritage System project, promoted by the Santa María la Real of Historical Heritage Foundation. The project consists in monitoring environmental, structural, energy and operating conditions in order to improve the preventive maintenance, the energy efficiency and the temperature and humidity control. In this sense the *hybrid* model could become a new way to manage ancient architectures. In fact in this case Building Information Model isn't a 3D parametric model, not even a way to read a database, but a methodology that includes parametric objects and relationships between them, monitored data and analysis results. Machine learning algorithms (neural networks, support vector machines, Markov models, etc.) could be used to predict environmental parameters, such as temperature, humidity, energy consumption or building occupancy [10-11]. Moreover, not only environmental conditions can be predicted, but also structural defects in the building [12], which enable a predicted maintenance.

This kind of model could be automatically updatable, for example for what concern the energy analysis evaluation based on machine learning models, and could associate 3D representation to these results, reporting critical situation and objects at risk. This approach allows us to become independent from modeling every component of an existing building, that could be very challenging to recognize in depth, when we can refer to monitored data. At the same time managing parametric objects could be useful in order to understand and calibrate the ones that have more influence.

5 CONCLUSIONS

In this paper we have briefly recalled the current status of the BIM application in the building monitoring systems matter. Then we have categorized the methods used nowadays to do energy simulation and forecasting performances of existing buildings. We have also found that there are no literature evidences of connections among HBIM and monitoring systems, like MHS. As a result we've proposed to implement an *hybrid* model through which manage physical elements and volumes and the large amount of data, and consequent analysis, related to them.

REFERENCES

[1] ISO Standard, ISO 29481-1:2010(E): Building Information Modeling — Information Delivery Manual — Part 1: Methodology and Format, 2010

[2] Volk R., Stengel J., Schultmann F., *Building information modeling (BIM) for existing buildings - literature review and future needs,* Automation in Construction 38, pp. 109–127, 2014

[3] Dore C., Murphy M. *Integration of Historic Building Information Modeling and 3D GIS for Recording and Managing Cultural Heritage Sites*, 18th International Conference on Virtual Systems and Multimedia: "Virtual Systems in the Information Society", Milan, Italy, pp. 369-376, 2012

[4] Bruno S., De Fino M., Fatiguso F., *Historic Building Information Modelling: performance assessment for diagnosis-aided information modelling and management*. Automation in Construction 86, pp. 256– 276, 2018

[5] Ilter D., Ergen E., *BIM for building refurbishment and maintenance: current status and research directions*, Structural Survey 33,2015

[6] Cho Y.K., Ham V., Golpavar-Fard M., *3D as-is building energy modeling and diagnostics: a review of the state-of-the-art*, Adv. Eng. Inform. 29, pp.184–195, 2015

[7] Woo J.-H., Menassa C., *Virtual retrofit model for aging commercial buildings in a smart grid environment*, Energy Build. 80,pp. 424–435, 2014

[8] Fumo N., *A review on the basics of building energy estimation*, Renewable and Sustainable Energy Reviews 31, pp. 53–60, 2014

[9] Ahmad A. S., Hassan M. Y., Abdullah M. P., Rahman H. A., Hussin F., Abdullah H., Saidur R., *A review on applications of ANN and SVM for building electrical energy consumption forecasting,* Renewable and Sustainable Energy Reviews 33, pp. 102–109, 2014

[10] Peng Y., Rysanek A., Nagy Z., Schlüter A. *Using machine learning techniques for occupancy-prediction-based cooling control in office buildings*, Applied Energy, 211, pp. 1343-1358, 2017

[11] Ahmad J., Larijani H., Emmanuel R. *Energy demand prediction through novel random neural network predictor for large non-domestic buildings*, 11th Annual IEEE International Systems Conference, SysCon 2017 - Proceedings

[12] R. Reffat, J. Gero, W. Peng, *Using data mining on building maintenance during the building life cycle*, Proceedings of the 38th Australian & New Zealand

Architectural Science Association (ANZASCA) Conference, 2004

1st Conference on Structural Dynamics (DinEst 2018)
Madrid, 20-21 June

MODAL SCALING OF STRUCTURES BY OPERATIONAL AND CLASSICAL MODAL ANALYSIS

F. Pelayo*, M.L. Aenlle*, R. Brincker†, A. Fernández-Canteli*

* Dpto Construcción e Ingeniería de Fabricación
Universidad de Oviedo
33204 Gijón, Spain
e-mail: fernandezpelayo@uniovi.es
ORCID: 0000-0001-7915-9513

† Technical University of Denmark
Department of Civil engineering
DK-2800 Kgs. Lyngby

Abstract. Modal masses cannot be obtained directly when operational modal analysis is used, therefore, additional techniques, such as the mass change method have to be applied. On the other hand, in classical modal analysis the scaling factors are identified directly from the frequency response functions but a relatively high level of uncertainty is also expected when this technique is applied. In this paper, the modal masses of two structures, tested in the lab, have been determined by classical modal analysis and by the mass change method. In classical modal analysis an impact hammer and an electro-mechanical shaker were used to excite the structures whereas many small hits random in time and space were used in the operational modal analysis testing. The results provided by both techniques are presented and the accuracy obtained is analyzed.

Key words: Operational Modal Analysis, Scaling factors, Modal Masses.

1 INTRODUCTION

The frequency response function (FRF) and the impulse response function (IRF) are commonly used in structural dynamics to describe the dynamic behavior of a structure [1]. The FRF and the IRF can be constructed using the mass [M], stiffness [K] and damping [C] matrices, respectively, or alternatively in terms of modal parameters [1]. In proportional damped models, the modal parameters needed to construct the FRF are the natural frequencies ω, damping ratios ζ and mass normalized mode shapes {ϕ}, i.e.:

$$[H(\omega)] = \sum_{r=1}^{Nmodes} \frac{\{\phi\}_r\{\phi\}_r^T}{(\omega_r^2 - \omega^2 + i2\zeta_r\omega\omega_r)} \qquad (1)$$

Mode shapes can be normalized in different ways, the most common techniques being:

- Mass normalization
- Normalization to the unit length of the vector mode shape
- Normalization to a component equal to unity or to the largest component equal to unity).

The un-scaled $\{\psi\}$ and the mass normalized $\{\phi\}$ mode shapes are related by the equation:

$$\{\phi\} = \alpha\,\{\psi\} \qquad (2)$$

where α is a new constant parameter usually denoted as scaling factor and which is related to the modal mass by means of the expression:

$$\alpha = \mathrm{m}^{-2} \qquad (3)$$

and eq. (2) can also be expressed as:

$$\{\phi\} = \frac{1}{\sqrt{m}}\{\psi\} \qquad (4)$$

In numerical models, the mass matrix $[M]$ of the system is known and the modal masses can be estimated with the equation:

$$m = \{\psi\}^T[M]\{\psi\} \tag{5}$$

The modal assurance criteria (MAC) is a technique widely used to compare experimental and numerical mode shapes. The MAC can be calculated by:

$$MAC = \{\psi_L\}_{FE}^T\{\psi_L\}_X \tag{6}$$

Where the subscript 'L' indicates normalization to the unit length and subscripts 'X' and 'FE' indicate experimental and numerical, respectively. Thus, this technique only compares mode shapes normalized to the unit length and no information is provided about the modal mass.

In classical modal analysis (CMA), also known as experimental modal analysis (EMA), mass normalized mode shapes can be directly estimated by curve fitting of the FRF (or IRF) using the different identification techniques proposed in the literature [1]. During curve fitting, three modal parameters are estimated for each mode, the natural frequency ω_r, the damping ratio ζ_r and the residue matrix $[R_r]$, which is related to the mode shapes by:

$$[R_r] = \{\phi\}_r\{\phi\}_r^T = \frac{\{\psi\}_r\{\psi\}_r^T}{m_r} \tag{7}$$

Finally, the mass normalized mode shapes, or alternatively the un-scaled mode shapes and the corresponding modal masses are estimated from the residue matrix.

In classical modal analysis (CMA), the modal mass is the least reliable parameter in a parameter estimation process, and moreover it is very sensitive to response magnitude [2]. Only few papers can be found in the literature devoted to the uncertainty in the modal mass.

When operational modal analysis is used to obtain the experimental modal parameters, the forces are not measured and consequently the mode shapes cannot be mass normalized, i.e., the modal masses cannot be determined from the operational responses.

In recent years, three different techniques have been used to estimate the modal masses in OMA:

- The mass change method.
- Combination of the mass matrix of a FE model and the experimental mode shapes
- To assume that the experimental modal masses are equal to those of a FE model.

In this paper, the modal masses of a T steel structure are estimated using the methods described in previous paragraphs and the results are compared.

2 MASS CHANGE METHOD

The mas change method consists of attaching masses to the points of the structure where the mode shapes of the unmodified structure are known and then, perform operational modal analysis on both the unperturbed and the perturbed structures. In order to facilitate the process, lumped masses are often used, in which case the mass-change matrix [ΔM] becomes diagonal. The modal mass corresponding to the r-th mode can be estimated by the equation:

$$m_r = \frac{\psi_{0r}^T \cdot (\omega_{Ir}^2 \cdot [\Delta M]) \cdot \psi_{Ir}}{(\omega_{0r}^2 - \omega_{Ir}^2) \cdot B_{rr}} \tag{8}$$

Where the subscript '0' indicates unperturbed structure, subscript 'I' indicates perturbed structure with matrix $[\Delta M]$ and B_{rr} is the r-th diagonal term of the transformation matrix $[B]$ which relates the perturbed and the un-perturbed mode shape matrices by means of the expression:

$$[\psi_I] = [\psi_0][B] \tag{9}$$

Other expressions for calculate the modal mass can be found in [3].

3 MASS MATRIX AND EXPERIMENTAL MODE SHAPES

If the dynamic behavior of the experimental model is described by the stiffness matrix $[K]_X$ and the mass matrix $[M]_X$, and the experimental is considered as a dynamic modification of the analytical one [3], the modification given by the mass $[\Delta M]$ matrix, the modal mass can be obtained by:

$$m_{Xr} = \{\psi\}_{Xr}^{T} \cdot [M]_X \cdot \{\psi\}_{Xr} = \{\psi\}_{Xr}^{T} \cdot [M]_{FE} \cdot \{\psi\}_{Xr} + \{\psi\}_{Xr}^{T} \cdot \Delta M \cdot \{\psi\}_{Xr} \quad (10)$$

if the matrix $[\Delta M]$ is small, i.e., a reasonably good estimation of the mass matrix can be achieved, we can take the approximation $[M]_X \cong [M]_{FE}$ and the modal mass of the r-th experimental mode shapes can be estimated from:

$$m_{Xr} \approx \{\psi\}_{Xr}^{T} \cdot [M]_{FE} \cdot \{\psi\}_{Xr} \quad (11)$$

4 MODAL MASS OF A FE MODEL

If we have a FE model and there is a reasonable correlation between the numerical and the experimental systems, the numerical modal masses can be used to scale the experimental mode shapes by means of the expression:

$$\widehat{\{\phi\}}_{Xr} \cong \frac{1}{\sqrt{m_{FEr}}}\{\psi\}_{Xr} \quad (12)$$

Where the superscript '^' indicates approximation. If both the numerical and the experimental mode shapes are normalized to the unit length, eq. (12) becomes:

$$\widehat{\{\phi\}}_{Xr} \cong \frac{1}{\sqrt{m_{FE_{Lr}}}}\{\psi\}_{X_{Lr}} \quad (13)$$

However, it must be emphasized that the normalization used in the experimental and numerical mode shapes influences the accuracy obtained in the experimental mode shapes. If both mode shapes are normalized to the largest component equal to unity, the equation:

$$\widehat{\{\phi\}}_{Xr} \cong \frac{1}{\sqrt{m_{FE_{Ur}}}}\{\psi\}_{X_{Ur}} \quad (14)$$

does not provide the same result as eq. (13). If we want both normalizations to provide the same result, eq. (14) must be corrected with the length of both the numerical and the experimental mode shapes by:

$$\widehat{\{\phi\}}_{Xr} \cong \frac{\sqrt{\{\psi\}^{T}{}_{X_{Ur}}\{\psi\}_{X_{Ur}}}}{\sqrt{\{\psi\}^{T}{}_{FE_{Ur}}\{\psi\}_{FEX_{Ur}}}}\frac{1}{\sqrt{m_{FE_{Ur}}}}\{\psi\}_{X_{Ur}} \quad (15)$$

5 EXPERIMENTAL RESULTS. A STEEL T STRUCTURE

A steel T structure consisting of two welded 80x40x4 mm rectangular hollow section beams, being the vertical beam 1.5 m long and the horizontal one 1.2 m, respectively, was used in the tests.

The operation modal testing was carried out measuring the responses in 24 DOF's and using 14 accelerometers (two data sets) with a sensitivity of 100 mv/g, located as is shown in figure 1. The responses were recorded for a period of approximately 3 minutes with a sampling frequency of 2000 Hz. Repetitive hits random in time and space were used as excitation.

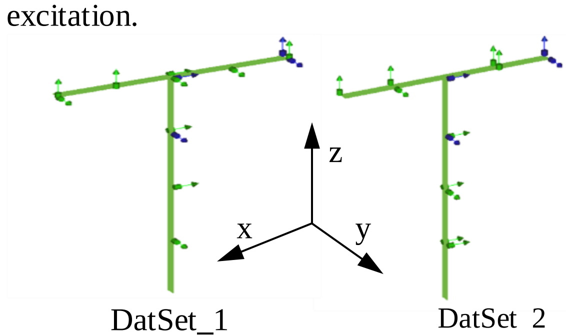

Figure 1: Test Setup.

In order to modify the dynamic behavior of the structure, 8 masses of 145 grams were attached in eight points (same location as sensors) uniformly distributed. The total mass change was 1168 g, which represents 5.8% of the total mass of the structure.

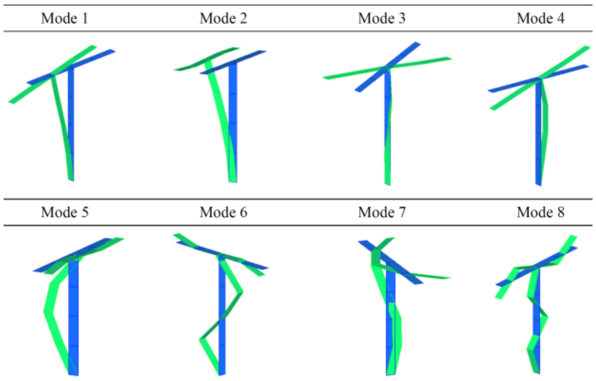

Figure 2: Experimental mode shapes

With respect to the CMA, the structure was excited with an impact hammer. The responses were recorded with a sampling frequency of 2000 Hz and 28 columns of the FRF's matrix were determined from the modal testing.

A finite element model (FEM) was also assembled in ABAQUS using 8 node quadratic shell elements.

The experimental and numerical natural frequencies for the first eight modes pare presented in table 1 whereas the experimental mode shapes are shown in figure 2.

Table 1. Natural Frequencies (Hz)

Mode	OMA Unperturbed (EFDD)	OMA perturbed (EFDD)	CMA	FEM
1	8.73	8.407	8.761	8.797
2	16.35	15.84	16.426	16.730
3	27	25.5	27.059	26.915
4	42.36	40.18	42.52	43.436
5	150.2	145.5	150.8	152.62
6	299.9	289.9	304.22	298.52
7	319.6	302.4	320.35	327.69
8	530.1	500.1	532.25	537.92

The modal masses estimated with the techniques described in this paper and corresponding to mode shapes normalized to the largest component equal to unity, are presented in table 2.

Table 2. Modal masses

Mode	Freq (Hz)	Modal mass			
		Eq. (8)	CMA	Eq. (11)	FEM
1	8.73	9.7778	11.0374	10.6102	11.3673
2	16.35	9.4384	9.92	9.6627	9.6208
3	27.00	2.6734	2.7348	2.6124	2.7927
4	42.36	3.2535	3.3348	3.1729	3.1763
5	150.2	5.7178	5.6367	5.341	5.3115
6	299.9	4.7589	4.5443	4.761	4.9405
7	319.6	2.985	3.1304	2.6166	2.7087
8	530.1	3.2547	3.3324	3.6826	3.9134

5 CONCLUSIONS

- Different techniques to estimate modal masses with both classical modal analysis and operational modal analysis have been presented.
- The techniques have been used to estimate the modal masses of a steel T structure, the discrepancies being less than 10%.

REFERENCES

[1] D.J. Ewins. *Modal Testing: Theory, Practice and Application*, 2nd Ed. Research Studies Press LTD, London, 2000.

[2] S. Zivanovic, A. Pavic, P. Reynolds. *Modal Testing and FE Model Tuning of a Lively Footbridge.* Engineering Structures, Vol. 28, pp: 857-868, 2006

[3] M.L. Aenlle, R. Brincker. *Modal Scaling in Operational Modal Analysis using a Finite Element Model.* International Journal of Mechanical Sciences, Vol 76, pp:86-101, 2013

1st. Conference on Structural Dynamics (DinEst 2018)
Madrid, 20–21 June

ENHANCEMENT OF VIBRATION PEDESTRIAN COMFORT OF A FOOTBRIDGE VIA TUNED MASS DAMPER

Maximilian Bukovics*, José M. Soria*, Iván M. Díaz*, Jaime H. García Palacios*, Joaquín Arroyo† and Juan Calvo†

*ETS Ingenieros de Caminos, Canales y Puertos
Universidad Politécnica de Madrid
28040 Madrid, Spain
e-mail: jm.soria@upm.es
ORCID: 0000-000-2-9507-5704

† Pondio Ingenieros
c/Infanta Mercedes, 90
28020 Madrid

Abstract. Modern footbridges tend to be light and might not fulfill the requirements of the Vibration Serviceability Limit State. Passive damper devices such as tuned mass dampers (TMD) are a solution to reduce vibration without adding significant mass to the structure. Usually these damping solutions are considered as a solution strategy for a vibration problem, but not as part of the design. The aim of this study is to investigate the consideration of these devices in the design phase and assess the improvement to the dynamic response of the structure. It was shown how a finite element program can be used to model a footbridge equipped with a TMD and to execute a dynamic analysis. For that purpose an exemplary structure was modeled in SOFiSTiK software and several methods of dynamic analysis have been tested. The benefits of the incorporation of the TMD in the design process is quantified in term of material saving. Furthermore, a physical design of the TMD was carried out including an economic evaluation.

Key words: footbridge dynamics; vibration serviceability limit state; tuned mass damper.

1 INTRODUCTION

Nowadays, damping systems are usually considered as a solution strategy for a vibration problem, but not as part of the design. However, including TMDs already in the design process lets the engineer plan exactly how slender a bridge can be while at the same time meeting the standards of comfort necessary for the project. To achieve this, the designer has to be able to generate a model that provides information about type and amplitude of vibrations under serviceability conditions and decides what improvements have to be made to satisfy the criteria of the Serviceability Limit State. The Veterinary Footbridge (Madrid, Spain) has been taken as an example to redesign a structure including a TMD.

2 STRUCTURE MODEL

The footbridge examined in this study is a cable-stayed box-girder beam mixed bridge (Figure 1 shows a frontal view of the bridge). and is considered to be a lively bridge, making it interesting for this study. It is located in the north of Madrid, connecting the two sides of the highway A6. The bridge itself is about 45 meters long. On the western side it is supported on the embankment on two elastomer supports. On the eastern side it is connected to an 18 meters high pillar. As an additional support the bridge is connected to the top of the pillar with two cables.

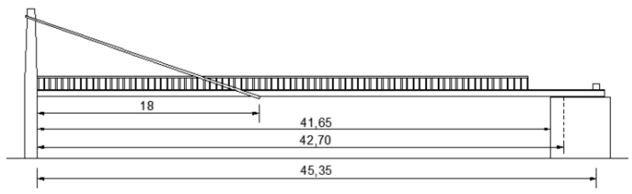

Figure 1: Sketch of the bridge

The damping, which can only be determined by measurment, is a key parameter for the vibration response of the structure. The fib Bulletin 32 [3] provides a method for estimating the damping of footbridges, considering several different aspects of the structure, such as material, connections and bearings. According to this method, the damping coefficient of the entire structure was calculated as 0.92 %. A definite FE model was generated in SOFiSTiK software. Based on this model, the dynamic analysis of the footbridge was executed.

3 DYNAMIC ANALYSIS

3.1 Load model

To check if this footbridge is prone to be excited under pedestrian load, it had to be analyzed, if one or more of the natural frequencies of the structure are inside the range of the usual step frequency of pedestrians. The HIVOSS guide [4] defines the critical frequencies of vertical vibrations as between 1.25 Hz and 2.30 Hz for the first harmonic and between 2.50 Hz and 4.60 Hz for the second harmonic of excitation. Horizontal and lateral vibrations were not subject of this study. A modal analysis done directly in Sofistik via the method of vector iteration showed that there are two vertical modes inside the critical range, $f_1 = 1.851$Hz and $f_2 = 4.237$ Hz (see figure 2).

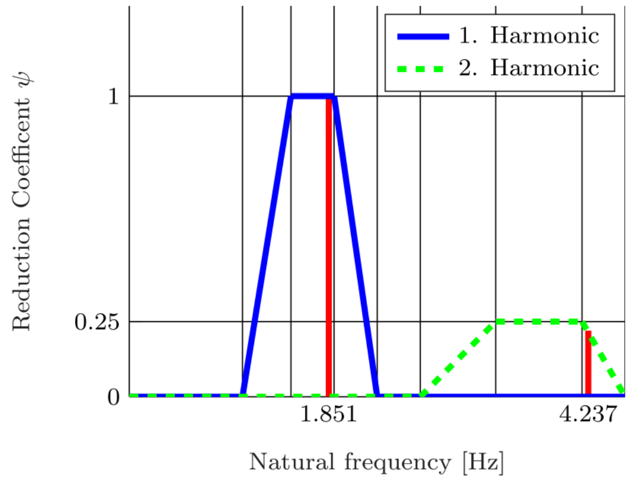

Figure 2: Critical frequency range

So, a detailed examination of the dynamic loading was necessary. Two major cases of pedestrian loads can be distinguished: First, the pedestrians are crossing the bridge in a continuous stream and therefore exciting the bridge constantly over a longer period of time, so the the response will converge to the steady state solution. Second, pedestrians are only occasionally crossing the bridge, individually or in larger groups [4], giving the structure not enough time to to settle into a steady state. For this report only the first type, the continuous stream will be specified. A detailed description of loading force models can be found in [2].

$$p(t) = P \cdot n' \cdot \psi \cdot \cos(2\pi f_n t) \tag{1}$$

The pedestrian load $p(t)$ was simulated with a harmonic sinusodial wave that was applied as a continuous load over the whole bridge deck. The amplitude was calculated by the force P of a single pedestrian (P = 280 N) multiplied with an equivalent number of pedestrians n' on the surface and a reduction factor ψ that depends on the natural frequency (see figure 2). Five traffic classes were defined according to HIVOSS [4], depending on the level of occupacy: from 0.1 to 1.5 pedestrians per squaremeter.

3.2 Structure response

The defined load cases were applied to the FE model. The response was calculated via the method of direct integration. The time history of the response under the five load cases can be seen in figure 3. After calculating the response, comfort levels were assigned to the footbridge for each of the load cases. The results are compiled in table 1. The comfort levels are defined by the maximum acceleration according to the HIVOSS guide [4].

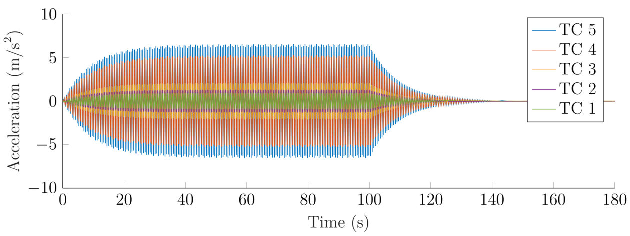

Figure 3: System response

After the response was calculated, the TMD was introduced into the model to reduce the amplitudes of the vibration and to enhance the comfort classes of table 1.

4 IMPROVING THE LEVEL OF COMFORT

The TMD was modelled as a simple point mass (fixed in all directions except in the Z-Axis) that is attached to the bridge deck via a spring and a damper element (see figure 4).

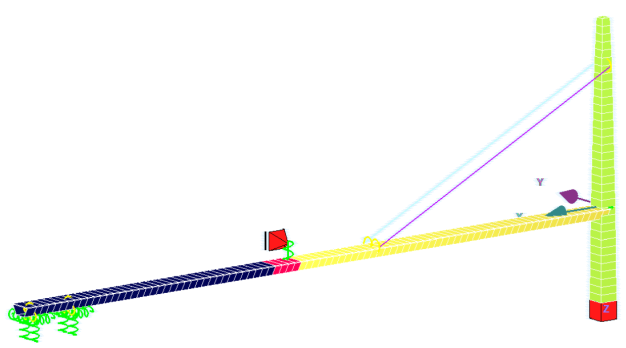

Figure 4: FE model with TMD

The values of the mass, the damper and the spring can be calculated via different formulas. A comparison of 4 different formulas was undertaken for load case 5 to find out the best suiting formula for this model (see figure 5).

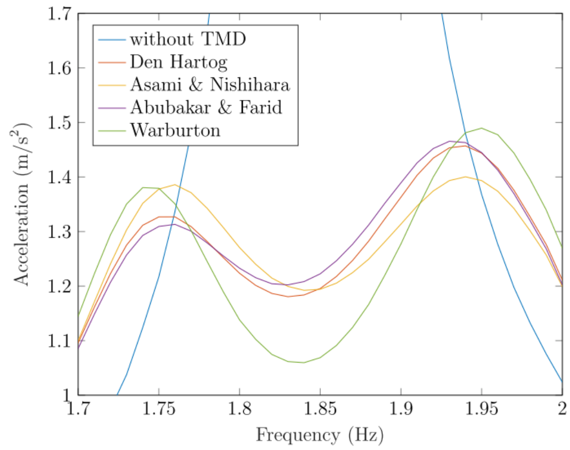

Figure 5: Comparison of TMD tuning

It can be seen, that the formula by Asami and Nishihara [1] delivers the smallest maximum and was therefore taken as the best soulution. After that, the mass of the TMD was chosen. In theory, the heavier a TMD is, the bigger is its damping effect. So, a study was undertaken to find out the damping effect of a TMD with a mass ratio between 0% and 3.5 % (the mass ratio is the ratio bewteen the mass of the TMD and the modal mass of the system at the critical frequency). In the end, 1.5 % was considered to be sufficient (see figure 6).

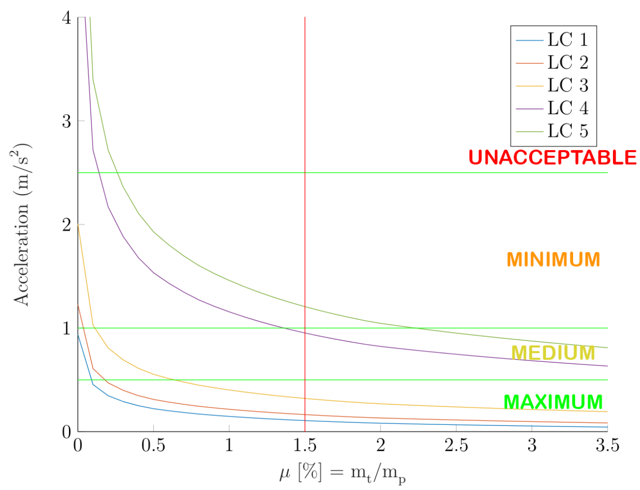

Figure 6: Max. acceleration in respect to mass ratio. Green lines represent limits of comfort classes

The result is, that the original first mode (1.851 Hz) is now split up into two modes with the TMD swinging in phase (f=1.74Hz) and in opposite phase (f=1.96Hz) as can be seen in figure 7.

Table 1: Comparison of response before and after attaching TMD

Traffic Class	Density [Ped./m^2]	Max. acc. no TMD [m/s^2]	Old Comfort Class	Max. acc. with TMD [m/s^2]	New Comfort Class
TC 1	0.1	0.94	Medium	0.16	Maximum
TC 2	0.2	1.33	Minimum	0.23	Maximum
TC 3	0.5	2.11	Minimum	0.36	Maximum
TC 4	1.0	5.27	Unacceptable	0.91	Medium
TC 5	1.5	6.54	Unacceptable	1.13	Minimum

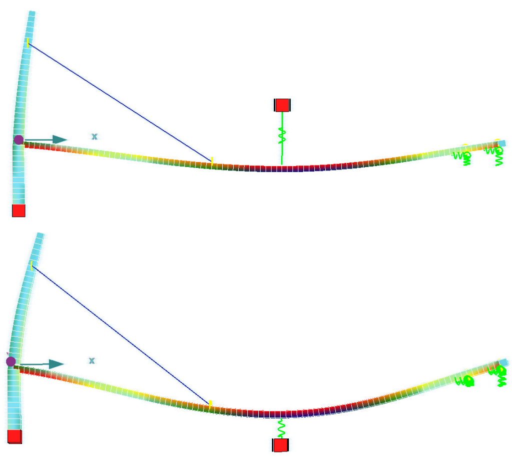

Figure 7: New mode shapes with TMD

With the TMD defined and included in the model, the response was calculated again. Figure 8 shows a comparison between the response of the orignial and the improved system (Only Traffic class 5). The values for the maximum acceleration for each traffic class are compiled in table 1.

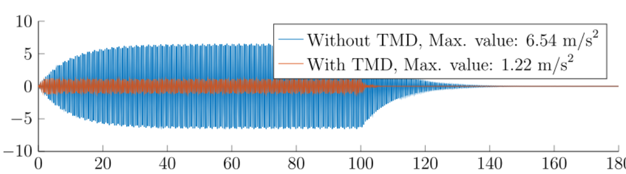

Figure 8: Response with and without TMD, TC 5

In the end, the results of the calculation were used to design a TMD. The mass was chosen as 340 kg according to the mass ratio defined earlier. The spring and damping values (45.2 kN/m and 590 Ns/m) were calculated based on the formula of Asami and Nishihara. Figure 9 shows the final design made based on these parameters.

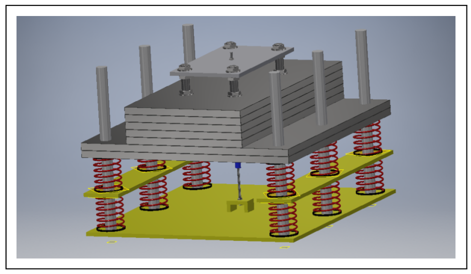

Figure 9: CAD view of the TMD

5 CONCLUSION

As seen in table 1, the improvements made by the TMD are quite significant. A comparison showed that achieving the same result just with adding thickness to the bridge section, would require a 50 % increase in mass. Considering that the estimated implementation cost of the TMD would only be around 10000 Euro makes the result even more impressive.

REFERENCES

[1] Asami and Nishihara. Analytical Solutions to H∞ and H2 Optimization of Dynamic Vibration Absorbers. *J. Vib. Acoust 124(2)*, 2002.

[2] Maximilian Bukovics. Analysis of the dynamic behavior of a footbridge under pedestrian loading. Enhancement of vibration comfort via a TMD. Master's thesis, UPM, 2018.

[3] Federetaion internationale du beton (fib). Guidelines for the Design of Footbridges. *Fib Bullettin*, 32:160, 2005.

[4] HIVOSS. Design of Footbridges - Guideline, 2007.

DYNAMIC ANALYSIS OF A LIVELY DINNING HALL FLOOR: TESTING AND MODELLING

Jaime H. García-Palacios*, Iván M. Díaz*, Xidong Wang*, José C. Deniz*, José M. Soria* and Carlos Martín de la Concha*

*Civil Engineering: Hydraulics, Energetics and Environment Department
ETS Ingenieros de Caminos, Canales y Puertos
Universidad Politécnica de Madrid
28040 Madrid, Spain

e-mail: jaime.garcia.palacios@upm.es

Abstract. Long-span open plan floors are structures that may suffer excessive vibrations when subjected to dynamic human-induced loading. When a multi-input multi output vibration control strategies is planned to be installed in order to reduce vibration levels, a modal model should be derived for designing purposes. Thus, the research team has planned the dynamic testing of an in-service open planned dinning hall sited in Pozuelo (Madrid, Spain), as a previous step of the control design.

First, a finite element model (FEM) of the structure has been made from architectural drawings and visual inspection of the structural elements. Second, an operational modal analysis has been undertaken using 18 high-sensitivity accelerometers and through several setups covering the whole floor. Also, frequency-response-function analyses have done using an electrodynamic shakers placed consecutively at two different selected locations. The input excitation was a chirp signal exciting the structure in a broad-band frequency spectrum. Finally, the FEM model has been calibrated taking into account all the test undergone and accurate broad-band-frequency modal model has been derived for the design the active control strategy.

Key words: floor vibration; operational modal analysis; frequency-response-based modal analysis, model updating

1 INTRODUCTION

Actually, the comfort associated to the use of a structure must be considered as a serviceability state in the design [3]. The dynamic behaviour of a building or some of its elements may be a source of discomfort at given locations on the structure for the users. This discomfort depends, not only in the frequency and magnitude of the generated disturbance but also on the activity developed by the receiver and the time span exposed to it. A vibrating floor it's different perceived by a person doing gymnastics on it from another one trying to write on a desk, even if they are the same time on the structure. After some time, a low level vibration can became a source of stress. In this paper, an in-service open planned dinning hall floor sited in Pozuelo (Madrid, Spain) has been identified as a vibrating structure (see figure 1). The vibration source is human-induced and can be easily feel it during lunch time. In order to investigate a possible solution able to cope with this issue, a multi-input multi output vibration control strategy will

Figure 1: Panoramic picture of the dinning hall

be proposed. This paper focuses in the first part of this work where the structure has been identified and a model has been calibrated in order to have the necessary data to carry on with the design of the control system proposed in the paper by Xidong et al. of this congress.

The structure of the paper follows with a description of the finite element model (FEM) of the structure in section 2, the operational modal analysis (OMA) and experimental modal analysis (EMA) obtained from on-site measures in section 3. Section 4 continues with the model calibration and finally some conclusions are drawn.

2 DESCRIPTION OF THE FINITE ELEMENT MODEL

The floor under study corresponds to the open dinning hall sketched in figure 2. It corresponds to the top floor of a three storey building. Three sides are external walls, with large windows separated with columns and load bearing walls. In the other side there are more rooms and some columns that must be taken into account The floor below has many rooms with brick walls separating them and two line of columns. These are boundary conditions that must be introduced in the finite element model (FEM) of the dinning hall. Most of this information has been taken from architectural drawings and visual inspection of the structural elements whenever they are accessible. However, there are some geometrical uncertainties, as the floor slab thickness, that are difficult to determine. The mechanical properties of the materials, the stiffness introduced by brick walls and the embedding ratio of the columns in the slabs add some uncertainties to the FEM.

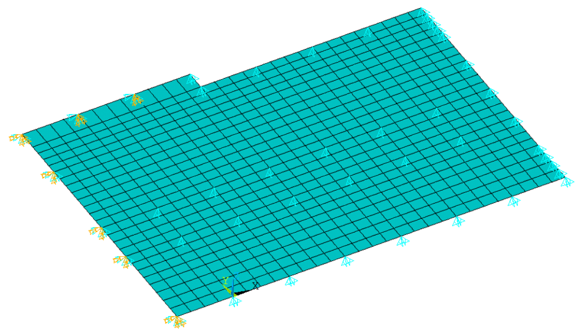

Figure 2: Ansys model with boundary conditions

The model has been done in ANSYS [6] and SOFISTIK [1] considering shell elements for the slab. Columns are introduced as a boundary condition constrained in the vertical direction (Z) and with a variable rotation stiffness in the other two directions (X, Y), depending on their situation. Load bearing walls are also boundary conditions with the movement constrained in vertical and in the direction parallel to the maximum length of the wall.

3 EXPERIMENTAL ANALYSIS

In order to know the real behaviour of the structure some measurements has been planned and done on the structure. These results are used to calibrate the FEM model. Three setups with 18 accelerometers have been planned, with 8 fixed sensors and 10 roving. Also an electrodynamic shaker has been used in some of the experiments. The shaker acceleration signal has been measured together with the floor accelerations. Data have been acquired using a NI cRIO distributed equipment and high sensitivity PCB accelerometers measuring in the vertical direction. A total of 11 test are summarized in table 1.

Table 1: Description of the tests

test	setup	Excitation
1	1	Shaker at TP3 random signal, 2Hz-20Hz, 10min
2	1	Shaker at TP3 random signal, 4Hz-15Hz, 10min
3	1	No signal, 10min
4	1	No signal, All night
5	1	Shaker at TP3 random signal, 0Hz-30Hz, 20min
6	1	Shaker at TP3 chirp signal, 5Hz-12Hz, 10min
7	1	Heeldrops and jumpings at TP3 or TP18, 5min
8	2	Shaker at TP6 random signal, 0Hz-30Hz, 20min
9	2	Shaker at TP3 random signal, 0Hz-30Hz, 20min
10	3	Shaker at TP3 chirp signal, 20min
11	3	Shaker at TP6 chirp signal, 20min

3.1 Operational Modal Analysis

All test from table 1, except for number 7, can be used for OMA. The most interesting one corresponds to the measures taken during the whole night (test 4), but tests 1, 2, 5, 8 and 9 give also very good information due to the energy introduced in the analysis. Test with Chirp signal are also interesting to evaluate the resonance phenomena in the time histories. They can be also used to identify modal shapes and frequencies.

The modal identification has been done with the Stochastic Subspace Identification (SSI) method [7]

Table 2: Frequency of identified modes

Mode	Frequency	Mode	Frequency
1	6.626 Hz	2	7.438 Hz
3	10.121 Hz	4	13.397 Hz

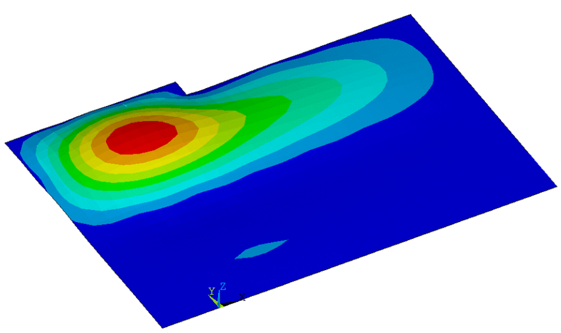

Figure 3: Mode 1.

All these tests have allow to identify the modes summarized in table 2. The first two modes are shown in figures 3 and 4.

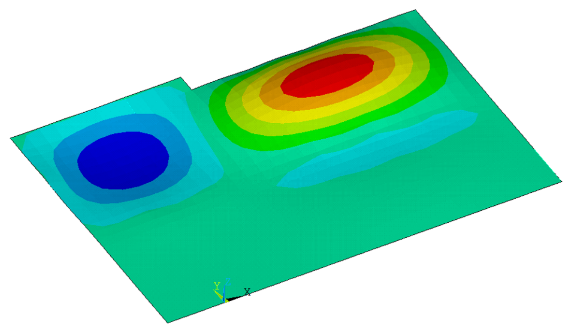

Figure 4: Mode 2.

3.2 Experimental Modal Analysis

The use of one shaker in some of the test with a moving mass of 31 kg and and accelerometer attached on it allows to obtain the input force. Therefore, a frequency response analysis (FRF) can be done and the modal mass associated to each mode can also be estimated. This extra information is very helpful in the calibration process of the FEM. Figure 5 shows the FRF obtained in test 6.

The measured force can be also used as an input for a transient analysis on the FEM to compare the resulting time histories at the same locations measured in the real tests. The same force can be used in an harmonic analysis of the FEM.

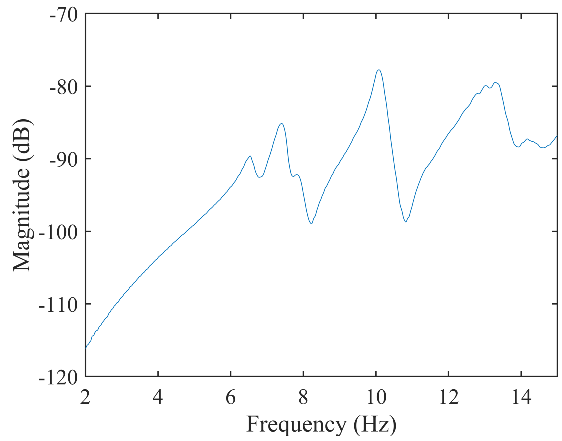

Figure 5: Frequency Response Function (m/N s^2)

4 MODEL CALIBRATION

The information obtained in the experimental analysis has been used to calibrate the FEM model. First, the design parameters are chosen. Second, a reasonable range of variation for the design parameters has been adopted. Third, the influence of each design parameter on the modal response of the structure has been evaluated. Afterwards, the modes identified in the measure and in the FEM are related using the Modal Assurance Criterion (MAC) [2]. Finally, the minimization of the following objective function has been proposed:

$$OF = min \left\{ \sum_{i=1}^{nmodes} \alpha_i |f_{m_i} - f_{FEM_i}| \right\} \tag{1}$$

where, f_{FEM_i} is the frequency of mode i in the FEM, f_{m_i} the measured one, α weights the importance applied to each mode. Using an iterative process between ANSYS and MATLAB, and the previous experience of the authors [4], [5] the optimum is reached. The design variables in the optimal solution have been updated in the final FEM before to carry on with the design of the vibration control system.

5 CONCLUSIONS AND FURTHER RESEARCH

The difficulty to make an accurate FEM from architectural drawings that dynamically behaves as the real structure is outstanding. This becomes crucial when the FEM is going to be used as a way to optimize vibration control. Therefore, the need of a measurement campaign is justified and a complete methodology to calibrate a FEM of a structure has been described.

The engineering work done to understand the importance of the influence of the design parameters as well as their selection, allows to understand the structural behaviour and it is necessary to converge in an optimal solution with physical meaning. A larger mesh of measuring points would help to have a better spatial resolution for higher modes.

Finally, this work still goes on introducing the results of the EMA analysis into the calibration process.

6 ACKNOWLEDGMENTS

The authors acknowledge the support provided by the Civil Engineering: Hydraulics, Energetics and Environment Department of ETSICCP at UPM and by the Research Net VIBRASTRUNET (BIA2015-71942- REDT).

REFERENCES

[1] SOFiSTiK AG. *SOFiSTiK*, 2018.

[2] D.J. Ewins. *Modal Testing: Theory and Practice.* RESEARCH STUDIES PRESS LTD. Letchworth, Hertfordshire, England. JOHN WILEY & SONS INC., 1984.

[3] ISO 10137. *Bases for Design of Structures – Serviceability of Buildings and Walkways against Vibrations*, international organization for standardization edition, 2007.

[4] J.M. Soria, I.M. Díaz, J.H. García-Palacios, and N. Ibán. Vibration monitoring of a steel-plated strees-ribbon footbridge: uncertainties in the modal estimation. *Journal of Bridge Engineering*, 108(5):1175–1183, 2016.

[5] J.M. Soria, I.M. Díaz, E. Pereira, J.H. García-Palacios, and X. Wang. Exploring vibration control strategies for a footbridge with time-

varying modal parameters. In *MOVIC & RASD 2016*, Southhampton, 2016.

[6] Dr. John Swanson. *ANSYS*, swanson analysis systems, inc edition, 1970.

[7] P. Van Overschee and B. De Moor. *Subspace Identification for Linear Systems.* Subspace Identification for Linear Systems., 1996.

OPERATING STATE IDENTIFICATION OF A HIGH-SPEED TRAIN WITH ANALYSIS OF THE VIBRATION SIGNAL

A. Bustos*, H. Rubio*, C. Castejon*, J.C. Garcia-Prada*

*MAQLAB, Mechanical Engineering Department
Universidad Carlos III de Madrid
28911 Leganés, Madrid, Spain
e-mail: albustos@ing.uc3m.es
ORCID: 0000-0001-7513-6058

Abstract. High-speed rail is a strategic sector in the Spanish industry that is in continuous innovation. What concerns the rolling stock, the analysis of the train dynamic behavior, especially bogie dynamic behavior, is a key aspect in order to get advance over competitors. Vibration analysis is a good tool for studying railway dynamics, for which train are usually equipped with measurement systems that record the axle box vibrations. The bogie is a complex moving mechanical system consisting of several components that interact between them: bogie structure, wheelset, primary suspension, axle boxes, etc. This interaction between elements generates complex vibration signals, which are the result of the addition of the vibrations generated in different elements. The processing of the vibration signals acquired by the measurement system allows us to identify the main frequency components. If the proper signal processing technique is applied, it is possible to establish a relation between the main frequency components of the frequency diagrams and the physical source that generate them. However, vibration sources are not only limited to the bogie structure and components, but also to external factors as the track condition, the wheel-rail contact, etc. In this work, a set of classical-based techniques for signal processing is applied to a practical case: the study of the vibration signal behavior of a high-speed train bogie in regular service. The train is equipped with an online measurement system that comprises a set of accelerometers attached to the axle box cover and aligned with the three spatial directions. The utility of the proposed signal processing techniques is explored in this work to identify the train operating state.

Key words: High-Speed Train, Vibration Signal, Frequency Diagram and Spectral Power.

1 INTRODUCTION

The analysis of vibration signals is a widely used technique for the inspection of railway mechanical components. This technique is suitable for the conduction of test on an extensive range of elements of the infrastructure and rolling-stock [1].

Many publications in the technical literature have studied the vibration of rolling stock from different points of view: the improvement of the dynamic behavior of rolling stock [2], the condition identification of specific mechanical components through signal processing [3], etc.

What concerns the railways infrastructure, many authors have conducted vibration analysis focused on the ground or track perturbations induced by the transit of rolling stock [4,5]. In fact, the reference [5] summarizes the ground vibration levels recorded at 17 high speed rail sites across 7 European countries.

Some researchers [4,6] classify the track condition through the vibration measurements recorded by accelerometers mounted in the axle boxes of rolling stock.

This work studies the dynamic behavior of a high-speed train bogie with the aim of establishing a set of features that allows for the fast identification of the bogie's operating state.

2 EXPERIMENTAL SYSTEM

Vibration signals are collected from a high-speed train in regular operation. To that end, the measurement system is able to record signals at speeds above 300 km/h.

The measurement system is composed of two main blocks. The first block includes the vibration measuring, the data acquisition and the data transmission systems and are installed inside the train. The second block encompasses the recording system and contains a database located at the MAQLAB Laboratory in the Universidad Carlos III de Madrid.

The onboard measurement system comprises a DC power supply unit, two electronic devices for signal amplification and acquisition, an UMTS (3G) router for data transmission, a speed sensor and three uniaxial accelerometers.

All sensors are mounted in the axle box cover of a trailer axle. Each axle box is equipped with double row tapered roller bearings. The three accelerometers are arranged to measure vibrations in the three directions of space (longitudinal, axial and vertical), as it is shown in Figure 1. The speed sensor is embedded inside the axle box cover.

The vibration sensors are ICP accelerometers of industrial use with a measurement range of ±50 g, a frequency range from 0.52 Hz–8 kHz, and a sensitivity of 100 mV/g. The measurement system were configured to acquire acceleration signals in a speed range between 75 and 2000 rpm, approximately between 13 km/h and 346 km/h. Acceleration measurements are acquired during 3.2 seconds at a sampling rate of 5120 Hz, which results in 16384 data points per measurement. Subsequently, vibration signals are transmitted and recorded in the remote database.

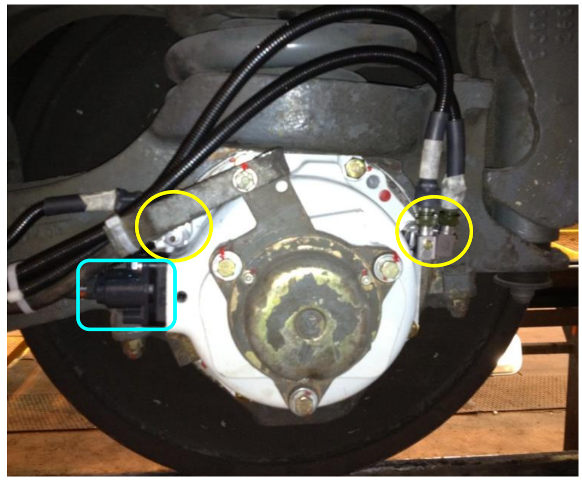

Figure 1: Location of the longitudinal, axial, and vertical accelerometers (highlighted in yellow circles) and speed sensor (highlighted in blue square) in the axle box.

3 METHODS

Classical signal processing methods (as the PSD and the EMD decomposition) are applied in this work. The PSD is a widely known technique and does not need explanation. The EMD or Empirical Mode Decomposition identifies the intrinsic oscillatory modes of a signal and decomposes the original signal into a set of Intrinsic Mode Functions or IMF. This technique works computing the upper and low envelopes of the signal, calculating the average and subtracting it from the original signal until some conditions are achieved. The reference [7] explains this method in detail.

With the aim of summarizing the recorded data, the PSD and the spectra of the six first IMF of all the analyzed signals will be computed, and then the average spectra of PSD and IMFs will be calculated and plotted [3].

4 RESULTS

In order to get enough measurements for data analysis and a uniform behavior, the experiments were carried out in a 150 km –length sector of a high-speed line. The train runs at a constant speed of 270 km/h in this sector. Due to the limited space, only the vertical accelerometer signal is analyzed.

The Figure 2 shows the average spectrum of the recorded signals. There are two frequency bands of high activity in both spectra: the first one between 0 Hz and 1000 Hz, which contains the main peaks of the spectrum, and the second one between 1900 Hz and 2500 Hz.

The third multiplier of the wheel rotating frequency, located at 80 Hz, is clearly visible in the spectrum of Figure 2.

Three other significant frequency components or peaks are marked as P_1, P_2 and P_3. P_1 is located at 123 Hz, approximately and its frequency coincides with the sleeper passing frequency –given by equation (1) – and to the BSF of the bearing –given by equation (2).

$$f = v / \lambda = 123.4 Hz \tag{1}$$

$$BSF = \frac{D}{2d} F_s \left[1 - \left(\frac{d}{D} \right)^2 \cos^2 \beta \right] = 123.6 Hz \tag{2}$$

$$BPFO = \frac{N_b}{2} F_s \left(1 - \frac{d}{D} \cos \beta \right) = 269.3 Hz \tag{3}$$

P_2 is located at 255 Hz, approximately. This peak was not observed in other conditions within a wider study carried out [8]. It were only discovered in the HSL and date analyzed in this work. These facts lead us to believe that P_2 has its origin in a track defect. Using equation (1), we obtain a wavelength of 0.289 m. According to [9], this wavelength is within the short waves defects range. This fact would indicate the need of a maintenance action in the track.

P3 is located at 269 Hz, approximately, which coincides with the BPFO of the bearing –given by equation (3).

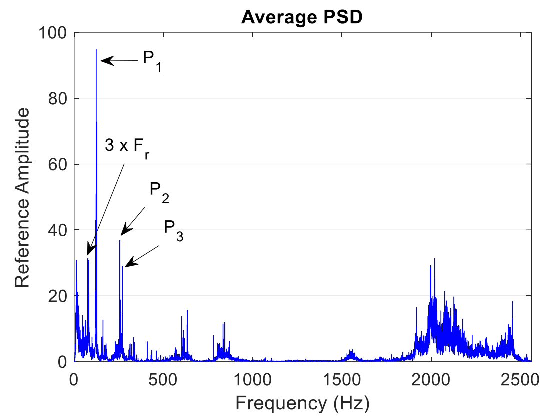

Figure 2: Average PSD of the recorded vibration signals.

The average spectra of the IMF are shown in Figure 3. The application of the EMD allows for the easier classification of the active bands of the spectra. P_1 and P_2 are contained in different IMF, which would indicate they have different mechanical origins.

In addition, IMF 1 covers the entire high frequency band (above 1900 Hz). This matches the wheel-corrugation frequency region [10], which would indicate the need of an imminent maintenance action in the wheel.

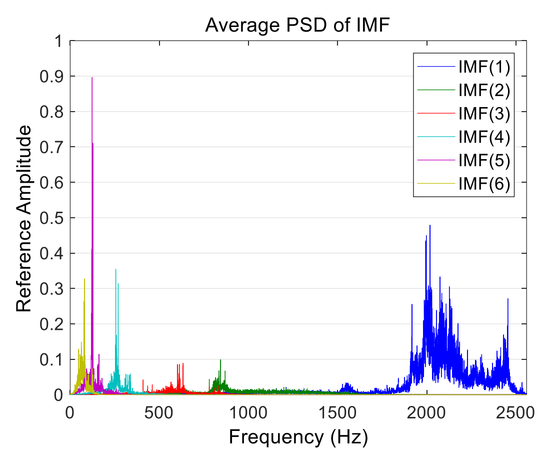

Figure 3: Average spectra of the IMF of the recorded vibration signals.

5 CONCLUSIONS

This work uses well-established signal processing techniques to identify the operating state of a high-speed train through vibration signals.

Obtained results show a high frequency band (1900-2500 Hz) of the spectra related with wheel corrugation. The analyzed spectra also show three significant peaks. The first of them, called P_1, is related to the sleeper passing frequency and/or a bearing defect; while the second, named P_2, is related to short waves defects in the track. The last one, called P_3, is related to a bearing defect.

In essence, the applied methods lead to interesting results not only about the operating state of the high-speed train, but also about the condition of the track.

ACKNOWLEDGEMENTS

The Spanish Government supports this work through the MAQ-STATUS DPI2015-69325-C2-1-R project. The authors also gratefully acknowledge the help of the participating companies (Renfe, Alstom Spain, SKF Spain and Dano-Rail).

REFERENCES

[1] A. Alemi, et al. *Condition monitoring approaches for the detection of railway wheel defects*. Proc. Inst. Mech. Eng. Part F J. Rail Rapid Transit. 2017;231:961–981.

[2] L. Mazzola, et al. *Evaluation of the hunting behaviour of a railway vehicle in a curve*. Proc. Inst. Mech. Eng. Part F J. Rail Rapid Transit. 2015;229:530–541.

[3] A. Bustos, et al. *EMD-Based Methodology for the Identification of a High-Speed Train Running in a Gear Operating State*. Sensors. 2018;18:793.

[4] J.S. Lee, et al. *A Mixed Filtering Approach for Track Condition Monitoring Using Accelerometers on the Axle Box and Bogie*. IEEE Trans. Instrum. Meas. 2012;61:749–758.

[5] D.P. Connolly, et al. *Large scale international testing of railway ground vibrations across Europe*. Soil Dyn. Earthq. Eng. 2015;71:1–12.

[6] P. Weston, et al. *Perspectives on railway track geometry condition monitoring from in-service railway vehicles*. Veh. Syst. Dyn. 2015;53:1063–1091.

[7] N.E. Huang, et al. *The empirical mode decomposition and the Hilbert spectrum for nonlinear and non-stationary time series analysis*. Proc. R. Soc. Lond. Math. Phys. Eng. Sci. 1998;454:903–995.

[8] A. Bustos. *Metodología para la mejora del diseño de sistemas mecánicos de responsabilidad para el uso de tecnologías avanzadas de mantenimiento DM&M*. Universidad Carlos III de Madrid. Leganes, Madrid, 2017.

[9] M. Melis. *Apuntes de introducción a la dinámica vertical de la vía y a las señales digitales en ferrocarriles: con 151 programas en Matlab, Simulink, Visual C++, Visual Basic y Excel*. Escuela de Ingenieros de Caminos; 2008.

[10] D.P. Connolly, et al. *Benchmarking railway vibrations – Track, vehicle, ground and building effects*. Constr. Build. Mater. 2015;92:64–81.

1st Conference on Structural Dynamics (DinEst 2018)
Madrid, 20-21 June

DYNAMIC TEST AND VIBRATION CONTROL OF A TWO-STORY SHEAR BUILDING MODEL

Ignacio Embid*, Carlos Martín de la Concha*, Iván M. Díaz*, Jaime H. García Palacios*, Juan C. Mosquera Feijoo*

* ETS Ingenieros de Caminos, Canales y Puertos
Universidad Politécnica de Madrid
28040 Madrid, Spain
e-mail: i.embidruizdec@alumnos.upm.es

Abstract. The aim of this paper is to study the dynamic behaviour of a two-story shear building employing a standard measurement equipment and a mobile phone application. A building model is constructed using methacrylate for floors and aluminium alloy for columns. The model is calibrated using both measurement techniques. A control strategy based on a pendulum tuned mass damper is designed and installed, then, the improvements are assessed from damping estimation.

Key words: Vibration Control, Pendulum Tuned Mass Damper, Dynamic Analysis

1 INTRODUCTION

Nowadays, the design process of slender structures must take into account the vibration serviceability. This has become one of the main challenge for modern structural engineers. This fact is due to the current trends for lighter and much slender structures built using high-performance materials and innovated construction process [1]. Under these circumstances, the serviceability state associated with the vibration of slender structures, such as high-rise buildings, high-span floors, cantilevered grandstands or slender footbridges [2-4], becomes the critical issue the design.

This paper has been written by master students under the supervision of professors of *Dynamic and Experimental Analysis of Structures*. A model of a very flexible two-story shear building has been constructed. Its dynamic has been analysed by using a high-quality standard-measurement equipment and a mobile phone. These devices have triaxial MEMS accelerometers with enough sensitivity to measure the expected accelerations [5].

In order to demonstrate the effect of passive control to reduce the vibration level. A pendulum tuned mass damper (PTMD) has been design and installed in order to reduce the vibration response and bending moments at joints.

2 STRUCTURE DYNAMIC

2.1 Description of the Structure

A two-story shear-building model has been constructed. The building model is made of methacrylate and aluminium and it is designed to ensure a two-degree-of-freedom (2-DOF) behaviour. For the analytical analysis, it is simplified as a 2-DOF shear-building model whose masses are concentrated on storeys and its stiffness comes from the column rigidities. The dimensions of the structure, in cm, are: first floor 30.5x10x3, second floor 30.5x10x1.5, height of first floor 73.5 and height of second floor 50 (See Figure 1). Noting that the design was done in such way that both vibration modes were easily observed visually.

Figure 1: Building model.

2.2 Dynamic Analysis

Firstly, the modal analysis of the structure is computed as a basic eigenvalue problem (Figure 2). The natural frequencies estimated were f_1=1.23 Hz and f_2=4.88 Hz.

Secondly, experimental free response to estimate the frequency and damping of the fundamental mode is undertaken. A non-zero displacement initial condition is applied at the top of the building $u_2(0)=0.02\,\mathrm{m}$.

A commercial acquisition system (cDAQ-9191) with two piezoelectric accelerometers (PCB 352 C33), each in a floor, conditioned by the NI- 9234 are used. Additionally, a Xiaomi Mi A1 smartphone installed on 2nd floor is also used for the same purpose. The free available app, *Accelerometer Analyzer from Mobile Tools*, is used to record the data. It should be noted that the time associated to each sample is not perfectly equally spaced and a MATLAB script has been developed to interpolate and resample the data to equally spaced discrete-time points. Figure 3 shows the response in both cases.

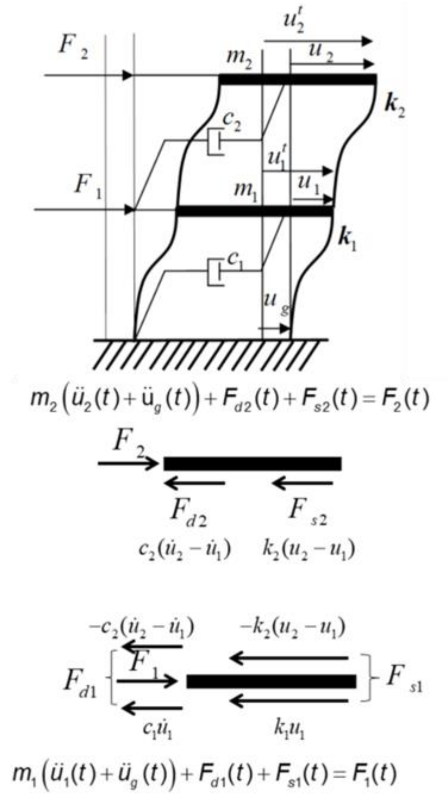

Figure 2: Building model. Free body diagrams

Thirdly, the Fast Fourier Transform (FFT) of time histories is undertaken for frequency estimation: f_1=1.15 Hz and f_2=5.21 Hz. The same results are obtained from both equipment (see Figure 4). Obviously, for low-amplitude response, the FFT from the mobile phone response is noisier.

2.3 Model updating

The model is now calibrated from the experimental results. The sources of uncertainty are studied and the difference between estimated and measured natural frequencies is minimized. The main source was identify to be the stiffness of joints column-floor, such that semi-rigid joints were considered. Thus, the final model presents the following natural frequencies: f_1=1.15 Hz and

f_2=5.23 Hz. A loss of stiffness at 1st floor-joint of 33% and at 2nd floor-joint of 8% have been included into the model.

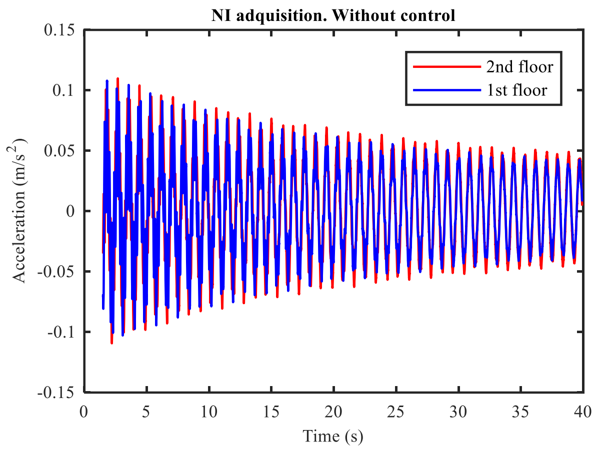

a) NI- DAQ acquisition

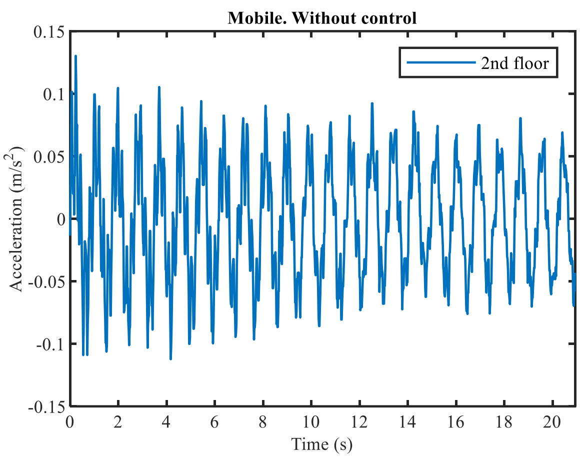

b) Xiaomi Mi A1

Figure 3: Free response.

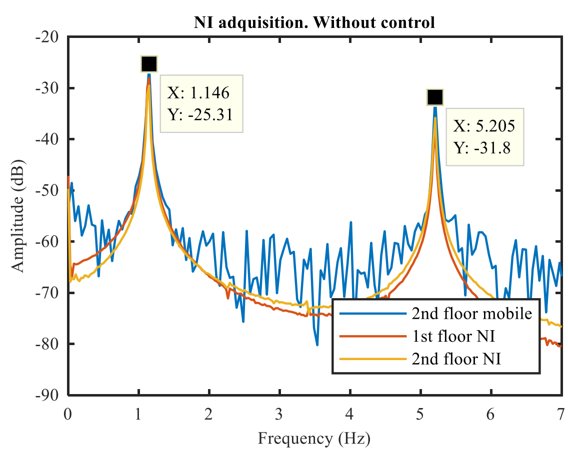

Figure 4: FFT of the free response.

3 VIBRATION CONTROL

A TMD is designed, constructed and installed on the structure in order to drastically reduce the vibration coming from the first mode [6] (see Figure 1). Thus, a PTMD is the option adopted since it is a solution that has been used for motion control of high-rise building. Den Hartog approach is used for the TMD tuning. Then, once the tuned frequency of the TMD is computed, the length L of the pendulum is obtained. These steps are depicted by the following equations:

$$\frac{f_{TMD}}{f_1} = \frac{1}{1+\mu},\ \mu = \frac{m_{TMD}}{m_1};\ \zeta_{TMD} = \sqrt{\frac{3\mu}{8(1+\mu)^2}} \qquad (1)$$

$$f_{TMD} = \frac{1}{2\pi}\sqrt{\frac{g}{L}}$$

Thus, the theoretical tuned frequency of the pendulum is: f_{TMD}=1.09 Hz.

The 3-DOF system is now analysed including the PTMD. The case of the PTMD can be reduced to a moving mass connected to the structure by a spring and a viscous damper. The new mass and stiffness matrices are as follows:

$$\mathbf{M} = \begin{bmatrix} m_1 & 0 & 0 \\ 0 & m_2 & 0 \\ 0 & 0 & m_3 \end{bmatrix},$$

$$\mathbf{K} = \begin{bmatrix} k_1+k_2 & -k_2 & 0 \\ -k_2 & k_2+k_{TMD} & -k_{TMD} \\ 0 & -k_{TMD} & k_{TMD} \end{bmatrix}, k_{TMD} = \frac{m_{TMD}\, g}{L_{TMD}} \qquad (2)$$

Figure 5 shows the Frequency Response Function of the final tuning. As it is well-known, the no-control 1st mode is split into two modes.

Once, the PTMD is installed and the same test is carried out. Figure 6 and 7 shows the time response and the FFT. Finally, the damping ratio is estimated using the logarithm decrement. Thus, this is interestingly increased from 1.7 % to 15 %.

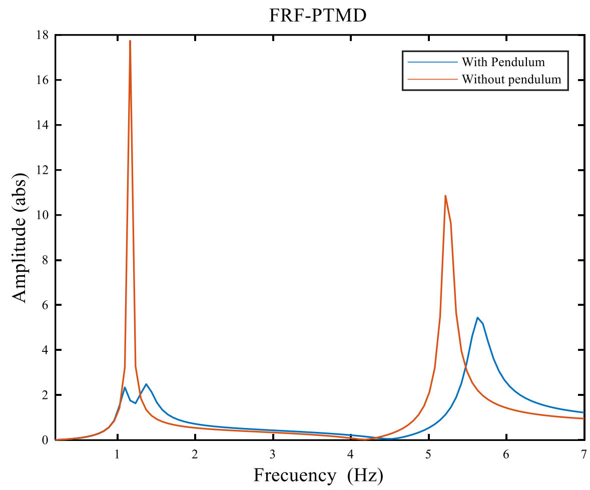

Figure 5: Theoretical FRF.

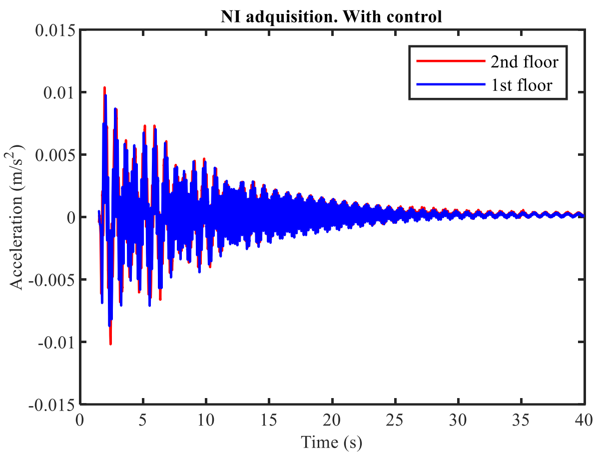

Figure 6: Time response under control.

4 CONCLUSIONS

It has been shown that a complete dynamic study using smartphone can be carried out. The results have been compared with a traditional measurement equipment. A PTMD has also be installed showing to be effective in reducing the vibration response.

ACKNOWLEDGMENTS

The authors acknowledge the support provided by the Continuum Mechanics and Theory of Structures Department.

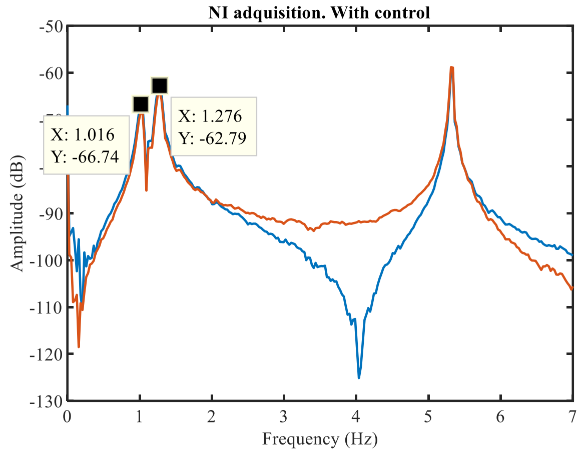

Figure 7:FFT of the time response.

REFERENCES

[1] Schladitz, F., Frenzel, M., Ehlig, D., Curbach, M. Bending load capacity of reinforced concrete slabs strengthened with textile reinforced concrete. *Engineering Structures*. 2012; 40: 317-326.

[2] Bachmann, H., et al. *Vibration problems in structures*. 2012

[3] Sebastián, J., Díaz, I.M., Casado, C.M, Poncela, A.V., Lorenzana, A. Evaluación de la predicción de aceleraciones debidas al tránsito peatonal en una pasarela en servicio. *Informes de la construcción*, 2013.

[4] Roffel, A. J., Narasimhan, S., Haskett, T. Performance of pendulum tuned mass dampers in reducing the responses of flexible structures. *Journal of Structural Engineering*. 2013; 139.

[5] Matarazzo, TJ., Santi, P., Pakzad, S.N., Carter, K., Ratti, C., Moaveni, B., Osgood, C., Jacob, N. Crowdsensing framework for monitoring bridge vibrations using moving smartphones. *Proceedings of the IEEE*. 2018; 106(4): 577 – 593.

[6] Weber, F., Feltrin G., Huth, O. *Guidelines for Structural Control. Thematic network SAMCO (Structural Assessment, Monitoring and Control)*, 2006.

ACTIVE VIBRATION CONTROL OF HUMAN-INDUCED VIBRATIONS: FROM SISO TO MIMO

Iván M. Díaz*, Emiliano Pereira†, Xidong Wang*, Jaime García Palacios*

*Department of Continuum Mechanics and Theory of Structures
ETS Ingenieros de Caminos, Canales y Puertos
Universidad Politécnica de Madrid
28040 Madrid, Spain
e-mail: ivan.munoz@upm.es

† Escuela Politécnica Superior
Universidad de Alcalá de Henares
28805 Alcalá de Henares, Spain

Abstract. Up to 2008, only direct velocity feedback control had been applied to cancel floor vibration using an electromagnetic proof-mass actuator. Since then, the authors have been intensely working on the active vibration control (AVC) of human-induced vibration using inertial actuators. Unlike passive vibration control (PVC), AVC can be used to cancel several vibration modes simultaneously, being more robust to changes in the system dynamics than PVC. However, unlike PVC, ACV can present instability problems. The solution of these instability problems has motivated many research works about novel/modified control laws and their practical implementation, which have been used to design and implement single-input single-output and multi-input multi-output AVC approaches.

Key words: Human-induced vibration, Active Vibration Control, Structural Control, Stability.

1 REVIEW

Advances in construction materials and technologies are leading to the design of lighter and more slender civil structures which are constructed with less material, less human resources and less construction time. These structures might be prone to excessive vibration. More precisely, structures, such as long-span floors, footbridges or cantilevered grandstands, could be excited under human-induced excitations [1], [2]. The vibration caused might be excessive in such a way that recommended levels by codes and guidelines might be clearly exceeded. Under these circumstances, the critical design issue is the vibration serviceability state.

During the last decades, active vibration control (AVC) strategies, which have being used in robotics, automation or aeronautics [3], have been proposed for civil engineering structures. However, up to now, the civil engineering community does not generally accept these strategies although they have shown great potential for cancelling vibrations, such as those caused by human excitation. AVC implementation have been carried out in in-service floors, laboratory full-scale floors and footbridges [4]. In particular, when several vibration modes have to be cancelled and modal properties may change, an active solution may be a competitive alternative. Moreover, if the structure is only used during a short period of time (like concert hall, dining hall, etc.), the solution of AVC via inertial mass actuators is quite attractive (since no significant structure modifications are needed, i.e., reduction costs). In addition, AVC has been shown to significantly reduce the level of response, allowing structures to satisfy vibration serviceability limits.

This paper reviews one-decade working on the AVC of human-induced vibrations. Control strategies have evolved from single-input single-output (SISO) strategies based on the ideal direct velocity feedback theoretically unconditionally stable into more sophisticated multi-input multi-output (MIMO) strategies [5]. The evolution can be summarized as follows:

- i) Velocity feedback, linear and non-linear [6].
- ii) Phase-lag acceleration feedback [2].
- iii) Feed-though term acceleration feedback control [7].
- iv) Integral resonant control [8].
- v) Two-nested control loops [9].
- vi) Decentralized MIMO control.
- vii) Centralized MIMO control.
- viii) Optimal designed MIMO control [10].
- ix) Input-output frequency weighted-based design MIMO control [11].

Each new strategy pursues new goals regarding stability (safety of the AVC) and performance (increase the reduction capability for a broader band frequency). All these control strategies are implemented driven by these premises:

- i) Controller design should focus on the implementation. That is, all the dynamics involved in the control process should be considered.
- ii) Actuator dynamics are extremely important to analyze rigorously the stability of the system.
- iii) Human induced excitation perception characteristics are introduced into the design process.
- iv) Stability should be rigorously demonstrated.
- v) Non-linearities, especially coming from the actuator, should be considered.

The last three developments involved a fairly simple way to design SISO control strategies, which is the results of 10-year experience [12]. Firstly, simple rules to design a band past filter are proposed taking into account the main spurious dynamics and actuator nonlinearities (mainly stroke saturation).

Second, a complete MIMO AVC strategy has been proposed. MIMO control strategies that consider the vibration control of the whole structure globally perform better. The MIMO design involves an optimization problem that finds simultaneously the sensor/actuator pairs' optimal placements and tunes the control gains. Figure 1 shows the general control scheme that is mainly based on the theoretical velocity feedback control, introducing elements that makes the control scheme implementable in practice (filters, saturation, etc.). The nature of human-induced loading (frequency bandwidth and dynamic load factors, Figure 2) and human vibration perception (Figure 3) are considered within an optimization procedure [11], [13].

Thirdly, a common design framework to design passive and active strategies with multiple controller has been developed [14]. This design procedure may considered inertial mass dampers, both passive and active.

2 EXPERIMENTAL IMPLEMENTATIONS

The research group has addressed several practical implementations. Up to now, commercial electrodynamics shakers (APS model 400) working in voltage mode or current (depending on the control strategy used) have been used. The structure response is measured by piezoelectric accelerometers and the actuator force is estimated by an accelerometer attached to the inertial mass. The control system is implemented using National Instrument Equipment and the Real Time module or FPGA programming.

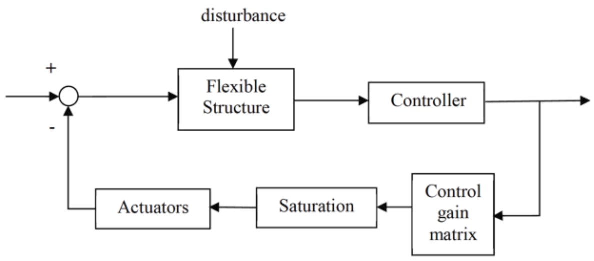

Figure 1: General control scheme.

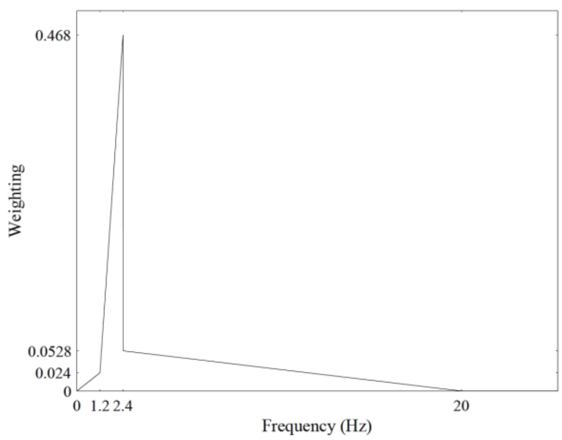

Figure 2**: Nature of the excitation. Dynamics load factor due to a human walking.**

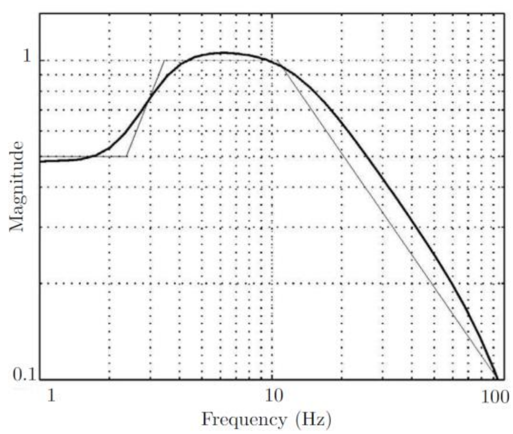

Figure 3: **Nature of the human perception. W_k frequency weighting from ISO 2631.**

2.1 Post-tensioned concrete slab

The first implementation was in a simply supported slab strip made of in-situ post-tensioned concrete with a span of 10.8 m (Figure 4). Several SISO control strategies were applied. Best performances were achieved by [7], considering the inclusion of a feedthrough term. Excellent stability conditions were achieved.

Figure 4**: Slab strip sited in Sheffield (UK).**

2.2 In-service office floor

A composite steel-concrete floor in a steel frame building sited in Leeds (Figure 5) was tested and an AVC control was evaluated during one week time. Excellent results in term of cumulative distribution of response factors were reported [2].

Figure 5: **Floor overview.**

2.3 In-service Footbridge

One of the spans of the Science Museum footbridge in Valladolid is singularly lively (Figure 6). Passive and active mass dampers were installed and their performances evaluated there [4]. This is the very first AVC implemented in an in-service footbridge.

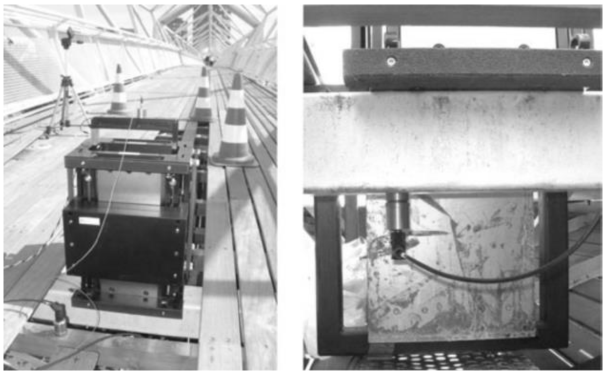

Figure 6: **Floor overview**

2.4 In-service indoor footbridge

The fist MIMO control designed by the research group was implemented in an in-serviced footbridge sited the University of Exeter Forum Building [10] (Figure 7).

Figure 7: **General view of the walkway.**

2.5 Lightweight mixed steel-concrete slab

Recently, a very lightweight, but realistic, composite floor has been constructed at the Laboratory of Structures of ETSI Caminos, Universidad Politécnica de Madrid (Figure 8).

2.5 In-service dining hall floor

Currently, an AVC strategy is being implemented in a lively floor corresponding to a dining hall sited in Pozuelo de Alarcón (Madrid). Several vibration modes around 6 Hz have been estimated. This is clearly a very interesting floor to show the whole capacities of a MIMO control (Figure 9).

Figure 8: **Lightweight mixed steel-concrete slab sited at the ETSI Caminos-UPM.**

Figure 9: **Lightweight mixed steel-concrete slab sited at the ETSI Caminos-UPM.**

3 PERPECTIVES FOR THE NEAR FUTURE

- Even MIMO controllers have been studied, their implementation in an in-service floor is still an open issue. Cope with spillover effects (instabilities due to uncontrolled high-order modes), actuator nonlinearities, etc., makes the problem challenging.
- Carrying on working in optimization procedure for MIMO design more efficient and effective.

- The development of ad hoc actuators is the most important development that should be faced in order to get this technology as an alternative to be considered.

3 ACKNOWLEDGEMENT

The authors acknowledge the support provided by the *Department of Continuum Mechanics and Theory of Structures* of *Universidad Politécnica de Madrid.*

REFERENCES

[1] J. de Sebastián, I. M. Díaz, C. Casado, A. Poncela, and A. Lorenzana. Evaluación de la predicción de aceleraciones debidas al tránsito peatonal en una pasarela en servicio. *Informes de la Construcción*, 65(531), pp. 335–348, 2013.

[2] I. M. Díaz and P. Reynolds. Acceleration feedback control of human-induced floor vibrations. *Engineering Structures*, 32(1), pp. 163–173, 2010.

[3] I. M. Díaz, E. Pereira, V. Feliu, and J. J. López-Cela. Concurrent design of multi-mode input shapers and link dynamics for flexible manipulators. *IEEE/ASME Transactions on Mechatronics*, 15(4), pp. 646–651, 2010.

[4] C. M. Casado, I. M. Díaz, J. De Sebastián, A. V. Poncela, and A. Lorenzana. Implementation of passive and active vibration control on an in-service footbridge. *Structural Control and Health Monitoring*, 20, pp. 70–87, 2013.

[5] I. M. Díaz, E. Pereira, C. Zanuy, and C. Alén. A comparative study of SISO and MIMO control strategies for floor vibration damping. In *6th ECCOMAS Thematic Conference on Smart Structures and Materials* (SMART2013), 2013.

[6] I. M. Díaz and P. Reynolds. On-off nonlinear active control of floor vibrations. *Mechanical Systems and Signal Processing*, 24(6), pp. 1711–1726, 2010.

[7] I. M. Díaz and P. Reynolds. Robust saturated control of human-induced floor vibrations via a proof-mass actuator. *Smart Materials and Structures*, 18(12), p. 125024, 2009

[8] I. M. Díaz, E. Pereira, and P. Reynolds. Integral resonant control scheme for cancelling human-induced vibrations in lightweight pedestrian structures. *Structural Control and Health Monitoring*, 19, pp. 55–69, 2012.

[9] I. M. Díaz, E. Pereira, M. J. Hudson, and P. Reynolds. Enhancing active vibration control of pedestrian structures using inertial actuators with local feedback control. *Engineering Structures*, 41, pp. 157–166, 2012.

[10] E. Pereira, I. M. Díaz, E. J. Hudson, and P. Reynolds. Optimal control-based methodology for active vibration control of pedestrian structures. Engineering Structures, 80, pp. 153–162, 2014.

[11] X. Wang, I. M. Díaz, and E. Pereira. MIMO control design including input-output frequency weighting for human-induced vibrations. In EACS 2016, 6th European Conference on Structural Control, 2016.

[12] X. Wang, E. Pereira, I. M. Díaz, and J. García-Palacios. Band-pass filter design to implement direct velocity control of human-induced vibrations. Smart Structures and Systems. (accepted)

[13] C. Camacho-Gómez, X. Wang, E. Pereira, I.M. Díaz. Active vibration control design using the Coral Reefs Optimization with Substrate Layer algorithm. Engineering Structures, 157, pp. 14-26, 2018.

[14] X. Wang, I.M. Díaz, E. Pereira. A common framework for the design of active and passive inertial mass dampers for human-induced vibrations. Submitted to Structural Control and Health Monitoring.

1st. Conference on Structural Dynamics (DinEst 2018)
Madrid, 20–21 June

STEP-BY-STEP GUIDE FOR MIMO ACTIVE VIBRATION CONTROL: FROM THE DESIGN TO THE IMPLEMENTATION

Xidong Wang*, **Emiliano Pereira**†, **Iván M. Díaz*** **and Jaime H. García-Palacios***

*Departamento de Mecánica de Medios Continuos y Teoría de Estructuras
ETS Ingenieros de Caminos, Canales y Puertos
Universidad Politécnica de Madrid
28040 Madrid, Spain

e-mail: wangxidong@caminos.upm.es

† Escuela Politécnica Superior
Universidad de Alcalá de Henares
28805 Alcalá de Henares, Spain

Abstract. Multi-input multi-output (MIMO) active vibration control (AVC) design methodologies, which have been proposed during the last decade, have been used to simultaneously find the sensor/actuator pairs' optimal placements and to tune the control gains. This work shows the complete process for the MIMO AVC implementation: from the initial stages related to structure identification to the active control implementation via LabVIEW and CRIO (NI) acquisition system.

Key words: Active control, MIMO control, Human-induced vibrations, Light-weight floor.

1 INTRODUCTION

Improvements in design and construction are leading to light and slender floor structures that have increased susceptibility to vibrations. These structures satisfy ultimate limit state criteria but have the potential of attracting complaints coming from excessive human-induced vibrations. Active vibration control (AVC) via inertial-mass actuators has been shown to be a viable technique to mitigate such vibrations in civil structures. Multi-input multi-output (MIMO) AVC design methodologies, which have been proposed during the last decade, have been used to simultaneously find the sensor/actuator pairs' optimal placements and to tune the control gains [1]. The authors have developed a methodology (really thought to be implemented practically) that takes into consideration practical issues, including input-output weighting functions, high-pass and low-pass filters in the design stage.

As a testbed structure, a full-scale lightweight steel-concrete composite slab, with a dimension of 5.5 m × 1.85 m and a depth of only 14 cm, was used (Fig. 1). Thus, this paper shows the complete process for the AVC implementation : from the initial stages related to structure identification to the active control implementation via LabVIEW. This paper mainly focuses on the practical issues regarding the experimental implementation and can be seen as a guideline for practical implementation using LabVIEW and CRIO (NI) acquisition system.

2 IMPLEMENTATION PROCESS

First of all, the floor structure and actuator models are identified. Based on these experimental tests, a state-space representation is obtained from an updated finite element (FE) model of the floor structure, and a third-order transfer function (TF) of the actutor can be deduced. Then the optimal placement of the actuators for the MIMO control are decided using a methodology which can find the optimal control gain matrix at the same time. Thirdly, the MIMO control are performed using LabVIEW Real-Time Module.

The detailed steps to implement AVC are as follows:

i) Create a FE model of the structure;

ii) Identification of the structure dynamics;

iii) Update the FE model and obtain its state-space representation;

iv) Identify the actuator models;

v) Select the control methodology and the control filters;

vi) Run the optimization process to obtain the optimal placement of actuators and control gain matrix;

vii) Install setup and convert control filters from contiunous into discrete time;

viii) Programming of control laws in LabVIEW Real-Time Module or LabVIEW FPGA Module;

ix) Check stability margins experimentally and retune if necessary;

x) Run the AVC for control performance evaluation.

Figure 1: Whole view of AVC of the floor structure.

3 EXAMPLE DESCRIPTION

3.1 Structure and actuator identifications

The experimental identification of the structure is carried out firstly by measuring the force exerted by the actuator and the acceleration of the structure. The excitation (vertical forces) is configured as a random signal from 0 Hz to 50 Hz with a duration of 600 seconds and a sampling frequency of 1000 Hz. The modal parameters are then identinal excitaions with the actuator placed at the maximum sags of each vibration modes, with peak picking method.

State-space matrices are established using 45 nodes (Fig. 2) of the floor structure, which is updated according to modal parameters of the first three vibration modes. The frequency response functions (FRFs) (experimental test and FE model) of N20 are shown in Fig. 3.

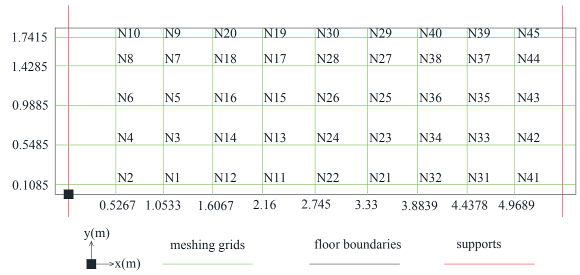

Figure 2: Node numbers and coordinates.

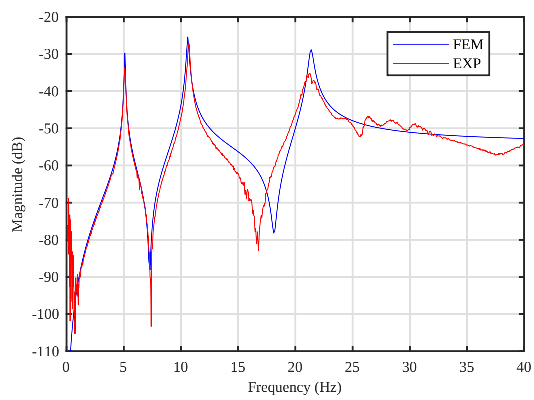

Figure 3: FRFs of the structure at N20, with magnitude in dB refered to $(m/s^2)/N$.

Actuators are identified by using an input voltage being chirp signal on rigid floor, by estimating the TF between actuator force (acceleration of the actuator multiplied by moving mass) and the chirp signal, the identified modal parameters of APS Dynamics model 400 electrodynamic actuator are obtained: $\omega_A = 2\pi \cdot 1.47$ rad/s, $\xi_A = 0.55$, $K_A = 145$ N/V and $\epsilon = 23$ for actuator 1; $\omega_A = 2\pi \cdot 1.5$ rad/s, $\xi_A = 0.45$, $K_A = 290$ N/V and $\epsilon = 6$ for actuator 2. The third-order model of the actuators can be represented as follows:

$$G = \frac{K_A s^2}{\ldots} \frac{2\pi\epsilon}{\ldots} \quad (1)$$

in which the term ϵ models the high-frequency dynamics of the actuator.

3.2 Optimization methodology

This section explains the optimization design process of an optimal direct velocity feedback (DVF) MIMO control, whose general scheme is shown in Fig. 4. The structure, whose state vector is $\mathbf{x}_s = [x_{s_1}, \cdots, x_{s_n}, \dot{x}_{s_1}, \cdots, \dot{x}_{s_n}]$, is modelled by first n vibration modes.

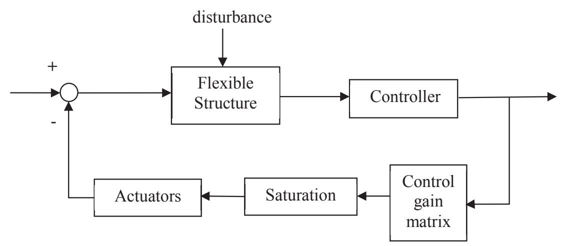

Figure 4: Control scheme.

The optimal sensor/actuator placement and the gain matrix is obtained by minimizing a performance index (PI) that considers the amplitude and duration of the vibration and the maximum force imparted for each actuator. The PI, calculated in MATLAB Simulink and optimized by MATLAB function *fminsearch*, is defined as follows:

$$\mathbf{z} = \frac{1}{2}\int_0^{t_f} \mathbf{x}_{sw}^T \mathbf{Q} \mathbf{x}_{sw} \mathrm{d}t, \tag{2}$$

in which $\mathbf{x}_{sw}$ is frequency weighted state vector. The matrix $\mathbf{Q}$ is a $2n \times 2n$ positive definite matrix, based on the n frequencies n maximum values of each mode shapes. Finally, the value of t_f is the simulation time to obtain the PI, which must be large enough to achieve the steady state of $\mathbf{z}$ (i.e., the weighted vector $\mathbf{x}_{s_w} \cong \mathbf{0}$).

The human vibration perception [2] is considered in the controller design by weighting the state vector of the structure as follows:

$$x_{sw_l} = (e^{\alpha t} x_{s_l}(t)) * g_{OFW}, l \in [1, \cdots, 2n], \tag{3}$$

in which $(*)$ denotes the convolution process and g_{OFW} is the impulse response function of a system with the FRF shown in Fig. 5. The exponential constraint in the relative stability of the controlled system.

Initial conditions ($\mathbf{x}_s(0)$) for modal coordinates are used in the methodology, and in real life, different vibration modes of the structure might be excited with a specific dynamic loading factor (DLF) corresponding to a certain frequency range. In order to cope with this fact, the initial conditions are weighted by the input frequency weighting (Fig. 6). That is, the input force is weighted according to the frequency range of human excitation:

$$\begin{aligned}\mathbf{x}_s(0) =& [x_{s_1}(0), \cdots, x_{s_n}(0), \dot{x}_{s_1}(0), \cdots, \dot{x}_{s_n}(0)] \\ =& [0, \cdots, 0, F_0\phi_{1,max} g_{IFW}(f_1), \cdots, \\ & F_0\phi_{n,max} g_{IFW}(f_n)].\end{aligned} \tag{4}$$

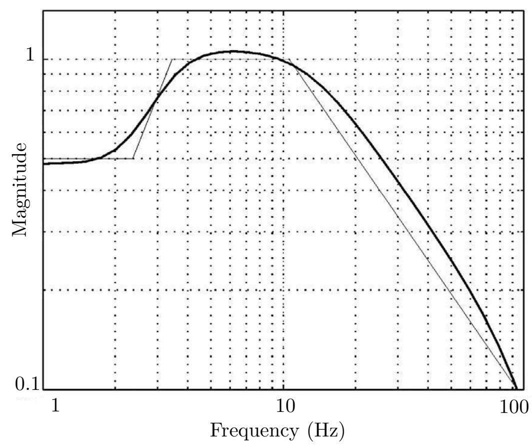

Figure 5: Output frequency weighting function g_{OFW} (thicker curve) and its asymptotic definition (thinner curve).

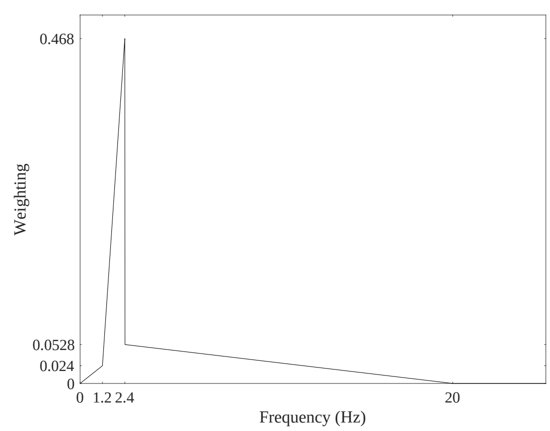

Other issues [3] such as the closed-loop system stability, actuator stroke problems and spillover effects due to the unidentified dynamics can be considered into the methodology by introducing control voltage saturation blocks and band-pass filters. Also, Coral Reefs Optimization algorithm [4] can be used to solve the MIMO control design, in order to reduce the computational burden of the nonlinear optimization problem.

3.3 AVC implemetations

The controller used in the MIMO and SISO design is a lossy integrator, which integrates the measured acceleration to velocity, thus making the control loop DVF:

$$Controller = 50/(s + 10), \tag{5}$$

which is converted from continuous to discrete time, by using MATLAB function *c2d* with Tustin transform method.

The controls are carried out using LabVIEW Real-Time Module (Figs. 7 and 8) and CRIO (NI) acquisition system (Fig. 9).

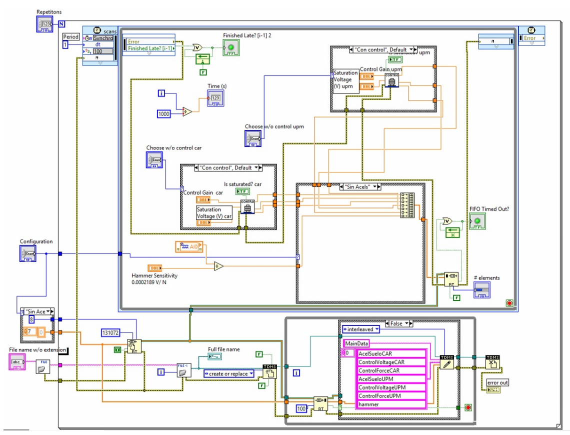

Figure 7: LabVIEW block diagram of AVC.

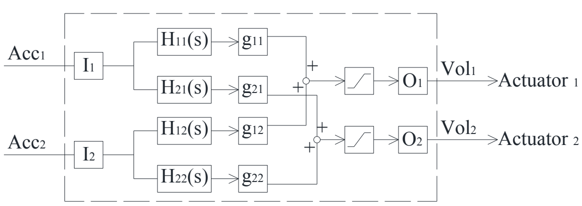

Figure 8: MIMO AVC implementation flowchart for two actuators.

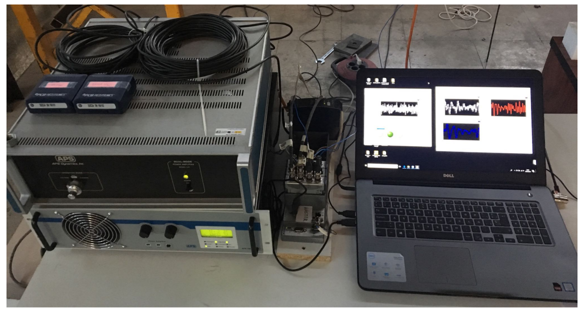

Figure 9: Experimental setups.

4 CONCLUSIONS

This paper shows a guideline for the MIMO AVC implementation: from the initial stages related to structure identification to the active control implementation via LabVIEW and CRIO(NI) acquisition system.

ACKNOWLEDGMENTS

The authors acknowledge the financial support provided by the Spanish project DPI2013-47441-P, the Research Net VIBRASTRUNET BIA2015-71942-REDT and China Scholarship Council.

REFERENCES

[1] E. Pereira, I. M. Díaz, E. J. Hudson, P. Reynolds, Optimal control-based methodology for active vibration control of pedestrian structures, Engineering Structures 80 (2014) 153 – 162.

[2] ISO 10137, Bases for Design of Structures – Serviceability of Buildings and Walkways against Vibrations, international organization for standardization Edition (2007).

[3] X. Wang, I. Díaz, E. Pereira, MIMO control design including input-output frequency weighting for human-induced vibrations, in: EACS 2016, Sheffield, 2016.

[4] C. Camacho-Gómez, X. Wang, E. Pereira, I. Díaz, S. Salcedo-Sanz, Active vibration control design using the coral reefs optimization with substrate layer algorithm, Engineering Structures 157 (2018) 14 – 26.

1st Conference on Structural Dynamics (DinEst 2018)
Madrid, 20-21 June

EFFICIENT SIZING OF ISOLATED FOUNDATIONS FOR TESTING SYSTEMS

José Ramírez Senent*, Gonzalo Marinas Sanz¤, Jaime H. García Palacios† and Iván M. Díaz†

* VZERO ENGINEERING SOLUTIONS, SL
28002 Madrid, Spain
e-mail: jramirez@vzero.eu
ORCID: 0000-0002-1332-8182

¤Pondio Ingenieros, SL
28020 Madrid, Spain

† ETS Ingenieros de Caminos, Canales y Puertos
Universidad Politécnica de Madrid
28040 Madrid, Spain

Abstract. The current increasing demand to accurately reproduce the load environment to which certain specimens from automotive, aerospace or civil engineering industries will be subjected during their service life, has led to the design of more and more sophisticated testing systems, able to exert dynamic loads with a wide frequency content. In order to avoid the transmission of the mentioned loads to testing system environment, special foundations, independent from the rest of the building, and sprung on vibration isolation systems must be designed. Typically, these foundations have been oversized using traditional methods. In this work, simple models to simulate motion of seismic mass and interaction with soil, from loads acting on it, are presented with the aim to develop a simple tool for the efficient sizing of this type of foundations. Results obtained are compared with Finite Element Method studies to validate simple models. As well, a method to predict vibration transmission to the environment is assessed.

Key words: Testing Systems, Seismic Mass, Vibration Isolation

1 INTRODUCTION

The current development of modern testing systems (TS) has led to the design of sophisticated MIMO servoactuation systems able to exert wide frequency range solicitations on devices under test (DUTs). Some examples worth mentioning are: multiaxial shake tables (for automotive, aerospace or civil works applications), bogie testing systems (for railway) or torpedo impact simulators (for military)

These TS constitute a source of unwanted vibration that could lead to issues related to building integrity, people comfort or distortion on close vibration sensitive devices, among others, and must be addressed from the very beginning of the design process.The solution normally adopted is the use of a reaction (seismic) mass (RM), independent from the rest of the building and sprung on a vibration isolation system (VIS) of some kind; i.e.: airsprings or metallic springs with hydraulic dampers or polymeric material layers. Case under study can be seen on figure 1.

The geometrical-mass properties of these seismic masses have been often oversized attending to *rules of thumb* depending on the VIS used, leading in some cases to inefficient isolation or even catastrophic results. The main aim of this work is to develop a simple method to analyze the dynamics of the reaction mass and, on one hand retain the most important consequences to the resultant motion; i.e.: kinematics of characteristic points (CoG, corners), stresses on VIS, stresses on supporting terrain and vibration transmission to the vicinities of the test laboratory, while on the other, to allow for efficient and fast estimates at the early stages of the projects.

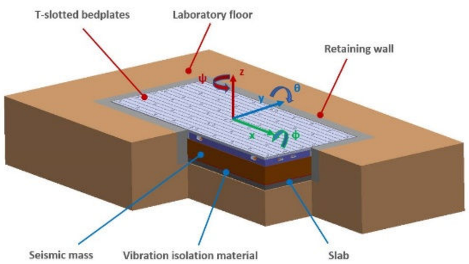

Figure 1: Typ. morphology of a seismic mass system.

Work presented here is based on a real project carried out in Spain for a complex Component in the Loop testing system. VIS used was a layer of a polymeric material.

The model developed for this purpose (fig. 2) is described in section 2. Stresses simulations performed according to the second model are summarized in section 3. Section 4 explores a method to estimate the vibration transmission to the neighborhood of the TS. Finally, conclusions of this work and suggestions for further works are presented.

2 MODEL DESCRIPTION

The developed model basically consists on the linearization of the equations of motion for two masses representing the RM and the pit, constituted by slab, retaining walls and slab, and the mass concrete on which it lays. Both of them are considered as rigid solids. The RM is sprung on a set of springs and viscous dampers which simulate VIS stiffness and internal damping respectively. These elements exert an action on the second mass which is sprung on a set of springs and viscous dampers simulating soil elastic and dissipative properties. Equations governing system behavior are:

$$[M] \cdot \{\ddot{x}\} + [C] \cdot \{\dot{x}\} + [K] \cdot \{x\} = \{F\} \tag{1}$$

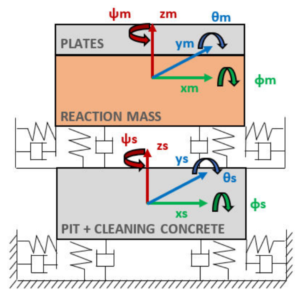

Figure 2: 12 DoF lumped mass model

2.1 Mass, damping and stiffness matrices

The mass matrix is:

$$M = diag(M_m, M_m, M_m, I_{xm}, I_{ym}, I_{zm}, M_s, M_s, M_s, I_{xs}, I_{ys}, I_{zs}) \tag{2}$$

The stiffness and damping matrices result in (damping matrix can be obtained similarly):

$$K = \begin{bmatrix} K_{mm} & K_{ms} \\ K_{ms} & K_{ss} \end{bmatrix} \tag{3}$$

$$\begin{aligned} K_{mm} &= diag(k_{xm}, k_{ym}, k_{zm}, k_{\varphi m}, k_{\theta m}, k_{\psi m}) \\ K_{ms} &= -K_{mm} \\ K_{ss} &= K_{mm} + diag(k_{xs}, k_{ys}, k_{zs}, k_{\varphi s}, k_{\theta s}, k_{\psi s}) \end{aligned} \tag{4}$$

The elements of the mass matrix correspond to the masses, and the moments of inertia with respect to its center of gravity (CoG) of RM and pit. These values are easily obtained from CAD software.

The elements of the stiffness and damping matrices corresponding to VIS are obtained using a Lagrangian approximation. Defining the total potential energy accumulated and the energy dissipated by the VIS system by:

$$U = \frac{1}{2} \cdot \iiint_v \{\sigma\}^t \{\varepsilon\} dv \tag{5}$$

$$F = \frac{1}{2} \cdot \iiint_v \{\sigma\}^t \{\dot{\varepsilon}\} dv \tag{6}$$

The following contributions to the total potential energy stored and power dissipated by the VIS are obtained (angular deformations for roll and pitch DoFs have been neglected).

$$
\begin{aligned}
U_x &= \frac{1}{2}\iiint_v \tau_{xz}\cdot\gamma_{xz}\cdot dv = \frac{w\cdot l\cdot G}{2\cdot t}\cdot x^2\\
U_y &= \frac{1}{2}\iiint_v \tau_{yz}\cdot\gamma_{yz}\cdot dv = \frac{w\cdot l\cdot G}{2\cdot t}\cdot y^2\\
U_z &= \frac{1}{2}\iiint_v \sigma_z\cdot\epsilon_z\cdot dv = \frac{w\cdot l\cdot E}{2\cdot t}\cdot z^2\\
U_\varphi &= \frac{1}{2}\iiint_v \sigma_z\cdot\epsilon_z\cdot dv = \frac{E\cdot I_x}{2\cdot t}\cdot\varphi^2\\
U_\theta &= \frac{1}{2}\iiint_v \sigma_z\cdot\epsilon_z\cdot dv = \frac{E\cdot I_y}{2\cdot t}\cdot\theta^2\\
U_\psi &= \frac{1}{2}\iiint_v (\tau_{xz}\cdot\gamma_{xz}+\tau_{yz}\cdot\gamma_{yz})\cdot dv = \frac{G\cdot J_o}{2\cdot t}\cdot\psi^2
\end{aligned}
\tag{7}
$$

$$
\begin{aligned}
F_x &= \frac{1}{2}\iiint_v \tau_{dxz}\cdot\dot{\gamma}_{xz}\cdot dv = \frac{w\cdot l\cdot c_l}{2\cdot t}\cdot\dot{x}^2\\
F_y &= \frac{1}{2}\iiint_v \tau_{dyz}\cdot\dot{\gamma}_{yz}\cdot dv = \frac{w\cdot l\cdot c_l}{2\cdot t}\cdot\dot{y}^2\\
F_z &= \frac{1}{2}\iiint_v \sigma_{dz}\cdot\dot{\epsilon}_z\cdot dv = \frac{w\cdot l\cdot c_v}{2\cdot t}\cdot\dot{z}^2\\
F_\varphi &= \frac{1}{2}\iiint_v \sigma_{dz}\cdot\dot{\epsilon}_z\cdot dv = \frac{c_v\cdot I_x}{2\cdot t}\cdot\dot{\varphi}^2\\
F_\theta &= \frac{1}{2}\iiint_v \sigma_{dz}\cdot\dot{\epsilon}_z\cdot dv = \frac{c_v\cdot I_y}{2\cdot t}\cdot\dot{\theta}^2\\
F_\psi &= \frac{1}{2}\iiint_v (\tau_{dxz}\cdot\dot{\gamma}_{xz}+\tau_{dyz}\cdot\dot{\gamma}_{yz})\cdot dv = \frac{c_l\cdot J_o}{2\cdot t}\cdot\dot{\psi}^2
\end{aligned}
\tag{8}
$$

The terms of the stiffness and damping matrices are obtained by differentiation with respect to each generalized coordinate and velocity of the total stored energy and dissipated power, respectively, resulting:

$$K_m = diag\left(\frac{wlG}{t},\frac{wlG}{t},\frac{wlE}{t},\frac{EI_x}{t},\frac{EI_y}{t},\frac{GJ_o}{t}\right) \tag{9}$$

$$C_m = diag\left(\frac{wlc_l}{t},\frac{w\square_l}{t},\frac{wlc_v}{t},\frac{I_xc_v}{t},\frac{I_yc_v}{t},\frac{J_oc_l}{t}\right) \tag{10}$$

Numeric values for terms of stiffness matrix were obtained from manufacturer of VIS and application data. Since material is considered isotropic, the coefficients c_v and c_l have been assumed to be equal. Identification of damping ratio was performed making use of the manufacturer's transmissibility curve (vertical) and the well-known transmissibility equation. Figure 3 illustrates manufacturer's transmissibility curve, linear identification and identification error.

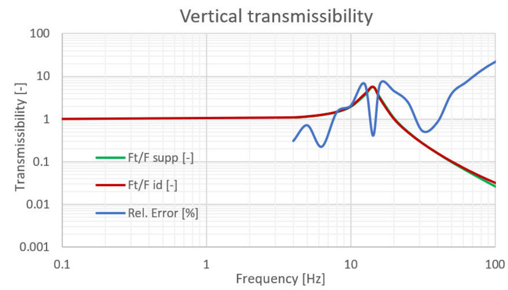

Figure 3: Vertical transmissibility of the system

With next expression and the previously identified value of ζ, c_v value can be obtained.

$$C_z = \frac{w\cdot l\cdot c_v}{t} = 2\cdot\zeta\cdot\omega_n\cdot m \tag{11}$$

The elements of stiffness matrix related to the terrain have been determined according to [1], from available geotechnical data (table 1).

PARAM.	VALUES			UNITS
E, G		6.50	2.32	[MPa]
υ			0.40	[-]
σ_{adm}			1.00	[kg/cm^2]
k_x, k_y, k_z	37.05	37.05	53.39	[MN/m]
$k_\varphi, k_\theta, k_\psi$	245.14	814.82	621.70	[MNm/rad]

Table 1: Terrain elastic parameters

Following the same procedure as before, soil damping matrix elements were estimated. A value of 14 % damping ratio has been used.

2.2 Forces vector

Forces and moments on the RM are shown in figures 4 and 5.

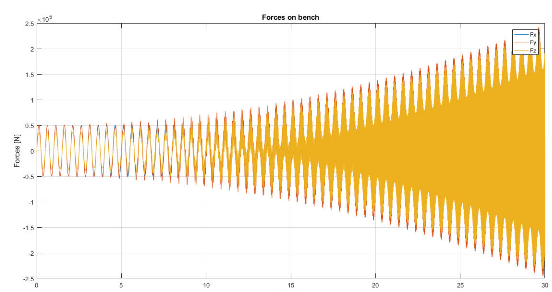

Figure 4: Forces on test bench

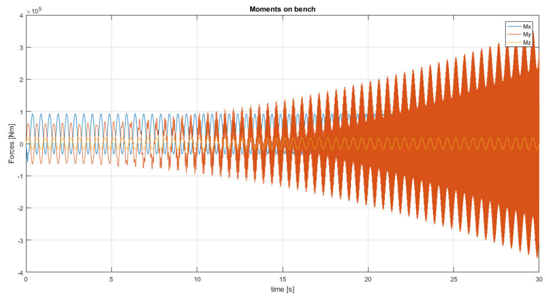

Figure 5: Moments on test bench

There are three sources, besides weight, of forces applied on the RM: (a) moments in dynamic rotation tests; (b) due to a system of three eccentric actuators; (c) due to the rotating shafts dynamic imbalance.

4 MODEL SIMULATION RESULTS

Maximum pressure contours obtained by FEA and simplified method are shown next.

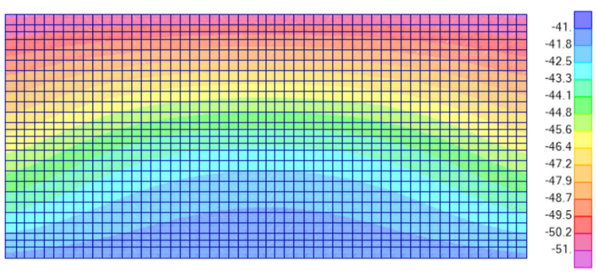

Figure 6: Maximum pressure contours. FEM

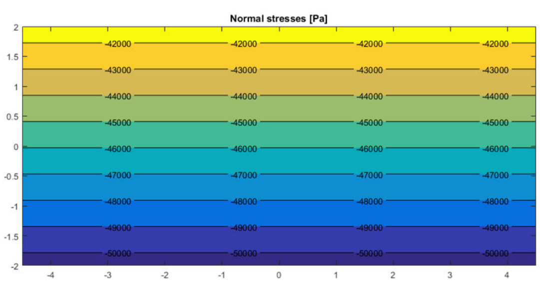

Figure 7: Maximum pressure contours. Simp. method

5 VIBRATION TRANSMISSION

Below, A method to quantify vibration transmission to TS surroundings is presented. Hypotheses assumed are those of confined elastodynamics of a half space [2]. Thus, there is only displacement along z direction and one equilibrium equation (12). In case of an oscillatory point load, a simple solution exists (13).

$$G\frac{\partial^2 w}{\partial x^2} + G\frac{\partial^2 w}{\partial y^2} + (\lambda + 2G)\frac{\partial^2 w}{\partial x^2} = \rho\frac{\partial^2 w}{\partial t^2} \tag{12}$$

$$w = \frac{Fm}{2\pi(\lambda+2G)}\frac{\sin[\omega(t-t_0)]}{\sqrt{r^2+z^2/m^2}}H(t-t_0);\ t_0 = \frac{\sqrt{r^2+z^2/m^2}}{c} \tag{13}$$

Integrating differential point loads over the contact area, allows for estimation of displacement at desired probe points.

$$w = \iint_{\Omega(x_0,y_0)} \frac{p(x_0,y_0)m}{2\pi(\lambda+2G)}\frac{\sin\left[\omega\left(t-1/c\sqrt{(x-x_0)^2+(y-y_0)^2}\right)\right]}{\sqrt{(x-x_0)^2+(y-y_0)^2}}dx_0dy_0 \tag{14}$$

Figure 10 shows values of accelerations at distances of 10 and 50 m to the center of the of the RM for the dynamic imbalance load case.

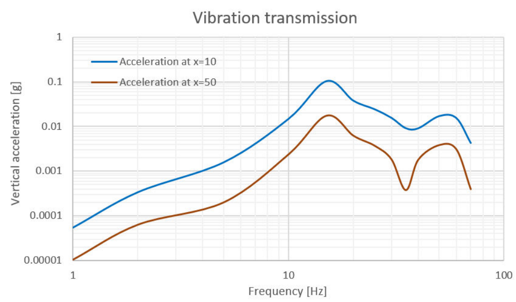

Figure 8: Vibration transmission chart

7 CONCLUSIONS

The simple methods developed are able to predict the order of magnitude of soil stresses accurately for sizing purposes with a run and setup time much more reduced in comparison with FE, thus allowing for fast iterations.

Vibration transmission prediction accuracy must be evaluated via appropriate data acquisition systems.

REFERENCES

[1] J.A. Jiménez. Geotecnia y Cimientos II. Rueda Ediciones, 1976

[2] A. Verruijt. *Soil Dynamics.* Delft University of Technology, 1994.

SECTION 3: Bridge dynamics

DYNAMIC RESPONSE OF A SHORT SIMPLY-SUPPORTED GIRDER BRIDGE UNDER RAILWAY EXCITATION: EFFECT OF BRACING BEAMS ON THE TRANSVERSE BEHAVIOUR

E. Moliner*, A. Romero† P. Galvín† and M.D Martínez-Rodrigo*

*Departamento de Ingeniería Mecánica y Construcción
Universitat Jaume I
12071 Castellón, Spain

e-mail: molinerer@uji.es
ORCID: 0000-000-2-8142-1936

† Escuela Técnica Superior de Ingeniería
Universidad de Sevilla
41092 Sevilla, Spain

Abstract. In this contribution results and conclusions from an experimental and numerical analysis of a short simply-supported girder bridge belonging to a High-Speed railway line in Spain are presented. In particular, a finite element (FE) model which adopts common assumptions in engineering practice is implemented and updated in terms of frequencies and mode shapes with the experimental measurements. The attention is focused on the influence of the transverse bracing beams commonly present at the abutments position on the transverse behaviour and also the importance of including these elements in the numerical models for an accurate prediction of the dynamic response. The influence of the bridge skewness, the span length and the flexibility of the neoprene bearings on the effects of the bracing beams is also evaluated after the modal analysis of a representative ensemble of girder bridges.

Key words: Railway bridges, Dynamics, numerical models, experimental measurements

1 INTRODUCTION

The resonance effects caused by the modern railway transportation systems on the railway infrastructures, at circulating speeds above 200 km/h, can entail harmful consequences on railway bridges, such as ballast destabilization, passenger discomfort or a raise in the maintenance costs of the line. For that reason the Serviceability Limit State of vertical acceleration is one of the most demanding specifications for the design or upgrading of many railway bridges. In this regard short-to-medium span simply-supported (SS) bridges are especially critical [2, 3] and therefore, there is a need to realistically predict the behaviour of railway structures in the design phase and during the life of the bridge.

However, as indicated in [4], the dynamic response of short-to-medium span railway bridges is difficult to predict during the design or upgrading stages, since the influence of the non-structural environment and of the super-structure components (rails, ballast) can be significant and are not well known. In this regard the application of FE model updating techniques becomes crucial.

In this contribution the authors include results and conclusions from the experimental and numerical analysis of Arroyo Bracea I railway bridge, which belongs to the Madrid-Sevilla High-Speed railway line in Spain. This structure has been monitored due to its short length and typology, which make it susceptible to experience high transverse vibration levels. In a previous work the authors have implemented and updated several FE models of this structure, showing a reasonable good correspondence with the identified natural frequencies and mode shapes that is less accurate with three dimensional modes such as torsion or transverse bending ones. In the authors' opinion the presence of transverse beams bracing the longitudinal girders at the supports position, which was not included in the numerical models, could justify the discrepancies.

This work shows the effect of the transverse bracing beams on the vertical response of the deck. The study is extended to other girder bridges with different span lengths, deck skewness and flexibility of the neoprene bearings, in a view to identify the importance of an accurate modelling of the deck boundary conditions for a safe and accurate prediction of the maximum dynamic response of the structure.

2 CASE STUDIES: DESCRIPTION OF THE BRIDGES

In this section a general description of the main properties of the girder bridges that are used in the study is presented. Figure 1 shows a general cross section of the decks, where the main dimensions h, d_g and h_g are provided in Table 1.

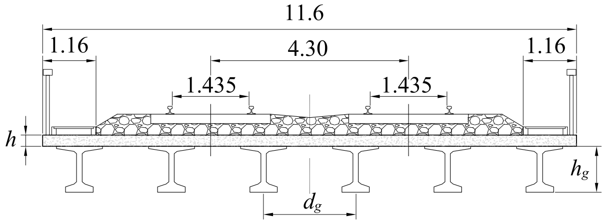

Figure 1: Cross section of reinforced concrete slab bridges under study. Units (m)

2.1 Arroyo Bracea I bridge

This railway bridge is composed of two identical SS bays of 15.25 m equal spans and belongs to the Madrid-Sevilla high-speed railway line in Spain. Additionally the deck has a 45° skew angle. An experimental campaign was carried out by the authors in July of 2016. From ambient vibration measurements at the deck five modes were identified in the frequency range 1-30 Hz and the finite element (FE) model explained in Section 3 has been updated. The first row of Table 1 shows the main properties of the deck considered in this study after the calibration of the numerical model, where $k_{v,dyn}$ stands for the elastic vertical stiffness of the concentrated supports considered for dynamic loads.

2.2 Representative ensemble of girder bridges

Apart from Bracea I bridge, several representative girder bridges have been dimensioned for this study covering the span lengths between 10 and 25 m and with slenderness ratio (depth/span) lower than 1/13. Their main properties are also shown in Table 1. For each span length, a different number of longitudinal girders N_g is considered an also several stiffness ratios L/δ (span length/maximum vertical displacement under static UIC-71 train loading [1]) in the range 2000 and 4000.

3 NUMERICAL MODEL

An isotropic plate FE model has been implemented in ANSYS (Figure 2) with the following: features: (i) the upper slab behaviour is simulated by means of an isotropic thin plate discretised in shell elements with 6 degrees of freedom (dof) per node; (ii) different mass density elements are defined in order to concentrate the weight of the ballast, sleepers and rails over the central portion of the plate; (iii) the longitudinal girders and the transverse bracing beams located at the abutment position are included as beam elements with 6 dof per node; (iv) The girder and bracing beam nodes are connected one another and also to the upper plate and by means of rigid kinematic constraints; (v) the laminated rubber bearings of the bridge are

Bridge	Slab	Girders			Mass	Supports	L/δ
	h (m)	N_g	d_g (m)	h_g (m)	(kg/m)	$k_{v,dyn}(N/m)$	
Bracea I	0.27	5	2.275	1.05	28355	1.4E9	3847
L=10 m	0.25/0.22	5/6	2.275/2.0	0.6	19066/18765	9.7E8/8.34E8	2049/2119
	0.25/0.22	5/6	2.275/2.0	0.65	21395/21560	1.57E9/1.47E9	3320/3740
L=12.5 m	0.25	6	2.0	0.8	19995	7.56E8	2299
	0.22	5/6	2.275/2.0	0.85	21542/22100	1.60E9/1.31E9	3607/3560
L=15 m	0.22/0.25	5/6	2.275/2.0	1.05/1.0	19485/20355	8.93E8/7.44E8	2154/2154
	0.25	5/6	2.275/2.0	1.05	23221/23510	1.54E9/1.26E9	3710/3657
L=17.5 m	0.25	5/6	2.275/2.0	1.2	22018/20715	9.89E8/6.88E8	2506/2090
	0.25	5/6	2.275/2.0	1.25	22745/24050	1.22E9/1.01E9	3079/3495
L=20 m	0.25	5/6	2.275/2.0	1.4	22393/21075	9.26E8/6.42E8	2441/2031
	0.25	5/6	2.275/2.0	1.45	23896/	1.28E9/	3387/3351
L=22.5 m	0.25	5/6	2.275/2.0	1.6	22768/24078	8.72E8/8.27E8	2383/2717
	0.25	5/6	2.275/2.0	1.65	24396/25130	1.18E9/9.85E8	3250/3223
L=25 m	0.25	5/6	2.275/2.0	1.7	22956/24303	7.26E8/6.89E8	2037/2320
	0.25	5/6	2.275/2.0	1.85	24896/25670	1.11E9/9.23E8	3126/3106

Table 1: Main properties of the girder bridges

introduced in discrete positions by means of longitudinal springs with vertical stiffness $k_{v,dyn}$.

4 RESULTS

Table 2 shows the experimental frequencies (f_{exp}), numerical without transverse bracings (f_{num}) and numerical considering the transverse bracing beams ($f_{num,brace}$), along with the correlation between the experimental and numerical mode shapes in terms of the Modal Assurance Criterion (MAC) for the first three modes of Bracea I bridge (first bending, first torsion and first transverse bending mode). As can be seen the effect of the transverse bracing beams is more evident in terms of frequencies and for the modes different from the longitudinal bending one.

In a view to evaluate the influence of the span length, deck skewness and other characteristics of the deck such as the stiffness and the number of longitudinal girders on the effect of the transverse bracing beams, the natural frequencies and mode shapes of the bridges defined in Table 1 have been calculated with the numerical model of Figure 2 using two approaches: neglecting the transverse bracing beams and including them in the FE model as seen in Figure 2. Additionally, the frequencies and modes have been calculated for two skew angles, 0 and 45°. The results for the first three modes (first longitudinal bending, first torsion and first transverse bending mode, respectively) can be seen in Figure 3 in terms of the differences in frequencies, defined as Difference = ($f_{num,brace}$-f_{num})/f_{num} · 100.

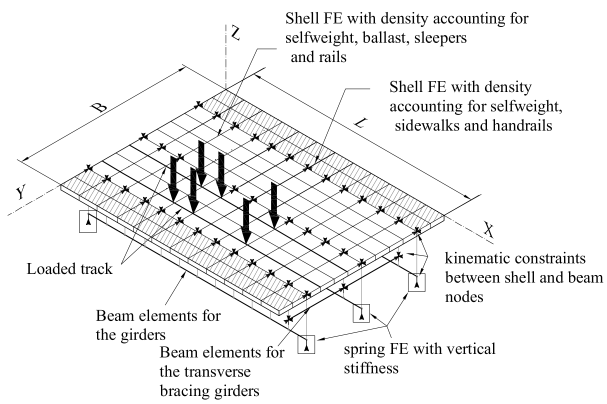

Figure 2: FE model

In Figure 3 the markers in grey color correspond to bridges with a stiffness ratio L/δ in the range 2000-3000, which is an usual ratio for girder bridges belonging to conventional railway lines. The results in black color correspond to stiffness ratios between 3000-4000, which is more common in high-speed lines. Bracea I bridge belongs to this cate-

	$f_{exp}(Hz)$	$f_{num}(Hz)$	$f_{num,brace}(Hz)$	$MAC_{exp,num}$	$MAC_{exp,brace}$
1	9.25	9.13	9.13	0.95	0.96
2	10.63	9.86	10.17	0.93	0.93
3	12.75	11.83	12.81	0.95	0.96

Table 2: Bracea I bridge: experimental and numerical frequencies, MAC values

gory, with L/δ= 3847. Furthermore, the square marker has been assigned to bridges with N_g= 6 longitudinal girders, whereas the diamonds correspond to bridges with N_g= 5. A summary of the main conclusions is provided in section 5.

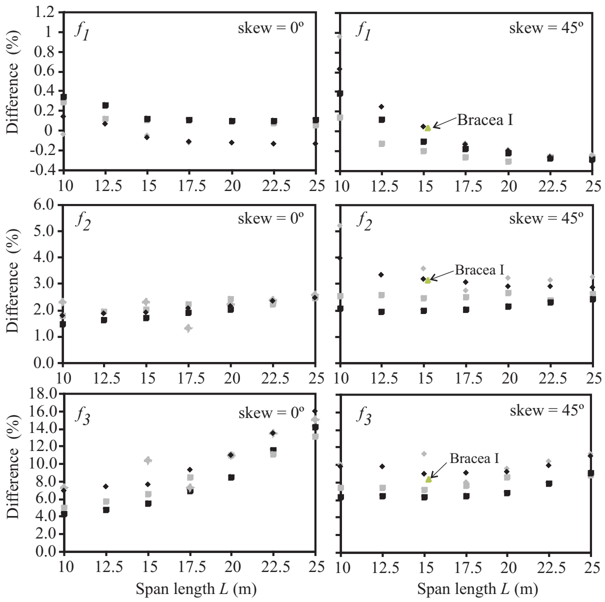

Figure 3: Effect of transverse bracing beams on the prediction of the natural frequencies.

5 CONCLUSIONS

- The presence of transverse bracing beams leads to an increment of the natural frequencies of the bridge deck, which is less noticeable in the frequency of the fundamental bending mode, though higher for the mode shapes with significant transverse deformation, such as the first torsion mode and first transverse bending mode which correspond to the second and third mode shapes, respectively.

- The effect of the transverse bracing beams on the natural frequencies of the first two modes is, in general, more significant for skewed decks. However, this tendency is not clear for the frequency of the third mode.

- Among the different girder bridges that have been analysed in this study, for the first two mode shapes the effect of the transverse bracing beams is, in general, more noticeable for the skewed shortest spans (L= 10 m) with a stiffness ratio δ/L in the range 1/2000-1/3000 and with a lower number of longitudinal beams. In these bridges, the frequency difference associated to the first and second mode attains, respectively 0.96%, 5.2% and 10.1%.

6 ACKNOWLEDGMENTS

The authors would like to acknowledge the financial support provided by the Spanish Ministry of Economy and Competitiveness under the research project [BIA2016-75042-C2].

REFERENCES

[1] CEN, EN 1991-2. *Eurocode 1: Actions on Structures - Part 2: Traffic loads on bridges*. European Committee for Standardization, Brussels, 2002.

[2] ERRI-D-214/RP9. *Ponts Rails pour vitesses > 200km/h. Rapport final*. European Committee for Standardization, Brussels, 2000.

[3] L. Frỳba. Dynamic behaviour of bridges due to high-speed trains. *Workshop Bridges for High-Speed Railways*, Porto:137–158, June 2004.

[4] C. Rebelo, L. Simoes da Silva, C. Rigueiro, and M. Pircher. Dynamic behaviour of twin single-span ballasted railway viaducts- field measurements and modal identification. *Engineering Structures*, 30(9):2460 – 2469, 2008.

1st Conference on Structural Dynamics (DinEst 2018)
Madrid, 20-21 June

RESONANCE AND CANCELLATION IN DOUBLE-TRACK SIMPLYSUPPORTED RAILWAY BRIDGES: THEORETICAL PREDICTIONS VERSUS EXPERIMENTAL MEASUREMENTS

María D. Martínez-Rodrigo*, Emmanuela Moliner*, Pedro Galvín† and Antonio Romero†

* Universitat Jaume I
12071 Castellón, Spain
e-mail: lola.martinez@uji.es
ORCID: 0000-0003-4748-9133

† Escuela Técnica Superior de Ingeniería
Universidad de Sevilla
41092 Sevilla, Spain

Abstract. Short-to-medium span simply-supported (SS) railway bridges may experience high deck vertical accelerations under the circulation of trains. It is necessary to accurately predict the maximum response of such structures at design stages, in order to evaluate the Serviceability Limit State (SLS) for traffic safety. The dynamic response of SS railway bridges depends on the free vibrations that each single axle leaves on the deck, and on how these add when a train of several loads crosses the bridge. The aims of the investigation are to (i) formulate the conditions for maximum free vibration and cancellation in rectangular orthotropic plates analytically; (ii) investigate their evolution numerically with the plate obliquity, supports flexibility and structural damping; (iii) relate these conditions with the resonance amplitudes; and (iv) validate the conclusions with experimental measurements.

Key words: Railway bridges, Resonance, Cancellation, Orthotropic plates, Moving loads.

1 INTRODUCTION

Short-to-medium span SS railway bridges may experience excessive deck vertical accelerations under passing trains. For this reason the SLS for traffic safety is one of the most restrictive design limits. Since the opening of the first High Speed (HS) railway lines there has been experimental evidence of excessive transverse vibrations in bridges which have been attributed to resonance of the deck [1]. A resonant behaviour builds up from the free vibrations that each axle load leaves on the structure. The amplitude of these free vibrations depends on the ratio between the load speed and the deck natural frequency. Maximum free vibration and cancellation conditions have been formulated for S-S and elastically supported (E-S) beams in the past [2]. In the resonant case, depending on the amplitude of these free vibration waves and on how they combine when a train of loads crosses the structure, resonances entailing noticeable amplification levels or almost imperceptible ones should be expected.

In what follows, the conditions for maximum free vibration and cancellation, as well as those for resonance and cancellation of resonance are studied in the case of orthotropic plates. These type of models should be used when the deck dynamic response is not that of a beam-type structure due to the deck dimensions, eccentricity of the track, level of obliquity, etc.

2 FREE VIBRATION OF RECTANGULAR ORTHOTROPIC PLATES AFTER A MOVING LOAD

The partial differential equation governing the transverse oscillations $w(x,y,t)$ of a thin S-S orthotropic rectangular plate under a generic load distribution $q_z(x,y,t)$ is given by

$$D_x \frac{\partial^4 w}{\partial x^4} + 2H \frac{\partial^4 w}{\partial x^2 \partial y^2} + D_y \frac{\partial^4 w}{\partial y^4} + \rho h \frac{\partial^2 w}{\partial t^2} = q_z \quad (1)$$

where x and y coincide with the principal directions of orthotropy, D_x, D_y are the bending stiffnesses per unit length in the XZ and YZ planes; H is the torsional rigidity; and L, B, h and ρ are the length, width, thickness and mass density of the plate, respectively.

Admitting S-S conditions and expressing $w(x,y,t)$ as a linear combination of the normal modes of vibration

$$w(x,y,t) = \sum_{i=1}^{m} \sum_{j=1}^{n} \psi_{ij}(t) C_{ij} \, sin\left(\frac{i\pi x}{L}\right) Y_{ij}(y)) \quad (2)$$

The equations defining the modes and natural frequencies of the plate may be consulted in [3]. Admitting modes orthogonality and neglecting structural damping the equation governing the mn-th modal amplitude under a single load circulating along a certain path $y=y_p$ at constant speed may be obtained. In this particular study, special attention is given to the free vibrations after the load passage. The amplification of the response for a particular mode, nondimensionalized by the static modal solution, in terms of the travelling speed can be obtained analytically as:

$$R_{mn} = \frac{K_{mn}\sqrt{2}}{1-K_{mn}^2} \sqrt{1 - cos(m\pi) cos\left(\frac{m\pi}{K_{mn}}\right)} \quad (3)$$

In the previous equation, valid for $K_{mn} \neq 1$, $K_{mn} = m\pi V/\omega_{mn} L$ is the nondimensional velocity and ω_{mn} the circular frequency for the mn-th mode. Comparing the normalized amplitude of the free vibrations given by eq. (3) with eq. (7) of reference [2] it may be concluded that the conditions that maximize and minimize the modal amplitudes in free vibration of an orthotropic rectangular plate after the passage of a moving load are the same as those of the S-S Bernouilli Euler (B-E) beam. Figure (1) shows plots of R_{mn} computed analytically (red trace only) for modes with 1, and 2 half sine-waves along the load path (a)-(c) and (b)-(d), respectively. It can be observed that maximum free vibration and cancellation conditions alternate as the velocity increases. These conditions may be analytically obtained and, as equation (3) is the same for the B-E S-S beams, maximum free vibration and cancellation non-dimensional speeds for plates with m half-sine waves along the load path coincide with those for the beam for the first m longitudinal bending modes of vibration. These conditions are given in [2].

3 INFLUENCE OF PLATE OBLIQUITY, STRUCTURAL DAMPING AND SUPPORTS FLEXIBILITY

In what follows a particular orthotropic plate Finite Element (FE) model is used. The plate properties are obtained from a real railway bridge with two S-S 15.25 m span identical bays and double track pre-stressed concrete girders deck (section 4). This bridge is selected as (i) the span length to with ratio is close to unity; (ii) it has a 45º skew angle; (iii) experimental measurements are available under ambient vibrations and railway traffic. Due to the deck geometry and the eccentric excitation several modes contribute to the dynamic response of the bridge deck under railway traffic, and its behaviour considerably differs from a beam-type structure.

First R_{mn} is numerically computed for two skew angles of the plate: 22.5 º and 45º. Results are plotted in Figure (1) (black and grey trace) for the first two modes (n=1,2) of modes with 1 and 2 half-sine waves along the load path (i.e. m=1,2). It is concluded that as long as the modal deformed shape along the load path is approximately sinusoidal, (i) cancellation conditions do occur; (ii) maximum free vibration conditions take place in between them; and (iii) the values of K_{mn} for these two situations may be approximated with analytical values for straight plates.

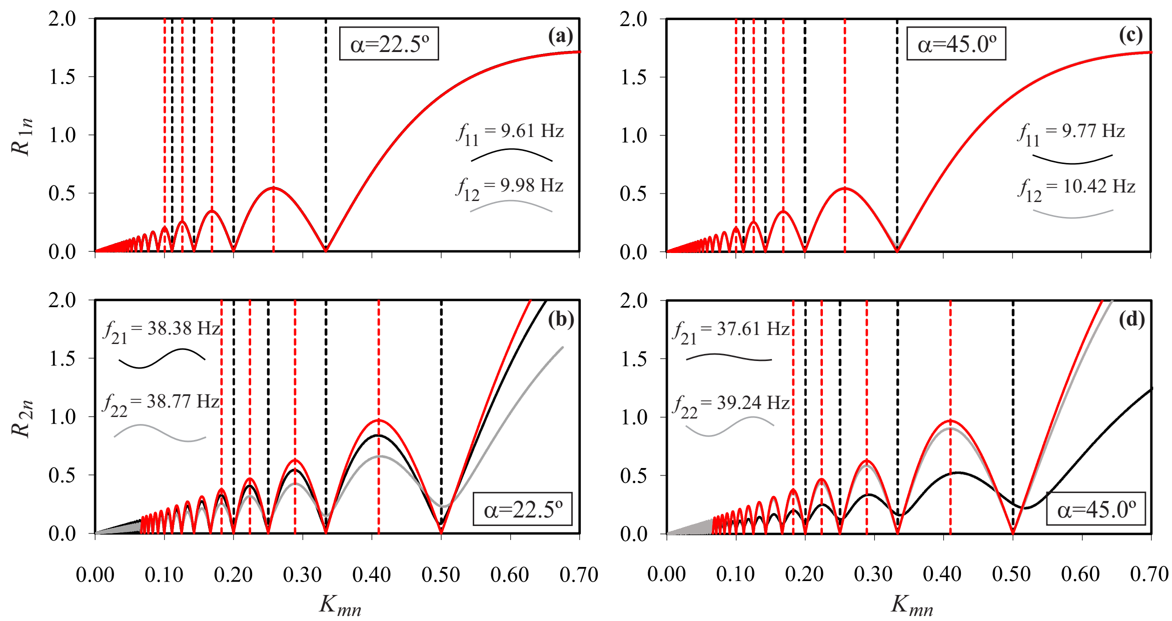

Figure 1:. R_{mn} for modes with m=1,2,3 and n=1,2 considering skew angles of 22.5º and 45º. Red trace: analytical evolution of R_{mn} for rectangular plates. Black and red dashed lines: analytical cancellation and maximum free vibration conditions.

The same type of sensitivity analysis is performed with the presence of structural damping and the vertical flexibility of the plate supports. Regarding structural damping it is concluded that cancellation and maximum free vibration conditions remain practically unmodified, even for the highest level of damping (5%) considered. Nevertheless, free vibrations do not completely cancel in the presence of structural damping.

As per the flexibility of the supports, it may be concluded that: (i) the evolution of R_{mn} presents a similar form when flexible distributed supports are included; (ii) cancellation and maximum free vibration conditions reduce mildly as a consequence of the reduction experienced by the natural frequencies; (iii) in the particular case under consideration the analytical cancellation conditions derived from the elastically supported (E-S) B-E beam equations predict excellently the real cancellation conditions in the case of the first two modes in frequency order with a number of half-sine waves m=1,2 and 3. The particular values of these conditions may be consulted in [2].

When a railway bridge is subjected to a train of loads, equating the nondimensional resonant velocities to the cancellation or maximum free vibration conditions it is possible to obtain ratios of span length /characteristic distance causing very soft or considerably amplified resonances. In the following section, these two situations are shown in a real railway bridge belonging to the Spanish railway network.

4 RESONANCE IN A REAL STRUCTURE

Figure 2 shows the vertical acceleration measured by the authors at the mid-span section border of Arroyo Bracea Bridge, which belongs to the Madrid-Sevilla HS line. The bridge is S-S, presents a skew angle of 45º, and it is composed by a pre-stressed concrete girders deck. Under the circulation of two commercial trains (ICE3-S103 and Talgo 250-S130) the bridge experiences a 3rd resonance of its fundamental longitudinal bending mode (9.25 Hz) and a 2nd resonance of the first torsion mode (10.63 Hz). The former is near to a theoretical maximum free vibration condition (L/d_k=0.61) and the latter is close to a cancellation condition (L/d_k=1.16). As it may be observed in Figure 2, S103 leads to a clear resonance in the frequency domain while S130 does not, even though the latter induces a lower order resonance on the bridge deck.

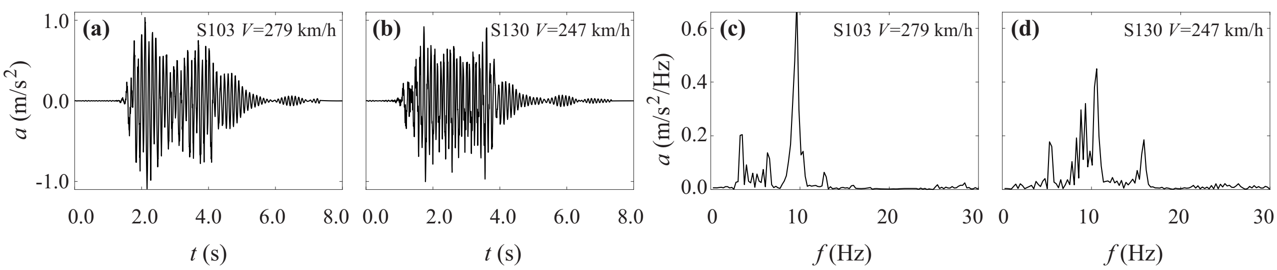

Figure 2:. Vertical acceleration at mid-span and deck border in the time and frequency domains induced by trains S103 (a)-(c) and S130 (b)-(d).

5 CONCLUSIONS

- Analytical maximum free vibration and cancellation conditions for rectangular orthotropic plates may be used to predict these situations in real structures as long as the deformed modal shape along the load path may be approximated by a sinusoidal function.
- Depending on the span length to the train characteristic distance ratio resonances induced on railway bridges may present noticeable amplitudes or may become even imperceptible.

ACKNOWLEDGEMENTS

The authors acknowledge the financial support provided by (i) the Spanish MINECO under research project [BIA2016-75042-C2]; and (ii) the Andalusian Scientific Computing Centre (CICA).

REFERENCES

[1] ERRI D214. *Rail bridges for speeds >200 km/h. Final report. Part A. Synthesis of the results of D 214 research*, European Rail Research Institute, 1999.

[2] P. Museros, E. Moliner, M.D. Martínez-Rodrigo. *Free vibrations of simply supported beam bridges under moving loads: maximum resonance, cancellation and resonant vertical acceleration*, Journal of Sound and Vibration 332: 326–345, 2012.

[3] N.J. Huffington, W.H. Hoppmann. *On the transverse vibrations of rectangular orthotropic plates,* Journal of Applied Mechanics 25: 389–395, 1958.

1st. Conference on Structural Dynamics (DinEst 2018)
Madrid, 20–21 June

DYNAMIC ANALYSIS OF A SKEW I-BEAM RAILWAY BRIDGE: EXPERIMENTAL AND NUMERICAL

Carlos Velarde*, J.M. Goicolea*, K. Nguyen*, J. García-Palacios*, I. M. Díaz*, J.M. Soria*

*ETS Ingenieros de Caminos, Canales y Puertos
Universidad Politécnica de Madrid
28040 Madrid, Spain

e-mail: c.velarde@upm.es

Abstract. Skew bridges induce inherently coupled bending and torsion response. The actual relevance of this coupling in the dynamic response of this relatively common type of deck (slab supported on multiple I-beams for double-track width) is not well known. This paper presents the study of the dynamic behaviour of a skew I-beam railway bridge of the Valencia-Tarragona line in Spain. Both experimental and numerical analysis have been carried out. The experimental study consists of an Operational Modal Analysis (OMA) of the bridge from the data provided from 20 high-sensitivity accelerometers attached underneath the deck. The monitoring system is completed by six strain gauges attached to rails in groups of two. For the numerical study, different models have been used, including 2D analysis with the software Caldintav and 3D FEM analysis with Abaqus.

As a result of the experimental study, the modes of vibration of the structure have been successfully identified (modal shapes, natural frequencies and damping ratios) as well as the behaviour of the bridge under the action of some trains running across it. These results are compared with those obtained from the numerical analysis. Furthermore, some numerical simulations have been developed to predict the behavior of the structure under the action of some trains crossing at several speeds.

Key words: Dynamic Analysis, Railway Bridge, Modes of vibration, Numerical analysis, Operational Modal Analysis

1 INTRODUCTION

This paper studies the behavior of railway bridge from the Tarragona-Valencia line in Spain. First, a experimental analysis has been carried out obtaining the modal parameters of the structure. Afterwards, a numerical study has been developed, using the experimental data to adjust the numerical models. 3D FEM models in Abaqus software [6] have been used to simulate the response of the bridge for specific cases. Furthermore, in order to study the behavior of the bridge for a large number of cases, a 2D analytical model in Caldintav software [4] has been developed from the 3D model.

2 Bridge description

The bridge has three isostatic spans: two end spans of 9.60 m and 8.61 m and the center span of 15.40 m, measured along the beams direction. The structure has a skew angle of 25.2°. The width of the deck is 12.85 m.

The cross section of the deck is composed of prestressed concrete I-beams with 1.42 m depth and a concrete slab with 0.20 m depth. At the center span the cross section has 7 I-beams, while at the end spans it has only 6.

3 Study description

Both experimental and numerical analyses have been carried out. The experimental results have been used to adjust the parameters of the numerical model and to compare with numerical results.

3.1 Experimental test

The experimental test consists of an Operational Modal Analysis (OMA) of the bridge from the data provided from 20 high-sensitivity accelerometers attached underneath the deck, on the I-beams flanges.

The accelerometers were distributed in order to be able to capture bending and torsional modes of vibrations. In this study only those located within the center span are analysed. Three of them have not been taken into account due to their defective signal (Fig. 1).

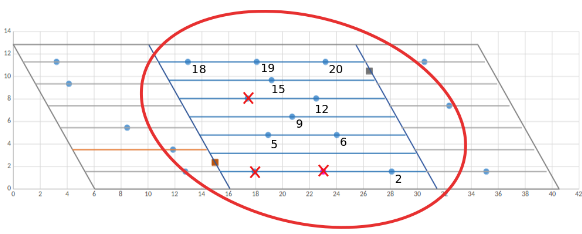

Figure 1: Situation of analysed accelerometers

The monitoring system is completed by six strain gauges attached to rails in groups of two. As they capture the pass of the axle loads, and the distance between gauges is known, they are useful to calculate the speed of the trains.

3.2 Numerical models

A 3D finite element model has been carried out using Abaqus. Shell elements have been used to model the flanges and web of the I-beams. The slab has also been modelled with shell elements.

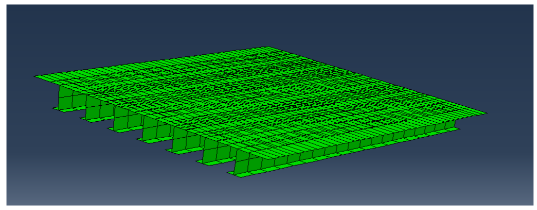

Figure 2: Bridge model in Abaqus

In this model an equivalent density has been computed to take into account the non-structural mass.

Furthermore, in order to evaluate a great number of cases, 2D analytical model in Caldintav software has been developed. It lets us compute the envelope of accelerations and displacements (maximum for each velocity between the desired range) and takes much less time than using 3D models. The relationship between 3D model and 2D analytical model is commented in the following section.

4 Results

4.1 Modal properties

The modal properties obtained from experimental and numerical analysis are shown in Tab. 1.

4.1.1 Experimental test

Experimental test data has been analyzed with two programs: UPMOMA software [3] and Macec [5].

Four significant modes have been correctly captured (Fig. 3).

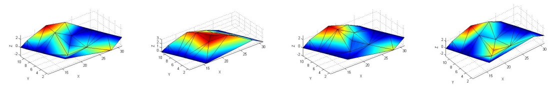

(a) Mode 1: torsion (b) Mode 2: bending (c) Mode 1-2: torsion 2 (d) Mode 3: 2D bending

Figure 3: Experimental mode shapes

Table 1: Vibration modes: experimental and numerical

Mode number	Exp. frequency [Hz]	Exp. Damping [%]	Num. frequency [Hz]
Mode 1: torsion	8.31	1.25	9.19
Mode 2: bending	10.04	1.87	9.86
Mode 1-2: torsion 2	11.27	1.01	-
Mode 3: 2D bending	14.03	1.51	12.77

4.1.2 Numerical model: 3D Abaqus

The modes of vibration obtained from the 3D model in Abaqus are shown in Fig. 4.

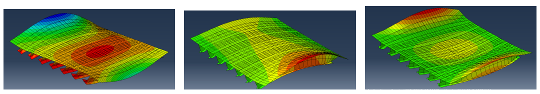

(a) Mode 1: torsion (b) Mode 2: bending (c) Mode 3: 2D bending

Figure 4: Numerical mode shapes

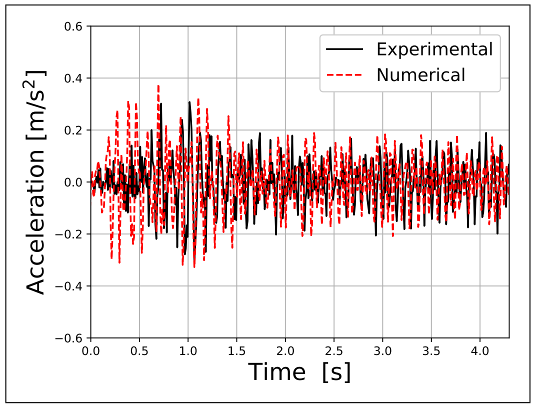

Figure 5: Acceleration sensor 15: experimental vs numerical

The model has been adjusted in such a way that the frequency of the first flexural mode ("Mode 2: flexion") in the numerical model is similar to the frequency obtained for that mode in the experimental test. The torsional mode called "Mode 1-2: torsion 2" in Tab. 1 does not appear in the numerical model.

4.2 Study of the bridge under the action of running trains

Within the experimental test a Talgo VI train running at 129 km/h was recorded. The accelerometers used in the experimental test have a sensitivity $S = 10\,\mathrm{V}/g$ and a saturation peak $a_{sat} = 5\,\mathrm{m/s}^2$. Most sensors situated near the track over which the train passed reached their saturation acceleration due to high-frequency peaks, so their signals during the pass of the train are not valid. However, the sensors situated far from that track recorded good signals. Fig. 5 shows a comparison between the acceleration time history of the sensor number 15 and the signal obtained in the numerical simulation at this point.

The signal obtained from the numerical model is reasonably similar to the experimental test signal.

By using the numerical model it is possible to simulate other cases. In this case s103, s100R and s112.5 high speed trains, running at several speeds have been studied. These results will be compared with those obtained from the large number of cases studied in the analytical beam model of Caldintav.

In order to calculate the values at mid span under the track with Caldintav, it is necessary to apply a coefficient to reduce the effective section because only a fraction of the deck section is collaborating during the pass of the train. Fig. 6 shows that there is an important difference between the displacement under the track and at the deck center.

Both the mass per unit length and the moment of inertia must be multiplied by the coefficient so that the relation between them is conserved and, therefore, the vibration frequency is conserved too. In this case the value of the coefficient is 0.59.

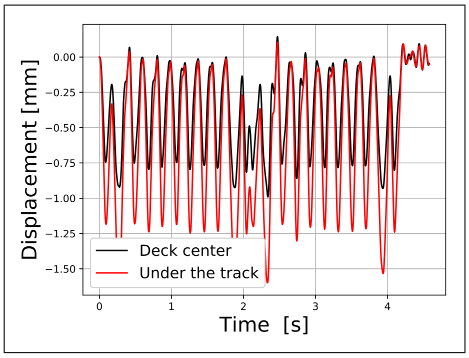

Figure 6: Displacements s100R train: under the track vs deck center

Figs. 7 and 8 show the comparison between displacements and accelerations obtained from 3D Abaqus and from 2D Caldintav.

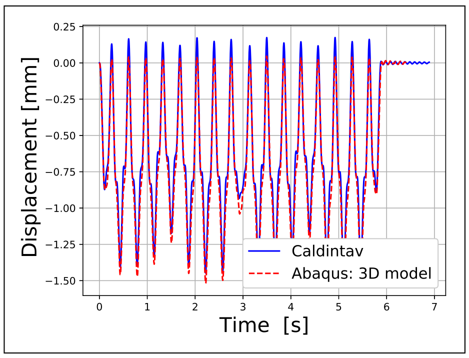

Figure 7: s103 train at 250 km/h: displacement in 3D Abaqus vs 2D Caldintav

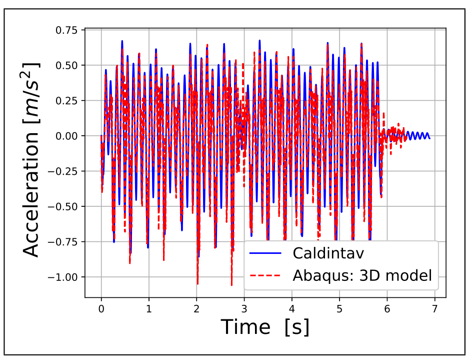

Figure 8: s103 train at 250 km/h: acceleration in 3D Abaqus vs 2D Caldintav

It can be seen that the results from 3D Abaqus model and 2D Caldintav are very similar.

Once the 2D Caldintav model is calibrated to represent the accelerations and displacements under the track, the envelopes can be computed. Figs. 9 and 10 show the envelope of acceleration and dynamic amplification factor (DAF) for the trains from High Speed Load Model - A (HSLM-A), developed in ERRI D214 [1] and included in the Eurocode EN 1991-2:2003 [2] , and for real trains s103, s112.5 and s100R, running at speed between 120-350 km/h.

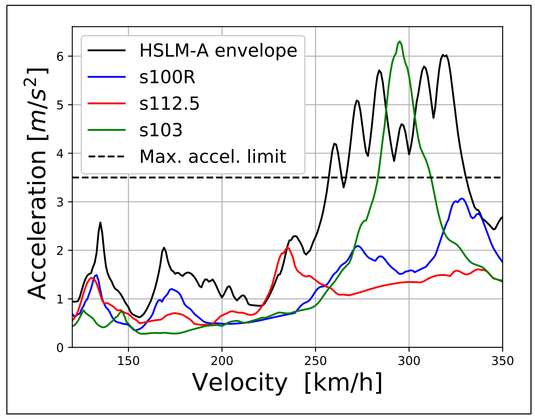

Figure 9: Envelope of acceleration : HSLM-A trains and real trains

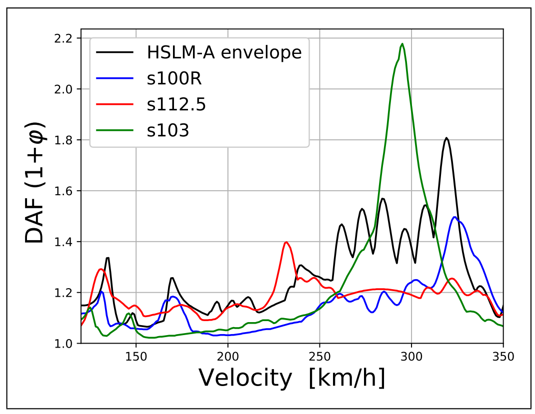

Figure 10: Envelope of DAF : HSLM-A trains and real trains

It can be seen in Fig. 9 that HSLM-A trains and s103 train exceed the max. accel. limit for ballasted tracks (3.5 m/s^2). But these cases are peaks due to resonance and when they are studied in the 3D Abaqus model, the maximum accelerations obtained is less than those from Caldintav. Fig. 11 shows the comparison between 3D Abaqus model and Caldintav for s103 train running at 295 km/h (resonant speed).

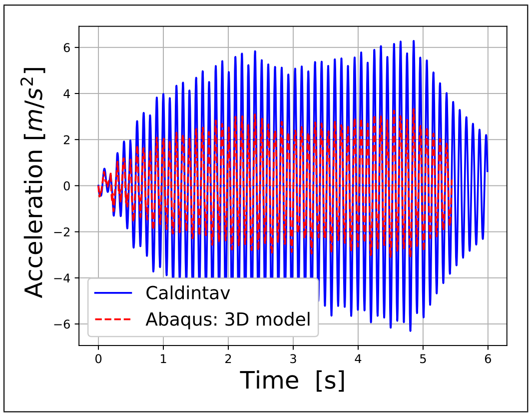

Figure 11: Acceleration for s103 train at 295 km/h

At resonance there is enough energy to move the whole section and not only the reduced section used in Caldintav and, therefore, in 3D model the maximum values are less than those obtained in Caldintav. To illustrate this idea, Fig. 12 shows the acceleration values under the track and at deck center for non-resonant and resonant speeds. In the first case there is a considerable difference between them (1.74 ratio) but in the second case the difference is smaller (1.20 ratio) because the whole section is collaborating.

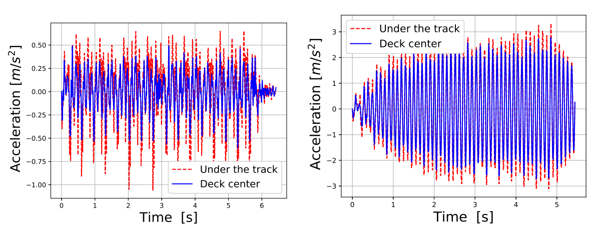

(a) Non resonant speed: 250 km/h

(b) Resonant speed: 295 km/h

Figure 12: Comparison of acceleration due to s103 train for resonant and non resonant speeds: deck center vs under the track

5 CONCLUSIONS

- Both experimental and numerical analysis have been carried out. The results from the experimental test and the adjusted 3D numerical model are reasonably similar.
- From the 3D numerical model a 2D analytical model has been developed in order to study a large number of cases.
- According to the 3D numerical and 2D analytical study for HSLM-A trains and three real trains, the behavior of the bridge (in terms of acceleration) is acceptable, within the studied speed range (up to 350 km/h), as the maximum values are under the limit level for ballasted tracks.
- In this bridge, with a deck composed of concrete I-beams and slab, the effective section used for the 2D model is appropiate for non resonant speeds, while it overestimates the accelerations and displacement values for resonant speeds because, for those cases, a bigger portion of the section is mobilised.

6 ACKNOWLEDGMENTS

The authors acknowledge the financial support provided by the Spanish MINECO under research project BIA2015-71016-R and FPI contract.

REFERENCES

[1] Comittee ERRI D 214. ERRI D214/RP 9. Rail bridges for speeds ¿ 200 km/h - Final Report Part A: Synthesis of the results of D 214 research Part B: Proposed UIC Leaflet, dec 1999.

[2] CEN. European Standard EN 1991-2: Eurocode 1 - actions on structures. part 2: Traffic loads on bridges. Technical report, rue de Stassart 36, B-1050 Brussels.

[3] J. Garcia Palacios, I.M. Diaz, and J.M. Soria. UPMOMA: un software para analisis modal.

[4] Jose M. Goicolea and Khanh Nguyen. CALDINTAV Version 3.0.

[5] Structural Mechanics Section KU Leuven. Macec.

[6] Simulia-Dassault Systemes. Abaqus Software.

1st. Conference on Structural Dynamics (DinEst 2018)
Madrid, 20–21 June

TRAIN-SPEED SENSITIVITY ANALYSIS FOR MAXIMUM ENVELOPES IN DYNAMICS OF RAILWAY BRIDGES

Alejandro E. Martínez-Castro*, **Enrique García-Macías**†

*ETS Ingenieros de Caminos, Canales y Puertos
Universidad de Granada
Avenida Fuentenueva sn, 18002 Granada, Spain

e-mail: amcastro@ugr.es
ORCID: 0000-0003-3023-1099

† Escuela Técnica Superior de Ingeniería
Universidad de Sevilla
Camino de los Descubrimientos, 41092 Sevilla, Spain
e-mail: egarcia28@us.es
ORCID: 0000-0001-5557-144X

Abstract. The design of railway bridges for high-speed train requires the numerical evaluation of the maximum response envelopes. This is usually carried out by direct time-domain solutions, based on modal superposition. The train is represented by constant forces traversing the structure at constant speed. The maximum response (displacements or accelerations) at a fixed point in the bridge is computed by sampling the corresponding function at each speed in the time domain. Particularly in the context of three-dimensional geometries and low-damped structures, this approach is time-consuming. In this work, an alternative approach is developed based on the use of the train-speed sensitivity in the governing equations. The formulation is developed by the direct differentiation of the semi-analytic solution of the moving load problem. The derivatives are obtained in closed form. The envelope theorem guarantees that tangential derivatives respect to train speed of the maximum values can be computed in the derivative at the fixed time in which the maximum value is reached. The main advantage of this approach comes from the fact that two values are computed at each single train-speed: the maximum, and the sensitivity of this maximum value respect to the train speed. An alternative construction of the envelope by hermitian cubic spline is presented. This avoids the explicit evaluation of time-series at intermediate train speeds. The proposed approach reduces the number of direct time-domain evaluations, which leads to substantial computing time reductions. Numerical tests show the effectiveness of the approach, from beam to large-scale three-dimensional finite element models. A drastic reduction in computing times are reported, particularly in the context of low-damped and complex structures.

Key words: Dynamics of railway bridges, Modal Superposition, Sensitivity analysis, Design envelopes, Semi-analytic solutions

1 INTRODUCTION

The design of a railway bridge requires particular attention to dynamic effects. In the European code [1] or the Spanish code [5] dynamic analysis are prescribed. The service limit states are strongly dependent on the modal characteristics of the bridge and the frequency content of the loads. Envelope curves are built in order to detect resonance amplifications. The classical approach to build the envelopes is the direct sampling of numerical time-series at each train speed.

The number of direct evaluations involved in the computation of envelopes is time-consuming. Several factors must be considered for adequate detection of amplification peaks in the envelope: i) the number of modes to be considered depends on the complexities of the model (from Bernoulli-Euler beams, to comples 3D models combining beams, shells and solid elements); ii) time step size must decrease for low damping ratio (steel or composite bridges); iii) higher speed resolution is required to evaluate the peak response at low damping; iv) the number of trains considered increases the computing times; v) the number of post-processing points increases with the complexities of the model; vi) in ballasted tracks, three mass hypothesis are prescribed by codes.

To illustrate an example, a simple case is described: the dynamic analysis of a continuous 3-span bridge, including the effect of 12 trains (HSML, AVE and TALGO), with train speed running from 20 km/h to 420 km/h, with step $\Delta v = 5$ km/h, will require the computation of 960 direct time series. When 3 mass ballast hypothesis are included, the number of direct simulations is increased to 2880. When low damping rate is considered, speed-step will require $\Delta v = 1$ km/h, and the number of direct evaluations rises to 14940.

In the literature, different numerical approaches have been developed to solve the moving load problem for design issues [2]. In the present work, the semi-analytic solution developed by Martínez-Castro *et al.* [4] is considered to develop a novel formulation to compute the analytic sensitivity of the response respect to the train-speed parameter. The main advantage of this formulation is the direct extension to complex geometries [6, 3], providing closed-form solutions in the time domain.

In this work an alternative envelope construction is presented, based on a C_1 cubic spline. This can be done by computing an additional parameter at each sampled speed: the sensitivity of the response respect to the train speed.

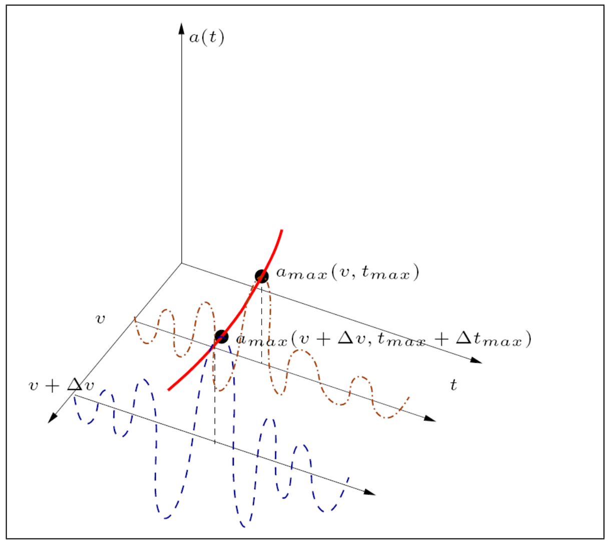

Figure 1: Evolution of maximum acceleration

Figure 1 shows two acceleration curves. At time v, the maximum acceleration tested at time $t = t_{max}$ is shown: $a_{max}(v, t_{max})$. The second curve corresponds to a close speed $v + \Delta v$, in which the maximum value is $a_{max}(v+\Delta v, t_{max}+\Delta t_{max})$. The envelope theorem guarantees that the slope of the acceleration envelope can be computed at the fixed time t_{max}, as the partial derivative:

$$\frac{\partial a_{max}}{\partial v} = \left.\frac{\partial a_{max}(v,t)}{\partial v}\right|_{t=t_{max}} \tag{1}$$

Based on this derivative, an alternative envelope is proposed, shaped as a C_1 cubic spline. (Figure 2). This approach requires few computational effort: despite the evaluation of the maximum is carried out by sampling the complete time series, the sensitivity computation does not require a time search: it just require the evaluation of a function at a fixed time.

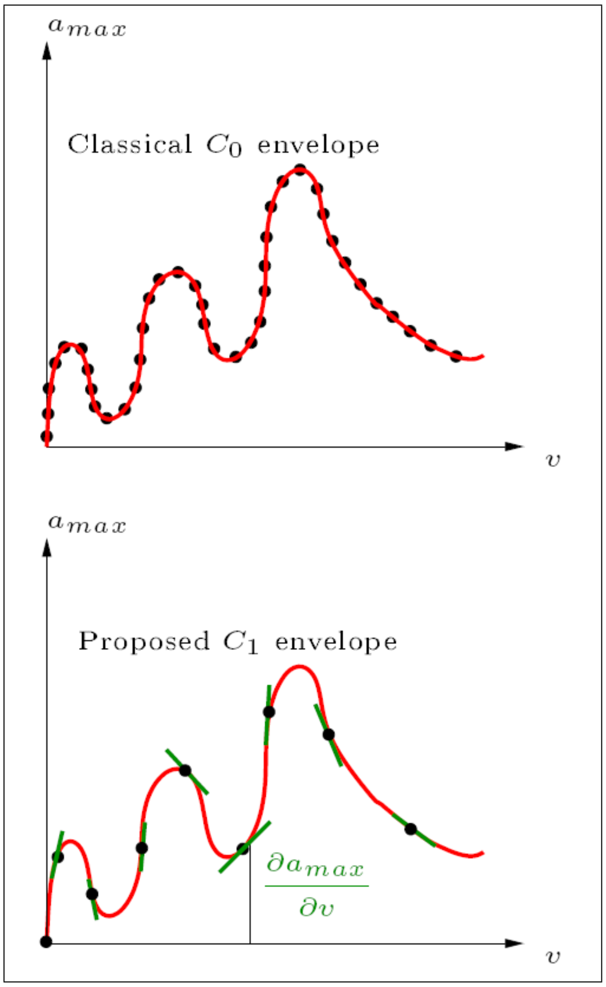

Figure 2: Classical and proposed envelope

2 DIRECT FORMULATION

The forward problem is solved by a semi-analytic solution, reported in [4]. A local reference $R(O;x,y)$ is introduced, in which the origin O is located at the first point of the lane, x stands for the location along the lane, and y is the vertical coordinate. A point-load traverses the bridge moving at constant speed v as $p(x,t) = P\delta(x - vt)$. The lane is divided in elements, where local cubic interpolation is considered. An element e is located in the spacial domain, with $e = \{x : x \in [L_e, L_{e+1}]\}$. The vertical displacement $w(x,t)$ is expanded in the base of natural modes as:

$$w^e(x,t) = \sum_{n=1}^{N_{max}} q_n^e(t)\phi_n^e(x) \tag{2}$$

with $q_n^e(t)$ the n-th time-dependent modal amplitude, and $\phi_n^e(x)$ the modal shape evaluated at point x. A global C_1 (exact or approximed) interpolation is considered for the displacement function along the lane, in which $h_i(x)$ represents the local interpolation of the approximated field in a polynomial Hermite basis.

$$w^e(x,t) = \sum_{n=1}^{N_{max}} q_n^e(t) \sum_{i=1}^{4} c_{ni}^e\, h_i(x) \tag{3}$$

Coefficient matrix c_{ni}^e are functions of the modal coordinates. Functions $q_n^e(t)$ have closed-form expressions. The solution is split into two terms: $q_n^e(t) = q_n^{e,h}(t) + q_n^{e,p}(t)$. Considering the local time $\tau = t - \frac{L_e}{v}$, and omitting the superscript e, solutions for the homogeneous and particular functions can be written as,

$$q_n^{e,h}(t) = e^{-\zeta_n\omega_n\tau}\left[A_n\cos(\omega_{Dn}\tau) + B_n\sin(\omega_{Dn}\tau)\right] \tag{4}$$

$$q_n^{e,p}(t) = \alpha_n^{(0)} + \alpha_n^{(1)}(v\tau) + \alpha_n^{(2)}(v\tau)^2 + \alpha_n^{(3)}(v\tau)^3 \tag{5}$$

Note that in Eq. (4), $\omega_{Dn} = \omega_n\sqrt{1-\zeta_n^2}$ is the damped angular frequency of the n-th mode. In Eq. (5), the four coefficients can be obtained in terms of 10 coefficients, nondependent on the train speed [4],

$$\begin{aligned}
\alpha_n^{(0)} &= v^3\alpha_n^{(01)} + v^2\alpha_n^{(02)} + v\alpha_n^{(03)} + \alpha_n^{(04)}\\
\alpha_n^{(1)} &= v^2\alpha_n^{(11)} + v\alpha_n^{(12)} + \alpha_n^{(13)}\\
\alpha_n^{(2)} &= v\alpha_n^{(21)} + \alpha_n^{(22)}\\
\alpha_n^{(3)} &= \alpha_n^{(31)}
\end{aligned} \tag{6}$$

3 SENSITIVITY FORMULATION

The sensitivity of the response respect to the train speed can be obtained by the derivative evaluation,

$$\frac{\partial w^e(x,v,t)}{\partial v} = \sum_{n=1}^{N_{max}} \frac{\partial q_n^e(v,t)}{\partial v}\phi_n^e(x) \tag{7}$$

The partial derivative can be evaluated as,

$$\frac{\partial q_n^e(v,t)}{\partial v} = \frac{\partial q_n^e(v,\tau)}{\partial v} + \frac{L_e}{v^2}\frac{\partial q_n^e(v,\tau)}{\partial v} \tag{8}$$

The first term one can be written as (omitting superscript e),

$$\frac{\partial q_n^h(v,\tau)}{\partial v} = e^{-\zeta_n \omega_n \tau}\left[D_n \cos(\omega_{Dn}\tau) + E_n \sin(\omega_{Dn}\tau)\right] \tag{9}$$

Parameters D_n, E_n, are determined from A_n, B_n, including the initial conditions and its derivatives at each element. Note that Eq. (9) has the same form than Eq. (4). The second term is derived as,

$$q_n^p(v,\tau) = \beta_n^{(0)} + \beta_n^{(1)}(v\tau) + \beta_n^{(2)}(v\tau)^2 + \beta_n^{(3)}(v\tau)^3 \tag{10}$$

$$\begin{aligned} \beta_n^{(0)} &= 3v^2\alpha_n^{(01)} + 2v\alpha_n^{(02)} + \alpha_n^{(03)} \\ \beta_n^{(1)} &= 3v\alpha_n^{(11)} + 2\alpha_n^{(12)} + \alpha_n^{(13)}/v \\ \beta_n^{(2)} &= 3\alpha_n^{(21)} + 2\alpha_n^{(22)}/v \\ \beta_n^{(3)} &= 3\alpha_n^{(31)}/v \end{aligned} \tag{11}$$

Note that Eq. (11) has been written similarly to Eq. (6). Thus, the way to compute and store the partial derivative is carried out with the 10 original terms in Eq. (6).

4 CONCLUDING REMARKS

A novel formulation for the evaluation of design envelopes is presented. By usin the sensitivity approach, an approximed C_1 envelope is proposed. Analytic closed-form formulation is presented to evaluate the sensitivity. The numerical evaluation of the sensitivity is carried out at a fixed time in which the maximum value is reached. The proposed approach reduces the number of direct evaluations required for envelope evaluation. Combined with complex and low-damped structures, the proposed approach leads to global time reductions in the evaluation of design envelopes. Numerical tests have been developed, showing excellent performances of the proposed approach.

REFERENCES

[1] CEN. *EN1990:1-2. Eurocode 1- Actions on Structures. Part 2. Actions on bridges*, european commitee for standardization edition, 1990.

[2] J. M. Goicolea and P. Antolin. Dynamics of High-Speed Railway Bridges: Review of Design Issues and New research for Lateral Dynamics. *International Journal of Railway Technology*, 1(1):27 – 55, 2012.

[3] A. Martínez-Castro and E. García-Macías. Two techniques for fast evaluation of design envelopes in high-speed train railway bridges: Train speed sensitivity and the Hilbert transform. In *Proceedings of the 9th International Conference on Structural Dynamics. EURODYN 2014*, Porto (Portugal), 2014.

[4] A.E. Martínez-Castro, P. Museros, and A. Castillo-Linares. Semi-analytic solution in the time domain for non-uniform multi-span Bernoulli–Euler beams traversed by moving loads. *Journal of Sound and Vibration*, 294(1):278 – 297, 2006.

[5] Ministerio de Fomento. *IAPF-07. Instrucción sobre las acciones a considerar en el proyecto de puentes de ferrocarril* , government of spain edition, 2007.

[6] P. Museros, A. Martínez-Castro, and A. Castillo-Linares. Semi-analytic solution for Kirchhoff plates traversed by moving loads. In *Proceedings of the 6th International Conference on Structural Dynamics. EURODYN 2005*, Paris (France), 2005.

1st Conference on Structural Dynamics (DinEst 2018)
Madrid, 20-21 June

ASSESSMENT OF LATERAL VIBRATIONS OF FOOTBRIDGES USING A FREQUENCY DOMAIN APPROACH

Rocío G. Cuevas*, Francisco Martínez*and Iván M. Díaz*

* ETS Ingenieros de Caminos, Canales y Puertos
Universidad Politécnica de Madrid
28040 Madrid, Spain
e-mail: rociogarcuevas@gmail.com

Abstract. Lateral vibrations of footbridges caused by the passage of pedestrian crowds have been the object of many studies over the last decade. However, the connection between experimental and analytical results remains tenuous and as a consequence, a common set of design criteria have not been established yet. Regarding the particular features of both the pedestrian load and the dynamic system (slender footbridges with little damping), the frequency domain analysis is a method especially efficient to evaluate the lateral response. Hence, the object of this study is to develop a general formulation, using a frequency domain approach, for assessing the lateral vibrations of any footbridge; considering the action of a crowd of pedestrians walking randomly with different frequencies. The effects of pedestrians in a swaying deck are not limited to imposing external loads; the people-structure interaction generates additional harmonics in the natural frequencies of the structure that are independent of the pedestrian frequency. Hence, human-structure phase synchronization is not a necessary condition for the development of the resonant component. The study states that it is accurate enough to calculate the structural response using only the resonant contribution. These considerations lead to a very simple formulation that permits to establish a positive relationship between the amplification of the response and the number of pedestrians.

Key words: Footbridges lateral vibration, frequency domain analysis, response amplification.

1 INTRODUCTION

In the frequency domain analysis, the dynamic response Y(f) to an action X(f), is obtained as the algebraic product of the action X(f), and the system´s complex frequency response function H(f), which defines completely the dynamic characteristics of the dynamic system. The pedestrian action is a random load that takes approximately the same value at equal slots or time-periods. Hence, in the frequency domain it is represented by a series of “comb teeth” or delta functions. It is a “narrow band process” because its spectral density occupies only a narrow band of frequencies, which are, the pedestrian frequency f_p, and its integer multiples. Additionally, for this particular case of low damped structures, H(f) presents a concentrated peak in $f = f_b$ (the bridge’s natural frequency) and tends to zero when moving away from this value. Therefore, the structural response is amplified only in a very narrow frequency interval centered in f_b. Consequently, two conclusions can be drawn. Firstly, the harmonics of the output signal will match the input ones. Secondly, the response will be amplified only if the input signal contains some harmonic very close to f_b.

Hence, the preceding analysis shows that pedestrians walking in a moving surface are not only external loads. There is an interaction pedestrian-structure and so, additional harmonics have to appear, including a component in the bridge natural frequency, which is the mainly responsible for the unexpected increment of the lateral vibration. Otherwise, the response calculated using a frequency domain analysis would be practically zero, which does not agree with the observed behavior of real footbridges. **Figure 1** presents the Frequency Response Function for the 1st lateral mode of the London Millennium Bridge (f_b=0.5Hz) and the Solférino Bridge (f_b=0.81Hz) overlapped with the two first harmonics of the pedestrian load (f_p=0.86Hz; 1.72Hz). In both cases, the response would be nearly zero.

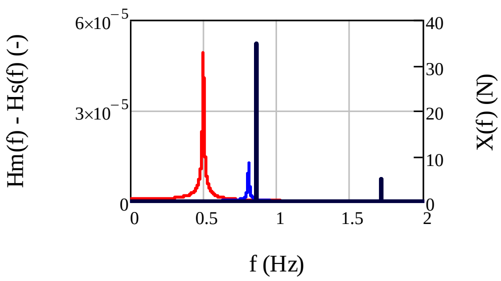

Figure 1: Pedestrian load X(f) and Frequency Response Functions $H_M(f)$ –$H_S(f)$.

Therefore, the pedestrian load model has to include the self-excitation components. This effect, known as "auto-excitation forces", is widely accepted in the current state of the art. Macdonald's [4]-[5] analytical formulation of the lateral walking action, based on the inverted pendulum model, includes a component in the natural frequency of the bridge. Otherwise, Pizzimenti and Ricciardelli [6] and Ingólfsson et al. [3], have measured the lateral forces exerted in a swaying treadmill with a lateral displacement of $x(t) = x_0 \sin 2\pi f_b$t. These experimental forces also contain the "auto-excitation" components, and they are expressed as the sum of the equivalent static force and the equivalent damping and inertia forces:

$$F(t) = F_{st}(t) + c_p\left(\frac{f_b}{f_p}, x_0\right)\dot{x}(t) + m_p q_p\left(\frac{f_b}{f_p}, x_0\right)\ddot{x}(t) \quad (1)$$

The equivalent damping and inertia components were determined through the cross-covariance between the measured pedestrian force and the velocity or acceleration of the treadmill. The damping and inertia coefficients c_p and q_p, are defined from the experimental data, using a stochastic model [3].

2 FREQUENCY DOMAIN MODEL

From this point on, the methodology exposed is based on the assumption that the resonant harmonic controls the dynamic response, and thus it is accurate enough to consider only its contribution neglecting the rest of the harmonics. Consequently, the spectral value and the time dependent estimated response will result in:

$$|Y_{f_b}| = |H_{f_b}||Q_{f_b}| \quad (2)$$

$$y(t) = 2|Y_{f_b}|\cos\left(2\pi f_b t + arg(Y_{f_b})\right) \quad (3)$$

The amplitude of the harmonic in the natural frequency f_b is expressed using the experimental damping coefficient c_p; as the steady-state velocity response of a damped system due to a resonant harmonic vibration ($f=f_b$) is in-phase with the load. Therefore, the value for a single pedestrian with lateral walking frequency f_p will be:

$$|P_{f_b}| = c_p\left(\frac{f_b}{f_p}, x_0\right) 2\pi f_b x_0 \quad (4)$$

In a real case assessment, there is a crowd of N pedestrians uniformly distributed, walking randomly with different frequencies f_{pi}. One of the advantages of the frequency domain analysis is that it is possible to apply the superposition principle. Hence, the coefficient c_{pm} gathers up the contribution of N pedestrians with “m” different frequencies:

$$c_{pm} = \sum_{i=1}^{m} \frac{n_i}{N} c_{pi}\left(\frac{f_b}{f_{pi}}, x_0\right) \tag{5}$$

In modal analysis, the response is individually evaluated in the main single vibration modes that contribute significantly to the response. Considering the case of a single span footbridge of length L, modal shape $\phi(x)$ and modal characteristics f_b, M, K, and C; the amplitude of the modal load exerted by N pedestrians takes the following expression:

$$|Q_{f_b}| = \frac{N c_{pm}}{L} 2\pi f_b u_0 \int_0^L [\Phi(x)]^2 dx \tag{6}$$

Considering equations (2) and (3), the amplitude of the displacement response is calculated and expressed in terms of the amplification ratio:

$$\frac{u}{u_0} = \left[\frac{4\pi f_b}{L} |H_{f_b}| \int_0^L [\Phi(x)]^2 dx\right] [N c_{pm}] \tag{7}$$

Equation (7) has two factors. The first one depends on the dynamic system and takes a constant value for one specific mode. The second one depends on the pedestrians, being the coefficient c_{pm} also constant for a certain composition of walking frequencies f_{pi}. Consequently, equation (7) can be rewritten, showing a positive relation between the amplification ratio u/u_0 and the number of pedestrians N, which can also be express in terms of damping ratio ξ:

$$\mathrm{AR}(\mathrm{N}, \xi) = \frac{\mathrm{u}}{\mathrm{u}_0} = \mathrm{G}(\xi)\mathrm{N} \tag{8}$$

3 NUMERICAL SIMULATION

The model performance is evaluated through numerical response simulation, using the 1st lateral mode of the LMB, Solférino Bridge and the CMB (Changi Mezzanine Bridge). The modal shape is considered to be a sin lateral wave. The data and results for the simulation are presented in **Table 1**.

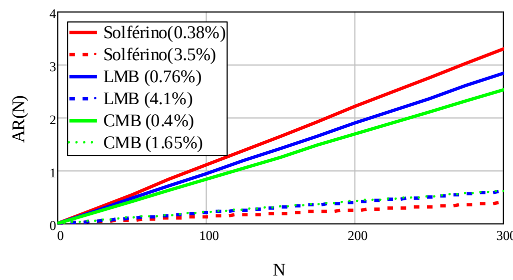

Figure 2. AR(N) 1st lateral mode Solférino Bridge, LMB and CMB for two damping states.

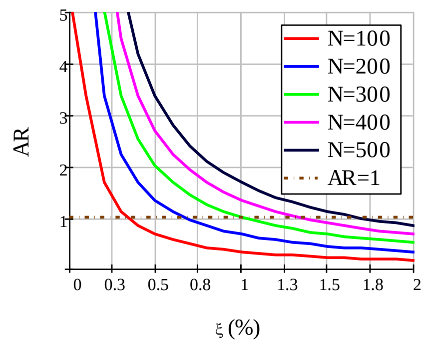

Figure 3: AR(ξ,N) 1st lateral mode of the CMB.

In order to consider the random character of pedestrian walking, a composition approaching the Normal Distribution (μ=0.86Hz, SD=0.08Hz) is considered: 38% pedestrians walking at μ Hz; 25% at (μ+/-SD) Hz, 6% at (μ+/-2SD) Hz. For every case, the structure ($2\pi f_b|H(f_b)|$) and pedestrian (C_{pm}) contributions to the response are calculated as well as the coefficient G, which is the gradient of the straight lines in **Figure 2.** Also, the number of pedestrians which would provoke 50% of response amplification and the corresponding a_{max}, considering initial amplitude of vibration of 4.5mm. The values can be compared with the comfort criterion according to Sétra (0.15-0.2m/s^2). **Figure 3** shows that expression (8) allows determining the damping ratio needed to prevent vibrations going over certain limit for a specific pedestrian traffic (N).

AR=1.5	LMB	Solfér. Bridge.	CMB	CMB (extra damp.)
fb (Hz)	0.5	0.81	0.9	0.9
M (ton)	129	400	453	454
ξ(%)	0.76	0.38	0.40	1.65
$2\pi f_b\lvert H(f_b)\rvert$ (m/Ns)	1.62 10^{-4}	6.46 10^{-5}	4.88 10^{-5}	1.18 10^{-5}
C_{pm} (Ns/m)	58	177	172	172
G (-)	9.45 10^{-3}	11.0 10^{-3}	8.40 10^{-3}	2.04 10^{-3}
N	159	131	178	**178**
N_{crit}(others)	165 [3]	140[2]	150[1]	--
a_{max} (m/s2)	0.07	0.18	0.22	**0.05**

Table 1. Numerical simulation: data and results.

4 CONCLUSION

- The analysis in the frequency domain evidences that people walking in a swaying deck are not only external loads. There is an interaction pedestrian-structure and harmonics in the bridge natural frequency appear.
- The dynamic response is controlled by the resonant component, as the other harmonics generate little amplification. Thus, it is considered accurate enough to evaluate the bridge response using only the resonant harmonic of the load.
- The resonant forces can be expressed by different ways. Since they are forces in phase with the velocity of the structure, it is possible to use the experimental damping coefficients c_p, [3], introducing the experimental results in the analytical formulation. Other possibility is to formulate the resonant amplitude directly from the analytical expression of the pedestrian load [4], providing it considers the pedestrian-structure interaction.
- These considerations lead to a simple formulation that permits either to evaluate the lateral response (a_{max}), as well as to define different vibration thresholds to different expected pedestrian scenarios and the damping requirements to fulfill all of them.
- The lateral response depends on the initial vibration u_o provoked by, for example, the static components of pedestrian force or the wind action.
- The precision of the results depends on how accurately the equivalent damping coefficient c_p represents the effects of the pedestrian action.

REFERENCES

[1] Brownjohn J., F. P. (2004). Long span pedestrian steel bridge at Singapore Changi airport-part 2. *The Structural Engineer 82 (16)*, 28-34.

[2] Charles, P., & Bui, V. (2005). Transversal dynamic actions of pedestrian syncronization. *Second International Conference, Venice.* Proceedings of footbridges 2005.

[3] Ingólfsson, E. T. (2011). Pedestrian-induced lateral vibrations of footbridges: experimental studies and probabilistic modelling. *DTU*, vol 231.p. 281.

[4] MacDonald, J. H. (2008). Lateral excitation of bridges by balancing pedestrians. *Proceedings of the Royal Society of London*, p. 19.

[5] McRobie, F. A. (2013). Long-term solutions of Macdonald´s model for pedestrian-induced lateral forces. *Journal of Sound and Vibration, vol. 332*(no. 11), pp. 2846–2855.

[6] Pizzimenti, A., & Ricciardelli, F. (2005). Experimental evaluation of the dynamic lateral loading of footbridges

by walking pedestrians. *Eurodyn 2005 – Sixth Eur. Conf. Struct. Dyn*.

1st Conference on Structural Dynamics (DinEst 2018)
Madrid, 20-21 June

DYNAMIC ANALYSIS OF A CULVERT-TYPE STRUCTURES IN HIGH SPEED LINES

Alberto Fraile*, Manuel F. Báez*, Javier Fernández †, Lutz Hermanns*

* ETS Ingenieros Industriales. Dpto. Ingeniería Mecánica
Universidad Politécnica de Madrid
28006 Madrid, Spain
e-mail: alberto.fraile@upm.es
ORCID: 0000-0001-9861-0728

† Centro de Modelado en Ingeniería Mecánica
Fundación para el Fomento de la Innovación Industrial
28006 Madrid, Spain

Abstract. Underpasses are low-cost solutions widely used in High Speed Lines (HSL) but their dynamic behavior has received far less attention than that of other structures such as bridges. Nonetheless, their frequent use makes their study an interesting challenge from the viewpoint of safety and cost savings. The dynamic characteristics differ from those of conventional bridges because the natural frequencies are significantly higher, typically in the range from 25 to 60 Hz, the mode shapes are not beam-like but plate-like and due to the soil-structure interaction the stiffness and damping properties are more complex.

The objective of this work is to present a new approximation with a simple and fast 3D method capable of estimating the dynamic behavior of culvert-type underpasses subjected to the dynamic loads induced by high-speed trains during normal operation. The aim of the method is to provide a cost-effective tool for the project engineers in order to obtain the dynamic solution of the problem.

Key words: Dynamic prediction model, Culvert-type structure, High-speed train, Experimental data.

1 INTRODUCTION

Some efforts have been developed to represent the dynamic behavior of these partially buried structures in order to simplify the problem and to propose an analytical approach [1, 2]. To calibrate the models presented in these papers, on-site measurements were performed for a group of underpass geometries belonging to the HSL between Segovia and Valladolid in Spain.

In the present paper, a new approximation with a simple and fast 3D method capable of estimating the dynamic behavior of culvert-type underpasses subjected to the dynamic loads induced by high speed trains during normal operation is presented. To this end, the same measurements have been used to validate the model and the results for the most common culvert type in the line (3 x 3 m) are presented.

2 NUMERICAL MODEL

The prediction method uses a sub-structuring approach to estimate the dynamic behavior of the underpass. The model has been divided in three sub-models i.e. emission, slab and sidewalls. The emission model is used to estimate the contact forces between the track and the culvert structure. The slab model is a combination of Kirchhoff plate theory and the Ritz method. For the sidewall model a finite-length beam on a viscoelastic foundation is used to address the soil structure interaction. The slab and sidewall models are coupled through compatibility relations at the shared edge for each shape function.

2.1 Emission model

The emission model is used to estimate the contact forces between the track and the culvert slab when a single train passes over the underpass. The model is formulated with the following assumptions: the vehicles are isolated by the primary suspension; consequently, the model includes only the moving unsprung mass of each axle and its static load. Wheel-rail contact is formulated with a Hertz contact model.

The railway superstructure is represented with a FE model: rails are modeled with Timoshenko beam elements, sleepers with point masses which are connected to the rails by 1D spring-dashpot elements and for the ballast, sub-ballast and subgrade layers again spring-dashpot elements are used.

Dynamic effects due to the wheel-rail irregularity are represented with rail surface profiles generated using a target power spectral density (PSD) which can be adjusted to match different maintenance levels. A classical approach to take into account this profile includes a balanced pair of forces acting on the wheel and rail nodes connected by each Hertz element.

To obtain the contact forces between the track and the culvert slab, a transient dynamic analysis is performed using the constant average acceleration time integration method. For this part of the analysis, the slab is considered as infinitely stiff support. Therefore, the emission model is completely decoupled from the rest of the model and can be run independently to generate a database considering different scenarios for rail surface profiles (maintenance level and/or PSD definition) and trains (train model and speed).

2.2 Structural culvert model

The structural culvert model combines the slab and the sidewall models by means of compatibility relations.

Slab model

The model is built using Kirchhoff's plate theory combined with the Ritz method: The displacement field is obtained adding the contributions of N shape functions,

$$w(x,y,t) = \sum_{n=1}^{N} \psi_n(x,y) \cdot \xi_n(t) \tag{1}$$

defined as a combination of sines in the x-direction (longitudinal direction following the railway track) and cosines in the y-direction (transversal):

$$\psi_n(x,y) = \sin\frac{i\pi x}{L}\cos\frac{j\pi y}{B}; \quad \begin{matrix} i = 1, 2, \ldots \\ j = 0, 1, \ldots \end{matrix} \tag{2}$$

where L and B are the span and the width of the culvert, respectively.

Figure 1 shows the shape functions for $i = 1$ to 3 and $j = 0$ to 2.

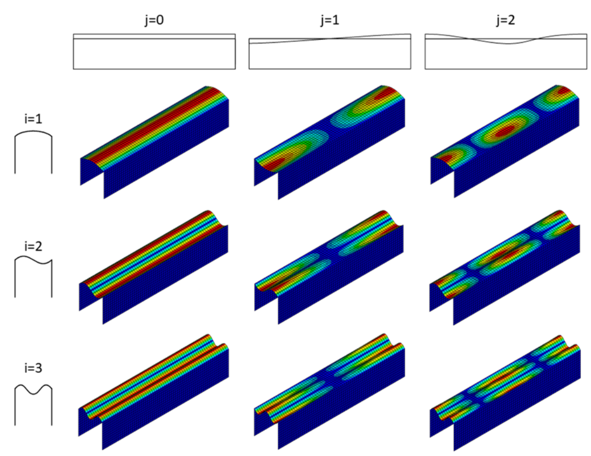

Figure 1: Slab shape functions

These shape functions assume a zero slopes at the free boundaries of the slab that, while being unrealistic, because of the length ratio L/B, have little impact on the results.

Due to the orthogonality of the chosen shape functions, the mass and stiffness matrices are diagonal:

$$\begin{aligned} M_{nn} &= mBL/2 \quad \text{if } j = 0 \\ M_{nn} &= mBL/4 \quad \text{if } j \neq 0 \end{aligned} \tag{3}$$

$$\begin{aligned} K_{nn} &= \frac{D\pi^4 i^4 B}{2L^3} \quad \text{if } j = 0 \\ K_{nn} &= \frac{D\pi^4 (j^2L^2 + i^2B^2)^2}{4B^3L^3} \quad \text{if } j \neq 0 \end{aligned} \tag{4}$$

where m is the mass per unit of surface and D is the bending stiffness of the plate:

$$D = \frac{Eh^3}{12(1-\nu^2)} \tag{5}$$

The structural damping matrix C has been built as a linear combination of the mass M and stiffness K matrices (Rayleigh damping).

Sidewall model

The wall is considered as several vertical unit-wide beams on viscoelastic foundation. The backfill soil is represented by a Kelvin-Voigt model that varies with the frequency as

$$k^* = k + i\omega c \tag{6}$$

where k and c are the stiffness and viscous damping coefficients of the spring per unit area. The differential equation governing the motion of the wall is:

$$EI\frac{d^4u}{dz^4} + \rho A\ddot{u} + k^*u = 0 \tag{7}$$

where u is the lateral displacement and E, I, A, ρ are elastic modulus, second moment of area, area and density of the wall.

The solution of this problem is documented in [3] and gives the dynamic stiffness $k_w(\omega)$:

$$\begin{aligned} k_w &= \frac{k_{ro}}{\beta(-C_1 s\beta + C_2 c\beta + C_3 sh\beta + C_4 ch\beta)} \\ s\beta &= \sin\beta\,; c\beta = \cos\beta \\ sh\beta &= \sinh\beta\,;\ ch\beta = \cosh\beta \end{aligned} \tag{8}$$

where $k_{ro} = EI/H$ is the reference stiffness and coefficients C_i have to be evaluated from:

$$\begin{bmatrix} -\beta^2 & \alpha_r\beta & \beta^2 & \alpha_r\beta \\ \alpha_h & \beta^3 & \alpha_h & -\beta^3 \\ c\beta & s\beta & ch\beta & sh\beta \\ -\beta^2 c\beta & -\beta^2 s\beta & \beta^2 ch\beta & \beta^2 sh\beta \end{bmatrix} \begin{Bmatrix} C_1 \\ C_2 \\ C_3 \\ C_4 \end{Bmatrix} = \begin{bmatrix} 0 \\ 0 \\ 0 \\ \frac{H^2}{EI} \end{bmatrix} \tag{9}$$

where

$$\alpha_r = \frac{K_r H}{EI};\ \alpha_h = \frac{K_h H^3}{EI};\ \beta = \left(\frac{-k^* H^4 + \rho A\omega^2 H^4}{EI}\right)^{\frac{1}{4}} \tag{10}$$

The frequency dependent rotational stiffness of the sidewalls $K_S(\omega)$ is evaluated considering the rotation around the y axis at the intersections of the slab and the sidewalls as:

$$\begin{aligned} Ks_{mn}(\omega) &= \\ &\int_0^B \left(\frac{d\psi_m(0,y)}{dx} k_w(\omega) \frac{d\psi_n(0,y)}{dx}\right) dy + \\ &\int_0^B \left(\frac{d\psi_m(L,y)}{dx} k_w(\omega) \frac{d\psi_n(L,y)}{dx}\right) dy \end{aligned} \tag{11}$$

The result is a frequency dependent total stiffness matrix obtained as the summation of the contributions of the slab and the sidewalls.

$$K_T(\omega) = K + K_S(\omega) \tag{12}$$

3 RESULTS

The model has been validated against on-site measurements from a box culvert of the HSL between Segovia and Valladolid in Spain [1, 2]. The structure has equal rise and span of 3 m and a width of 16 m. The slab and sidewalls thickness are 20 cm and are made of concrete ($E = 33$ GPa, $\upsilon = 0.2$ and $\rho = 2500\ \mathrm{kg/m^3}$). However, for the simulation the depth of the slab has been changed to 30 cm and the density to $8900\ \mathrm{kg/m^3}$ to account for the contribution of the railway track. The properties of the viscoelastic backfill are: $k = 50\ \mathrm{MN/m^3}$ and $c = 30\ \mathrm{kNs/m^3}$. A classical HS ballasted track is equipped with UIC-60 rails over a ballast layer 35 cm thick and a formation layer 60 cm thick. The first three mode shapes of the culvert are presented in Figure 2. As can be seen, the frequencies are very close together and the values are very high compared to those of typical railway bridges.

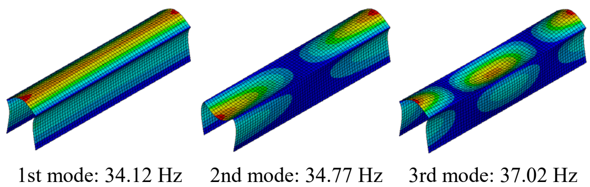

Figure 2: Culvert mode shapes

Several scenarios have been evaluated to match with in-situ data corresponding to trains S102, S121 and S130 travelling in both directions and with average speeds between 200 and 290 km/h. For the generation of rail surface profiles a well maintained track has been assumed. The solution of all trains going to Valladolid is presented in Figure 3. The Figure presents the one-third octave acceleration spectra, where the shaded area represents the envelope of the experimental data, whereas the scatter plot shows the numerical predictions.

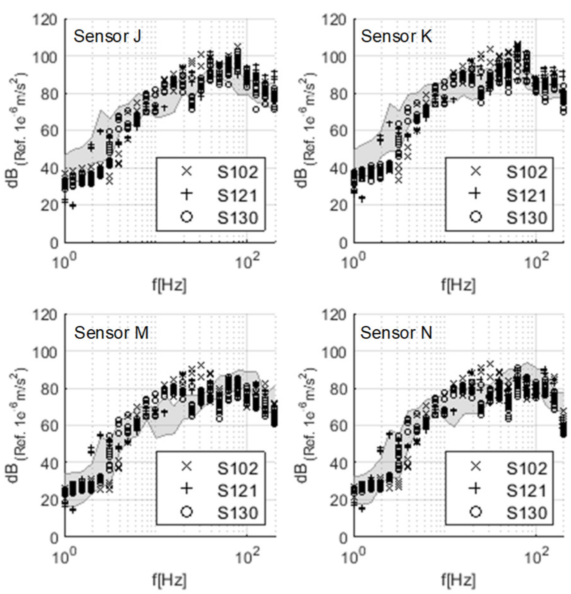

Figure 3: One-third octave acceleration spectra for trains traveling to Valladolid

Instrumented points are located at the slab midspan and half height of the sidewalls in three sections distributed along the culvert width. Sensors J and M correspond with the central section and K and N with the section closest to the travelled track.

The results show a good overall agreement between numerical and experimental data.

4 CONCLUSIONS

A vibration prediction model to estimate the structural response of the culvert structures is presented and calibrated to measurement data corresponding to an underpass of the Spanish HSL. In general, the agreement between numerical predictions and the experimental data is quite good.

The main advantage of the proposed model is its simplicity i.e. the input data has clear physical meaning and is easily available.

The dynamic characteristics of these structures differ from those of conventional bridges in terms of natural frequencies, mode shapes and the damping that is provided by the surrounding soil. For these reasons, resonant effects are not that important in this type of structures and small exceedances above the acceleration limits can occur without causing any ballast instability.

REFERENCES

[1] Vega J.; Hermanns L.; Alarcón E.; Fraile A. *Fórmulas para el cálculo del factor de impacto de estructuras semienterradas en líneas de ferrocarril de alta velocidad* RIMNI. Vol.30, Iss.3, pp 188–193. 2014.

[2] Alarcón E.; Fraile A.; Hermanns L.; Vega J.; Grande A.; Rodriguez V.; Corral A.; Santos J. *Guía para el cálculo de estructuras semienterradas en líneas ferroviarias* Doc. complementarios no contradictorios para la aplicación de los Eurocódigos para el cálculo de Puentes de Ferrocarril. Mo. Fomento. 2014.

[3] M. Saitoh. *Lumped parameter models representing impedance functions at the end of a finite beam on a viscoelastic medium* Computers and Structures, Vols. 92 - 93, pp. 317-327, 2012.

1st Conference on Structural Dynamics (DinEst 2018)
Madrid, 20-21 June

ANALYSIS OF THE LIFTING PROCESS OF BRIDGE SEGMENTS

Luis M. Lacoma, Javier Rodríguez, Francisco Martínez and Joaquín Martí

Principia
Velázquez 94
28006 Madrid, Spain
e-mail: luis.lacoma@principia.es

Abstract. The paper deals with the dynamics of the lifting of deck segments for constructing a bridge over water, with segments being brought by barge and lifted by an erection traveler while the barge and the bridge are undergoing the motions induced by the sea state and the wind. To investigate the process, a model was generated that included the barge and the mooring system, the supporting plinths, the bridge segment, the lateral restraints, the lifting strands, the erection traveler, and the bridge deck with its associated stiffnesses. Nearly 400 simulations were conducted, covering combinations of wave, wind, and current forces, as well as other aspects like the deck length and the cracked or uncracked state of the section. The analyses allowed establishing whether the success criteria were being satisfied, the influence of the various parameters, and the potentially more hazardous phases of the lifting process.

Key words: Bridges, Dynamics.

1 INTRODUCTION

The construction of a bridge over water, with segments being brought by barge and lifted into position, gives rise to complex dynamic phenomena. The segments are being lifted by cables while the barge and the bridge are undergoing the motions induced by the sea state and the wind. The authors were involved in conducting the necessary calculations, first for the bridge "Constitución de 1812" across the Bay of Cádiz and then for the Queensferry Crossing in Scotland. The present paper describes the problem, the methodology used and the results obtained for the latter bridge.

2 DESCRIPTION OF THE PROBLEM

2.1 Structural components

The barge may carry one or two bridge segments. Fig. 1 shows a view of the barge with two segments, a configuration termed S407; that with one segment is S408, and that with none is S414. Barge length is 91.5 m and beam is 24.4 m. The drafts forward and aft are a function of the configuration, as is the barge displacement and the location of its center of gravity.

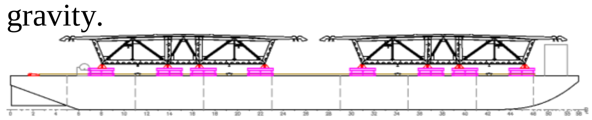

Figure 1: View of the barge with two bridge segments

During the lifting process the barge is moored with four lines. The stiffness and mass matrices representing the barge and its mooring system were determined by previous hydrodynamic simulations, as were the motions (during 1 h) caused by an uplift force of 7760 kN and a moment of 183 MNm. The Rayleigh damping coefficients were also estimated.

The supporting plinths for the segments and the restraint system are shown in Fig. 2. The segments have a weight of 792 t for the short and long deck, and 737 t for the medium deck. Their moments of inertia with respect to the three axes X, Y and Z are respectively 18.6, 95.9, and 120.0 (units are 10^3 t.m^2).

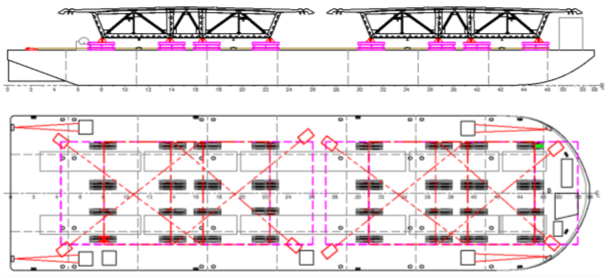

Figure 2: Segment support and restraint

Longitudinally, the plinths are centered 21.87 m from the bow; their offsets are +/- 2.55 m and +/- 13.10 m. Transversely, the plinths are centered on the barge centerline with offsets of 7.40 m, 1.25 m, -3.00 m, and -7.25 m, where positive refers to starboard and negative to port. The vertical stiffness of the plinths is 4878 kN/m. The restraint system is made of 36 mm diameter cables, with a stiffness times area of 62,000 kN, pretensioned to 10 t.

The lifting strands have an initial length of 72 m, diameter of 0.10 m and mass per unit length of 63.19 kg/m. Their stiffness times area is 1.55×10^6 kN. The lifting strands are connected 8.54 m above the top of the road segment, which corresponds to the height of the lifting tackle. The erection traveler has a weight of 730 kN. Its vertical stiffness is 10^5 kN/m and its rotational stiffness is 17.45 kNm/deg. Lifting takes place at a rate of 1 cm/s.

Three lengths of bridge deck are considered. The vertical stiffnesses are 155,560 kN/m for the short deck, 5720 kN/m for the medium deck, and 2410 kN/m for the long deck. The transverse stiffness is assumed infinite. The rotational stiffness depends on whether the section is taken as cracked or not: 69,813 kNm/deg for the uncracked section and 24,435 kNm/deg for the cracked section.

The equivalent concentrated mass at the cantilever end of the medium deck is 6485 t and 10,160 t in the case of the long deck. The dashpot constant governing energy dissipation was taken as 72 kNs/m.

2.2 Actions and acceptance criteria

The external actions considered arise from waves and winds. For waves, wave heights and periods were known at the site; given the operating envelope, the more significant scenarios were those of 0.05 m and 0.15 m waves with 2.5 s period, and that of 0.35 m waves with 3.5 s period. For wind, displacements and rotations were given for wind velocities up to 15 m/s for both the medium deck, with a 6.7 s period, and the long deck, with 12.5 s.

Some 400 simulations were conducted combining barge configurations (S407, S408, S414), wave heights and periods (0.05 m and 2.5 s, 0.15 m and 2.5 s, 0.35 m and 3.5 s), current headings with respect to the barge (150º, 180º, 210º), wind speeds (0 m/s, 4 m/s, 15 m/s), and deck lengths (short, medium and long).

The lifting process must satisfy: misalignment of supports below 50 mm in X direction and 300 mm in Y; plinth loads below 834 kN; uplift in erection traveler below 200 kN; dynamic load factor below 1.20; strand bundle load, when the other strand load is nil, below 750 kN; load in restraints below 500 kN; loads on strands below 5400 kN.

3 METHODOLOGY

To analyze the lifting process a model was generated (Fig. 3) that includes the barge and the effects of its mooring system, the plinths, the bridge segment, the lateral restraints, the lifting strands, the erection traveler, and the bridge deck with its associated stiffnesses.

The barge and its mooring system are represented with the corresponding mass and stiffness matrices. The transported segment is modelled with its mass and rotational moments of inertia. Truss elements are used for the lateral restraint system; the cables are active in tension but not in compression. Connector elements are used to model the plinths, with their compressional stiffness and damping. The barge is defined as a rigid body to which the plinths are attached. All the restraint cables have one end attached to the barge and the other to the segment being carried.

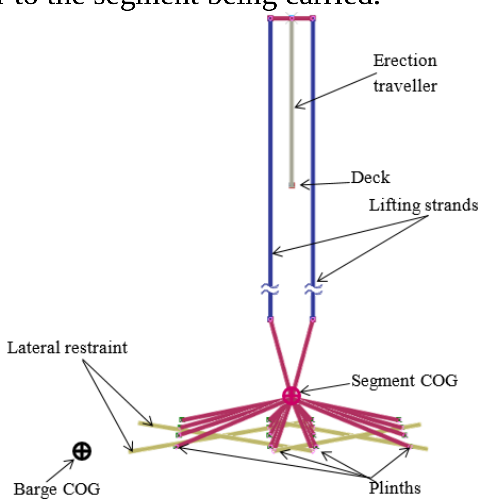

Figure 3: Schematic view of the model

The lifting strands are modelled with connector elements that allow lifting the segment by pulling up the strand. They are attached to the erection traveler, represented with a connector element with the appropriate stiffness. The erection traveler is also connected to the bridge deck, characterized with its stiffness, inertia, and damping, in respect of both translation and rotation. The deck is only allowed to translate vertically (Z direction) and to undergo torsional movements (rotation around the Y axis).

The external loads due to the waves are introduced at the center of gravity of the barge. The loads due to the wind are applied to the deck as concentrated loads.

After extracting the natural modes, the lifting process was studied. For this, the histories of the barge and bridge deck motions were converted into histories of forces, i.e.: the vertical displacements and the Y-rotations, whether caused by the waves or the wind. Those force histories, together with those of the other components of the motions, were introduced in the model and the time varying solution was obtained by implicit integration. The calculations proceeded for a duration equivalent to 1.5 times the separation time of the segment from the barge. The program used in the analyses was Abaqus (SIMULIA, 2014).

4 RESULTS AND DISCUSSION

The natural modes of the system were identified before any separations start to take place. This was done for the three deck lengths, for both uncracked and cracked sections. While the first mode corresponds to the rotation of the segment in the case of the short deck (0.226 Hz), for the medium and long decks it reflects the vertical translation of the deck (0.149 and 0.077 Hz, respectively).

Only the short deck results will be discussed. Two figures are provided as an example of the type of results obtained in the simulations. They correspond to an S408 configuration, with 0.35 m waves, 150º current, and cracked section in the bridge. Fig. 4 shows the forces in the lifting strands and Fig. 5 describes those in the support plinths.

A total of 12 simulations were conducted with 0.05 m waves for the short deck. The results allowed comparisons with all the acceptance criteria adopted; with this relatively small level of wave action, all the acceptance criteria are satisfied in all the cases analyzed. Additionally, 60 simulations were carried out for the same deck length when the wave height is increased to 0.15 m. Once again, all the acceptance criteria are satisfied. Finally, another 60 simulations were conducted for the same deck length when the wave height is increased to 0.35 m. Most of the acceptance criteria were again satisfied, except for the misalignment in the X direction; this parameter is in principle limited to 50 mm, a value that was exceeded in about 20% of the cases analyzed. The average value of the maxima, however, satisfies the limitation imposed. The uplift reaction at the erection traveler reaches a maximum value of 171.0 kN, lower but not too far from the limit of 200 kN. All the cases with the current at 180º satisfy all the conditions; the problems only arise with currents at 210º and 150º.

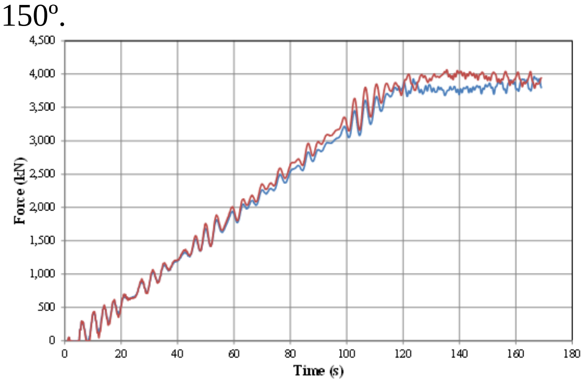

Figure 4: Forces in the strands for the long deck

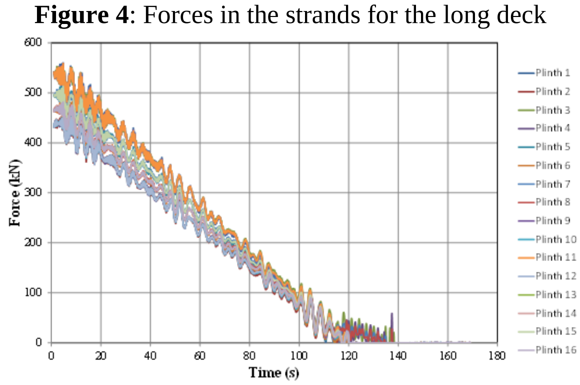

Figure 5: Forces in the plinths for the long deck

For the three deck lengths, a total of nearly 400 simulations were conducted, covering a large variety of operating conditions. All the acceptance criteria were satisfied in the large majority of them. The only exception is the misalignment in the X direction, with the 50-mm limit being exceeded in specific cases for the three deck lengths, with 0.35 m waves and misaligned currents (150º and 210º). It was presumed that this limit could be exceeded, given the large dimensions of the plinths. In any case the average of the maxima always satisfied the limit.

The 0.35 m wave height is rather demanding from other viewpoints as well. With those waves, the maximum uplift reaction at the erection traveler reached 199.4 kN in one of the simulations, with the allowable limit at 200 kN. Another significant observation is the role played by the direction of the current: no problems are experienced with the current at 180º, the extreme values arise for 210º and 150º. In comparison, the wind effects are relatively unimportant.

Finally, the more demanding phase of the lifting occurs when the segment is about to lose, or has just lost, contact with the barge. It is then that impacts and other undesirable effects can be triggered. Hence, this phase should be as brief as reasonably possible. Analyses performed halving the lifting rate to 0.5 cm/s, showed consistently worse results. Hence it may be advisable to forego balancing or other delays during this phase of the process.

5 CONCLUSIONS

As conclusions, practically all acceptance criteria are satisfied for all the combinations of parameters studied.

No problems are experienced with any of the criteria when the current is at 180º. The wind plays a relatively unimportant role within the range of conditions analyzed; the effect of the waves is far more significant.

The more critical phase is that in which the segment is about to lose, or has just lost, contact with the barge; this phase should be kept as brief as reasonably possible.

Finally, it must be highlighted that the lifting process operated without problems and the bridge was opened in September 2017.

REFERENCES

[1] SIMULIA (2014) "*Abaqus Analysis User's Guide*", Version 6.14.

1st. Conference on Structural Dynamics (DinEst 2018)
Madrid, 20–21 June

DYNAMIC LOAD MODELS FOR NEW OR EXISTING RAILWAY BRIDGES

José M. Goicolea*, **Khanh Nguyen***, **Carlos Velarde***, **Eduardo Barrios***

*ETS Ingenieros de Caminos, Canales y Puertos
Universidad Politécnica de Madrid
28040 Madrid, Spain

e-mail: jose.goicolea@upm.es ORCID: 0000-0003-0328-7345

Abstract. The dynamic response of railway bridges is a significant action to be considered in the design and evaluation of their performance, specially for high speeds. Design requirements have been included in the codes EN1991-2:2003, EN15528:2015. These requirements include verification of dynamic amplification factors as well as maximum accelerations experienced at the bridge deck. A high Speed Load Model (HSLM) was adopted in Europe in the late 1990's (ERRI D214, 1999). Relevant research publications include contributions by Fryba (1996), Yang et al (2004), Xia et al (2012).

In the last years new models of HS trains have been developed, and there is concern as to whether these are covered by the existing HSLM model. Furthermore, a wider range of new Multiple Unit (MU) trains are in operation at maximum speeds between 160 and 250 km/h which are also not covered explicitly by HSLM. Finally, new railway interoperability requirements in Europe prescribe the need for dynamic checks for passenger traffic exceeding 160 km/h in existing as well as new lines.

In this paper we discuss fast models for parametric dynamic analysis with the objective of performing a first check on the dynamic performance of the bridges in a given railway line. We discuss the load models to consider as well as the modelling options. The Dynamic models are based on beam models for the bridge deck and modal analysis under moving loads.

We also discuss further the results based on more realistic 3D FE models for different structural types, and their comparison with the 2D models.

Key words: railway, bridges, dynamics, moving loads, load models.

SECTION 4: Computational dynamics

1st. Conference on Structural Dynamics (DinEst 2018)
Madrid, 20–21 June

MESHFREE MODELING OF DYNAMIC FRACTURE IN FIBRE REINFORCED CONCRETE

Rena C. Yu*, **Pedro Navas and Gonzalo Ruiz**

ETS Ingenieros de Caminos, Canales y Puertos
Universidad de Castilla-La Mancha
13071 Ciudad Real, Spain

*e-mail: rena@uclm.es
ORCID: 0000-0003-4176-0324

Abstract. This work is concerned with the numerical study of dynamic mixed-mode fracture in fiber reinforced concrete (FRC). A recently developed eigensoftening algorithm to deal with the fracture of quasi-brittle materials is employed in a meshfree framework. In particular, the optimal transportation meshfree method, an updated Lagrangian numerical scheme that combines concepts from optimal transportation theory with a material-point sampling and the local max-ent meshfree approximation, is used. The eigensoftening approach to fracture engineered for the gradual dissipation of the fracture energy in quasi-brittle materials such as concrete, is employed. Three point bending tests on notched beams reinforced with steel fibers carried out through a drop weight device at two loading velocities are modelled herein. Since the notch was placed with an offset from the middle section, mixed-mode crack formation was facilitated. Three types of concrete with the same matrix reinforced with different amounts of steel fibers were used for these beams. The numerical simulations reproduced remarkably well the experimental results such as load-line displacements, crack patterns and reaction forces.

Key words: Meshfree, Eigensoftening, Dynamic mixed-mode fracture.

1 INTRODUCTION

In order to avoid the shear or punching failure in structural elements when dynamic effects such as seismic loads, impact or explosions are involved, it is essential to know how cracks initiate and propagate in the presence of both normal and tangential stresses. In other words, the knowledge on how mixed-mode fracture forms and grows is crucial. Compared to concrete reinforced with rebars, fiber reinforced concrete (FRC) is particularly adequate to resist dynamic actions due to its elevated ductility and great capacity to dissipate energy during fracture. Indeed, FRC is more and more employed in civil engineering structures. However, the studies on this topic are scarce. In this work, we take on this task in exploring the dynamic mixed-mode fracture in FRC. A recently developed eigensoftening algorithm to deal with the fracture of quasi-brittle materials is employed [4] within a meshfree framework [3]. The methodology is validated against experimental results obtained by Almeida et al. [2].

The rest of the paper is organised as follows. In Section 2, the experimental observations are described. In Section 3, the eigenesoftening approach is explained. Section 4 will provide the discussion of the computational results and Section 5 will present summary and conclusions.

2 EXPERIMENTAL OBSERVATIONS

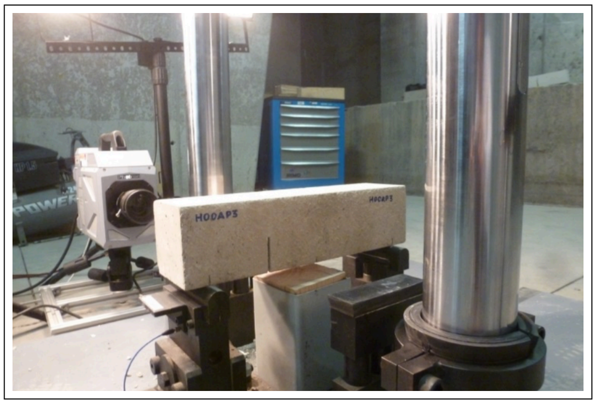

Figure 1: The drop-weight machine designed at the Laboratory of Materials and Structures, University of Castilla-La Mancha and the mixed-mode specimen.

In order to further explore the capacities of the developed eigensoftening algorithm, the experimental results on mixed-mode fracture [2] are modeled. The same drop-weight impact instrument employed for the mode-I case [6] (see Fig. 1), designed and constructed in the Laboratory of Materials and Structures at the University of Castilla-La Mancha, is utilized in the assessment of the mix-mode crack patterns. Three-point bending tests on notched beams are studied, in this case the notch is located with an offset of a quarter span from the middle section. An impact hammer of 120.6 kg was employed to drop from two different heights, 360 and 160 mm with the corresponding impact speeds of 2640 and 1760 mm/s respectively. The impact force is measured by a piezoelectric force sensor and the reaction force is determined by two force sensors located between the support and the specimen. The beam dimensions were 100 mm×100 mm in cross section, and 400 mm in total length. The initial notch-depth ratio was approximately 0.5, and the span was fixed at 333 mm.

The material was characterized with independent tests and the measured material properties for the base concrete, H00, are as follows, the compressive strength, f_c=31.6 MPa, the tensile strength, f_t=3.1 MPa, the specific fracture energy, $G_F = 87$ N/m, the elastic modulus, E=18.5 GPa and the Poisson's ratio, 0.17. The material density, ρ is of 2310 kg/m^3. The maximum aggregate size, d, is 12 mm. The two FRCs, H15 and H45, were made with the same matrix (the base concrete), but reinforced with steel fibers of 15 and 45 kg/m^3, respectively. The fibers were of 30 mm in length, 0.55mm in diameter.

3 THE NUMERICAL METHODOLOGY

For completeness, we summarize the basics of the eigensoftening algorithm to treat fracture within the meshfree framework. The Optimal Transportation Meshfree (OTM) framework can be referred to by the work of Li et al. [3].

3.1 Eigenerosion algorithm

Within the context of OTM formulation, fracture can be modeled simply by failing material points according to an energy-release criterion. When the material points are completely failed, they are neglected from the computation of stresses in the model, which approximates the presence of cracks, this is the so-called eigen-erosion algorithm developed by Pandolfi et al. [5]. However, the quasi-brittle behavior, which is typical of concrete, shows a softening process after the initiation of the crack. Thus, the eigensoftening algorithm [4] is more proper to reproduce such behavior.

The implementation is based on a strength criterion for the crack initiation subsequently followed by a softening law for propagation. For the stress measurement, the maximum principal stress theory is considered for brittle fracture at time t_{k+1} for the material point q. Consequently, the definition of an equivalent critical stress at the material point $x_{p,k+1}$ for a B_ϵ neighborhood can be calculated as follows

$$\sigma_p^\epsilon = \frac{1}{m_p} \sum_{x_q \in B_\epsilon(x_p)} m_q \sigma_{q,1} \tag{1}$$

where

$$m_p = \sum_{x_q \in B_\epsilon(x_p)} m_q. \tag{2}$$

The softening process is governed by the traction-crack opening displacement relation, often termed as a cohesive law. For the eigensoftening algorithm, a length scale, h^ϵ is defined, with a reference value between two and four times the maximum size of the aggregates for concrete (see Bažant [1]). The effective fracture strain, ε_f^ϵ, defined as the difference between the strain at crack initiation, $\varepsilon_1(x_{p,0})$, and the current strain, $\varepsilon_1(x_{p,k+1})$, for material point p, can be represented as the relationship between the current crack opening displacement, w, and the band width, h^ϵ,

$$\varepsilon_f^\epsilon = \varepsilon_1(x_{p,k+1}) - \varepsilon_1(x_{p,0}) = \frac{w}{h^\epsilon}. \tag{3}$$

The definition of the remanent stress σ and the damage χ depending on the crack opening w is defined for a linear softening relation,

$$\begin{aligned} \sigma(w) &= f_t\left(1 - \frac{w}{\alpha w_c}\right) \\ \chi(w) &= \frac{h^\epsilon \varepsilon_f^\epsilon}{\alpha w_c} \end{aligned}$$

where w_c the critical opening displacement of the base concrete, calculated as $w_c = 2G_F/f_t$, whereas α is the amplification factor of the fracture energy for FRC with respect to that of the base concrete.

It needs to be pointed out that when a material point is totally eroded its contribution to the internal force vector and to the material stiffness matrix is set to zero, but its contribution to the mass matrix is maintained, being only discarded when it is not connected to any nodes.

4 NUMERICAL RESULTS

The above methodology is applied herein to simulate the dynamic fracture propagation in a three-point bend beam with a notch located in the middle of the semi-span impacted by a drop-weight device. Both the projectile (the hammer) and the target (the concrete beam) are explicitly represented. The results are obtained in a 2D setting with a discretization of 2001 nodes, 3744 material points, and a nodal spacing of approximately 2 mm between the notch tip and the impact point, 4 mm between the impact point and the middle section at the bottom of the beam. These were expected locations of the cracks.

First we validate the computations with the load-line displacement against their experimental counterpart. Next, the reaction forces for different cohesive laws are depicted. Finally, the crack front evolution for these cases is compared with the observed one in the laboratory.

4.1 Load-line displacement and reaction forces

The recorded impact-line displacement contrasted with the numerical one is correctly captured for both studied velocities, see Fig. 2. Note that in the beginning, there is a small gap between the beam and the hammer. Once the hammer reached the beam they advanced with the same speed. However there is a final stage where the beam moved forward faster than the hammer. In addition, the time when the displacement of both the hammer and the beam top is coincident, around 0.5 ms, concurres with the time when the peak reaction forces were reached. Plots show the typical dynamic delay between the time of the first detection of the motion of the beam and the time when reaction forces were recorded.

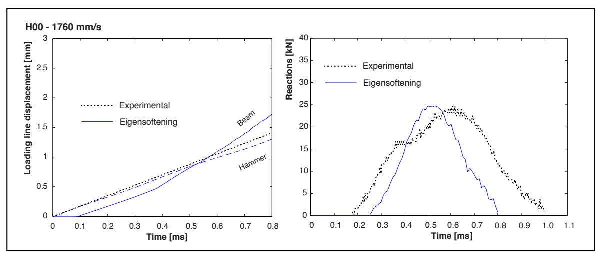

Figure 2: Comparison between experimental and computational impact-line displacement and reaction forces for H00, impact velocity of 1760 mm/s.

4.2 Crack propagation

In Fig. 3, the crack patterns observed experimentally are compared with the numerical ones obtained with linear or bilinear softening relations for H15 impacted at both velocities. Note that for the crack initiated from the crack tip, similar trajectories are obtained for both linear and bilinear relations. However, the bilinear softening relation does facilitate the formation of diffused micro cracks at the middle section, even though they did not coalesce into a main crack in the end. Unfortunately, this kind of micro cracks are not perceivable for a naked eye. Advanced experimental techniques such as Computed Tomography scan would help to discern the existence of this kind of micro cracks.

In Fig. 4, the influence of the notch position is demonstrated. Note that when the notch is moved away from the mid section, for the base concrete H00, the crack patterns changed from a single crack initiated from the notch tip (diagonal tension failure), two cracks (one flexural, one shear), to one main flexural crack with two arrested branches from the notch tip; for H15 and H45, the dominated failure moved from shear to flexural with arrested branches from the notch tip, without passing the stage where two main cracks were developed simultaneously.

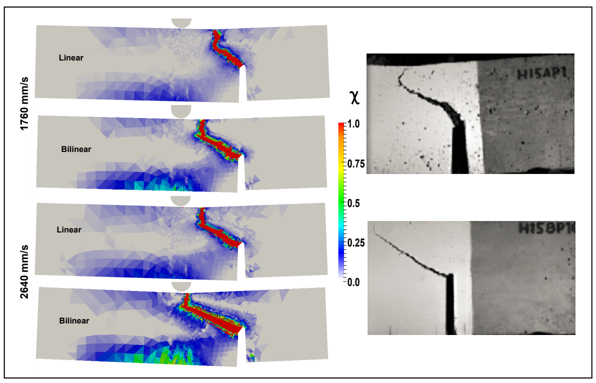

Figure 3: Comparison of the numerical and experimental crack patterns for H15.

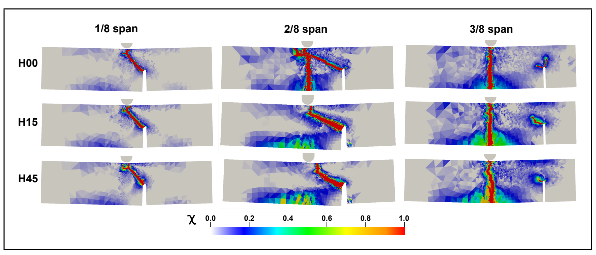

Figure 4: Crack patterns obtained with different locations of the notch, impact velocity at 2640 mm/s.

5 CONCLUSIONS AND FUTURE WORK

We have applied the Optimal Transportation Meshfree scheme and the eigensoftening algorithm to simulate the dynamic mixed-mode fracture propagation in fiber reinforced concrete. The results demonstrate that the eigensoftening algorithm is feasible for reproducing dynamic fracture. With correctly calibrated softening relations, it is highly predictive for both reaction forces and crack patterns. It is particularly noteworthy that, thanks to the intrinsic time parameter, similar to that of the cohesive theories of fracture, the model is able to capture dynamic events with static material properties.

6 ACKNOWLEDGMENTS

Financial support from the *Ministerio de Ciencia e Innovación*, under Grant Number BIA2015-68678-C2-1-R is greatly appreciated.

REFERENCES

[1] Z. P. Bažant and J. Planas. *Fracture and size effect in concrete and other quasi-brittle materials*. New directions in Civil Engineering, CRC Press, Boca Raton, Florida, USA, 1998.

[2] L. C. de Almeida, A. de la Rosa, G. Ruiz, E. Poveda, X. X. Zhang, and M. Tarifa. Fractura dinámica en modo mixto de hormigón autocompactante reforzado con fibras de acero. *Anales de la Mecánica de la Fractura*, 34:242–249, 2017.

[3] B. Li, F. Habbal, and M. Ortiz. Optimal transportation meshfree approximation schemes for fluid and plastic flows. *International Journal for Numerical Methods in Engineering*, 83:1541–1579, 2010.

[4] P. Navas, R. C. Yu, B. Li, and G. Ruiz. Modeling the dynamic fracture in concrete: an eigensoftening meshfree approach. *International Journal of Impact Engineering*, 113:9–20, 2018.

[5] A. Pandolfi and M. Ortiz. An eigenerosion approach to brittle fracture. *International Journal for Numerical Methods in Engineering*, 92:694–714, 2012.

[6] X. X. Zhang, G. Ruiz, and R. C. Yu. A new drop-weight impact machine for studying fracture processes in structural concrete. *Strain*, 46(3):252–257, 2010.

1st Conference on Structural Dynamics (DinEst 2018)
Madrid, 20-21 June

DYNAMIC ANALYSIS PERFORMED BY COMMERCIAL SOFTWARE

J. Pereiro-Barceló*

* Structural Engineer, Ph.D.
CYPE Ingenieros S.A.
Eusebio Sempere Avenue, 5 - 03003 Alicante, Spain
e-mail: javier.pereiro@cype.com

Abstract. The earthquakes have always worried humanity because of its devastating effects on structures. For this reason, the methods of the design codes have evolved remarkably. Currently, the main codes, such as Eurocode 8, allow performing two different types of calculations to design the structure against seismic loads: spectral modal analysis and dynamic analysis with time-integration (use of accelerograms). Most of the software used to design buildings employs spectral modal analysis, and this is what the CYPE structural design programs use (CYPECAD and CYPE3D). This article describes the analytical procedure to perform seismic analysis in these programs. In addition, CYPE has a new suite of structure design programs: StruBIM. StruBIM Suite is formed by StruBIM Analysis, StruBIM Design and StruBIM Foundations. These programs are in charge of analyzing, designing and checking structures, including their foundations, within a BIM workflow. This suite has integrated OpenSees as calculation engine. OpenSees is a well-known framework to perform linear or non-linear analysis, developed at the University of California, Berkeley. Its use is extended all over the world and allows users to create both serial and parallel analysis to simulate the response of structural and geotechnical systems subjected to earthquakes and other hazards. OpenSees will change how StruBIM performs dynamic analysis in the near future, which will include not only spectral modal analysis but also time integration dynamic analysis and non-linearity behavior. All these aspects will be shown in the article.

Keywords: Dynamics, OpenSees, CYPE.

1 INTRODUCTION

Structures subjected to an earthquake must bear high loads and its deformation capacity is essential to redistribute forces and dissipate energy. Several methods were developed to analyze structures against seismic loading. Two of the more used and widespread are response spectral analysis and time-integration dynamic analysis. Both of them are applicable according to main design codes such as Eurocode 8 [1] and ACI [2]. The two methods are very difficult to use without a computer tool, due to the high number of calculations to perform with the typical magnitude of actual buildings or civil structures. Consequently, several commercial computer programs to design structures incorporated seismic design, among them, CYPECAD and CYPE3D. In addition, CYPE S.A. has a new suite of structure design programs: StruBIM. StruBIM Suite is formed by StruBIM Analysis [7], StruBIM Design and StruBIM Foundations. These programs are in charge of analyzing, designing and checking structures, including their foundations, respectively, into a BIM workflow.

OpenSees [3] has been integrated in StruBIM as its calculation engine. OpenSees [3] is a well-known framework to perform linear or non-linear analysis, developed at

University of California, Berkeley. Its use is widespread all over the world and it allows users to create both serial and parallel finite element computer applications for simulating the response of structural and geotechnical systems subjected to earthquakes and other hazards.

OpenSees [3] is primarily written in C++ and uses several Fortran and C numerical libraries for linear equation solving, and material and element routines.

The objectives of this article are: (1) describe the analytical procedure to perform seismic analysis using StruBIM with OpenSees [3] as calculation engine, (2) show the future of seismic analysis in StruBIM.

2 ANALYTICAL PROCEDURE

CYPECAD and CYPE3D uses response spectral analysis. This method is based on computing just the maximum response of structure in each mode of vibration up to reach a percentage of activated mass above a limit.

Based on the free vibration equation of linear systems (1) and the modal expansion (2), the characteristic equation of the structure is obtained (3). The solution of this matrix equation gives the natural frequency of the structure in each mode (eigenvalues) and the modes (eigenvectors) [4,5]. Then, CYPECAD and CYPE3D gets the displacements in the dynamic degrees of freedom. They are deduced by considering the complete dynamic equation (4), the modal expansion (2) and the response spectral spectrum.

$$[M]\{\ddot{U}\} + [K]\{U\} = \{0\} \tag{1}$$

where:

$[M]$: Mass matrix
$[K]$: Stiffness matrix
$\{U\}$: Vector of displacement of degrees of freedom (DOFs)
$\{\ddot{U}\}$: Vector of acceleration of DOFs

$$\{U\} = \{\varphi\}\{q\} \tag{2}$$

$$\left[[K] - \{\omega\}^2[M]\right]\{\varphi\} = \{0\} \tag{3}$$

$$[M]\{\ddot{U}\} + [C]\{\dot{U}\} + [K]\{U\} = -[M]\{\ddot{U}_g\} \tag{4}$$

where:

$\{\varphi\}$: Eigenvectors
$\{q\}$: Modal coordinates
$\{\omega\}$: Natural frequency of vibration
$\{\ddot{U}_g\}$: Ground acceleration

In order to obtain the total response of the structure, the modal and the directional combinations are used. CQC [6] and weighted sum are adopted respectively.

The sectional forces obtained by using the previous combinations rules are not concomitants. For instance, the axial force is not concomitant neither the shear nor the bending moment. For this reason, CYPECAD and CYPE3D employ the modal expansion to calculate the concomitant sectional forces between each other.

The percentage of the mass, which is activated in each mode, is calculated with expression (5). Modes with the highest period are computed firstly.

$$\%M_{dir,i} = \frac{\left(\{\varphi_i\}^T \cdot [M] \cdot \{U_{b,dir}\}\right)^2}{\{\varphi_i\}^T \cdot [M] \cdot \{\varphi_i\}} \frac{100}{M_{total,dir}} \tag{5}$$

where:

$\%M_{dir,i}$: Percentage of activated mass in the "dir" direction for the ith mode.
$\{U_{b,dir}\}$: Vector with value "1" in the components of the "dir" direction and 0 in the rest.
$M_{total,dir}$: Total mass in the "dir" direction.

The dynamic degrees of freedom that CYPECAD considers are three per story: U_x, U_y and θ_z. Hence, all degrees of freedom are dynamically condensed in the mass center of each story. Then, the displacements calculated in the mass center with the spectral modal analysis are transferred to the rest of the nodes of the story considering the slab is rigid. For this, the stiffness center was previously computed.

On the other hand, CYPE3D considers that translational degrees of freedom in directions x and y as dynamics. Therefore, the number of dynamic DOFs is usually much bigger than in CYPECAD.

4 NON-STRUCTURAL ELEMENTS AGAINST HORIZONTAL LOADS

The façades and partitions of the building are considered as being "non-structural" elements. However, during an earthquake they do provide stiffness to the structure; hence they modify the distribution and magnitude of the forces caused by the seismic action. For example, when the stiffness has a non-uniform distribution between floors associated with the partitions, the horizontal forces have a greater impact on the columns belonging to the floors with less stiffness, producing shear forces of a high magnitude in the columns. If columns have not been designed accordingly, the forces can cause a fragile fracture, endangering the stability of the building, even leading to its collapse.

CYPECAD allows users to verify the behavior of the structure in different situations, by automatically generating design models that consider how the stiffness of the non-structural elements varies. The module verifies the behavior of the structure without partitions or façades, with all of them, considers intermediate states, and designs each resistant element for the worst-case situation. This way guarantees the correct response of the structure during an earthquake.

The non-structural elements are modeled as diagonal trusses within the frames. The load they transmit is diminished by a damage parameter, which depends on the relative horizontal displacements between two consecutive floors. This is computed by an iterative calculation process because the damage parameter means a non-linear process.

5 STRUBIM ANALYSIS

StruBIM Analysis [7] is a new program developed by CYPE S.A., which calculates the displacements and sectional forces of the structure. OpenSees [3] has been integrated in StruBIM Analysis [7] as its calculation engine.

4.1 Response spectral analysis

In near future, StruBIM Analysis [7] will perform response spectral analysis. The dynamic DOFs will be all translational ones (U_x, U_y and U_z). Therefore, vertical response will be computed. Besides, when a story is modeled as a rigid diaphragm, a dynamic condensation of U_x, U_y and θ_z DOFs is made. Consequently, just three DOFs per floor have the mass that will be horizontally activated. Vertical mass continues being distributed in all nodes of the story whether it is modeled as diaphragm or not.

The modal combinations that can be used will be: Absolut sum, SRSS [8], CQC [6], Double Sum [9] and GMC [10]. The directional combinations will be: Absolut sum, CQC3 [11], SRSS [8] and weighted sum.

4.2 Time-integration analysis

StruBIM Analysis [7] will also allow to perform time-integration analysis by using accelerograms thanks to the calculation power of OpenSees [3]. It will solve the complete dynamic equation (4) in every instant using Newmark method.

In order to account for the deformation capacity of structures in the time-integration analysis, non-linear calculations will be made in StruBIM Analysis [7]. Plastic hinges will be defined in parts of the structure by either providing a moment – curvature diagram or a cross section (the moment – curvature diagram will be computed automatically). Moreover, distributed non-linearity and soil-structure interaction will be considered.

5 CONCLUSIONS

- CYPECAD and CYPE3D uses CQC modal combination and weighted sum as directional combination. Both calculates the concomitant sectional forces of a determined modal and directional-combined sectional response by using modal expansion theory.
- CYPECAD considers three dynamic DOFs per floor (U_x, U_y and θ_z) and considers the non-structural elements in seismic calculations. The façades or partitions are considered as a truss: the more degraded it is the less load can bear.
- CYPE3D considers two horizontal dynamic DOFs per node (U_x, U_y).
- StruBIM Analysis [7] incorporates OpenSees [3] as calculation engine. It will consider three dynamic DOFs per node (U_x, U_y, U_z) unless diaphragm condition is imposed in a determined story. In this case, StruBIM Analysis [7] will condense all DOFs of this story in the mass center (except U_z DOF).
- StruBIM Analysis [7] will include non-linear features such as the possibility of inserting plastic hinges, distributed non-linearity and soil-structure interaction.
- StruBIM Analysis [7] will perform time-integration analysis with accelerograms.

REFERENCES

[1] Code P. Eurocode 8: Design of structures for earthquake resistance-Part 1: General rules, seismic actions and rules for buildings 2005.

[2] ACI Committee 318. ACI 318-14: Building Code Requirements for Structural Concrete and Commentary. 2014.

[3] McKenna F, Fenves GL, Filippou FC. OpenSees. University of California, Berkeley: n.d.

[4] Chopra AK. Dynamics of Structures: Theory and Applications to Earthquake Engineering. Pearson/Prentice Hall; 2007.

[5] Barbat AH, Canet JM, Miquel J, Enginyeria UP de CCI de MN en. Estructuras sometidas a acciones sísmicas: cálculo por ordenador. Centro Internacional de Métodos Numéricos en Ingeniería; 1994.

[6] Wilson EL, Kiureghian AD, Bayo EP. A replacement for the SRSS method in seismic analysis. Earthq Eng Struct Dyn 1981;9:187–92. doi:10.1002/eqe.4290090207.

[7] StruBIM Analysis. Alicante, Spain: CYPE Ingenieros, S.A.; 2018.

[8] Rosenblueth E. A basis for a seismic design of structures. The University, 1951.

[9] Gupta AP, Cordero K. Combination of Modal Responses. vol. K7/15, Paris: 1981.

[10] Gupta AP. Response Spectrum Method in Seismic Analysis and Design of Structures. Blackwell Scientific Publications, Inc.; 1990.

[11] Menun C, Der Kiureghian A. A Replacement for the 30%, 40%, and SRSS Rules for Multicomponent Seismic Analysis. Earthq Spectra 1998;14:153–63. doi:10.1193/1.1585993.

1st. Conference on Structural Dynamics (DinEst 2018)
Madrid, 20–21 June

GENERAL MULTI-REGION BEM-FEM MODEL FOR FLUID/SOIL AND SHELL INTERACTION PROBLEMS

Jacob D. R. Bordón, Juan J. Aznárez and Orlando F. Maeso

Instituto Universitario de Sistemas Inteligentes y Aplicaciones Numéricas en Ingeniería
Universidad de Las Palmas de Gran Canaria
35017 Las Palmas de Gran Canaria, Spain

e-mail: jacobdavid.rodriguezbordon@ulpgc.es
ORCID: 0000-0001-5820-2527

Abstract. In this contribution, we present a general multi-region boundary element and finite element dynamic model for fluid and/or soil interacting with shell structures. Shell structures can be surrounded by any combination of regions among inviscid fluids, elastic solids or poroelastic media. An approach based on Hypersingular Boundary Integral Equations is used when dealing with open shell structures. This idea avoids any superfluous subregioning of the problem, which leads to a natural, direct and efficient treatment of such structures. The use of this model is demonstrated through a fluid/soil-structure interaction problem.

Key words: boundary element, finite element, hypersingular formulation, shell structures, soil-structure interaction, fluid-structure interaction

1 INTRODUCTION

The Finite Element Method (FEM) and the Boundary Element Method (BEM) are well known numerical methods for the dynamic analysis of solid and structural mechanics problems. However, there are problems where neither of these are capable of solving these problems in a natural and efficient manner. The main advantages of the FEM are its versatility in handling structural members. However, when unbounded domains are present in a wave propagation problem, it requires a truncation of the volume mesh and the presence of some absorbing device to impose the Sommerfeld radiation condition. In that sense, the BEM is more appealing as it intrinsically satisfies the radiation condition [9].

In the present proposed model, both numerical methods are combined in order to solve three-dimensional linear Fluid-Structure and Soil-Structure Interaction problems, where the fluid is inviscid, the soil can be an isotropic and homogeneous elastic solid or a Biot poroelastic medium [4], and the structure is an elastic shell structure immersed or buried in such types of surrounding media. The main difference to other BEM-FEM models is its ability to deal with open shell structures, where both shell faces are in contact with the same region, in a natural and efficient way by resorting to the Hypersingular Boundary Integral Equation (HBIE) [6, 7, 8]. The Singular Boundary Integral Equation (SBIE) alone solves the other two situations: shells in contact with fluid or soil only on one face, and shells in contact with different fluids and/or soils on each face. Fig. 1 illustrates all three previously described situations. In the present research, the model from [8] is generalized and used in a illustrative example.

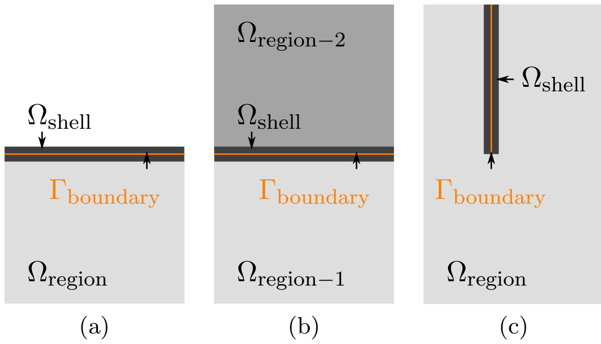

Figure 1: Shell interaction with surrounding media: (a) one-face interaction, (b) two-faces interaction with different regions, and (c) two-faces interaction with one region.

2 METHODOLOGY

The model is based on an appropriate combination of BEM and FEM equations.

BEM equations for fluid and soil regions are obtained from the discretization of Boundary Integral Equations (BIE) that relate primary and secondary variables throughout domain boundaries to variables at the collocation point where the point load (fundamental solution or Green's function) is applied. Let Ω be a region, and $\Gamma = \partial\Omega$ its boundary with outward unit normal $\mathbf{n}$. For a collocation point $\mathbf{x}^{\text{i}} \in \Omega$, the SBIE and the HBIE are respectively [10]:

$$u_l^{\text{i}} + \int_\Gamma t_{lk}^* u_k \, \mathrm{d}\Gamma = \int_\Gamma u_{lk}^* t_k \, \mathrm{d}\Gamma \tag{1}$$

$$t_l^{\text{i}} + \int_\Gamma s_{lk}^* u_k \, \mathrm{d}\Gamma = \int_\Gamma d_{lk}^* t_k \, \mathrm{d}\Gamma \tag{2}$$

where body loads have been neglected, and an elastic region is assumed in the following for the sake of brevity. u_k and $t_k = \sigma_{kj} n_j$ denote displacement and traction components respectively, u_k^{i} and t_k^{i} represent their value at the collocation point, and u_{lk}^*, t_{lk}^*, s_{lk}^* and d_{lk}^* are the fundamental solutions. For inviscid fluids and poroelastic soils, these can be found in [9, 10, 8, 5]. These equations contain only regular integrals, and they are useful at a post-processing stage for determining displacements and stresses at internal points. In order to obtain boundary displacements and tractions at boundaries, it is necessary to collocate these at a boundary point $\mathbf{x}^{\text{i}} \in \Gamma$, which results in the following regularized BIEs:

$$\frac{1}{2} u_l^{\text{i}} + \fint_\Gamma t_{lk}^* u_k \, \mathrm{d}\Gamma = \int_\Gamma u_{lk}^* t_k \, \mathrm{d}\Gamma \tag{3}$$

$$\frac{1}{2} t_l^{\text{i}} + \fint\!\!\!\!-_\Gamma s_{lk}^* u_k \, \mathrm{d}\Gamma = \fint_\Gamma d_{lk}^* t_k \, \mathrm{d}\Gamma \tag{4}$$

where a smooth boundary at the collocation point is assumed $\Gamma(\mathbf{x}^{\text{i}}) \in \mathcal{C}^1$ for the sake of simplicity. Regularized BIEs are obtaining after a regularization process which reduces Cauchy Principal Value ($\fint$, CPV) and Hadamard Finite Part ($\fint\!\!\!\!-$, HFP) integrals into regular and weakly singular integrals, which can be found in [10, 8]. The SBIE are used for exterior boundaries and interfaces between regions, and also when coupling with shells located at those (Figs. 1(a) and 1(b)). The use of the regularized HBIE is commonly limited to treating fictitious eigenfrequencies [9] through the Burton and Miller formulation and crack analysis [2] through the Dual Boundary Element Method (DBEM). In the latter case, both BIEs are simultaneously used in order to solve the indeterminacy posed by the idealization of a crack as two coincident faces (Fig. 1(c)). When both BIEs are used to that purpose, they are called Dual BIEs, and become:

$$\frac{1}{2}\left(u_l^{\text{i}+} + u_l^{\text{i}-}\right) + \fint_\Gamma t_{lk}^* u_k \, \mathrm{d}\Gamma = \int_\Gamma u_{lk}^* t_k \, \mathrm{d}\Gamma \tag{5}$$

$$\frac{1}{2}\left(t_l^{\text{i}+} - t_l^{\text{i}-}\right) + \fint\!\!\!\!-_\Gamma s_{lk}^* u_k \, \mathrm{d}\Gamma = \fint_\Gamma d_{lk}^* t_k \, \mathrm{d}\Gamma \tag{6}$$

where geometrically coincident displacements and tractions (u_k^+, u_k^-, t_k^+ t_k^-) at both faces of the crack can be determined.

The shell structure is modeled using shell finite elements based on the degenerated solid approach [1], which are versatile and relatively easy to handle. However, in its original conception they have shear and membrane locking, which are due to the inability of the displacement interpolation to represent thin shell (vanishing out-of-plane shear stresses in bending) and curved shell (vanishing in-plane stresses in inextensional bending) situations, respectively. Locking can be improved by using selective or reduced integration, but the resulting shell elements contain spurious zero-energy (hourglass) modes and hence are not reliable. There are several approaches to obtain shell elements free from locking and spurious modes. In the present model, the family of Mixed Interpolation of Tensorial Components (MITC) shell elements [3] developed by Bathe and co-workers is chosen due to its robustness. The equilibrium equation of an element e can be written as:

$$\tilde{\mathbf{K}}^{(e)}\mathbf{a}^{(e)} - \mathbf{Q}^{(e)}\mathbf{t}^{(e)} = \mathbf{q}^{(e)} \quad (7)$$

where $\tilde{\mathbf{K}}^{(e)} = \mathbf{K}^{(e)} - \omega^2\mathbf{M}^{(e)}$ is the stiffness matrix for time harmonic analysis, $\mathbf{Q}^{(e)}$ is the distributed mid-surface load matrix and $\mathbf{q}^{(e)}$ is the vector of equilibrating nodal forces and moments. Vector $\mathbf{a}^{(e)}$ contains the nodal degrees of freedom:

$$\mathbf{a}^{(e)} = \begin{pmatrix} \mathbf{a}_1^{(e)} & \dots & \mathbf{a}_p^{(e)} & \dots & \mathbf{a}_N^{(e)} \end{pmatrix}^T \quad (8)$$

where N is the number of nodes of the shell finite element. Each node p has three DOF associated with the displacement of the mid-surface ($u_{kp}^{(e)}$, $k = 1, 2, 3$), and two local ($\alpha_p^{(e)}$ and $\beta_p^{(e)}$) or three global ($\theta_{kp}^{(e)}$, $k = 1, 2, 3$) rotations. The vector of nodal values of the distributed mid-surface load $\mathbf{t}^{(e)}$ can be written as:

$$\mathbf{t}^{(e)} = \begin{pmatrix} \mathbf{t}_1^{(e)} & \dots & \mathbf{t}_p^{(e)} & \dots & \mathbf{t}_N^{(e)} \end{pmatrix}^T \quad (9)$$

$$\mathbf{t}_p^{(e)} = \begin{pmatrix} t_{1p}^{(e)} & t_{2p}^{(e)} & t_{3p}^{(e)} \end{pmatrix}^T \quad (10)$$

where $\mathbf{t}_p^{(e)}$ is expressed in global coordinates.

A direct boundary element - finite element coupling after discretization is considered, where both boundary element mesh and shell finite element mesh must be conforming. It is assumed that the shell mid-surface and the fluid/soil boundaries are in perfectly welded and impermeable contact.

3 EXAMPLE

In order to show the coupling capabilities of the present model, an illustrative example consisting of a buried shell structure under an SH incident wave field (along y axis) is analyzed, see Fig. 2. The shell structure consist of a cylindrical shell with a circular plate joined in the middle, in such a way that the upper part is a fluid tank, and the lower part is a cylindrical caisson. Its diameter is 20 meters, and the total length is 40 meters. The soil has a density $\rho_{\text{soil}} = 2060$ kg/m^3, shear modulus $\mu_{\text{soil}} = 74$ MPa, Poisson's ratio $\nu_{\text{soil}} = 0.4942$ and hysteretic damping ratio $\xi_{\text{soil}} = 0.03$. Fluid is assumed to be water with density $\rho_{\text{water}} = 1000$ kg/m^3 and phase velocity $c_{\text{water}} = 343$ m/s. The shell structure is made of concrete with density $\rho_{\text{shell}} = 2400$ kg/m^3, shear modulus $\mu_{\text{soil}} = 12$ MPa, Poisson's ratio $\nu_{\text{soil}} = 0.4942$ and hysteretic damping ratio $\xi_{\text{soil}} = 0.05$, and its thickness is 0.3 meters.

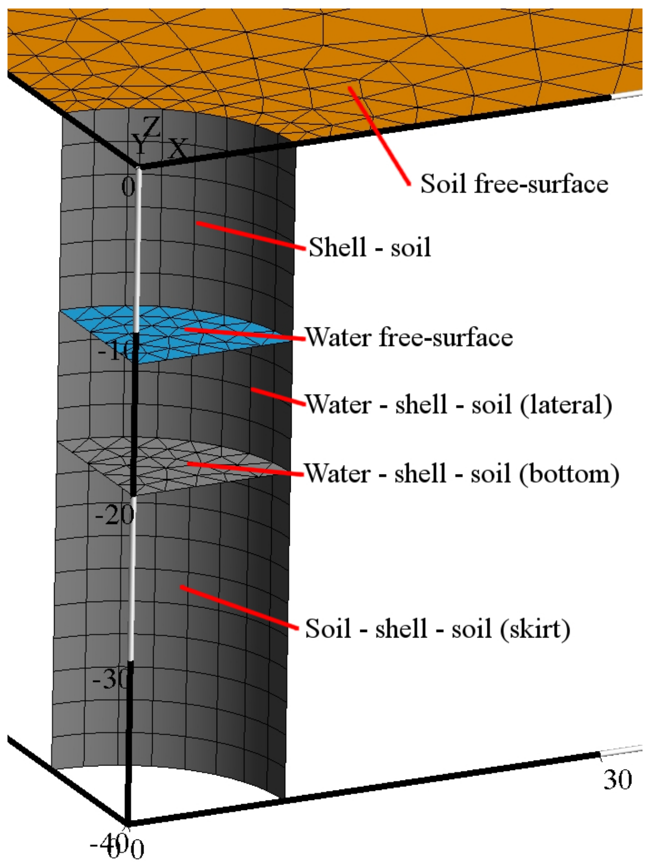

Figure 2: Buried shell structure example (water level at 40%)

Fig. 3 shows the displacement amplification u_2/u_2^{SH} in the excitation direction at a shell point ($\mathbf{x} = (0, 10, 0)$ meters). As expected, peaks related to system natural frequencies reduces their values as tank water level increases.

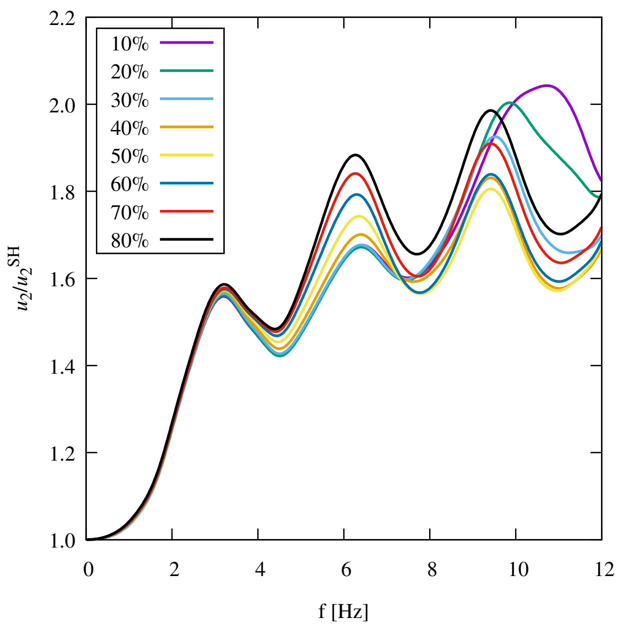

Figure 3: u_2/u_2^{SH} at shell point $\mathbf{x} = (0, 10, 0)$ meters.

4 CONCLUSIONS

In this contribution, we have presented a three-dimensional multi-region model for the dynamic analysis of shell structures interacting with surrounding soils and/or fluids. In the example, we have illustrated the range of couplings between shell and the surrounding media allowed.

5 ACKNOWLEDGMENTS

This work was supported by the Subdirección General de Proyectos de Investigación of the Ministerio de Economía y Competitividad (MINECO) of Spain and FEDER through Research Projects BIA2014-57640-R and BIA2017-88770-R. The authors are grateful for this support.

REFERENCES

[1] S. Ahmad, B. M. Irons, and O. C. Zienkiewicz. Analysis of thick and thin shell structures by curved finite elements. *Int J Numer Meth Eng*, 2(3):419–451, 1970.

[2] P. Ariza and J. Domínguez. General BE approach for three-dimensional dynamic fracture analysis. *Eng Anal Bound Elem*, 26:639–651, 2002.

[3] K. J. Bathe. *Finite Element Procedures*. Prentice Hall, 1996.

[4] M. A. Biot. Theory of propagation of elastic waves in a fluid-saturated porous solid. I. Low-frequency range. *J Acoust Soc Am*, 28(2):168–178, 1956.

[5] J. D. R. Bordón. *Coupled model of finite elements and boundary elements for the dynamic analysis of buried shell structures*. PhD thesis, Universidad de Las Palmas de Gran Canaria, July 2017.

[6] J. D. R. Bordón, J. J. Aznárez, and O. Maeso. A 2D BEM-FEM approach for time harmonic fluid-structure interaction analysis of thin elastic bodies. *Eng Anal Bound Elem*, 43:19–29, 2014.

[7] J. D. R. Bordón, J. J. Aznárez, and O. Maeso. Two-dimensional numerical approach for the vibration isolation analysis of thin walled wave barriers in poroelastic soils. *Comput Geotech*, 71:168–179, 2016.

[8] J. D. R. Bordón, J. J. Aznárez, and O. Maeso. Dynamic model of open shell structures buried in poroelastic soils. *Comput Mech*, 60(2):269–288, 2017.

[9] J. Domínguez. *Boundary Elements in Dynamics*. International Series on Computational Engineering. CMP/Elsevier, 1993.

[10] J. Domínguez, M. P. Ariza, and R. Gallego. Flux and traction boundary elements without hypersingular or strongly singular integrals. *Int J Numer Meth Eng*, 48:111–135, 2000.

SECTION 5: Dynamics of materials, vibroacoustics, wave propagation in solids

1st. Conference on Structural Dynamics (DinEst 2018)
Madrid, 20–21 June

EFFECT OF MAGNETIC FIELD ON THE DYNAMIC BEHAVIOUR OF THE SMART SANDWICH

Leire Irazu and María Jesús Elejabarrieta

Mechanical & Manufacturing Department
Mondragon Unibertsitatea
20500 Arrasate-Mondragon, Spain.

e-mail: lirazu@mondragon.edu

Abstract. Smart sandwich structures can be obtained by adding magnetic particles to the viscoelastic adhesive of conventional sandwiches. The dynamic behaviour of these smart sandwiches is modified in response to magnetic fields. In this work, a magneto-dynamic model of viscoelastic-magnetorheological sandwiches by finite element method is developed and validated with experimental results. The effect of the magnetic field intensity on the vibrational response and dynamic properties of the sandwich structure is analysed.

Key words: Smart sandwich, Magneto-dynamic model, Magnetic field.

1 INTRODUCTION

Vibrations are present in almost all machines and structures and their mitigation or control is of prime importance to achieve a desirable performance of the mechanical system. In the past last decade different vibration control techniques have been proposed classified on passive, semi-active and active techniques, for a wide range of applications [1].

Passive damping techniques using viscoelastic materials, have been one of the most widely applied structural vibration control techniques as they are cost-effective and simple to implement. The viscoelastic material can be confined between two metallic layers to form a sandwich structure with high damping-to-weight, strength-to-weight and stiffness-to-weigth ratios [2]. Owing to these characteristics viscoelastic sandwiches have resulted of special interest for applications in which the mass of components is critical. However, these sandwiches are unable to adapt to an application's requirements in real time unlike semi-active or active vibration control tecniques and this turns out to be a handicap in an increasingly demanding industry.

In recent years the viscoelastic core of sandwich structures have been replaced by magnetorheological materials (MR) in order to obtain smart sandwich structures. MR materials are smart materials possesing the unique ability to modify their rheological properties in response to external magnetic fields and so they offer attractive features for constructing smart sandwich structures with enhanced vibration control. MR materials are composed of micro or nanosized magnetic particles suspended in a non-magnetisable medium, and depending on the nature of the medium are classified into MR fluids, MR gels and MR elastomers [3].

This work is focused on smart sandwich structures composed of micron-size viscoelastic-magnetorheological (VEMR) cores. When applying magnetic fields to vibrating viscoelastic-magnetorheological sandwiches (VEMRS), their dynamic behaviour is modified as a consequence of the modification of the rheological properties and magnetization of the VEMR core. A new magneto-dynamic model of viscoelastic-magnetorheological sandwiches by finite element method is developed and validated with experimental results. The effect of the magnetic field intensiy on the vibrational response and dynamic properties of the sandwich structure is analysed.

2 MAGNETO-DYNAMIC MODEL OF THE SMART SANDWICH

The dynamics of viscoelastic-magnetorheological sandwich structures is modified in response to magnetic fields.

The rheological properties of the VEMR core change as a result of interactions generated between magnetic particles [3]. The dipole-dipole interaction based model developed by Jolly et al. [4] with the correction proposed by Agirre-Olabide et al. [5] is used to describe this behaviour. The shear complex modulus of the VEMR core as a function of the magnetic field is expressed as

$$G_{\mathrm{v}}^{*}(B) = \left(G_{\mathrm{v}} + G_{\mathrm{v_B}}(B)\right)\left(1 + \mathrm{i}\eta_{\mathrm{v}}\right), \qquad (1)$$

where G_{v} is the shear modulus, $G_{\mathrm{v_B}}(B)$ is the field-induced change according to Jolly et al and Agirre-Olabide et al. [4, 5] and η_{v} is the loss factor.

The VEMR core is magnetized under a magnetic field due to the ferromagnetic particles by which it is composed. The model developed by Moon and Pao [6] for linear ferromagnetic beams vibrating in homogeneous magnetic fields is used to describe the effect of this magnetization. The magnetic body couple in function of the magneti field can be expressed by

$$C(B) = \left(\frac{2\chi^2 B^2 \sinh\left(\frac{kh_2}{2}\right)}{\mu_0 \mu_{\mathrm{r}} k \Delta}\right)\frac{\partial w}{\partial x}, \qquad (2)$$

where $\frac{\partial w}{\partial x}$ is the rotation of the beam, χ is the magnetic susceptibility, k is the wave number, h_2 is the core thickness, μ_0 is the magnetic permeability of the vacuum, μ_{r} is the relative magnetic permeability of the VEMR film and $\Delta = \mu_{\mathrm{r}} \sinh\left(\frac{kh_2}{2}\right) + \cosh\left(\frac{kh_2}{2}\right)$.

2.1 Finite element model

The effect of magnetic field on VEMRSs is included in the finite element model in order to obtain a magneto-dynamic model of the smart sandwich.

A three-layer beam finite element based on the following assumptions is considered [7]:

- The skin layers bend according to Euler-Bernoulli beam theory.
- The core is subjected only to shear deformation.
- The transverse displacement is uniform on a cross section of the sandwich.
- There is no slippage between layers during deformation.

The finite element is defined by two nodes with four degrees of freedom (DOF) per node. The DOF include the axial displacements of the top and bottom skin layers, u_1 and u_3, the transverse displacement, w, and the rotational displacement of the beam, $\frac{\partial w}{\partial x}$. Lagrange linear shape functions, $\mathbf{N}_{\mathrm{u1}}$ and $\mathbf{N}_{\mathrm{u3}}$, are used for the axial displacement of the top and bottom skins, and the Hermite cubic shape function, $\mathbf{N}_{\mathrm{w}}$, for the transverse displacement.

The stiffness matrix of the sandwich element is obtained from the strain energy. This includes the bending of the skin layers, a negative bending stiffness due to the magnetization of the VEMR core obtained from Equation 2, the extension of the skin layers and the shear deofrmation of the VEMR core obtained from Equation 1. Thus, the stiffness matrix of the VEMRS depends on the intensity of the magnetic field and can be expressed as

$$\mathbf{k}^{e^*}(B) = \mathbf{k}^{e^*}_{\text{bending}}(B) + \mathbf{k}^{e^*}_{\text{extension}} + \mathbf{k}^{e^*}_{\text{shear}}(B). \qquad (3)$$

The mass matrix for the sandwich element is obtained from the kinetic energy, which includes the transverse displacement of all layers, the axial displacement of skin layers and the rotation of the core, given by

$$\mathbf{m}^e = \mathbf{m}^e_{\text{transverse translation}} + \mathbf{m}^e_{\text{axial translation}} + \mathbf{m}^e_{\text{rotation}}. \tag{4}$$

The governing equation of motion of the VEMRS in the finite element form is written as

$$\mathbf{M}\ddot{\mathbf{q}} + \mathbf{K}^*\mathbf{q} = \mathbf{F}, \tag{5}$$

where $\mathbf{q}$ and $\ddot{\mathbf{q}}$ are the displacement vector and the acceleration vector, and where $\mathbf{M}$, $\mathbf{K}^*$ and $\mathbf{F}$ are the global mass matrix, the global stiffness matrix and the global force vector, obtained by assembling the corresponding matrices for all of the elements. The transmissibility function is obtained by the direct frequency method.

2.2 Experimental validation

A thin VEMRS was tested in order to valdiate the proposed magneto-dynamic model. The VEMRS was composed of two alumiminum alloy 1050 H18 skins and an isotropic VEMR film. The micron-size VEMR film was synthesised by adding spherical carbonyl iron powder particles in a 12% volumetric concentration to a polyester-based adhesive. The geometrical and physical components of the VEMRS are shown in Table 1.

The experimental tecnique used to measure the transmissibility functions of the VEMRS consisted on forced vibrations with resonance according to ASTM E 756-05 standard[8] with the modification proposed by Cortés and Elejabarrieta [9]. The sandwich was tested in a cantilever configuration, a base excitation was generated by an electrodynamic shaker and the response of the beam was measured in the free end by a laser vibrometer [7]. The transmissibiity function was measured in the absence of and under a homogeneous transverse magnetic field.

Figure 1 shows the experimental and numerical transmissibility function of the VEMRS in the absence of a magnetic field and under a transverse magnetic field of 125 kA/m and it is observed the correlation is good in both cases. When applying a transverse magnetic field the resonance frequency of the VEMRS is decreased and the proposed magneto-dynamic model represents this behaviour.

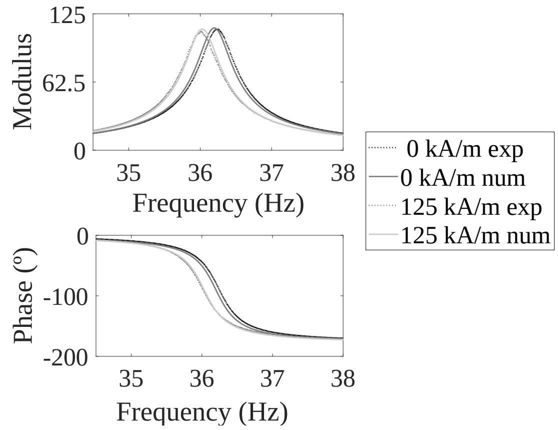

Figure 1: Experimental and numerical transmissibility function of the VEMRS beam with a free length of 160 mm in the absence of and under a magnetic field in the frist resonance.

3 INFLUENCE OF MAGNETIC FIELD

The influence of the magnetic field intensity on the dynamic behvaiour of the VEMRS is analysed. Figure 2 shows the transmissibility function of the VEMRS under different intensities of magnetic field. Incresing the magnetic field, the natural freuqency is decreased. In addition, the transmissibility modulus is slightly decreased which means vibration is attenuated. These results agrees with the experimental behaviour observed in [10].

4 CONCLUSIONS

In this work a new magneto-dynamic model of VEMRSs by finite element method is developed. The magneto-dynamic model accounts the modification of the rheological porterties and magnetization of the VEMR film. The numerical transmissibility function correlates well with the experimental one in the first resonance both in the absence of and under transverse magnetic field.

The numerical results show increasing the intensity of the magnetic field the resonance frequency of

Table 1: Geometrical and physical properties of the VEMRS.

Sandwich		Skins				Core		
Length (mm)	Thickness (mm)	Width (mm)	Thickness (mm)	Density (g/cm^3)	Complex modulus (GPa)	Thickness (mm)	Density (g/cm^3)	Complex modulus (GPa)
160 ± 0.5	1.162 ± 0.003	9.900 ± 0.002	0.564 ± 0.002	2.7*	68.11 + 0.1634i**	35 ± 2	1.91*	1.675 + 0.54i**

*Data provided by the manufacturer, Replasa S.A.

**Data obtained from forced vibration test according to ASTM E 756-05 standard.

the sandwich is decreased and vibration amplitude is slightly decreased.

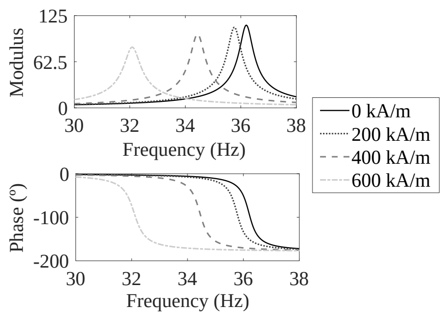

Figure 2: Numerical transmissibility function of the VEMRS beam with a free length of 160 mm under different intensities of magnetic field in the frist resonance.

5 ACKNOWLEDGMENTS

The authors acknowledge the financial support provided by AVISANI (DPI2015-71198-R) and AVISANI (PI 2016 1 0026) projects and Replasa S.A.

REFERENCES

[1] G. R. Tomlinson. State of the art review: damping. In *Structural Dynamics @ 2000: current status and future directions*. Research Studies Press, Philadelphia, 2001.

[2] Mohan D Rao. Recent applications of viscoelastic damping for noise control in automobiles and commercial airplanes. *Journal of Sound and Vibration*, 262(3):457–474, may 2003.

[3] J. David Carlson and Mark R Jolly. MR fluid, foam and elastomer devices. *Mechatronics*, 10(4-5):555–569, jun 2000.

[4] Mark R Jolly, J David Carlson, and Beth C Muñoz. A model of the behaviour of magnetorheological materials. *Smart Materials and Structures*, 5(5):607–614, oct 1996.

[5] I Agirre-Olabide, A Lion, and M J Elejabarrieta. A new three-dimensional magneto-viscoelastic model for isotropic magnetorheological elastomers. *Smart Materials and Structures*, 26(3):035021, mar 2017.

[6] F. C. Moon and Yih-Hsing Pao. Vibration and dynamic instability of a beam-plate in a transverse magnetic field. *Journal of Applied Mechanics*, 36(1):92, 1969.

[7] Leire Irazu and Maria Jesus Elejabarrieta. The effect of the viscoelastic film and metallic skin on the dynamic properties of thin sandwich structures. *Composite Structures*, 176:407–419, sep 2017.

[8] ASTM E 756-05. Standard test method for measuring vibration-damping properties of materials, 2005.

[9] F. Cortés and M. J. Elejabarrieta. Viscoelastic materials characterisation using the seismic response. *Materials & Design*, 28(7):2054–2062, jan 2007.

[10] Leire Irazu and Maria Jesus Elejabarrieta. Magneto-dynamic analysis of sandwiches composed of a thin viscoelastic-magnetorheological layer. *Journal of Intelligent Material Systems and Structures*, page 1045389X1770520, may 2017.

1st Conference on Structural Dynamics (DinEst 2018)
Madrid, 20-21 June

DYNAMIC BEHAVIOUR OF VISCOELASTIC LAMINATED ELEMENTS AT DIFFERENT TEMPERATURES

F. Pelayo*, M. López-Aenlle and G. Ismael,
Department of Construction and Manufacturing Engineering,
University of Oviedo, Gijón, Spain
*Corresponding Author : fernandezpelayo@uniovi.es

Abstract. Laminated glass elements are commonly used in floors, roofs and other horizontal glazing elements accessible to the public, where a high level of security is required. Although the mechanical behavior of glass layers can be considered linear-elastic, the polymeric interlayers determine a viscoelastic behavior of the laminated structure which must be considered in the static and dynamic calculations.

In this paper, the Dynamic Effective Stiffness concept is used to predict the modal parameters of a laminated glass element at different temperatures using simple analytical equations. The results show that natural frequencies and loss factors are highly dependent on temperature. The analytical predictions are validated by Operational Modal Analysis and a good correlation was obtained in the natural frequencies. With respect to the damping ratios, the discrepancies between the experimental and the numerical ones are higher but less than 40%.

Key words: laminated glass, viscoelastic behaviour, modal analysis, effective thickness concept.

1 INTRODUCTION

Laminated glass elements are nowadays of great interest in mechanical and structural applications due to several advantages such as vibration and noise isolation as well as safety improvement [1]. This laminated material consists of two or more layers of monolithic glass with one or more polymer interlayers (see Figure 1). In general, the monolithic glass is considered as a linear-elastic material, whereas the polymer interlayers is commonly assumed as linear viscoelastic, i.e. the mechanical behavior of the polymer interlayer is time and temperature dependent and so is the laminated glass element.

In order to simplify the calculations of laminated glass elements, the effective thickness concept (ETC) [3, 4] or its equivalent effective stiffness or effective Young modulus [2] are commonly used. The ETC is the thickness of a monolithic beam which presents the same deflections as the laminated one and is obtained assuming that both beams present the same deflection shape under the same loading and boundary conditions¨.

Several analytical models have been developed and applied recently for the calculation of laminated glass elements under static and dynamic loadings using the ETC [2, 3].

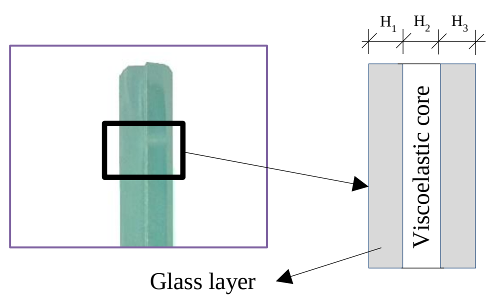

Figure 1: Laminated glass.

In this paper, the modal parameters of a laminated glass beam (natural frequencies and damping ratios) were determined using the EFC concept at different temperatures. The predicted results are compared with those obtained experimentally by means of an Operational Modal Analysis (OMA) identification.

2 ESTIMATION OF MODAL PARAMETERS BY THE DYNAMIC EFFECTIVE STIFFNESS CONCEPT

The model developed by Ross, Kerwin and Ungar (RKU) [5] is commonly used for calculating the natural frequencies and damping ratios in laminated glass beams because of its simplicity. In the case of a beam with length L, width b and thicknesses H_1, H_2, H_3 (see Figure 1), respectively, the modal parameters can be obtained using the following expression:

$$\omega^2(1+i\eta) = k_I^4 \frac{EI^*(\omega,T)}{\bar{m}} \tag{1}$$

where k_I is the wavenumber, EI^* is a dynamic effective stiffness and $\bar{m}$ is the mass per unit length:

$$\bar{m} = b(\rho H_1 + \rho_2 H_2 + \rho H_3) \tag{2}$$

with ρ being the density of the glass layers and ρ_2 the density of the interlayer. The dynamic effective stiffness $EI^*(\omega,T)$ is given by:

$$EI^*(\omega,T) = EI_T\left(1 + \frac{Y}{1 + \frac{EH_1\, H_2 H_3\, k_I^2}{G_2^*(\omega,T)(H_1+H_3)}}\right) \tag{3}$$

where $G_2^*(\omega,T)$ is the shear complex modulus of the interlayer and:

$$I_T = \frac{b(H_1^3 + H_3^3)}{12} \tag{4}$$

$$Y = \frac{H_0^2 H_1 H_3}{I_T(H_1+H_3)} \tag{5}$$

$$H_0 = H_2 + \left(\frac{H_1 + H_3}{2}\right) \tag{6}$$

The wavenumbers of an Euler-Bernoulli beam with the same boundary conditions are commonly assumed in Eqs. (1) and (3).

The loss factor η obtained in Eq. (1) can be related to modal damping ζ by [6]:

$$\eta = 2\,\zeta \tag{7}$$

3 EXPERIMENTAL PROGRAM

In this paper the modal parameters of a sandwich PVB glass beam ($H1 = 3.75\,mm$; $H2 = 0.38\,mm, H3 = 7.90\,mm, L = 1000\,mm$ and $b = 100\,mm$) were obtained using Operational modal analysis (OMA) under free-free conditions.

Experimental test at different temperatures from $15{-}45\ C^o$ were carried out using an oven (see Figure 2). Seven PCB accelerometers with a sensitivity of 100mV/g were used to record the acceleration responses of the beam with a sampling frequency of 2000 Hz.

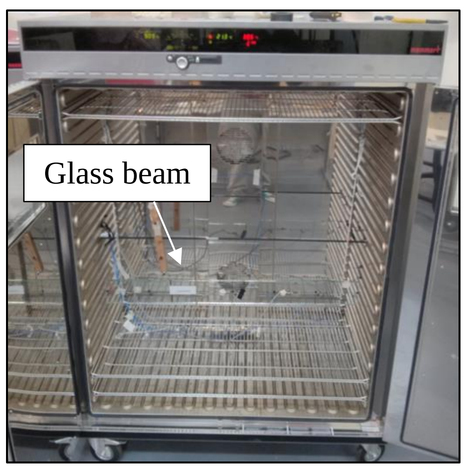

Figure 2: Experimental set-up.

The elastic material properties needed to predict the natural frequencies and the loss factors with Eq. (1) are presented in Table 1.

The viscoelastic properties of PVB were obtained in a previous work [2]. The Shear Complex modulus $G^*(\omega)$is presented in Figure 3.

Glass			PVB			
E	ν	ρ	G_0	K	ν	ρ
[GPa]		[kg/m^3]	[GPa]	[GPa]		[kg/m^3]
70	0.22	2500	0.37	2	0.40	1046

Table 1. Elastic properties of Glas and PVB.

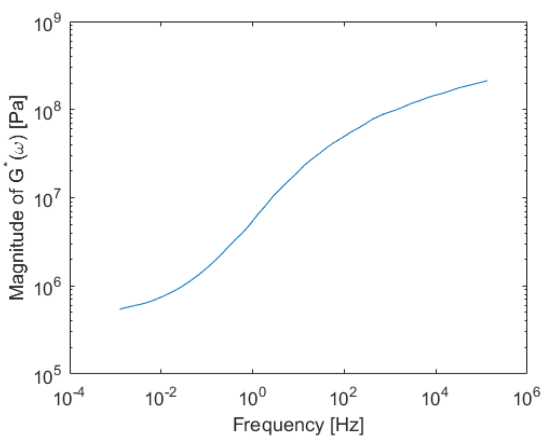

Figure 3: Shear Complex modulus for PVB.

4 RESULTS

The modal parameters were estimated using the EFDD) [7] technique implemented in the ARTEMIS MODAL software. The singular value decomposition of the measurements at 15 ^oC and 35 ^oC are presented in Figure 4.

The natural frequencies and damping ratios estimated by the EFDD technique, together with those predicted by the RKU model (Eq. 1) and Eq. (7), are presented in Tables 2 and 3, respectively.

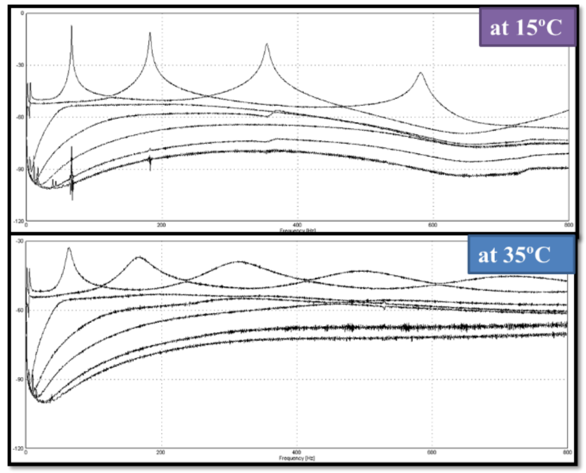

Figure 4: Singular Value Decomposition for different temperatures.

With respect to the natural frequencies (see Table 2), the results reveal that, the higher the temperature the lower the frequencies for all the modes considered in the investigation. The error between the experimental and the predicted natural frequencies is always less than a 10%, being the predicted values higher than the experimental ones.

	Tª [ºC]	f_n [Hz] RKU MODEL	f_n [Hz] OMA	[%] ERROR
MODE 1	15	66.16	66.65	0.73
	25	65.78	66.29	0.76
	35	64.86	65.37	0.78
	45	60.40	60.25	0.24
MODE 2	15	181.74	182.90	0.64
	25	179.70	181.10	0.77
	35	174.81	175.90	0.62
	45	157.97	153.70	2.78
MODE 3	15	354.38	357.10	0.76
	25	348.73	351.30	0.73
	35	334.00	335.50	0.45
	45	295.71	276.80	6.83
MODE 4	15	582.48	587.60	0.87
	25	569.63	574.50	0.85
	35	539.59	543.50	0.72
	45	473.32	432.70	9.39

Table 2: Experimental and predicted natural frequencies

On the other hand, the damping ratios (see Table 3) increase with increasing temperature. The maximum errors in the damping ratios between the analytical and the experimental values are close to a 40% which can be consider acceptable [6].

	Tª [ºC]	ζ [%] RKU MODEL	ζ[%] OMA	[%] ERROR
MODE 1	15	0.08	0.13	39.22
	25	0.45	0.48	6.11
	35	2.08	2.28	9.03
	45	6.72	9.46	28.96
MODE 2	15	0.16	0.23	28.19
	25	0.88	0.91	3.13
	35	2.77	4.70	41.20
	45	9.17	10.17	9.78
MODE 3	15	0.26	0.25	1.47
	25	1.21	1.32	7.98
	35	3.81	5.94	35.90
	45	10.98	12.53	12.41
MODE 4	15	0.39	0.34	12.87
	25	1.43	1.82	21.21
	35	4.69	6.48	27.72
	45	11.75	14.91	21.19

Table 3: Experimental and predicted damping ratios

With respect to the mode shapes, the modal assurance criteria (MAC) was used to compare the analytical and the experimental mode shapes, obtaining values very close to one. Thus, it is conclude that the effect of temperature in the mode shapes of a laminated glass beam is negligible.

6 CONCLUSSIONS

- The discrepancies in natural frequencies between the analytical predictions and those obtained from the OMA are less than 10%

- With regard to the damping ratios, the discrepancies between experimental the analytical predicted are consistently less than 40%.

ACKNOWLEDGMENTS

The financing support given by the Spanish Ministry of Economy and Competitiveness through the project BIA2014-53774-R is gratefully appreciated.

REFERENCES

[1] R.A. Behr, J.E. Minor, H.S. Norville. *Structural behavior of architectural laminated glass*. Journal of Structural Engineering. 119 (1) 202-222, 1993.

[2] M. López-Aenlle, F. Pelayo, *Dynamic effective thickness in laminated-glass beams and plates*. Composite: Part B, 67, 332-347, 2014.

[3] I. Calderone, P.S. Davies S.J. Benninson, *Effective Laminate Thickness for the Design of Laminated Glass*. In: Glass Processing Days, Tampere. Finland. 2009.

[4] L. Galuppi and G.F. Royer-Carfagni, *Effective Thickness of Laminated Glass Beams: New Expression via a Variational Approach*, Engineering Structures, 38. 53-67. 2012.

[5] D. Ross, E.E. Ungar, E.M. Kerwin, *Damping of Plate Flexural Vibrations by Means of Viscoelastic Laminate*, Structural Damping, ASME, 49-88, 1959

[6] D.I.G Jones, *Reflections on Damping Technology at the End of the Twentieth Century*, Journal of Sound and Vibration, 190(3), 449-462. 1996.

[7] R. Brincker, L-M. Zhang and P. Anderson. *Modal Identification from Ambient Response Using Frequency Domain Decomposition*, in:18th IMAC, 625-630. 2000.

SCOPING ASSESMENT OF FREE-FIELD VIBRATIONS DUE TO RAILWAY TRAFFIC

D. López-Mendoza[*a], P. Galvín[a], D.P. Connolly[b] and A. Romero[a]

[a]Escuela Técnica Superior de Ingeniería
Universidad de Sevilla
41092 Sevilla, Spain

e-mail: lopezmendoza@us.es
ORCID: 0000-0001-8408-7390

[b] Institute for High Speed Rail
Leeds University
LS2 9JT Leeds, UK

Abstract. Globally, the number of high speed railway (HSR) lines both operational and under construction is growing rapidly (e.g. HS2, UK). Vibration levels require prediction during early stages of planning/development, typically in the form of a desktop study. To achieve this, scoping models are used to allow engineers to assess long lengths of track quickly, in absence of detailed design information. This paper presents a methodology to construct such a scoping model, which includes the behaviour of train, track and soil. The methodology considers track-soil interaction, soil stiffness and the combination of both the dynamic and static forces generated due to high speed train passage. It can be used to predict the vibration levels in the free-field, using metrics compatible with international standards. To achieve large reductions in computational time, the model calculates free-field vibrations using a neural network (NN) procedure to assess the track-soil interaction. The model is validated by comparing soil predictions against a more complete finite element (FEM) -boundary element (BEM) model.

Key words: Scoping assesment, Free-field vibrations, Soil vibrations, Neural Network, Railway traffic.

1 INTRODUCTION

The emergence of high speed rail (HSR) has stimulated economic development in Europe, America and Asia. This has also caused an increasing number of properties and structures to be affected by ground-borne railway vibrations. International standard ISO2631 [3] addresses these negative effects and evaluates the whole-body human exposure to vibration. In addition, ISO14837 [4] is railway focused and outlines suggested numerical modelling approaches. At the construction stage of a new railway line, comprehensive and detailed design models are recommended. These are typically computationally expensive. If the vibration assessment is to be undertaken at an earlier stage of railway line development, simplified scoping models [4] are often more useful. This is because they are faster running and often do not require as many input parameters.

This paper presents a new scoping methodology to evaluate the free-field vibrations. It is able to model the effect of a large variety of input variables using minimal computational effort. This paper is organised as follows. First, the scoping model is presented. Next a numerical validation of the scoping model is undertaken.

2 NUMERICAL MODELLING

To calculate the field response (Figure 1), the train-track-soil system was divided into two primary sub-models: a track-soil sub-model (step 2.1) and a train-track sub-model (step 2.2).

To calculate the track-soil transfer function $\tilde{\boldsymbol{u}}_{\mathrm{ff}}$ (Figure 1, step 2.1) the soil Green's function is computed in the absence of track $\tilde{\boldsymbol{u}}_{\mathrm{g}}$. Then, to approximate the response of a combined track-ground system, the Green's function is modulated using a correction factor $\tilde{A}_g$, calculated via a neural network procedure.

The train-track forces $\boldsymbol{g}$ are calculated using a simplified FEM track model where the underlying soil is modelled using a spring element that approximates the underlying soil response (Figure 1, step 2.2).

Then free-field response $\boldsymbol{u}_{\mathrm{s}}$ (Figure 1, step 2.3) is assessed by combining the track-soil transfer function with train-track excitations. To do so, it is used the formulation by Lombaert et al. [5]. A detailed description of the scoping model formulation is give in [1].

3 NUMERICAL VERIFICATION

In this section a numerical verification of the proposed scoping model is undertaken. To further validate the scoping model, it's predictions were compared against a more comprehensive, 'reference' model. The reference model is based upon a 2.5D BEM-FEM methodology in the frequency-wavenumber domain [5, 2]. It was designed to compute the generation of railway vibrations and their propagation through the neighbouring soil.

A series of tests were performed to assess the accuracy ofthe scoping model. Three track cases (ballasted track over an embankment, an at-grade track section and a slab track over an embankment) were considered. Quasi-static excitation and dynamic excitation due to random track unevenness were taken into account, and the same track unevenness profile was considered for all the cases. The free-field mobility and free-field response by railway traffic were obtained at a point located at distance of $d = 20\,\mathrm{m}$ from the track centreline. Regarding the vehicle, a S-100 series train was simulated travelling at 100 km/h. The soil was modelled as a homogeneous elastic half-space with a shear wave velocity $c_{\mathrm{s}} = 200\,\mathrm{m/s}$, a dilatational wave velocity $c_{\mathrm{p}} = 400\,\mathrm{m/s}$ and density $\rho = 1800\,\mathrm{kg/m^3}$. The material damping ratio β for both deviatoric and volumetric deformation had a value of 0.05.

Figure 2 shows rail receptances for the three type of tracks. It is seen that low frequency response is slightly overestimated, however performance improves with increasing frequency. This is due to the dominant influence of track-soil interaction, the formulation for which is different for the reference and scoping models. The reference method rigorously models the soil using BEM, while the scoping model uses a simplified methodology with a linear spring to significantly reduce computational time.

Free-field mobilities for the three tracks are presented in Figure 3. It is seen that the shape and magnitude of response is a good match between models and considering the degree of input uncertainty for ground vibration models, the scoping model is within a reasonable range

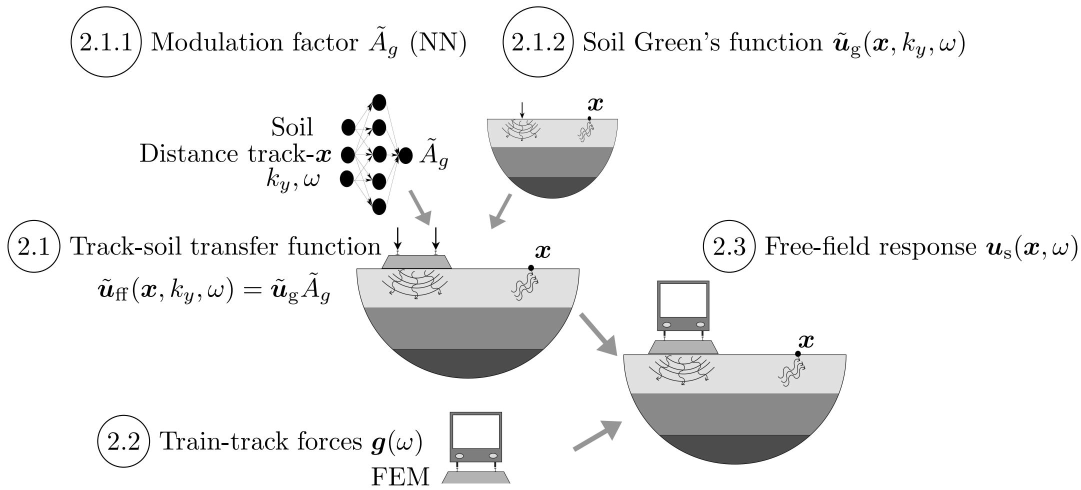

Figure 1: Scheme of the scoping model.

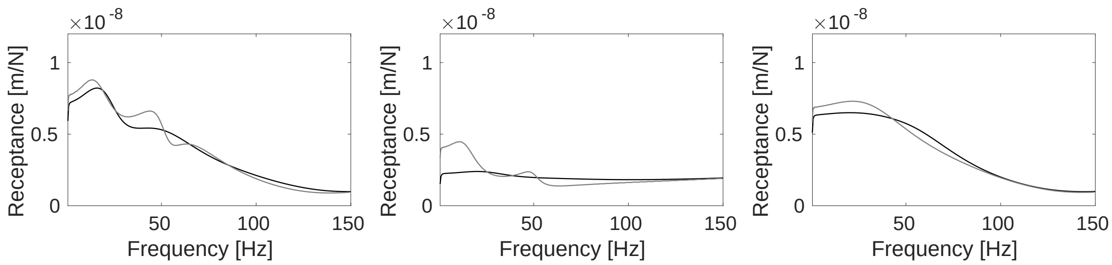

(a) (b) (c)

Figure 2: The displacement of the rail for the (a) ballasted track over an embankment, (b) slab track and (c) at-grade track, computed by the reference model (black line) and the scoping model (grey line).

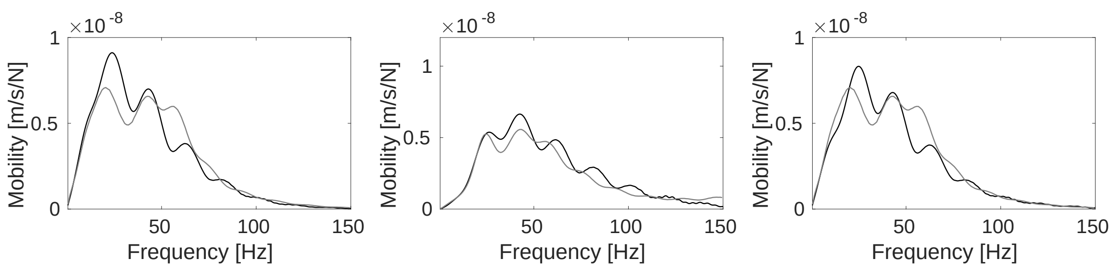

(a) (b) (c)

Figure 3: Free-field vertical mobility for the (a) ballasted track over an embankment, (b) slab track and (c) at-grade track, computed by the reference model (black line) and the scoping model (grey line).

of uncertainty.

Figure 4 presents the one-third octave band center frequency contents of the dynamic load of an axle computed using both models. The estimation of the dynamic load from the proposed model coincides very strongly with those obtained using the reference model.

Figure 5 shows frequency contents of the free-field response. The discrepancies between models are low and in accordance with those observed in the mobility results (Figure 3), and the results correlate well.

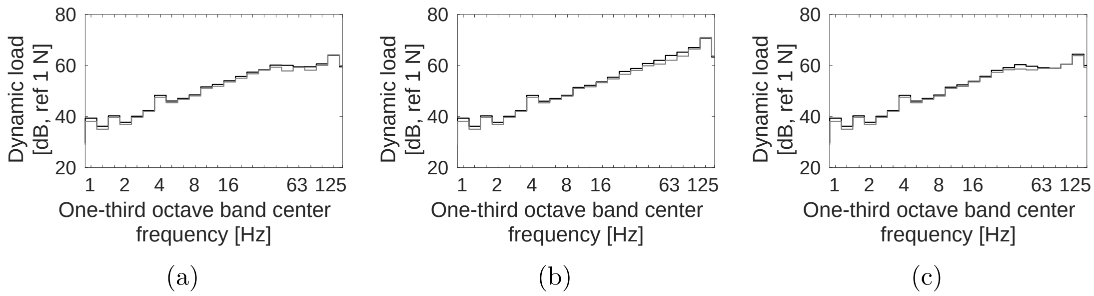

Figure 4: One-third octave band content of the dynamic load of an axle with unsprung mass $m_s = 2048\,\mathrm{kg}$ at $v = 100\,\mathrm{km/h}$ for the (a) ballasted track over an embankment, (b) slab track and (c) at-grade track computed by the reference model (black line) and the scoping model (grey line).

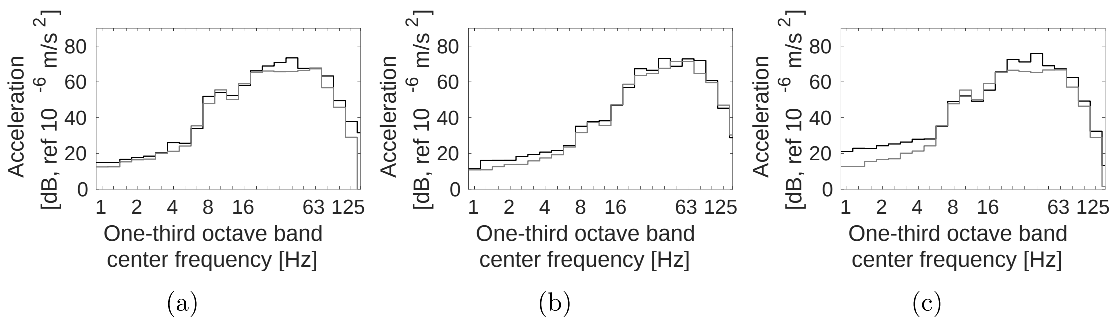

Figure 5: One-third octave band center frequency of the vertical acceleration in the free-field for the (a) ballasted track over an embankment, (b) slab track and (c) at-grade track computed by the reference model (black line) and the scoping model (grey line).

4 CONCLUSIONS

In this work, a simplified methodology to compute the propagation of railway vibrations from track to free-field was presented. Overall there was strong correlation between the reference and scoping model with regards to receptance, mobility, dynamic load and free-field results. Therefore it was concluded that the scoping model was capable of predicting railway vibration.

REFERENCES

[1] P. Galvín, D. López-Mendoza, D.P. Connolly, and A. Romero. Scoping assessment of the free-field vibrations due to railway traffic (under revision). *Soil Dynamics and Earthquake Engineering*, 2018.

[2] P. Galvín, S. François, M. Schevenels, E. Bongini, G. Degrande, and G. Lombaert. A 2.5D coupled FE-BE model for the prediction of railway induced vibrations. *Soil Dynamics and Earthquake Engineering*, 30(12):1500 – 1512, 2010.

[3] International Organization for Standardization. *ISO 2631-1:2003: Mechanical vibration and shock–Evaluation of human exposure to whole-body vibration–Part 1: General requirements*, 2003.

[4] International Organization for Standardization. *ISO 14837-1:2005 Mechanical vibration–Ground-borne noise and vibration arising from rail systems–Part 1: General guidance*, 2005.

[5] G. Lombaert, G. Degrande, J. Kogut, and S. François. The experimental validation of a numerical model for the prediction of railway induced vibrations. *Journal of Sound and Vibration*, 297(3):512 – 535, 2006.

1st. Conference on Structural Dynamics (DinEst 2018)
Madrid, 20–21 June

A 2.5D SPECTRAL FORMULATION TO REPRESENT GUIDED WAVES WITH ACOUSTIC AND SOLID INTERACTION

F.J. Cruz-Muñoz[a*], A. Romero[a], A. Tadeu[b] and P. Galvín[a]

[a]Escuela Técnica Superior de Ingeniería
Universidad de Sevilla
Camino de los Descubrimientos s/n
41092 Sevilla, Spain

e-mail: fjcruz@us.es
ORCID: 0000-0003-4637-3307

[b]Department of Civil Engineering
University of Coimbra, Polo II
3030-788 Coimbra, Portugal

Abstract. This work presents a two-and-a-half (2.5D) spectral formulation to study three-dimensional (3D) wave propagation in fluid acoustics and elastic media in the frequency domain. The analysis is carried out by superposition of two-and-a-half dimension (2.5D) problems for different longitudinal wavenumbers. The numerical method is based on the domain decomposition to study the fluid-solid coupled problem. The BEM is used to analyze the acoustic field in unbounded regions, whereas the FEM allows representing the solid waveguide with arbitrary cross-section. First, a 2.5D spectral finite element to represent guided waves in solids is presented. Later, the 2.5D fluid boundary element is derived from the Helmhotz equation. Both approaches use Lagrange interpolation polynomials as element shape functions defined at the Legendre-Gauss-Lobatto (LGL) integration points. The coupling of the fluid and solid subdomain is carried out by the application of the appropriate boundary conditions at the interface. The proposed method is verified from a benchmark problem: the acoustic scattered wave in an unbounded acoustic medium by either rigid or elastic cavities. The convergence and the computational effort are evaluated for different h-p strategies. Numerical results show a good agreement with the analytical solution. Later, the proposed technique is used to study the radiated pressure field and the insertion loss by a scatter configuration.

Key words: BSEM, SEM, fluid-structure interaction, waveguide, scattered waves.

1 INTRODUCTION

Time-harmonic wave propagation, such as fluid acoustics and solid scattering, is a common phenomenon that appears in many engineering fields. The propagation of acoustic waves triggered by static and moving pressure sources, the vibration assessment and the acoustic insulation, involve fluid and solid interaction and must be considered rigorously. The finite element method (FEM) has been used in several works to predict the response in fluid-structure interaction problems. For the low frequency range, the conventional finite elements with linear shape functions represent accurately the fluid and solid scattering waves. However, at high frequencies, these shape functions do not provide reliable results due to so-called pollution effects [3, 2]: the accuracy of the numerical solution deteriorates with increasing non-dimensional wave number and it is not sufficient the commonly employed rules of n elements per wavelength [4]. High element resolutions are required in order to obtain results with reasonable accuracy.

In this work, a two-and-a-half dimensional (2.5D) approach to represent scattered waves in fluid media is proposed. This approach is useful for problems where the material and geometric properties are uniform along one direction, and the source exhibits 3D behaviour.

2 NUMERICAL MODEL

The 2.5D formulation computes the problem solution as the superposition of two-dimensional (2D) problems with a different longitudinal wavenumber, k_z, in the z direction. An inverse Fourier transform is used to compute the 3D solution:

$$a(\mathbf{x},\omega) = \int_{-\infty}^{+\infty} \widehat{a}(\widehat{\mathbf{x}}, k_z, \omega) e^{-ik_z z} dk_z \tag{1}$$

where $a(\mathbf{x},\omega)$ is an unknown variable (e.g., displacement or pressure), $\widehat{a}(\widehat{\mathbf{x}}, k_z, \omega)$ is its representation in the frequency-wavenumber domain, $\widehat{\mathbf{x}} = \mathbf{x}(x, y, 0)$, ω is the angular frequency, and $i = \sqrt{-1}$.

The boundary element formulation presented in this work considers an arbitrary boundary submerged in an unbounded fluid medium. The integral representation of the pressure p^i for a point i located at the fluid subdomain $\Omega_{f\infty}$, with zero body forces and zero initial conditions may be written as [1]:

$$\begin{aligned} c^i p^i(\mathbf{x}^i,\omega) = &\int_{\Gamma_f} p^{i*}(\mathbf{x},\omega;\mathbf{x}^i) u^i(\mathbf{x},\omega) d\Gamma \\ &- \int_{\Gamma_f} u^{i*}(\mathbf{x},\omega;\mathbf{x}^i) p^i(\mathbf{x},\omega) d\Gamma \end{aligned} \tag{2}$$

where $u^i(\mathbf{x},\omega)$ and $p^i(\mathbf{x},\omega)$ are respectively the normal displacement and the pressure at point i. $u^{i*}(\mathbf{x},\omega;\mathbf{x}^i)$ and $p^{i*}(\mathbf{x},\omega,\mathbf{x}^i)$ are respectively the fluid full-space fundamental solution for normal displacement and pressure at point $\mathbf{x}$ due to a point load at $\mathbf{x}^i$. The integral-free term c^i depends only on the boundary geometry at point i. The integration boundary Γ_f represents the boundary between the unbounded fluid medium ($\Omega_{f\infty}$) and the solid subdomain (Ω_s).

Assuming that the unbounded medium is invariant in the longitudinal direction z, equation. (2) is expressed in terms of integrals in this direction and over the cross-section boundary, Σ_f:

$$\begin{aligned} c^i p^i(\mathbf{x},\omega) = &\int_{-\infty}^{+\infty} \int_{\Sigma_f} p^{i*}(\mathbf{x},\omega;\mathbf{x}^i) u^i(\mathbf{x},\omega) dSdz \\ &- \int_{-\infty}^{+\infty} \int_{\Sigma_f} u^{i*}(\mathbf{x},\omega;\mathbf{x}^i) p^i(\mathbf{x},\omega) dSdz \end{aligned} \tag{3}$$

Equation. (3) is then transformed to the wavenumber domain as:

$$\begin{aligned} c^i \widehat{p}^i(\widehat{\mathbf{x}},\omega,k_z) = &\int_{\Sigma_f} \widehat{p}^{i*}(\widehat{\mathbf{x}},\omega,k_z;\widehat{\mathbf{x}}^i) \widehat{u}^i(\widehat{\mathbf{x}},\omega,k_z) dS \\ &- \int_{\Sigma_f} \widehat{u}^{i*}(\widehat{\mathbf{x}},\omega,k_z;\widehat{\mathbf{x}}^i) \widehat{p}^i(\widehat{\mathbf{x}},\omega,k_z) dS \end{aligned} \tag{4}$$

where a hat above a variable denotes its representation in the frequency-wavenumber domain.

The problem is discretised into elements, leading to a boundary approximation of the normal displacement and pressure using the interpolation shape functions $\boldsymbol{\phi}^j$. Then, equation. (4) is written as:

$$\begin{aligned} c^i \widehat{p}^i &= \sum_{j=1}^{Q} \left[\left\{ \int_{\Sigma_f^j} \widehat{p}^{i*} \boldsymbol{\phi}^j d\Sigma \right\} \widehat{u}^i - \left\{ \int_{\Sigma_f^j} \widehat{u}^{i*} \boldsymbol{\phi}^j d\Sigma \right\} \widehat{p}^i \right] \\ &= \sum_{j=1}^{Q} \left[\widehat{\mathbf{H}}^{ij} \widehat{u}^i - \widehat{\mathbf{G}}^{ij} \widehat{p}^i \right] \end{aligned} \tag{5}$$

where Q is the number of boundary nodes at the boundary Σ_f and Σ_f^j are the elements which contains the node j. After interpolating the boundary variables, the integral representation defined by equation. (5) yields a system of equations that is solved for each frequency.

The system of equations for all the boundary elements becomes:

$$\widehat{\mathbf{H}}(\omega,k_z)\widehat{u}(\widehat{\mathbf{x}},\omega,k_z) = \widehat{\mathbf{G}}(\omega,k_z)\widehat{p}(\widehat{\mathbf{x}},\omega,k_z) \tag{6}$$

The proposed spectral boundary element method for the 2.5D fluid element uses Legendre polynomials of order p as interpolation shape functions. The shape interpolation functions $\boldsymbol{\phi}$ are given by:

$$\phi_i = \prod_{j \neq i} \frac{\xi - \xi_i}{\xi_j - \xi_i} \tag{7}$$

where the local nodal coordinates ξ are found at the LGL integration points:

$$(1 - \xi^2)\frac{\partial \phi(\xi)}{\partial \xi} = 0 \tag{8}$$

3 NUMERICAL VERIFICATION

The BEM model was verified with a benchmark problem. The model was validated by applying it to a fixed cylindrical circular cavity submerged in a homogeneous unboundend fluid medium. The cavity is subjected to a harmonic point pressure load. The analytical solution to this problem can be found in Reference [5].

The cavity had a radius $r = 5$ m , located at the origin $(x, y) = (0, 0)$. The unbounded fluid medium properties were: pressure wave velocity $\alpha = 1500$ m/s and density $\rho = 1000$ kg/m^3. The problem solution was computed for a dilatational point source placed at the fluid medium $\widehat{\mathbf{x}}_0 = (x_0, y_0) = (0, 15)$ i.e, 15 m away from the cavity centre. This loads emits a harmonic incident field $\widehat{p}_{inc}$ at a point $\widehat{\mathbf{x}}$ given by:

$$\widehat{p}_{inc} = (\widehat{\mathbf{x}}, \omega, k_z) = \frac{-iA}{2} H_0^{(2)}(k_\alpha r) \tag{9}$$

where A is the source amplitude, $H_0^{(2)}$ is the Hankel function of the second kind, $k_\alpha = \sqrt{\omega^2/\alpha^2 - k_z^2}$, and r is the distance to the source. In this problem, the longitudinal wavenumber was set to $k_z = 0$.

The problem solution was computed over a grid of 1376 receivers regularly spaced in a outer region defined by $-10\text{m} \leq x \leq 10\text{m}$ and $-10\text{m} \leq y \leq 10\text{m}$, at a frequency $f = 200$ Hz.

Four different $h - p$ strategies were investigated to get the optimal discretisation with the lowest computational effort. The characteristic element sizes were $1/h = \{0.4/\pi, 1/\pi, 2/\pi, 4/\pi\}$ m^{-1}. The numerical results were compared with the analytical solution and scaled L_2 error, ϵ_2, was used to asses the accuracy:

$$\epsilon_2 = \frac{||f_{ex} - f_h||}{||f_{ex}||} \tag{10}$$

where f_{ex} denotes the reference solution and f_h is the results computed by the proposed methodology.

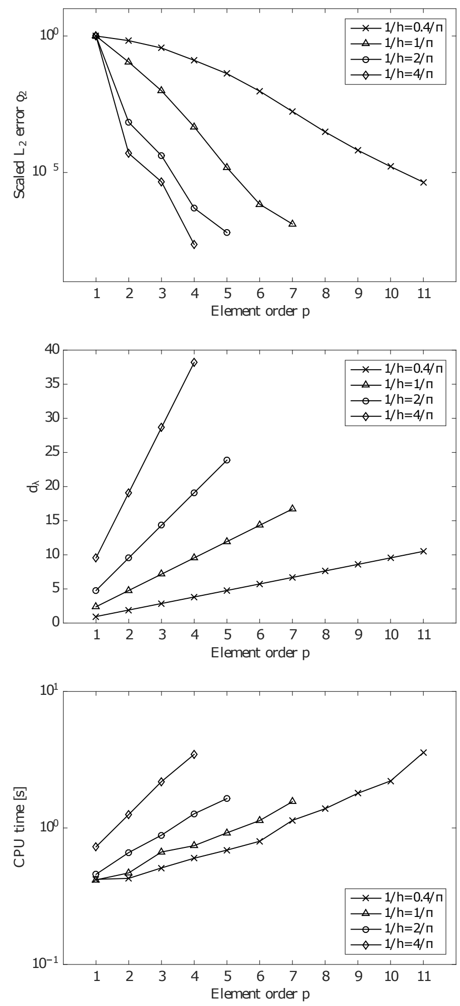

Figure 1: (a) Scaled L_2 error ϵ_2, (b) nodal density per wavelegth d_λ and (c) CPU time for different discretisations $1/h$ and element polynomial order p.

Figures ?? shows the error ϵ_2, the nodal density per wavelength d_λ, and the CPU time for different $h - p$ configurations. All the error curves have an initial value $\epsilon_2 = 1$ for $p = 1$ and start to decrease

Table 1: Summary of L_2 scaled error ϵ_2, CPU time and nodal density (d_λ) for different spectral $h-p$ discretisation to approximate the problem solution at excitation frequency 200Hz with the accepted accuracy $\epsilon_2 \leq 10^{-4}$.

$1/h$ $[m^{-1}]$	p [-]	L_2 scaled error ϵ_2	CPU time [s]	d_λ [-]
0.4	9	$6.52 \times 10^{-}5$	1.796	8.59
1	5	$1.50 \times 10^{-}5$	1.133	11.94
2	3	$4.15 \times 10^{-}5$	0.886	14.32
4	2	$4.99 \times 10^{-}5$	1.256	19.10

depending on the mesh discretisation. The error curves show a monotonic convergence with the element order p. Denser meshes tend to a minimum error with a lower element order p.

Table 1 summarizes the nodal density per wavelength and the CPU time for the optimal $h-p$ discretisation to reach the solution with the acceptable error $\epsilon_2 \leq 10^{-4}$. This analysis shows that the configuration $(1/h, p) = (2, 3)$ allows the minimum computational effort for the given accuracy. Other $h-p$ pairs involve higher computational effort due to the high order interpolation functions or the higher number of nodes.

4 CONCLUSIONS

This work proposes a spectral formulation based on the BEM to study acoustic wave propagation. This method looks at 3D problems whose materials and geometric properties remain homogeneous in one direction. The developed methodology avoids the pollution effect at high frequencies. The approach has been verified with a benchmark problem with known analytical solution. The numerical results were in good agreement with the reference solution.

5 ACKNOWLEDGMENTS

The authors would like to acknowledge the financial support provided by the Spanish Ministry of Economy and Competitiveness under research projects [BIA2013-43085-P and BIA2016-75042-C2-1-R]. Additionally, the authors also wish to acknowledge the support provided by the Andalusian Scientific Computing Centre (CICA). This research was also supported by the project POCI-01-0247-FEDER-003474 (coMMUTe - Multifunctional Modular Train Floor), funded by Portugal 2020 through the Operational Programme for Competitiveness Factors (COMPETE 2020).

REFERENCES

[1] J. Domínguez. *Boundary elements in dynamics*. Computational Mechanics Publications and Elsevier Aplied Science, Southampton, 1993.

[2] I. Babuska F. Ihlenburg and S.A. Sauter. Reliability of finite element methods for the numerical computation of waves. *Advances in Engineering Software*, 28(7):417–424, 1997.

[3] E.T. Paik I. Babuska, F. Ihlenburg and S.A. Sauter. A generalizaed finite element method for solving the helmholtz equation in two dimensions with minimal pollution. *Computer Methods in Applied Mechanics and Engineering*, 128(3-4):325–359, 1995.

[4] F. Ihlenburg. The medium-frequency range in computational acoustics: Practical and numerical aspects. *Journal of Computational Acoustics*, (2):175–193, 2003.

[5] A.J.B. Tadeu and L.M.C. Godinho. Three-dimensional wave scattering by a fixed cylindrical inclusion submerged in a fluid medium. *Engineering Analysis with Boundary Elements*, 23(9):745–755, 1999.

SECTION 6: Seismic engineering, soil-structure dynamic interaction

ANALISYS OF CRITICAL SITUATION IN THE DYNAMIC AND SEISMIC STRUCTURAL RESPONSE OF A CANTILEVER BRIDGE. DDBD AND ENERGY BALANCE.

Carlos Iturregui Arranz*, Khanh Nguyen Gia*, Iván M. Díaz*, Jaime H. García Palacios*, José M. Soria*, Ander Atorrasagasti Villar†,

* ETS Ingenieros de Caminos, Canales y Puertos
Universidad Politécnica de Madrid
28040 Madrid, Spain
e-mail: carlos.iturregui@upm.es
ORCID: 0000-0002-8315-427X

† Arbro Consulting S.L.
Agustín de Foxá 27, 7B
28036 Madrid, Spain

Abstract. Frequently, in the professional practice during the design phase of bridges with a very evolutionary character, the phenomenon of their structural response at different instants of the useful life is not sufficiently analysed, both for vertical dynamic actions and for the seismic actions. Since the processes of shrinkage, creep and tendons relaxation interact continuously, added to the initial tendon losses and Young's modulus time evolution, there are reflected into a variation of the hyperstatic reactions and therefore into the resistant capacity for the earthquake in the piles and for the vertical dynamic action in the deck.

To illustrate the analysis, it is proposed a cantilever bridge of three spans and variable height of the two piles that support the deck, that is designed using with the Spanish IAPF standard and the concrete code EHE-08. In the case of seismic analysis, it is evaluated with inelastic time history analysis (ITHA), due to the highly non-linear character of the structural response, and in the case of vertical actions with a dynamic analysis by modal superposition method.

In both cases, the different design situations will be evaluated taking into account the evolution of the static scheme, making a comparative analysis with other methodologies such as the Direct Displacement Based Design (DDBD) and the method based on the energy balance for the case of seismic action.

Key words: Cantilever bridges, seismic response, creep, DDBD, energy balance.

1 INTRODUCTION

Despite of not being usual the application of the cantilever construction method in High Speed Railways' bridges, has been used in some occasions.

During the design phase, one of the most interesting analysis is to focus on the critical situation of the bridge against usual dynamic actions such as the passage of the train, or even more virulent and exceptional actions such as earthquakes.

During the construction and service phases of the bridge and due to a joint interaction of creep, shrinkage and relaxation phenomena deferred losses on the prestress are produced, added up to the instantaneous ones because of the mentioned rheological factors. Additionally, the bridge becomes more rigid increasing its modulus of elasticity up to a 20% on fast hardening cements according to [1].

The combination of the mentioned factors causes a variation on the modal properties of the bridge, affecting directly on its structural response. However, as the response depends mainly on the frequencies and the modal shapes, there is not an analysis that can be considered as a safer one.

The aim of this paper is to present an application exercise for the mentioned structural typology, where under different load scenarios and calculating methodologies the structural response of the bridge and its critical short-term and long-term situation will be understood. The response will be compared among the non-linear static method, linear dynamic based on modal integration method and non-lineardirect integration based on Hilber-Hughes'[2], contrasting them with the Direct Displacement Based Design (DDBD) as well as the energy balance.

2 MODEL AND MAIN RESULTS

The main characteristics of the analysed bridge are the following:

- Spans: 40 + 80 + 40 meters
- Total width: 14 meters
- Cross-section edge on the Start Segment, central span and supports: 6.5, 3.25 and 3.25 meters respectively
- Variance of cross-section: Parabolic
- Height of the pillars: 30 and 40 meters

The Staged construction method is made as follow:

- Segment 0: 5 meters over pillar (2.5 meters each side)
- Segments 1, 2 to 7 and 8: 6, 5 and 1.5 meters respectively

The construction prestress is constituted as of a family per each precast concrete with a different value and the continuity prestress acts on the central 35 meters, remaining the pillars embedded during the operational phase.

The control joints numbers are the 73, start segment over tallest pillar, and the 201, middle point of segment 8 of the main span as the figure 1 shows.

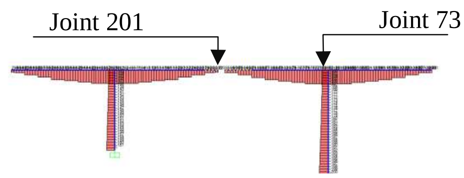

Figure 1: Axial forces during construction phase. Step 7. Before to "join the bridge".

The rebar reinforces and tendons have been obtained applying the Spanish IAPF [3] and EHE-08 [1]codes and using SAP2000 FEM software, without including the kinematic actions caused by the temperature and gradient. About the seismic loading, the spectrums I and II have been considered, corresponding to a basic acceleration of 0,24g and a D ground type according to EC-8 [4]. The longitudinal acceleration is only considered with importance coefficient of 1.

2.1. Modal Analysis approach.

The initial natural frequencies entail a problem of eigenvalues and eigenvectors of the $\left[K_0 * M_0^{-1}\right]$ (1) tensor. Adding the prestress and calculating the forces balance on the deformed position, the geometric stiffness matrix (K_{G0}) is added, being possible to get a second diagonalisation $\left[(K_0 + K_{G0}) * M_0^{-1}\right]$ (2). Once the permanent load and the prestress losses are added a third modal analysis is undertaken $\left[(K_0 + K_{G1}) * M_1^{-1}\right]$ (3). Lastly, the way the material has evolved in the time and the total losses of the prestress are evaluated $\left[(K_\infty + K_{G2}) * M_1^{-1}\right]$ (4).

Figure 2.1: Mode 1. Case service t=3650 days. f=1.339 Hz.

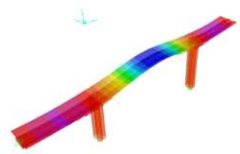

Figure 2.2: Mode 2. Case service t=3650 days. f=2.387 Hz

The results for the first five modes are shown in the next figure:

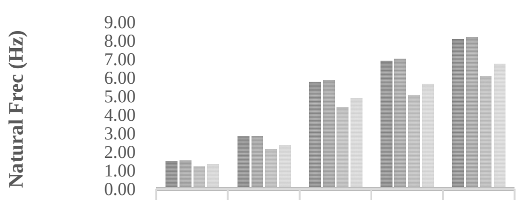

	1	2	3	4	5
Linear	1.53	2.85	5.81	6.92	8.08
Weigth+Prestress	1.54	2.87	5.87	7.01	8.19
Service t=150 days	1.20	2.17	4.38	5.07	6.08
Service 3650 days	1.34	2.39	4.89	5.68	6.76

Figure 3: Comparative first 5 natural frequencies in different construction and analysis phases.

2.2. Railway Loads response

In this section, in order to attempt the dynamic response of the bridge under the railway loads, ten high speed loading models (HSLM) proposed by [5]are used. The dynamic calculation for the different scenarios: service t=150 days and service t=3650 days are performed for different train speed ranging from 200 km/h to 400 km/h using the modal decomposition approach. The envelope of maximum vertical and acceleration at mid-span of the second span are depicted as shown in the following figure 4. It can be seen that after the 3650 of service days, the dynamic responses of the bridge are changed as consequence of the change of its natural frequencies. However, this change is not very important. In the whole range of train velocities, the maximum amplitude is barely modified.

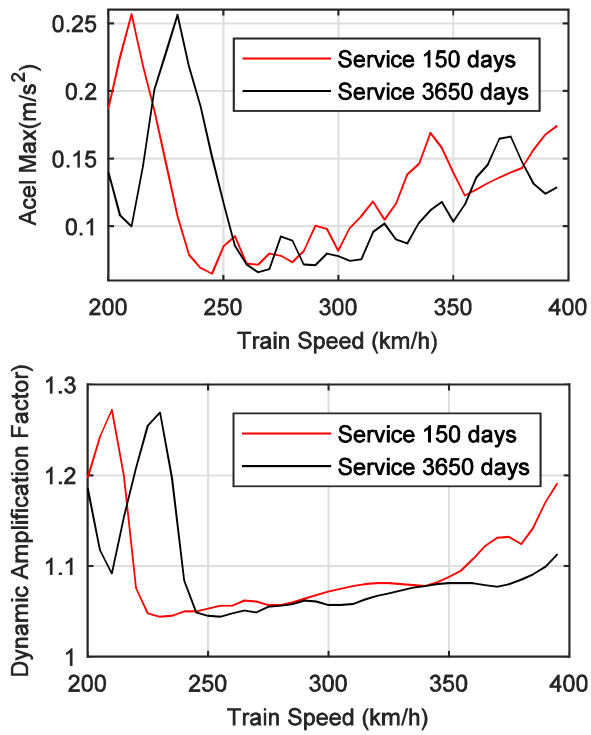

Figure 4: Envelope of the maximum acceleration and Dynamic Amplification Factor Joint 201.

2.3. Seismic Loads response

The model has been calculated based on a spectral modal calculation, using the spectra mentioned previously. The results for ductility with a value of 1 and 2 are shown in the figure 5:

	q=1		q=2	
	EC 1	**EC2**	**EC 1**	**EC2**
150 days	196,2	73,6	98,1	36,8
3650 days	163,7	65,6	81,9	32,9

Figure 5: Displacements in joint 73 for EC-8 response spectrum Type I and II.

Afterwards, a capacity calculation has been computed based on the response spectrum applying the FEMA [6]methodology, obtaining the results shown below:

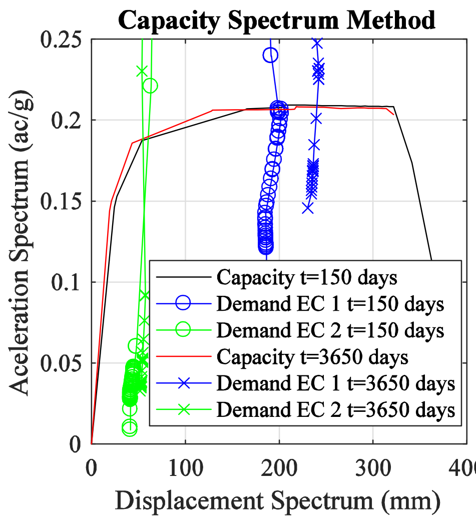

Figure6: Capacitycalculation method. In the spectrum II case the result is similar.In the spectrum I case, the difference is a 15% higher at 3650 daysdue to a higher demand in first case.

Based on the spectrums I and II, 12 accelerograms have been developed, 6 each spectrum. Applying the action of each of the accelerograms the modal dynamic integration has been undertaken, as well as the non-linear dynamic integration considering both the mechanical and geometrical non-linearity. The obtained displacements are as shown in figure 7:

	t=150 days		t=3650 days	
Record	Modal Linear	ITHA	Modal Linear	ITHA
1	64.6	157.6	58.1	<u>*182*</u>
2	69.9	133.6	58.5	<u>*151.8*</u>
3	73	111.9	56.8	94.1
4	67.7	132.8	60.1	125.8
5	59.2	110.9	55.4	<u>*134.6*</u>
6	74.1	132.7	56	124.7
7	35.6	63.9	33.5	47.6
8	37.9	51	36.2	<u>*60*</u>
9	36.9	86.5	31.2	82
10	32	56.9	31.7	43.4
11	40	77.3	28.5	65.4
12	36.2	50.7	32.9	50.1

Figure 7: Comparative displacement in joint 73 (mm). Underline in cases $U^{73}_{150}<U^{73}_{3650}$ days.

3. COMPARATION OF RESPONSE WITH OTHER METHODOLOGIES

Comparing results with the displacement based direct method [7], the result obtained for spectrum I shows that it is very similar to the modal spectral one and the capacity, with a spectral displacement for the joint 73 of 190 mm, an equivalent damping of 32,5% and an inelastic period of 1,9 sec, developing a ductility of 4.

In the spectrum II case, very small inelasticity is developed, being the deformation about 60 mm. It should be emphasized that the DDBD method foresees bigger values for the elastic drifts, so consequently the pillar will stay at an elastic range.

Regarding to the method based on the energy balance[8], the results show a spectral velocity of 0,6 m/s in the spectrum I case and 0,4 m/s in the spectrum II case in the joint 73, matching with the results obtained in the displacements.

4. CONCLUSIONS

i) The inclusion of strains caused by the prestress affects in a very slight way on the modal properties, about 1,5%, in the case of railway bridges because the sectional medium compressive stress is low.

ii) The prestress losses do not imply a severe variation on these properties, as long as the system does not get into a non-linear range.

iii) In the case of cantilever bridges, the construction process affects also in a mild way, as the bending deformations are compensated, and the axial deformation is also low.

iv) The essential structural response parameters over the pass of a train shows similar amplitude values, even though at long-term the peak are produced for running speeds at 230 km/h instead of 210 km/h.

v) The seismic deflections obtained through integration, have the tendency to be higher at short-time than long-time. Nevertheless, this does not happen in a generalized way, being in some cases a 20% higher at long-term, as the energy input is also higher because it is a more rigid situation, which is concordant with the non linear static analysis.

According with the results, the influence of the constructive process, as well as the prestress, can be negligible for the purpose of modal calculations in the case of railway bridges built by the cantilever construction method, due to the low deformations expressed on the geometrical stiffness matrix, being necessary the computation through non-linear dynamic integration over the structure's life expectancy and a compared analysis of the eventual effects, both positive and negative, as these could vary depending on the initial modal information and its evolution.

The energy balance-based and the Direct Displacement Based Design (DDBD) method appear as the fastest and simplest comparison methods in all cases.

REFERENCES

[1] Ministerio de Fomento. Reino de España., *Instrucción del Hormigón Estructural EHE-08*.

[2] E. L. Wilson, *Análisis Estático y Dinámico de Estructuras*.

[3] Ministerio de Fomento, "Instrucción de acciones a considerar en puentes de ferrocarril (IAPF)," p. 134, 2010.

[4] Comité Técnico AEN/CTN 140 Eurocódigos estructurales, "Eurocode 8: Design of structures for earthquake resistance. Part 1: General r ules, seismic actions and rules for buildings," p. 208, 2006.

[5] Ministerio de Fomento. Reino de España., "Eurocódigo 2.Parte 2: Reglas generales y reglas para puentes.," 2013.

[6] FEMA, "Improvement of Nonlinear Static Seismic Analysis Procedures," *FEMA 440, Fed. Emerg. Manag. Agency, Washingt. DC*, vol. 440, no. June, p. 392, 2005.

[7] G. M. Calvi, M. J. N. Priestley, and M. J. Kowalsky, "Displacement – Based Seismic Design of Structures," *3rd Greek Conf. Earthq. Eng. Eng. Seismol.*, p. 24, 2008.

[8] A. Benavent-Climent, "Espectros de Input de Energía en Zonas de Sismicidad Moderada. CIMNE IS-43." 2001.

1st. Conference on Structural Dynamics (DinEst 2018)
Madrid, 20–21 June

KINEMATIC BENDING MOMENTS IN OWT MONOPILES AS A FUNCTION OF THE GROUND TYPE

Luis A. Padrón, Javier Herrera, Juan J. Aznárez and Orlando Maeso

Instituto Universitario de Sistemas Inteligentes y Aplicaciones Numéricas en Ingeniería
Universidad de Las Palmas de Gran Canaria
35017 Las Palmas de G.C., Spain

e-mail: luis.padron@ulpgc.es
ORCID: 0000-0002-5693-051X

Abstract. Offshore wind energy has already proven to be a competitive technology for contributing to the generation of renewable electrical energy. With costs falling very rapidly as the technology matures, the capacity installed, for instance, in Europe, grew a significant 25% in 2017, with 13 new offshore wind farms and additional 3.1 GW. This expansion will lead to the installation of offshore wind turbines (OWT) in locations even more challenging from the geotechnical point of view, with greater depths, less capable soils and/or increasing seismic risk. In order to contribute to the field of earthquake resistant design of foundations for OWTs, this papers tackles the computation of kinematic bending moments in OWT monopiles, which is the most common type of foundation in this kind of structures. A parametric study involving different foundations and geotechnical profiles was carried out, involving large diameter monopiles, realistic material and geometrical properties for soils and pile, and a large set of layered soil profiles. For each case, compatible earthquake excitation, described through the elastic response spectra provided by Eurocode 8 - Part 1 for each ground type, is used. Kinematic bending moments were estimated using a Beam-On-Dynamic-Winkler approach. For these large–diameter monopiles, the peak bending moments are not necessarily found in the interfaces between strata, as observed with not so large diameters. Results are presented as a function of the ground type (according to Eurocode 8) and an empirical regression, based on the parameter $c_{s,30}$, for the estimation of a normalized maximum kinematic bending moments is proposed. As expected, the largest kinematic bending moments arise for C, D and E ground types.

Key words: Offshore wind turbines, piles, kinematic interaction, earthquake response

1 INTRODUCTION

This paper summarizes the results of a parametric study on the kinematic bending moments arising in OWT monopiles embedded in different soil profiles. Results are synthesized so that they can be used to estimate these maximum moments as a function of the average value of the S waves velocity in the upper 30 m of the soil profile ($c_{s,30}$).

2 PROBLEM DEFINITION

Four different steel pipe monopile configurations, defined by two different pile external diameters D and two different slenderness ratios L/D are considered (see Table 1). Steel Young's modulus, density and Poisson's ratio of $E = 210\,\text{GPa}$, $\rho = 7850\,\text{kg/m}^3$ and $\nu = 0.25$, respectively, have been adopted. The minimum pile wall thickness

Table 1: Pile configurations.

Configuration	L (m)	D (m)	t (mm)	L/D	$\delta = D_{int}/D$
1	10.5	3.5	41.37	3	0.97636
2	24.5	3.5	41.37	7	0.97636
3	18.0	6.0	66.37	3	0.97788
4	42.0	6.0	66.37	7	0.97788

recommended by the API 2A-WSD [1] is adopted. Two different boundary conditions at the pile head (free head and zero–rotation head are considered).

These monopiles are assumed to be embedded in 28 different soil profiles ranging from homogeneous half-space (profiles 1 to 4) to layered soils characterized by 6 layers over an stiff half-space (profile 12). These profiles are defined in Table 2, where h is the depth of the layer, ρ_s is the soil density and G_s is the elastic shear modulus, with each layered modeled as a viscoelastic region with 5% histeretic damping and a 0.3 Poisson's ratio. The table also presents the corresponding ground type according to the EC-8 classification.

The system is assumed to be subjected to vertically–incident S seismic waves producing ground surface earthquake motions compatible with the corresponding Eurocode 8 type 1 elastic response spectrum for 5% damping, with $a_g = 0.25\,\mathrm{g}$. Three different artificial earthquakes are used for each soil configuracion.

3 METHODOLOGY

The time histories of the bending moments along the piles are computing through the frequency domain method of response using the Frequency Response Functions obtained from an efficient semi-analytical harmonic Beam-On-Dynamic Winkler model [2, 4] of the problem in which the pile is modelled as a linear–elastic Euler–Bernoulli beam, and the expressions provided by Novak et al. [3] are used to model the soil response as a series of independent horizontal viscoelastic springs and dashpots. Maximum bending moments at a given depth computed for any time during the seismic excitation are used to build bending moment envelopes from which the maximum bending moments at any depth shown below are obtained.

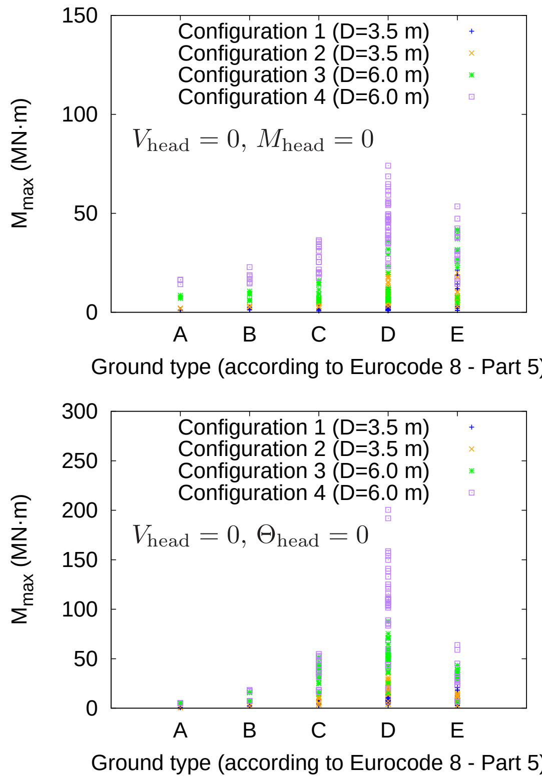

Figure 1: Maximum kinematic bending moments as a function of ground type and pile configuration. Free head (top) and Zero–rotation head (bottom) boundary conditions

4 RESULTS

Figure 1 summarizes the results as maximum bending moments, at any depth, for each ground type, pile configuration and boundary condition at the pile head. Each point represents one specific case (given pile configuration and soil profile). The results are presented in figure 2 as a function of the parameter $c_{s,30}$ together with a representation of the regression analysis performed on the data. For each boundary condition and pile configuration, an expression of the type $M_{\max}(c_{s,30}) =$

Table 2: Definition of soil profiles.

Profile	$c_{s,30}$ (m/s)	Ground Type	h (m)	c_s (m/s)	ρ_s (kg/m^3)	G_s (MPa)
P1	160	D	0-42	160	2000	51.20
P2	250	C	0-42	250	2000	125.0
P3	400	B	0-42	400	2000	320.0
P4	800	A	0-42	800	2500	1600.0
P5 A	93.33	D	0-5 (5-42)	70 (100)	1650 (1750)	8.08 (17.50)
P5 B	113.75	D	0-5 (5-42)	70 (130)	1650 (2000)	8.08 (33.80)
P5 C	131.77	D	0-5 (5-42)	70 (160)	1650 (2000)	8.08 (51.20)
P5 D	175.00	D	0-5 (5-42)	70 (250)	1650 (2000)	8.08 (125.0)
P5 E	224.00	C	0-5 (5-42)	70 (400)	1650 (2000)	8.08 (320.0)
P5 F	292.14	E	0-5 (5-42)	70 (800)	1650 (2500)	8.08 (1600.0)
P6 A	87.50	D	0-10 (10-42)	70 (100)	1650 (1750)	8.08 (17.50)
P6 B	101.11	D	0-10 (10-42)	70 (130)	1650 (2000)	8.08 (33.80)
P6 C	112.00	D	0-10 (10-42)	70 (160)	1650 (2000)	8.08 (51.20)
P6 D	134.62	D	0-10 (10-42)	70 (250)	1650 (2000)	8.08 (125.0)
P6 E	155.55	D	0-10 (10-42)	70 (400)	1650 (2000)	8.08 (320.0)
P6 F	178.72	E	0-10 (10-42)	70 (800)	1650 (2500)	8.08 (1600.0)
P7 A	154.07	D	0-5 (5-42)	130 (160)	2000 (2000)	33.80 (51.20)
P7 B	216.66	C	0-5 (5-42)	130 (250)	2000 (2000)	33.80 (125.0)
P7 C	297.14	C	0-5 (5-42)	130 (400)	2000 (2000)	33.80 (320.0)
P7 D	430.34	B	0-5 (5-42)	130 (800)	2000 (2500)	33.80 (1600.0)
P8 A	148.57	D	0-10 (10-42)	130 (160)	2000 (2000)	33.80 (51.20)
P8 B	191.18	C	0-10 (10-42)	130 (250)	2000 (2000)	33.80 (125.0)
P8 C	236.36	C	0-10 (10-42)	130 (400)	2000 (2000)	33.80 (320.0)
P8 D	294.34	E	0-10 (10-42)	130 (800)	2000 (2500)	33.80 (1600.0)
P9	140.54	D	0-5	130	2000	33.80
			5-10	100	1750	17.50
			10-42	160	2000	51.20
P10	200.00	C	0-5	160	2000	51.20
			5-10	130	2000	33.80
			10-42	250	2000	125.0
P11	201.82	E	0-5	70	1650	8.08
			5-10	130	2000	33.80
			10-15	250	2000	125.0
			15-42	800	2500	1600.0
P12	179.22	E	0-5	70	1650	8.08
			5-10	100	1750	17.50
			10-15	130	2000	33.80
			15-20	160	2000	51.20
			20-25	250	2000	125.0
			25-30	400	2000	320.0
			30-42	800	2500	1600.0

Table 3: Regression coefficients for each case

	Free head					Zero-rotation head				
Conf.	a	b	d	E^2	S	a	b	d	E^2	S
1	$-9.5 \cdot 10^{-5}$	0.049	-1.9	1462.0	4.3	$5.3 \cdot 10^{-5}$	-0.093	31.1	6947.2	9.4
2	$-1.1 \cdot 10^{-5}$	-0.017	11.5	1215.3	3.9	$3.6 \cdot 10^{-4}$	-0.26	47.1	790.6	3.2
3	$-2.6 \cdot 10^{-5}$	0.13	-1.4	6875.7	9.4	$-3.5 \cdot 10^{-5}$	-0.17	86.3	21896.2	16.8
4	$1.8 \cdot 10^{-4}$	-0.20	68.5	7457.5	9.8	$2.4 \cdot 10^{-3}$	-1.58	269.3	42683.2	23.4

$a\,c_{s,30}^2 + b\,c_{s,30} + d$ has been fitted to the results. The fitted parameters for each case are given in Table 3, together with the root mean square of the residuals $S = \sqrt{E^2/N}$, with N the number of degrees of freedom of the regression and E^2 the weighted sum of the squares residual.

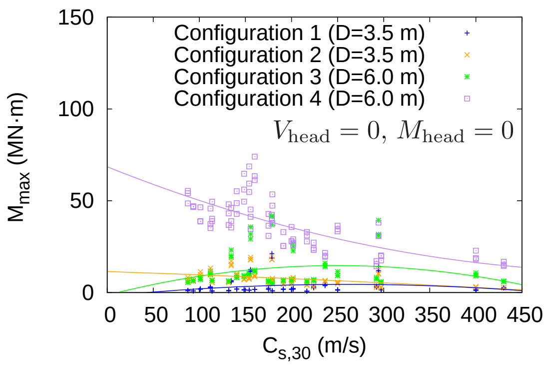

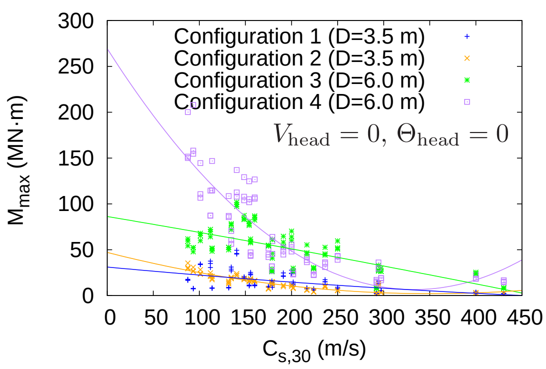

Figure 2: Maximum kinematic bending moments as a function of $c_{s,30}$ and pile configuration. Free head (top) and Zero–rotation head (bottom) boundary conditions

5 CONCLUSIONS

Seismic kinematic bending moments of 4 different offshore wind turbine monopiles in 28 different layered soil profiles have been computed for three different compatible earthquake signals and two different boundary conditions at the pile head, making a set of 672 cases modelled through a Beam–On–Dynamic Winkler formulation.

The largest maximum kinematic bending moments are obtained for D ground types (Deposits of loose–to–medium cohesionles soil or of predominantly soft–to–firm cohesive soil with $c_{s,30} < 180\,\text{m/s}$. The value of these maximum kinematic bending moments are fitted to quadratic polynomials that can be used during the initial stages of the analysis and design of these foundations in earthquake–prone areas.

6 ACKNOWLEDGMENTS

The authors acknowledge the financial support provided by the Ministerio de Economía, Industria y Competitividad and the Agencia Estatal de Investigación of Spain, and FEDER, through research project BIA2017-88770-R

REFERENCES

[1] American Petroleum Institute. Planning, Designing, and Constructing Fixed Offshore Platforms – Working Stress Design. API Recommended Practice 2A-WSD, November 2014.

[2] M Kavvadas and G Gazetas. Kinematic seismic response and bending of free-head piles in layered soil. *Géotechnique*, 43(2):207–222, 1993.

[3] M Novak, T Nogami, and F Aboul-Ella. Dynamic soil reaction for plane-strain case. *J Eng Mech Div*, 104(4):953–959, 1978.

[4] E Rovithis, G Mylonakis, and K Pitilakis. Dynamic stiffness and kinematic response of single piles in inhomogeneous soil. *Bull Earthq Eng*, 11:1949–1972, 2013.

PARAPET WALL FRAGILITY

Navas-Sánchez L.*, Cervera J.† ,Gaspar-Escribano J.M.†† and Benito B. †††

* ETS Arquitectura
Universidad Politécnica de Madrid
28040 Madrid, Spain
e-mail: laura7.l@hotmail.com
ORCID: 0000-000-2-3667-6358

† ETS Arquitectura
††,††† ETS Ingeniería en Topografía, Geodesia y Cartografía
Universidad Politécnica de Madrid
28040 Madrid, Spain

Abstract. The seismic performance of parapets is important to prevent loss of property and life due to debris falling into open spaces, such as streets and roads. Recent earthquakes had shown the fatal impact of parapet failures, without loss of structural integrity. The Mw 5.2 2011 Lorca (SE Spain) event is one example, where most of the casualties were related to falling debris.

We address the seismic vulnerability of unreinforced masonry parapets commonly found in Spain. To this aim, we develop capacity curves adopting the criteria used in the assessment of out-of-plane stability of unreinforced masonry walls subjected to seismic excitation. Subsequently, we elaborate fragility curves giving the probabilities of different damage states of parapets for different seismic inputs (spectral displacement levels).

We also develop a comparative analysis of the floor seismic demand predicted by the regulations with those estimated dynamic structural analysis applied to an analytical model of a typical building using recorded ground motion from the 2011 Lorca earthquake. The 5-storey case study structure of RC frame system is representative of residential typology built in Lorca in the 70s. Several displacement-based seismic analyses are carried out on this model, considering linear and non-linear time-history analysis especially. Some floor spectra and peak floor accelerations comparisons are shown to study the accuracy of predictions made by regulations in Lorca. To conclude, a discussion of the factors that have an impact on the fall of parapets is presented.

Key words: Parapet, Fragility, Unreinforced Concrete Masonry Walls, Secondary Structures, Seismic Assessment.

1 INTRODUCTION

Some seismic events, such as 2011 Lorca´s Earthquake, has shown that falling debris cause lost of human lifes, and hinders emergency service works. Besides, characterization of buildings and non-structural component vulnerability allows more accurate seismic risk assessments.

Orta et al., 2018, study most vulnerable Spanish buildings, made from URM load-bearing walls.

This work is focused on non-structural elements and aims two objectives; firstly, characterising the fragility of some URM parapet walls commonly found in Spain against seismic loading, and, secondly, contrasting analytical with experimental methods, in order to evaluate the accuracy of a set of latest response prediction methods in Lorca.

2 METHODOLOGY

Performance of a non-structural element depends on both, capacity and demand spectra.

2.1 Capacity and fragility curves

The method chosen to characterize URM parapet wall capacity is based on experimental studies carried out by Doherty et al. that conclude this non-structural element can be model as deformable blocks. This method is widely described in the reference number [1]. According to them, the capacity of a cantilever URM wall, as a parapet wall performs against seismic, could be represent as follows.

In first place, it is necessary to carry out a rigid body idealization that gives, by equilibrium, a maximum deformation. After that, point of yielding and ultimate point are determined as a percentage of this maximum deformation. This percentage, according to experimental studies, depends on its joint mortar state of degradation. Authors propose a URM parapet walls state of degradation definition for Spanish elements in table 1.

Finally, a trilinear capacity curve depending on weight, slenderness and state of degradation of mortar joins is obtained.

For fragility curves, cumulative probability P for being in or exceeding certain damage index at certain S_d level (normal distribution) with standard deviation ß is calculated based on equation number (1), according to S. Lagomarsino and G. Giovinazzi (2006).

$$P\ [D_{sk}|D_{s*}] = \Phi\ [\frac{1}{\beta}\ln(\frac{S_{d*}}{S_{d,k}})] \qquad (1)$$

$$\beta = 0{,}4\ln\mu, \qquad (k = 1{,}2{,}3{,}4).$$

In this way, authors propose to establish four states of damage: slight, when a non-degraded parapet wall reaches its point of yielding; moderate, when a moderate degraded parapet wall reaches its point of yielding; severe, when a severely degraded reaches its point of yielding; and collapse, when a severely degraded parapet wall reaches its ultimate point.

2.2 Demand curves

In order to characterise seismic demand adequately, it has to be considered two types of analysis. Both of them depend on the type of media that transmits seismic energy until it reaches non-structural elements. First one is due to the emplacement soil characteristics, and second one to the building movement, that at the same time, mainly depends on the dynamic properties of it and the seismic register on the building base.

3 VULNERABILITY OF SOME URM PARAPET WALLS IN SPAIN

According with Spanish literature this type of URM parapet walls are extremely common. Current Spanish regulation forbids building an URM parapet wall of less than a foot of thickness.

Most relevant URM parapet characteristics would be a height of 100cm, of a foot perforated brick wall (24 cm thickness, 1400 kg/m^3 of density and standardized resistance of masonry, f_{wm}, of 10 MPa) with mortar joints of M-5 (mortar resistance, f_m, of 5 MPa).

In addition, fragility curves will depend on the state of degradation of cracked mortar joint and the state of damage defined. Although it would be better to consider actual state of each parapet wall depending on its own maintenance and reparation or retrofit; this study is impossible for the big scale, so authors proposed the following definition of the three states of degradation for Spain.

Table 1 summarizes our state of degradation proposal criteria including potential reparations or retrofits of NSC and the existence of a previous seismic event.

Table 1: Definition of cracked mortar joint state of degradation

Joint mortar state of degradation	Parapet´s age [years]	Previous earthquake $M_w > 4$
Without degrading	< 30, face brick <50, protected façades	No, repaired or retrofitted
Moderately degraded	> 30, face brick > 50, protected façades	No, repaired or retrofitted
Severely degraded	Historical or poorly preserved buildings	Yes

It seems reasonable to take as a reference that the first 30 years of life a building structure and its enclosures are of good quality; moreover, until 50 years considering that the majority of them are covered by protecting coating or finishing for walls.

3.1 Spanish URM Parapet capacity and fragility curves

Figures number 1 and 2 summarize our results in term of capacity and fragility of URM parapet walls.

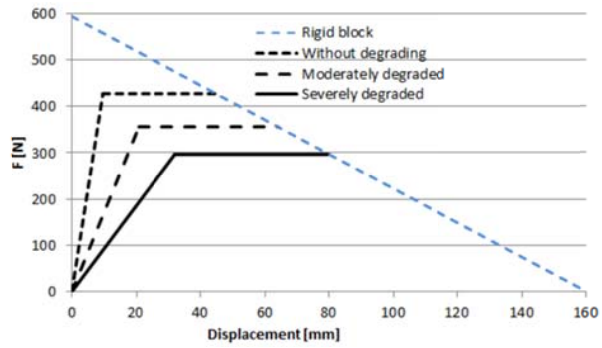

Figure 1: Capacity curve of a foot of perforated brick parapet wall of 100 cm height, one of the most common types of dangerous non-structural Spanish element against low and medium earthquake, 5-7 $M_{w.}$

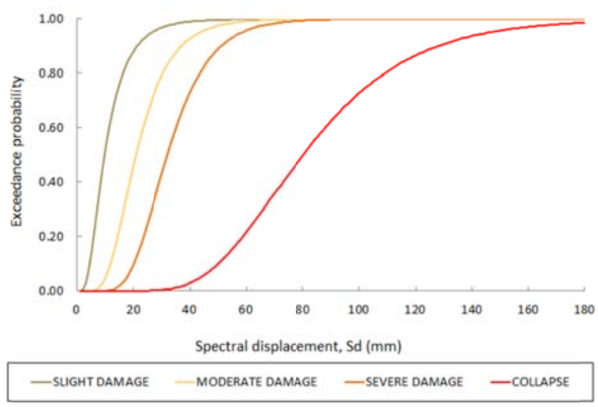

Figure 2: Capacity curve of a foot of perforated brick parapet wall of 100 cm height, one of the most common types of dangerous non-structural Spanish element against low and medium earthquake, 5-7 $M_{w.}$

4 CASE STUDY BUILDING IN LORCA

In this section, a Lorca´s building case study will be submitted to a series of seismic analysis.

4.1 Lorca´s Earthquake

The seismic event occurred in Lorca in May 2011 could be considered a medium magnitude earthquake. In the M_w 5.2 main shock, horizontal peak ground acceleration reached 0.37 g at the LOR accelerograph station in the north-central part of the town. This type of earthquake mainly affects to non-structural elements in countries with a tradition of good quality regulations, as is the case of Spain.

4.2 Case study building

The 5-storey case study structure of RC frame system is representative of residential typology built in Lorca in the 70s. Figure number 3 shows all the elements that have been modelled in the structural software SAP2000 with the objective of simulating its actual dynamic properties.

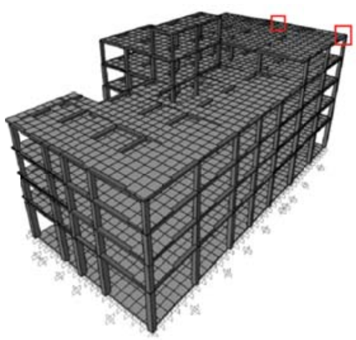

Figure 3: SAP 2000 Lorca´s building model

Design and structural dimensioning can be made according to the criteria of original architects thanks to expert data collected after the 2011 incident

4.2 Strong ground motion and seismic floor spectra

These analyses comprise all the transformations that an accelerogram suffers from the accelerograph recording station to the non-structural element base.

First necessary transformation is from the LOR station to the building emplacement. Alguacil et al., (2014), carried out this analysis. We use as accelerogram and ground spectra their result at SP11, the nearest point to the building.

Second alteration of the seismic wave is due to it is filtered by the own building movement and their main periods of vibration. This is carried out through a THA in SAP2000, being the SP11 accelerogram the input, and the seismic floor spectra and the displacement of the parapet wall head the outputs. Results of both methods are presented in figure number 4.

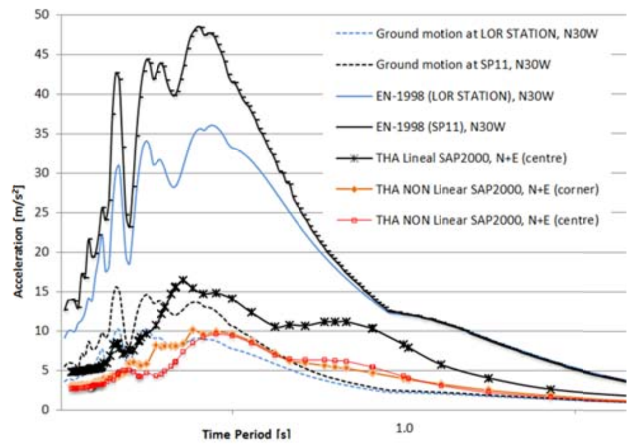

Figure 4: Spectral acceleration at the building base and the fifth floor according to different methods (EN-1998, Linear THA and Non Linear THA)

We choose to consider the parapet wall of this building before Lorca´s seismic event as without degrading; due to it presents protection in its interior face. For this case, Parapet fundamental period would be around 0,47 s, due to its height is approximately 100 cm in its most unfavourable direction.

The following maximum displacements have been obtained applying an adaptation of the N2 method or a THA carried out in SAP2000 considering capacity and demand curves developed in this paper. In all cases it is considered that the parapet wall is placed on the centre of the 5^{th} floor marked in figure number 3.

Table 2: Maximum spectral displacements according to different analysis

Input at the building base (program or method) / Input at the parapet wall base (program or method)	Behaviour of: B: building P: parapet wall	Max. displ. (mm)
Accelerogram N+E (THA Linear, SAP2000)/ Accel. (SAP2000) [Absolute Acceleration]	B: elastic P: elastic	89
Spectrum N30W (EN1998)/ Response Floor Spectrum (N2 Method)[42m/s]	B: elastic P: elastoplastic	269
Accelerogram N+E (THA Linear, SAP2000)/ Response Floor Spectrum (N2 Method) [14,5 m/s2]	B: elastic P: elastoplastic	86
Accelerogram N+E (THA Non Linear, SAP2000)/ Response Floor Spectrum (N2 Method) [9,4 m/s2]	B: elastoplastic P: elastoplastic	56
Accelerogram N+E (THA Non Linear, SAP2000)/ Response Floor Spectrum (Spectral Analysis, SAP2000) [9,4 m/s2]	B: elastoplastic P: elastic	59
Accelerogram N+E (THA Non Linear, SAP2000)/ Accel. (THA Non Linear, SAP2000) [Abs. Acc.]	B: elastoplastic P: elastoplastic	49

4 CONCLUSIONS

Several analytical case results indicate a noticeable difference with actual situation after the event. Photographs taken in May 2011 show that after the earthquake this parapet resulted moderately damaged. Besides, it has to be taken into account great differences between methods, especially EN-1998 results. According to our fragility curves, it the element shows a moderate damage, spectral displacement should be around 20 mm.

This article aims to propose a methodology, the results are still not good in their adaptation to the facts, and some more reflection is required in the characterization of the damage thresholds, in this particular building.

5 ACKNOWLEDGMENTS

This work has been partially funded by MERISUR PROJECT (National Spanish R+D+I Program for Societal Challenges, Ministry of Economy and Competitiveness (ref. CGL2013- 40492-R)

REFERENCES

[1] K. Doherty , M. C. Griffith, N. T. K. Lam and J. L. Wilson . Displacement-based seismic analysis for out-of-plane bending of unreinforced masonry walls. *Earthquake Engineering and Structural Dynamics* Vol 31, págs.000-000 (2002). doi: 10.1002/eqe.126

[2] G. Alguacil, F. Vidal, M. Navarro, A. García-Jerez and J. Pérez-Muelas. Characterization of earthquake shaking severity in the town of Lorca during the May 11, 2011 event, *Bulletin Earthquake Engineering* (2014) Vol. 12 pages 1889–1908 doi 10.1007/s10518-013-9475-y

[3] S. Lagomarsino and G. Giovinazzi. Macroseismic and mechanical models for the vulnerability and dammage assessement of current buidings. En: *Bull Earthquake* Eng 4, págs. 415-443 (2006). doi:10.1007/s10518-006-9024-z.

[4] Ratzlaff, S. *Informe de daños en edificios de viviendas causados por el terremoto de Lorca el 11/05/2011* "Edificio en Lorca". 10 de Junio de 2011

[5] B. Orta, S. San Segundo and J. Cervera, First results of fragility curves of single story, double bay unreinforced masonry buildings in Lorca. DinEst 18 (2018)

1st. Conference on Structural Dynamics (DinEst 2018)
Madrid, 20–21 June

DIRECT MODEL FOR THE DYNAMIC ANALYSIS OF PILED STRUCTURES ON NON-HOMOGENEOUS MEDIA

Guillermo M. Álamo*, Juan J. Aznárez*, Luis A. Padrón*, Alejandro E. Martínez-Castro†, Rafael Gallego† and Orlando Maeso*

*Instituto Universitario de Sistemas Inteligentes y Aplicaciones Numéricas en Ingeniería (SIANI)
Universidad de Las Palmas de Gran Canaria
Edificio Central del Parque Científico y Tecnológico, Campus Universitario de Tafira
35017 Las Palmas de Gran Canaria, Spain

e-mail: guillermo.alamo@ulpgc.es
ORCID: 0000-0001-5975-7145

† Departamento de Mecánica de Estructuras e Ingeniería Hidráulica
ETS de Ingenieros de Caminos, Canales y Puertos, Universidad de Granada
Avenida Fuentenueva s/n 18002 Granada, Spain

Abstract. A time-harmonic numerical model for the direct dynamic analysis of piled structures including soil-structure interaction effects is presented in this work. Superstructures are defined as a combination of beam and shell finite elements with the possibility of including concentrated masses and inertias. The soil-foundation interaction is limited to the one produced along the pile shaft and is modelled by a formulation based on the integral expression of the reciprocity theorem in elastodynamics and the use of specific Green's function for the layered half space. In this formulation, piles are modelled as Timoshenko's beam finite elements and treated as load lines acting within the soil. The coupling between piles and superstructures is made by imposing equilibrium and compatibility conditions at the shared pile head nodes. Because of the employed soil formulation, the resulting model only involves variables related to the structural or pile nodes, omitting any discretization of the surrounding soil. The present model was originally developed for the seismic analysis, including soil-structure interaction effects, of offshore wind turbines structures with pile foundations. However, its general formulation allows the computation of the dynamic response of any typology of piled structures (or group of structures) taking dynamic soil-structure interaction and wave propagation through the layered soil into account.

Key words: Soil-Structure Interaction, Integral Model, Finite Elements, Direct Approach, Layered Soil

1 INTRODUCTION

Pile foundations are commonly used in bridge piers, tall buildings and marine constructions. They are specially useful in soils where the superficial layers present low bearing capacity and to transmit large horizontal loads to the terrain.

Generally, when analysing the response of piled structures, substructuring approaches are used. They include the stiffness and filtering effects of the foundation through impedance functions and kinematic interaction factors, respectively. However, piled structures can also be analysed through direct models that compute, in one single step, the coupled response of the structure and foundation. In this work, a direct model for the dynamic analysis of piled foundations in layered soils is presented.

2 MODEL OVERVIEW

The proposed three-dimensional model is formulated in the frequency domain, within the scope of linear elasticity. The structures and piles are modelled through finite elements, while the interaction between the piles and soil is represented through distributed forces acting along load lines inside the soil domain. The coupling between the foundation and the structural elements is made by imposing compatibility (in terms of nodal displacements and rotations) and equilibrium (through pile-structures coupling reactions) conditions. The system can be excited by body waves that propagate through the layered soil from a far-away source. The material damping for all components is assumed to be hysteretic, through the definition of complex elastic constants.

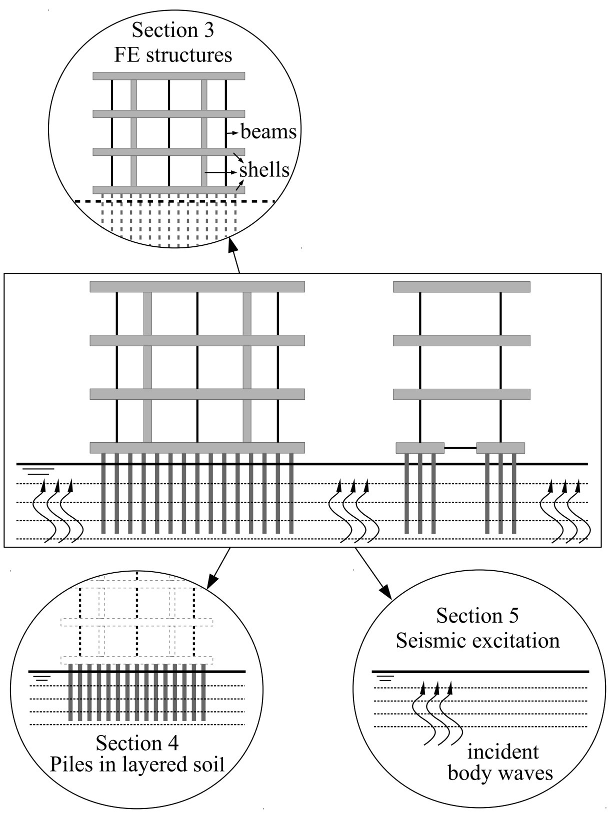

Figure 1: Sketch of the model.

The model and its different components are sketched in Fig. 1. In the following sections, the formulation of each part of the system (i.e., structures, foundation and seismic excitation) is briefly detailed. Once the equations of each of them are considered, and the proper boundary conditions are imposed, a linear system of equations (LSE) is obtained that can be solved to compute the structural and foundation response. This system has the form:

$$\mathcal{A}\ \left\{\bar{\mathbf{u}}^{\mathrm{p}}, \bar{\mathbf{q}}^{\mathrm{p}}, \bar{\mathbf{F}}^{\mathrm{pb}}, \bar{\mathbf{u}}^{\mathrm{b}}\right\}^{\mathrm{T}} = \mathcal{B}(\mathrm{b.c.}, \bar{\mathbf{F}}^{\mathrm{b}}_{\mathrm{ext}}, \bar{\mathbf{u}}_{\mathbf{I}}) \qquad (1)$$

where $\mathcal{A}$ is the matrix of coefficients of the LSE; the unknowns of the system correspond to the pile nodal displacements and rotations $\bar{\mathbf{u}}^{\mathrm{p}}$, the nodal values of the soil-pile interaction tractions $\bar{\mathbf{q}}^{\mathrm{p}}$, the pile-structure reactions $\bar{\mathbf{F}}^{\mathrm{pb}}$ and the structural nodal displacements and rotations $\bar{\mathbf{u}}^{\mathrm{b}}$; and $\mathcal{B}$ is the vector of known coefficients obtained from the boundary conditions (b.c.), the external forces acting over the structures $\bar{\mathbf{F}}^{\mathrm{b}}_{\mathrm{ext}}$ and the nodal displacements of the incident field $\bar{\mathbf{u}}_{\mathbf{I}}$. Note that the proposed model, despite including soil-foundation interaction effects, presents no variables related to any soil discretization.

3 STRUCTURES MODEL

The analysis of the superstructures is conducted by a finite element (FE) representation of them. Unidimensional (beam) and bidimensional (shell) elements can be freely combined, with the only restriction that the different elements have to be connected through their nodes.

Six degrees of freedom per node are considered corresponding to the three displacements and the three rotations in the space. For the beam elements, 2-noded elements are used. Cubic and quadratic shape functions that satisfy the static governing equation of the Timoshenko's beam [1] are considered for the lateral behaviour, while linear shape functions are used for the axial and torsional modes. On the other hand, 4-noded and 9-noded Mixed Interpolation of Tensorial Components (MITC) shell elements [2, 3] are used for the bidimensional elements. In addition to the afore-mentioned elements, additional concentrated masses or moments of inertia can be included at the structural nodes.

By assembling the elemental stiffness and mass matrices of all structural elements, the FE equations can be written as:

$$\left(\mathbf{K}^{\mathrm{b}} - \omega^2\mathbf{M}^{\mathrm{b}}\right)\bar{\mathbf{u}}^{\mathrm{b}} = \bar{\mathbf{F}}^{\mathrm{b}}_{\mathrm{ext}} + \bar{\mathbf{F}}^{\mathrm{pb}} \tag{2}$$

where $\mathbf{K}^{\mathrm{b}}$ and $\mathbf{M}^{\mathrm{b}}$ are the global stiffness and mass matrices of the structure, and ω is the excitation circular frequency.

4 SOIL-PILE MODEL

The soil-pile model corresponds to the integral model previously presented by the authors for the analysis of pile foundations [4]. In this model, the soil behaviour is obtained from the application of the integral expression of the reciprocity theorem in elastodynamics and the use of specific Green's functions for the layered half space [5]. In the soil equations, piles are reduced to unidimensional load lines, and the interaction phenomena are taken into account through distributed forces along these lines, avoiding any meshing of the pile-soil interfaces. On the other hand, the use of the layered half space Green's functions that already satisfy the free-surface and layer interfaces conditions, avoids any meshing of the soil contours. The additional stiffness and mass introduced by the piles are taken into account through their FE equations, which are coupled to the soil equations by imposing compatibility and equilibrium conditions. In the following, each part of the foundation system is detailed.

4.1 Pile finite element equations

For the pile discretization, the same beam elements than the ones used for the structures are considered. In addition to the 6 displacements and rotations, 3 extra unknowns per node are included corresponding to the nodal values of the soil-pile interaction tractions acting over the piles. Linear shape functions are used to model these interaction tractions inside each element. The corresponding FE equations are:

$$\left(\mathbf{K}^{\mathrm{p}} - \omega^2\mathbf{M}^{\mathrm{p}}\right)\bar{\mathbf{u}}^{\mathrm{p}} = \mathbf{Q}^{\mathrm{p}}\bar{\mathbf{q}}^{\mathrm{p}} - \bar{\mathbf{F}}^{\mathrm{pb}} \tag{3}$$

where $\mathbf{K}^{\mathrm{p}}$ and $\mathbf{M}^{\mathrm{p}}$ are the global stiffness and mass matrices of the piles, and $\mathbf{Q}^{\mathrm{p}}$ is the global matrix that transforms the distributed loads into equivalent nodal loads.

4.2 Soil equations

The integral expression of the reciprocity theorem in elastodynamics once the boundary conditions of the Green's functions and the studied problem are considered results in:

$$\mathbf{u}^{\kappa} = \int_{\Gamma_p} \mathbf{u}^{*}\mathbf{q}^{s}\ \mathrm{d}\Gamma_p \tag{4}$$

where $\mathbf{u}^{\kappa}$ is the vector containing the three displacements of the collocation point κ, Γ_p denotes the load lines representing the piles, $\mathbf{u}^{*}$ is the tensor containing the fundamental solution in terms of displacements and $\mathbf{q}^{s}$ is the vector of soil-pile interaction distributed loads acting over the soil.

Applying Eq. (4) to all pile nodes, and considering linear shape functions to discretize $\mathbf{q}^{s}$ inside each pile element, the following LSE is obtained:

$$\bar{\mathbf{u}}^{\mathrm{s}} = \mathbf{G}^{\mathrm{s}}\bar{\mathbf{q}}^{\mathrm{s}} \tag{5}$$

where $\bar{\mathbf{u}}^{\mathrm{s}}$ is the vector of soil displacements at the pile nodes, $\mathbf{G}^{\mathrm{s}}$ is the influence matrix obtained by Gaussian integration of the fundamental solution times the linear shape functions, and $\bar{\mathbf{q}}^{s}$ is the vector with the nodal soil-pile interaction tractions acting over the soil.

4.3 Soil-pile coupling

The pile and soil systems of equations are coupled together by imposing compatibility ($\bar{\mathbf{u}}^{\mathrm{s}} = \bar{\mathbf{u}}^{\mathrm{p}}$) and equilibrium ($\bar{\mathbf{q}}^{\mathrm{s}} = -\bar{\mathbf{q}}^{\mathrm{p}}$) conditions. This way, all soil variables are expressed in terms of the pile ones.

5 SEISMIC EXCITATION

The seismic excitation is modelled through planar wave-fronts that propagates through the soil. The total displacement field is assumed to be the superposition of the incident field produced by these waves plus the scattered field produced by the diffraction and refraction phenomena induced by the presence of the piles. Noting that Eq. (5) is written in terms of the scattered field, it can be easily rewritten in terms of the total displacements field as:

$$\bar{\mathbf{u}}^{\mathrm{s}} = \mathbf{G}^{\mathrm{s}}\bar{\mathbf{q}}^{\mathrm{s}} + \bar{\mathbf{u}}_{\mathbf{I}} \tag{6}$$

6 APPLICATION EXAMPLE

To illustrate the abilities of the presented model, the 4-storey building defined in Fig. 2 is considered. The transfer functions of the lateral displacements of the first and last floors with respect to the free-field motion are presented in Fig. 3. Two scenarios are compared in order to manifest the influence of soil-structure interaction: the infinitely-rigid base (no SSI), and the flexible soil (SSI).

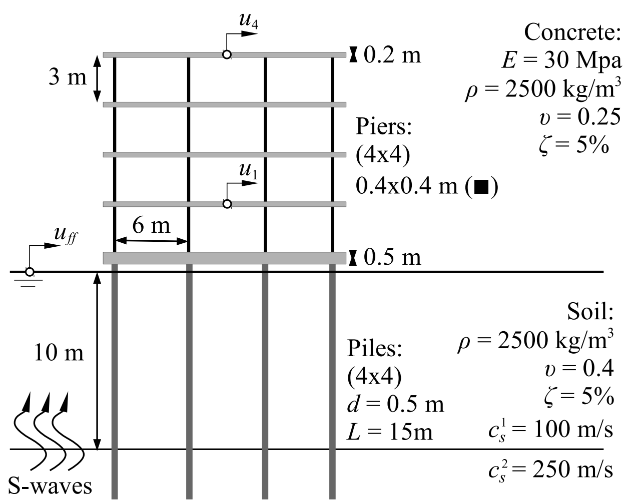

Figure 2: Definition of the application example.

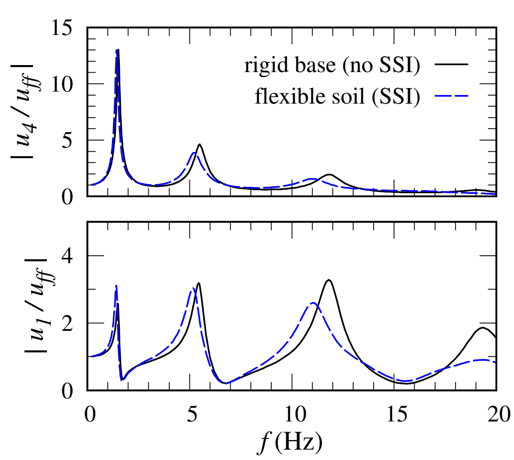

Figure 3: 1st and 4th floor displacements.

7 CONCLUSIONS

This work presents a direct model for the analysis of piled structures in layered soils including soil-structure interaction effects. The use of specific Green's functions for the layered half space in the soil equations and the treatment of the piles as load lines avoid any meshing of the soil domain, significantly reducing the number of degrees of freedom of the model. The capabilities of the proposed formulation are shown through an example.

8 ACKNOWLEDGMENTS

The authors acknowledge the financial support provided by the Ministerio de Economía, Industria y Competitividad (MINECO) and the Agencia Estatal de Invectigación (AEI) of Spain and FEDER through research projects BIA2014-57640-R and BIA2017-88770-R; and by the Ministerio de Educación, Cultura y Deporte of Spain through research fellowship FPU14/06115 (G.M. Álamo).

REFERENCES

[1] Z. Friedman and J.B. Kosmatka. An improved two-node timoshenko beam finite element. *Computers and Structures*, 47(3):473–481, 1993.

[2] E.N. Dvorkin and K.J. Bathe. A continuum mechanics based four-node shell element for general non-linear analysis. *Engineering Computations*, 1:77–88, 1984.

[3] M.L. Bucalem and K.J. Bathe. Higher-order MITC general shell elements. *International Journal for Numerical Methods in Engineering*, 36:3729–3754, 1993.

[4] G.M. Álamo, A.E. Martínez-Castro, L.A. Padrón, J.J. Aznárez, R. Gallego, and O. Maeso. Efficient numerical model for the computation of impedance functions of inclined pile groups in layered soils. *Engineering Structures*, 126:379–390, 2016.

[5] R.Y.S Pak and B.B Guzina. Three-dimensional green's functions for a multilayered half-space in displacement potentials. *Journal of Engineering Mechanics*, 128(4):449–461, 2002.

1st Conference on Structural Dynamics (DinEst 2018)
Madrid, 20-21 June

DEFINITION OF THE SEISMIC ENVIRONMENT OF THE TOKAMAK COMPLEX BUILDING OF ITER FUSION FACILITY

Fernando Rueda[1], Didier Combescure[2], Luis Maqueda[1], Jorge Olalde[1], Luis Moya[1], Víctor Domínguez[1]

[1]ESTEYCO
28036 Madrid, Spain
e-mail: fernando.rueda@esteyco.com

[2] Fusion for Energy (F4E)
ITER Dept, Technical Support
08019 Barcelona, Spain

Abstract: The Tokamak Complex is the main building of the ITER fusion reactor and it houses the 23000-ton Tokamak machine where the fusion reaction will take place. The Tokamak Complex is a single structure with a footprint of about 150 x 90 m that comprises the main systems of the nuclear facility and is supported by low damping neoprene pads, becoming one of the largest seismically isolated structures ever built. In the case of ITER, seismic requirements drive the design of the building itself as well as the vast diversity of specific equipment housed in the building. This article presents a set of analyses carried out for the seismic analysis of the Tokamak Complex. The presented works provide an overview on the modelling and analysis strategies used for the derivation of the floor response spectra and the interface loads.

Key words: ITER, seismic analysis, floor response spectra, base isolation.

1 INTRODUCTION

ITER [1],[2] is probably the most ambitious energy project in the world today, whose main objective is demonstrating the scientific and technical feasibility of nuclear fusion as an energy source. 35 nations are collaborating to build the world's largest tokamak fusion reactor, a magnetic fusion device that has been designed to prove the feasibility of fusion as a large-scale and carbon-free source of energy based on the same principle that powers our Sun and stars. ITER facility is currently under construction in the south of France. The completion of the construction works is scheduled for the end of this decade, so that the scientific experimental campaign can start around 2025.

The ITER design must face a large variety of potential threats and complex loads, including seismic events, which often drive the design of buildings and components. The seismic design of ITER must ensure the corresponding seismic safety requirements of a nuclear facility. On the other hand, too conservative approaches may have important technical and financial consequences.

This article provides a global summary of the latest works carried out by the European Domestic Agency, Fusion for Energy (F4E), for the definition of the seismic environment within the ITER Tokamak Complex, including the derivation of seismic floor response spectra as well as the characterisation of the complex interface seismic forces between the Tokamak machine and the building.

2 GENERAL DESCRIPTION OF ITER FACILITY AND SEISMIC ACTION

2.1 The ITER Tokamak Complex

The ITER Tokamak Complex (see Figure 1) is a rectangular reinforced concrete building, roughly 120 m long and 80 m wide, supported on a 1.5 thick concrete slab.

Instead of resting on the solid ground, the Tokamak Complex is partially embedded in an excavation, called the seismic pit, supported by reinforced concrete lateral walls and a concrete basemat. The building structure is seismically isolated from the seismic pit basemat by 493 anti seismic bearings (ABSs) which support the bottom basemat of the entire building.

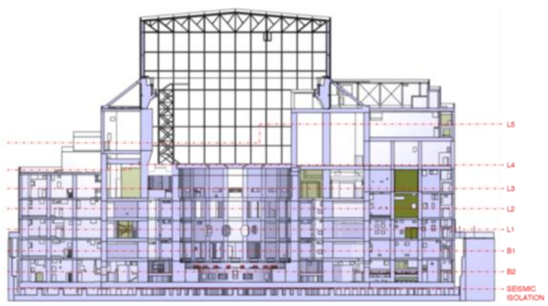

Figure 1: ITER Tokamak Complex cut view

2.2 The ITER Tokamak machine

The ITER experiment builds on the concept of the tokamak, a torus continuous tube surrounded by coils that produce a magnetic cage to confine the high-energy plasma. The ITER Tokamak machine (see Figure 2) will be 24 metres high, 30 metres wide and weight around 23000 tons. The most relevant components of the Tokamak machine from a global dynamic point of view are:

- The 10000 tons superconducting magnets in charge of producing the magnetic fields.
- The Vacuum Vessel, a 8000 tons stainless steel chamber that houses the fusion reactions.
- The 3800 tons cryostat, a stainless steel chamber surrounding the vacuum vessel and superconducting magnets to ensure an ultra-cool, vacuum environment.

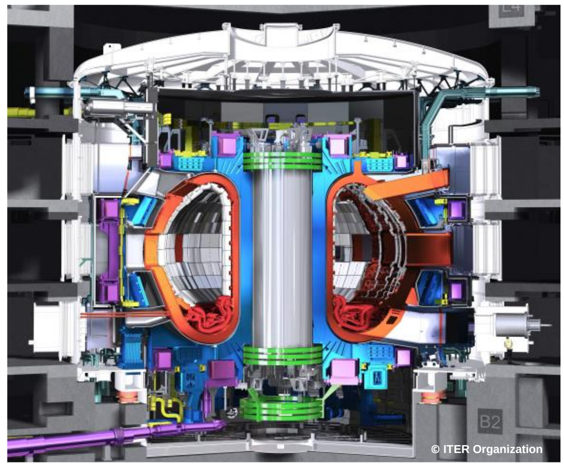

Figure 2: ITER Tokamak machine [1]

2.3 Definition of the seismic action

The design earthquake for ITER (Safe Shutdown Earthquake -SSE-) is generated as the envelope of two seismic events called the SMS and the paleoseism. The Zero Period Acceleration (ZPA) is equal to 0.315g. The vertical motion is derived by multiplying the horizontal motion by 2/3. Six statistically independent artificial signals (three for the SMS and three for the Paleo) are used in the seismic analyses.

3 OVERVIEW OF SEISMIC ANALYSIS

3.1 Dynamic representation of components

Complete new independent dynamic FE models of the Tokamak Complex have been developed (Figure 3), both with ANSYS and ABAQUS commercial packages. These models have been used for the cross-check of the reference FRS within the building and for an independent assessment of the in-machine seismic FRS and the seismic interface forces between the Tokamak machine and the building.

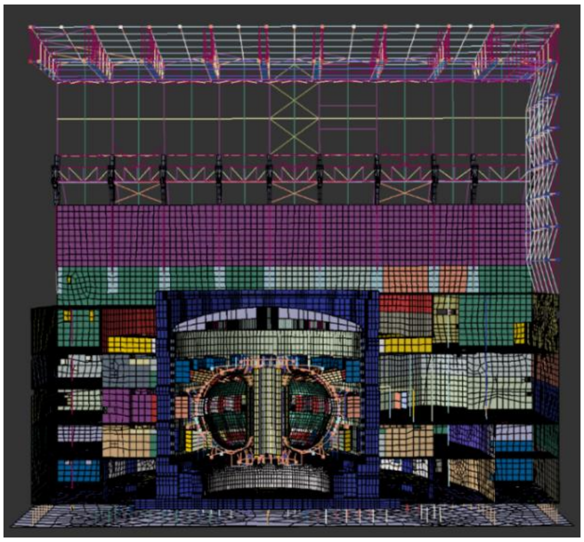

Figure 3: Independent dynamic FE model of the ITER Tokamak Complex - ESTEYCO

The dynamic FE representation of the Tokamak machine developed by ITER Organization has been assembled to the independent Tokamak Complex FE representation. This is shown in Figure 4, where specific machine parts are depicted, namely, cryostat (2*), vacuum vessel and the extension ports (3*) and central solenoid, poloidal and toroidal field coils (4*).

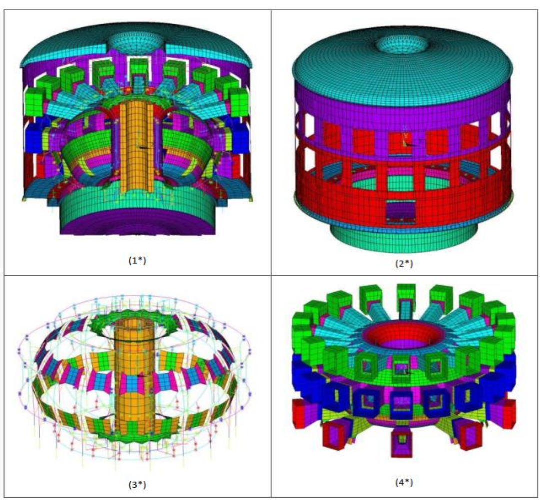

Figure 4: Global dynamic FE model of the ITER Tokamak machine – ITER Organization

3.2 Reference methodology

The seismic response of the Tokamak Complex has been obtained based on time history analyses of the assembled FE representations by the "time history method", in which the dynamic response of the system is obtained as a linear combination of its modal responses. That is, the dynamic equations of motions are integrated for the modal coordinates of the system, which is thus assumed to be linear and elastic. The resulting absolute displacements have been stored at every time step and used to obtain the acceleration time histories.

In order to account for uncertainties related to the mechanical properties of the different materials: soil, seismic isolation pads and concrete, lower bound (LB) and upper bound (UB) sets of analyses with different FE models have been carried out. The variability of seismic signals has also been considered by performing the transient analysis of each FE model for six different seismic scenarios.

4 SUMMARY OF RESULTS

4.1 Seismic FRS within the Tokamak Complex

A reference set of seismic FRS have been generated based on the results obtained from the official Tokamak Complex FE representation developed by the Architect Engineer. A full detailed set of FRS has been derived for reference damping levels (see Figure 5) in more than a thousand locations throughout the Tokamak Complex.

An additional set of seismic FRS has been derived with the independent FE model of the Tokamak Complex, in order to establish a direct and detailed comparison to validate and approve the reference seismic FRS previously described, which will be used for design purposes. This comparison has yielded a very good level of correspondence between both sets of FRS, specially when taking into account the complexity of the models, and is believed to provide a good level of confidence regarding the quality of the FE models and the procedures followed to obtain the reference seismic FRS within the Tokamak Complex.

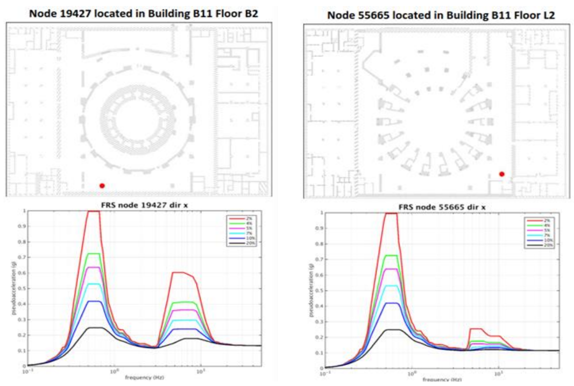

Figure 5: Examples of seismic FRS at discrete locations within the Tokamak Complex

4.2 Assessment on the seismic response of the Tokamak machine

An updated representation of the Tokamak machine seismic response has been obtained based on the same sort of linear dynamic analyses, though non-linear representations are also being used. A coupled FE model representation where the TKC and the Tokamak machine are assembled together has been used. These seismic analyses are being used to update the current estimations regarding three main aspects:

- The seismic FRS generated at a representative sample of locations within the Tokamak machine.
- The seismic forces developed at the interface between the Tokamak machine and the surrounding concrete structure.
- The relevance of non-linear effects expected to take place under severe seismic conditions.

5 CONCLUSIONS

A significant effort is being deployed to improve the knowledge of the expected seismic response of the two main ITER systems: the Tokamak machine and the Tokamak Complex.

Many analyses have been carried out in order to derive a detailed and robust representation of several global and local seismic responses. These have confirmed the conservative nature of previous studies and have provided a significant amount of information that will be used, both in the short and long term, to improve the level of understanding of the dynamic response of such a complex system, to derive a better and more robust design of the facility and to support the licensing of ITER.

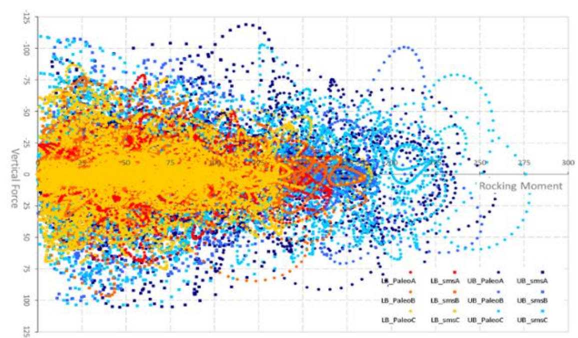

Figure 6: Seismic forces at the Tokamak machine / Building interface

ACKNOWLEDGEMENTS

The authors would like to acknowledge the continuous support and co-operation received from ITER Organization throughout this work, in particular from Mr Giulio Sannazzaro, Mr Tyge Schoiler and Mr Xiaotan Zhang, who have been crucial for the successful completion of these activities.

REFERENCES

[1] https://www.iter.org

[2] http://fusionforenergy.europa.eu

LOOKING FOR CRITERIA TO ASSESS THE RELEVANCE OF STRUCTURAL FLEXIBILITY ON THE RESPONSE OF LARGE BURIED STRUCTURES SUBJECT TO SEISMIC ACTION

Ariel Santana, Juan J. Aznárez, Luis A. Padrón and Orlando Maeso

Instituto Universitario de Sistemas Inteligentes y Aplicaciones Numéricas en Ingeniería (SIANI)
Universidad de Las Palmas de Gran Canaria
35017 Las Palmas de Gran Canaria, Spain

e-mail: asantana@iusiani.ulpgc.es
ORCID: 0000-0003-1284-190X

Abstract. This work analyzes the requirements of the models needed to estimate the seismic motions observed along large cylindrical buried structures by performing a parametric analysis of the problem using two models: one in which the structure is considered as perfectly rigid, and another one in which its actual structural flexibility is taken into account. The properties of the soil, the flexibility of the structure and the variability of the seismic incident field along the buried length are the three key aspects that affect the seismic response of the system. The parametric analysis has been carried out using a wide range of properties for both, structure and soil. Thus, computing the seismic response of a relatively large number of configurations is needed and it makes advisable the use of a numerical tool of low computational cost but accurate enough. This is why the study is performed using two models based on a Beam-on-Dynamic-Winkler-Foundation approach. These two models were previously verified by comparison against results obtained for the problem at hand using a more rigorous 3D multidomain boundary element model. The amount of results obtained by comparison of the seismic responses estimated by both models is significantly large and needs to be synthesized. These results are used to build and propose a specific criterion that can be used to elucidate under which circumstances is it possible to neglect the structural flexibility. It is found that, contrary to what is commonly assumed, the structural slenderness ratio alone cannot be used, in general, to predict the validity of the rigid structure approach: embedment lengths, soil stiffness, depth of interest and natural period of study are, also, key parameters that need to be taken into account. A close-form criterion is proposed in table form taking all such parameters into account.

Key words: Buried Structures, Seismic Response, Structural Flexibility, Design Criterion

1 INTRODUCTION

One aspect to consider when setting up a model for studying the motions of seismic origin within a buried structure is whether it is really needed to take into account its actual structural flexibility or, on the contrary, a perfectly rigid representation of it is enough. It might be tempting to consider large non-slender structures as perfectly rigid in relationship with the surrounding soil. The kinematic response of an actual structure of that kind was studied for instance in Vega et al. [4], where differences between rigid and flexible approaches were quantified and, even though the structure was non-slender and, apparently, very rigid. The rigid and flexible models provided results with important discrepancies.

This work contributes to this issue by presenting a criterion that can be used for practical purposes by structural and geotechnical engineers to establish if a structure under seismic excitation can be considered as a rigid body or, on the contrary, its real flexibility can not be neglected. The criterion is based on a parametric analysis that studies the errors between the motions of seismic origin provided by two Beam-on-Dynamic-Winkler-Foundation (BDWF) models in which the buried structure is considered respectively from both points of view (perfectly rigid or with its actual flexiblity).

2 PROBLEM DESCRIPTION

The structure is idealized geometrically as a completely buried solid cylinder of diameter D or a cylindrical shell with constant outer and inner diameters D and D_{int}, and length L. The type of section will be specified by a parameter $\delta = D_{\mathrm{int}}/D$ defining a hollow ($0 < \delta < 1$) or solid ($\delta = 0$) cross section. Welded contact conditions are assumed at the interface between the structure and the surrounding soil, which is assumed to be a isotropic and homogenous half–space with Poisson's ratio ν_s, density ρ_s and shear wave velocity V_s. The system, for which a linear–elastic behaviour is assumed, is subjected to vertically–incident shear waves.

The properties of the soil, the flexibility of the structure and the variability of the seismic incident field along the buried length of the structure are three key aspects that affect the seismic response of the system. In this study, the flexibility of the structure depends on the type of cross section (solid or hollow), the material properties, and the slenderness ratio. The variability of the incident field, on the other hand, is related to the soil wave velocity (or soil stiffness) and the characteristics of the seismic waves. Thus, the study will be performed varying the following four parameters of the problem: a) Type of structural cross section: hollow ($\delta = 0.85$) or solid ($\delta = 0.00$); b) Slenderness ratio of the structure ($L/D = 2-10$); c) Soil shear wave velocity ($\mathrm{V}_s = 200 - 1000\,\mathrm{m/s^2}$) and; d) Embedment lengths of the structure (L = 20, 40, 60 and 80 m).

The rest of properties, considered as non–relevant for the aim of this study, are kept constant. The following properties, characteristic of concrete, are assumed for the structure: Young's modulus $E = 2.76 \cdot 10^{10}\,\mathrm{N/m^2}$, Poisson's ratio $\nu = 0.2$ and density $\rho = 2500\,\mathrm{kg/m^3}$. On the other hand, Poisson's ratio $\nu_s = 0.3$ and density $\rho_s = 1570\,\mathrm{kg/m^3}$ are kept constant for the soil. With all this, a wide range of values for the ratio E/E_s is covered, going from below 3 for ground type A to over 200 for ground type D (see Eurocode–8 [1]).

The vertically–incident S wave field that impinges the system generates free–field ground surface accelerations compatible with the type 1 design elastic horizontal ground motion acceleration response spectra also provided by Eurocode–8 [1] for each ground type. Therefore, different synthetic accelerograms, one for each ground type, are used as excitation motion according to the shear wave velocity defining the soil in each configuration.

The results need to be synthesized and presented in terms of the deviation of the response obtained from the rigid body assumption with respect to a flexible structure model. This deviation is defined as differences between the horizontal acceleration elastic response spectra characterizing the horizontal motions at different depths z/L. These differences will be quantified in terms of average differences along every one of the three branches defining the elastic response spectra used (see figure 1). The average difference $\bar{\epsilon}(z)_j$ along branch j is defined as

$$\bar{\epsilon}(z)_j[\%] = \frac{1}{n_j}\sum_{i}^{n_j}\left|\frac{S_e^f(T_i,z) - S_e^r(T_i,z)}{S_e^r(T_i,z)}\right|\Psi_i \quad ; \quad j = \begin{cases} 1,\, T_i & / \quad T_i \leqslant T_{\mathrm{B}} \\ 2,\, T_i & / \quad T_{\mathrm{B}} \leqslant T_i \leqslant T_{\mathrm{C}} \\ 3,\, T_i & / \quad T_{\mathrm{C}} \leqslant T_i \leqslant 2 \end{cases} \tag{1}$$

where

$$\Psi_i = \frac{1 + \mathrm{sign}\left(S_e^f(T_i,z) - S_e^r(T_i,z)\right)}{2} \times 100 \tag{2}$$

and n_j is the number of specific periods at which the elastic response spectrum is computed along branch j, while $S_e^r(T_i, z)$ and $S_e^f(T_i, z)$ are the elastic horizontal acceleration response spectra characterizing the horizontal motions of the embedded structure either as a perfectly rigid or flexible body, respectively. The values of the periods T_{B} and T_{C} depend on the ground type according to Eurocode–8 [1]. For the present study, the responses are always computed at 120 different periods distributed from $T = 0.01\,\mathrm{s}$ to $T = 2\,\mathrm{s}$. Note that errors are not added when the solution provided by the rigid model is more conservative than that of the flexible one. The rotational motions along the structure are not taken into account when computing those elastic horizontal acceleration response spectra.

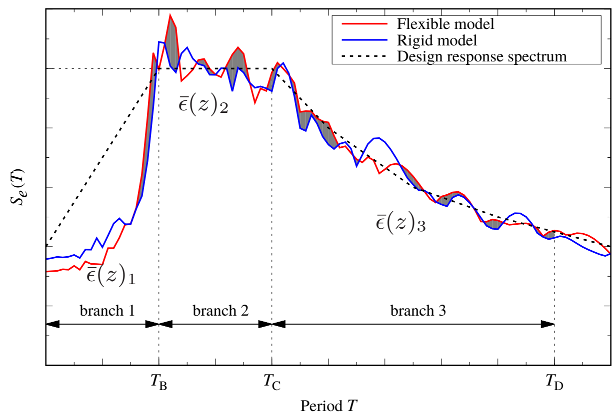

Figure 1: Representation of average difference $\epsilon(z)_j$ (shaded area) between rigid body assumption and flexible response spectra along three branches defining the design response spectrum.

3 METHODOLOGY

Carrying out the wide parametric study established in the previous section makes advisable the use of a numerical tool of low computational cost but accurate enough. This is why the present study is carried out through the use of a frequency domain analysis procedure in which the frequency response functions (FRFs) for each case are computed by means of a linear–elastic model based on the Beam-on-Dynamic-Winkler-Foundation (BDWF) approach, considering a vertically–incident S wave field as excitation. The response of the system is then computed for a given seismic input signal compatible with the corresponding response spectrum. In order to be able to adequately represent the behaviour of the non-slender configurations, the Timoshenko beam formulation [3], as part of a BDWF approach, is adopted in this work to model the buried structure. Verification and detailed explanation of these BDWF models can be seen at Santana et al. [2].

4 RESULTS

The amount of results obtained from the parametric analysis is significantly large, and need to be synthesized. First, a cut–off value for the average error (as defined in equation (1)) is established as the maximum error for which the rigid approach can still be considered adequate for the problem at hand. For practical applications, and taking into account the uncertainties associated to data and models, an average error below 10% is considered acceptable and is used as limit value.

The average errors obtained in the low-periods branch when using the rigid assumption are much larger than along the intermediate-periods branch, while they are generally below 10% in the high-periods branch for the values of the slenderness ratios (L/D) and wave propagation velocity (V_s) considered in this study. In any case, discrepancies increase with the embedment length L of the structure, with softer soils and also, as expected, for more slender structures, although in many cases, and contrary to what was anticipated, the error is quite independent of the slenderness ratio. The discrepancies also tend to increase for hollow structures, but this is not always true and, in any case, the differences between the errors in the solid and hollow configurations are not significant, which allows to propose a criterion not dependent on this character.

The obtained results can be synthesized in table form with the aim of serving as a practical guide for helping to know if the hypothesis of infinite rigidity of a large buried structure (with the mentioned safety margin of 10%) is applicable when evaluating its seismic response (see Table 1). The criterion is proposed only for the low- and intermediate-periods branches, as the rigid model is considered always valid for calculations in the high-period branch. As an application example, consider a

Table 1: Conditions that should hold for considering the rigid assumption as valid for computing the spectral seismic response of a buried structure for each spectrum branch and depth of interest ($\bar{\epsilon}(z) \leqslant 10\%$)

	Low-periods branch	Intermediate-periods branch
$z/L = 0$	$L \leqslant 60$ and $\frac{V_s}{L} \geqslant 12$	$\frac{V_s}{L} \geqslant 7.5$
$z/L = 0.25$	$L \leqslant 40$ or $600 \leqslant V_s \leqslant 900\,\mathrm{m/s}$	$L \leqslant 60$ or $-6 \leqslant \left(\frac{L}{D} - \frac{V_s}{85}\right) \leqslant 2$
$z/L = 0.50$	$L \leqslant 40$ and $V_s \geqslant 600\,\mathrm{m/s}$	$L \leqslant 60$ and $\frac{V_s}{L} \geqslant 10$
$z/L = 0.75$	$L \leqslant 40$ and $V_s \geqslant 600\,\mathrm{m/s}$	$L \leqslant 40$ or $\frac{V_s}{L} \geqslant 8$
$z/L = 1.00$	$\frac{V_s}{L} \geqslant 10$	$\frac{V_s}{L} \geqslant 4$

structure with slenderness ratio $L/D = 7$ embedded in a soil characterized by a wave propagation velocity $V_s = 700\,\mathrm{m/s}$ (ground type B). Following the criterion defined in table 1, using a rigid model for computing the response at $z/L = 0.25$ is always suitable for the embedment lengths studied herein. However, for a different wave velocity $V_s = 400\,\mathrm{m/s}$ (even if it is the same ground type), the rigid body assumption is only valid if $L \leqslant 40\,\mathrm{m}$ in the low-periods branch, or $L \leqslant 60\,\mathrm{m}$ in the intermediate-periods branch.

5 CONCLUSIONS

It is not possible to elucidate whether a buried structure behaves as rigid or not, based only on the slenderness ratio L/D. It is also necessary to take into account soil stiffness and embedment length, as both parameters are directly related to the variability of the seismic excitation along the buried structure. Besides, the depth of the point of study and the value of the period of interest can also influence the type of response.

6 ACKNOWLEDGMENTS

The authors would like to thank Professor Enrique Alarcón, as his ideas, questions and suggestions triggered this piece of research. They also wish to thank him for his contributions and the fruitful discussions concerning to the problem studied and model developed.

This work was supported by the Ministerio de Economía, Industria y Competitividad and the Agencia Estatal de Investigación of Spain and FEDER through research projects BIA2014-57640-R and BIA2017-88770-R .

REFERENCES

[1] Eurocode-8. *Design of Structures for Earthquake Resistance. Part 1: General Rules, Seismic Actions and Rules for Buildings*. European Standard EN-1998-1, CEN/TC 250: Brussels, 2003.

[2] A. Santana, J. J. Aznárez, L. A. Padrón, and O. Maeso. A criterion to assess the relevance of structural flexibility on the seismic response of large buried structures. *Soil Dynamics and Earthquake Engineering*, 106:243–253, 2018.

[3] S. P. Timoshenko. On the correction for shear of the differential equation for transverse vibrations of prismatic bars. *Philosophical Magazine Series 6*, 41(245):744–746, 1921.

[4] J. Vega, J. J. Aznárez, A. Santana, L. A. Padrón, E. Alarcón, J. J. Pérez, and O. Maeso. On soil-structure interaction in large non-slender partially buried structures. *Bull Earthq Eng*, 11:1403–1421, 2013.

NUMERICAL MODEL FOR THE ANALYSIS OF THE DYNAMIC RESPONSE OF THE SORIA DAM INCLUDING SOIL—STRUCTURE INTERACTION

J.C. Galván, L.A. Padrón, J.J. Aznárez, O. Maeso

Instituto Universitario de Sistemas Inteligentes y Aplicaciones Numéricas en Ingeniería

(SIANI) Universidad de Las Palmas de Gran Canaria

Edificio Central del Parque Científico y Tecnológico

Campus Universitario de Tafira, 35017, Las Palmas de Gran Canaria, Spain

e-mail: jgalvan@diea.ulpgc.es
ORCID: 0000-0001-8515-0881

Abstract. Soria arch dam and reservoir is the largest infrastructure of this type that exists in the Canary Islands both in capacity (32 hm^3) and height (120 m). It is located in the south of the Island of Gran Canaria, between the municipalities of Mogán and San Bartolomé de Tirajana.

The goal of this paper is the development of a numerical model for the analysis of the dynamic and seismic behavior of this arch dam. The model includes both the concrete arch dam and the surrounding area, so that soil-structure interaction phenomena can be taken into account as accurately as possible. On the contrary, the water-soil-structure interaction effects are not included in the model. The model is used to evaluate the magnitude of soil-structure interaction and also the influence of the accuracy of the geometrical representation of the surrounding topography on such soil-structure interaction effects.

To do so, two different numerical models are built. On the one hand, a Finite Element Model of the actual geometry of the concrete dam wall is developed and used to perform a modal analysis of the fixed-base model. Then, several three-dimensional frequency-domain Boundary Element models of both the concrete dam and the surrounding topography are built. All of these models include the actual geometry of the dam wall and different approximations of the surrounding soil, ranging from a very simplified straight prismatic canyon to an elaborate model of the actual topography. These BEM models are used not only to estimate compliant-base natural frequencies and mode shapes, but also to study the seismic response of the system when subjected to incident planar seismic waves.

The results show that the influence of the soil—structure interaction effects on the dynamic response of the system is quite significant. At the same time, the relevance of developing a very precise mesh of the surroundings is not important when studying the dynamic response of the dam itself, unless the response around the abutments is of interest.

Key words: Arch dam, Boundary Element Method, dynamic soil—structure interaction.

1 INTRODUCTION

Located in the south of the Island of Gran Canaria, between the municipalities of Mogán and San Bartolomé de Tirajana, the Soria dam is a concrete double-curvature arch dam. The structure was constructed from 1962 to 1972. It is 120 meters in height (above foundation) and with a thickness of the crown cantilever decreasing from 17,30 m at the base to 3 m at the crest. It is provided with 5 galleries inside its body [1]. Some pictures of Soria dam are shown in Fig. 1.

Fig. 1 : Soria arch dam (Gran Canaria).

The present study aims at building a three-dimensional numerical model for the analysis of the dynamic and seismic behavior of the Soria arch dam, that can later be used for monitoring the structural health of this infrastructure. In order to do so, the influence of the soil-structure interaction effects, and of the accuracy of the geometrical representation of the surrounding topography, will need to be assessed.

2 METHODOLOGY

Firstly, a geometrical model was developed consisting of two parts: the dam wall and the canyon. The geometry of the dam wall was constructed according to the information gathered from a specific study made in 1991 [2]; on the other hand, a geometrical representation of the actual canyon and surroundings was obtained from topographic information available in the databases of Gobierno de Canarias [3].

Secondly, a modal analysis was carried out. For that, a 3D finite element model of the dam wall was developed to obtain the mode shapes of vibration of the fixed-base model. The finite element mesh corresponding to the geometry of the dam wall was constructed by means of 4250 tetrahedral 3D elements and 7805 nodes (Fig. 2). For the Finite Element Analysis, Code_Aster was used, which is a Finite Element Analysis software engine [4].

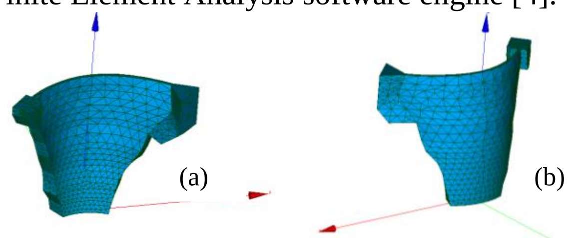

Fig. 2: 3D mesh used for the FEM analysis. (a) downstream side view (b) upstream side view.

Thirdly, harmonic analyses of the system, considering both fixed- and compliant-base configurations, were carried out using the multidomain Boundary Element Method code in the frequency domain described in Maeso et al. [5]. Wall and surrounding ground are modelled as coupled homogeneous viscoelastic media. In this case, the Boundary Element Method allows to take intrinsically into account the unbounded character of the soil medium, without the need of absorbing boundaries or any other mathematical artifact. On the contrary, the free-field mesh is truncated at a distance such that only the scattered wave fields are sufficiently damped. Nine-node quadrilateral elements and six-node triangular boundary elements are used to mesh the boundaries.

Fig. 3 shows the boundary element mesh used for the fixed-base model. At the same time, the influence of soil-structure interaction and of the accuracy of the geometrical representation of the surrounding topography on such soil-structure interaction effects needs to be evaluated. In order to do so, three of the BE discretizations are used. Figures 4, 5 and 6 show the actual geometry of the dam wall and different approximations of the surrounding soil, from a straight prismatic canyon with two different amounts of free-surface (Fig. 4 and 5, for free-surface extensions equal to two or three times the height of the dam wall) to a model of the actual topography (Fig. 6).

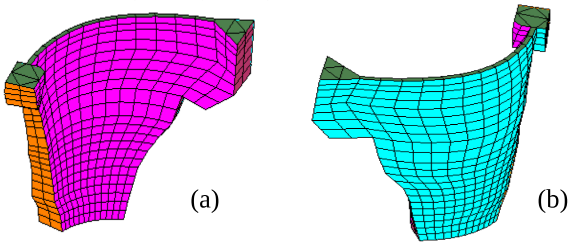

Fig. 3: 3D mesh used for the BEM analysis of the dam wall. (a) downstream side view (b) upstream side view.

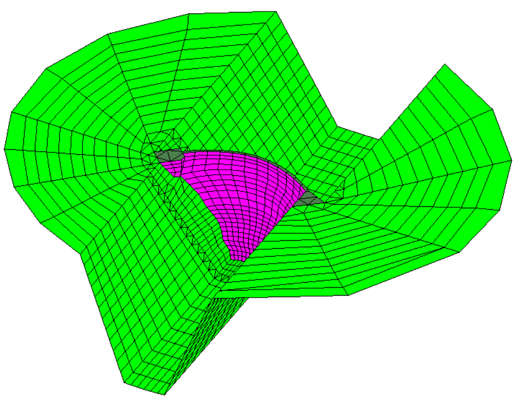

Fig. 4: BE model, prismatic canyon. Extension of the free-field discretization: 240 m

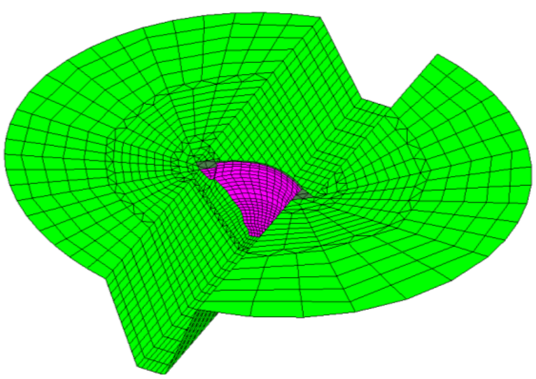

Fig. 5: BE model, prismatic canyon. Extension of the free-field discretization: 360 m

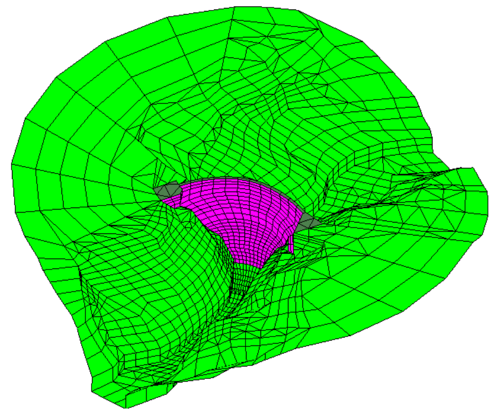

Fig. 6: BE model. Approximation of the actual topography of the canyon. Extension of the free-field discretization: 240 m

The node studied is approximately located at the midpoint of the dam crest, so frecuency response functions obtained by BE method in this node will be plotted for 4 cases: Fixed-base, and compliant-base with different geometries (Fig 4, 5 and 6). On the one hand, in the fixed-base analysis, a unit harmonic horizontal displacement along the upstream direction was given at the abutment of the dam; on the another hand, for the compliant analysis, the system is assumed to be impinged by seismic time-harmonic plane waves. For this analysis, it was assumed that the incident wave field consists solely of plane SH waves propagating vertically with a horizontal upstream free-field ground surface motion (upstream).

The concrete dam wall and the foundation rock material are assumed to be viscoelastic with the properties shown in Table 1 [1, 6].

Property	Dam concrete	Foundation rock
Shear modulus, G (MPa)	8167	12083
Mass density, ρ (kg/m^3)	2300	2143
Poisson's ratio, υ	0,2	0,2
Internal damping ratio, ξ	0,01	0,01

Table 1: Material properties

4 RESULTS

The first three symmetrical mode shapes of vibration obtained with a modal analysis of the fixed-base FEM model, together with the modes infered from the harmonic analysis with the fixed-base BEM model, are shown in Figure 7. A very good agreement is observed between the two sets of results, in terms of both frequency and shape, which contributes to validate the BE wall mesh used below in the compliant-base analysis.

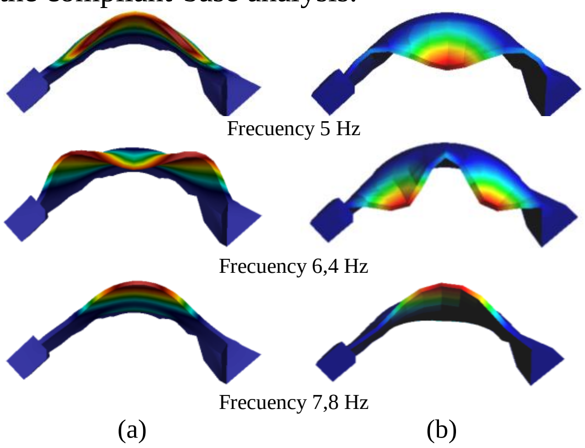

Fig. 7: Symmetrical mode shapes : (a) FEM ; (b) BEM.

The frequency response functions obtained with the frequency domain analysis of the fixed-base and compliant-base models with different geometries at the node studied are plotted in Fig. 8.

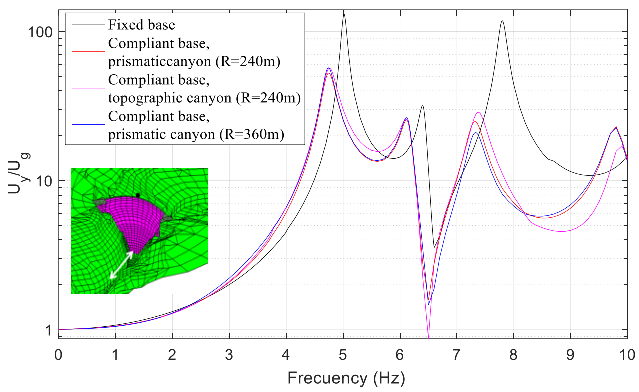

Fig. 8: FRFs. Transversal response of the midpoint of the dam crest.

5 CONCLUSIONS

The frequency-domain analyses carried out show that the soil—structure interaction has an important influence on the seismic response of the dam wall (the vibration frequencies on compliant base are 7% lower than in fixed base); nevertheless, the actual topography of the canyon around the dam wall seems to have a very low influence.

After having estimated the most relevant natural frequencies and modal shapes of the structure, an experimental campaign will be carried out in order to extract the empirical dynamic properties of the system and perform a model updating procedure on the numerical model presented herein.

ACKNOWLEDGEMENTS

The authors wish to thank Jaime J. González Gonzálvez for the information provided about the Soria dam.

REFERENCES

[1] Jaime J. González. Presa de Soria. Una historia de proyectos, informes y notas informativas. Gran Canaria 1935-1972. Depósito Legal: GC.562-2010.

[2] INPROES, S.A. and Hermanos Garrote de Marcos, S.A. Documento XYZT de la presa de Soria, 1991.

[3] Infraestructura de Datos Espaciales de Canarias. www.idecanarias.es. 2017.

[4] EDF R&D, Code_Aster software: Analysis of Structures and Thermomechanics for Studies & Research, 2017.

[5] O. Maeso, J.J. Aznárez, J. Domínguez. Three-dimensional models of reservoir sediment and effects on seismic response of arch dams. Earthquake Engineering and Structural Dynamics, 33, pp. 1103-1123, 08/2004.

[6] Instituto Eduardo Torroja de la construcción - Ministerio de Vivienda (España). Catálogo de Elementos constructivos del Código Técnico de la Edificación, 2010. Disponible en <https://www.codigotecnico.org/images/stories/pdf/aplicaciones/nCatalog_infoEConstr/CAT-EC-v06.3_marzo_10.pdf>

1st Conference on Structural Dynamics (DinEst 2018)
Madrid, 20-21 June

NUMERICAL SIMULATION OF SHAKING TABLE TESTS ON A REINFORCED CONCRETE WAFFLE-FLAT PLATE STRUCTURE USING OPENSEES

D. Galé-Lamuela*, A. Benavent-Climent* and G. Gonzalez-Sanz*

* ETS Ingenieros Industriales
Universidad Politécnica de Madrid
28040 Madrid, Spain
e-mail: david.gale@upm.es
ORCID: 0000-0002-3110-0050

Abstract. Numerical simulations and dynamic tests are the most powerful tools for performance-based earthquake engineering research. This paper presents an analytical study conducted on a model that represents a 2/5 scaled reinforced concrete waffle-flat plate structure tested on a shaking table. The numerical model was built using OpenSees, an open source software used specially in research tasks for nonlinear analysis of structures. The structure tested in the shaking-table was subjected to successive seismic simulations of increasing amplitude until collapse. In each seismic simulation the history of acceleration applied to the shaking table reproduced the ground motion recorded during the Campano-Luchano earthquake at Calitri, scaled to four levels of acceleration ranging from 100% to 350%. The numerical model was subjected to the four histories of acceleration actually recorded on the shaking table during the tests. It is concluded that the numerical model reproduces accurately the experimental response in terms of maximum displacements, forces and history of input energy. The correspondence in terms of history of displacements and accelerations is also satisfactory.

Key words: Shaking-table tests; numerical simulations; waffle-flat plate structures.

1 INTRODUCTION

Reinforced concrete (RC) structures consisting of waffle-flat plates (WFP systems herein) are commonly used in several earthquake-prone regions as main seismic force resisting systems. The development of seismic codes within the framework of Performance Based Design requires information on the inelastic response characteristics and on the behavior of typical structures designed under current codes. This information comes from both experiments (preferably shaking table tests) and nonlinear time history analyses of numerical models calibrated with test results. Shaking table tests can reproduce in a very realistic way the seismic demands on structures, and can capture accurately complex phenomena such cumulative damage and rate-of-loading effects. However, shaking table tests are very expensive and time consuming. This makes this experimental approach unfeasible for conducting parametric studies that require obtaining and summarizing the responses of a large number of structures subjected to a different types of ground motions. On the other hand, the capabilities of modern computers and specialized software allow to conduct a large number of nonlinear time history analyses of complex models with a reasonable limited amount of time. For the results of these analyses to be reliable and valid, it is important to use numerical models properly calibrated with test results. The best calibration is attained using the results of shaking table tests. In this context the investigation presented in this paper is the first part of a broader ongoing research project aimed at investigating the response of RC WFP systems subjected to seismic loadings. This paper presents a detailed description of the development of a numerical model that represents a WFP structure recently tested by the authors in a shaking table. This numerical model constitutes the benchmark model that is being used in on-going parametric studies.

2 TEST SPECIMEN DESCRIPTION

The test specimen was a structure scaled 2/5 from a three-story prototype struture of RC WFPs supported on insolated columns designed following the limit state design method of the Spanish RC code EHE-08 [1] to sustain the gravity loads and the lateral seismic loads prescribed by the current Spanish seismic code NCSE-02 [2]. Figure 1 shows the geometry and reinforcing details of the test specimen. The yield stress of the steel reinforcement was 525 and 543 MPa for the longitudinal rebars of diameter 8mm (Ø8) and 6mm (Ø6) respectively, and 656 MPa for the stirrups. The concrete compression strength the day of the tests was 43 MPa.

The tests specimen was subjected to four seismic simulations referred to as C100, C200, C300 and C350 herein. In these simulations the test specimen was subjected to the ground motion recorded at Calitri during the Campano Lucano (1980) earthquake, scaled in amplitude to 100%, 200%, 300% and 350%. The corresponding peak ground accelerations, PGAs, were 0.16g, 0.31g, 0.47g and 0.55g. A more detailed description of the tests can be found in Benavent-Climent et al. (2016).

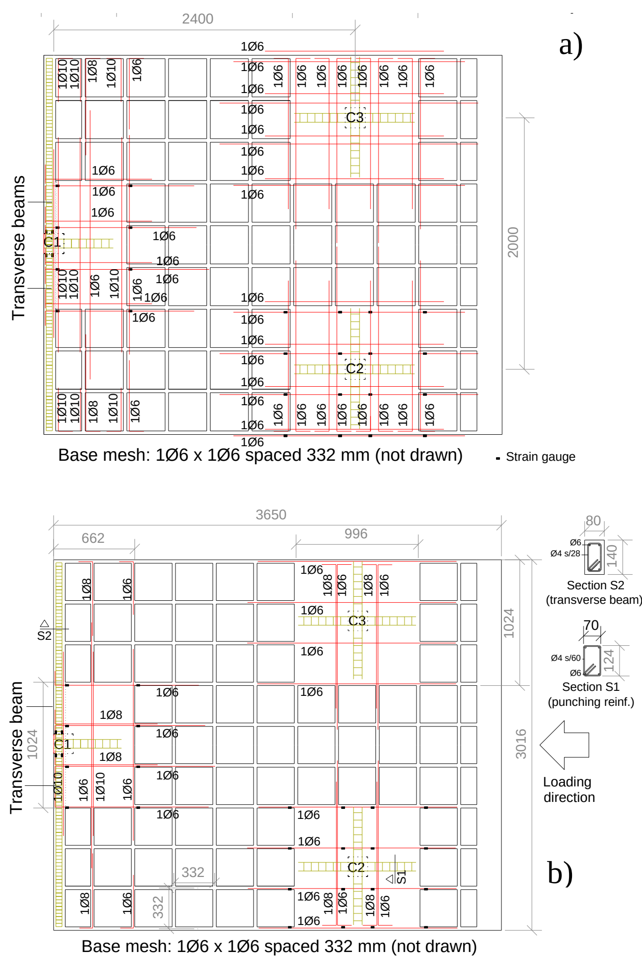

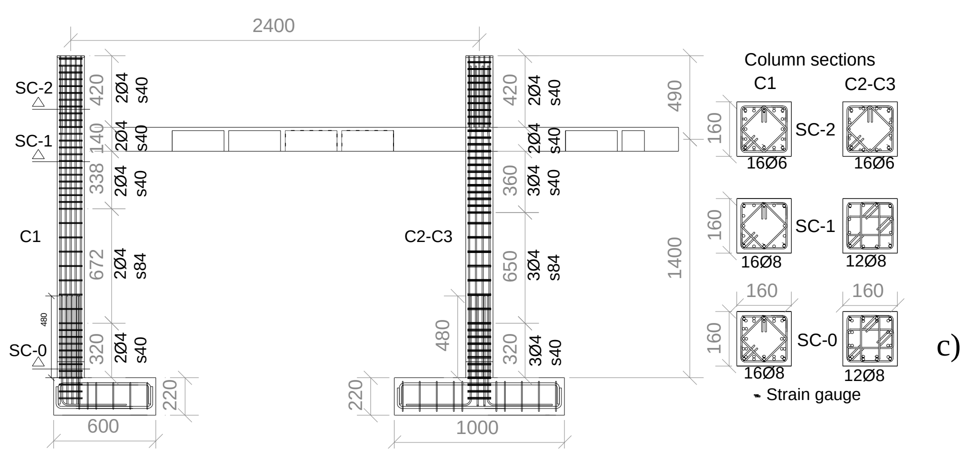

Figure 1. Test model: (a) elevation; top (b) and bottom (c) reinforcement

3 BENCHMARCK NUMERICAL MODEL

The finite element package OpenSess has been used to generate the numerical model. The model must be able to simulate accurately the response of RC WFP structure tested in the shaking table and described in previous sections. In this regard, the model assembles different types of elements. The waffle-flat plate area with voids is made up of linear frame elements while solid part is composed of multi-layer shell element [4]. Then, columns are definded as nonlinear frame elements based on the iterative force-based formulation implemented on fiber elements. Finally, on the top of the specimen there are elements with very high stiffness, which are defined as rigid elements. A sketch of the model together with the type of element used are shown in figure 2.

The constitutive models used for nonlinear materials are those already implemented in OpenSees such as Concrete04 and Steel02. Their main features, firstly for concrete are the initial stiffness whose value is 24500MPa, the compressive strength at 28 days whose value is 52MPa, strain at maximum strength whose value is 0.42%, strain at crushing strength whose value is 2.5%, the maximum tensile strength whose value is 2.8MPa.

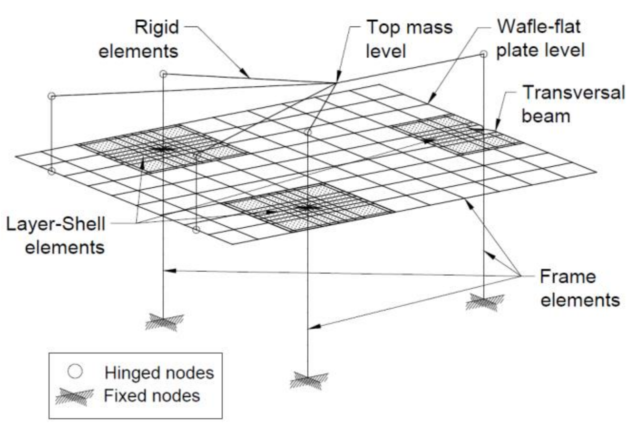

Figure 2. Wire-frame model

Secondly, for steel are yield strength whose value is 525MPa, initial elastic tangent whose value is 2.1E5MPa and strain-hardening ratio whose value is 0.01.

During the shaking table test it was observed that the torsional failure of the trasnverse beam of the exterior plate-column subassemblage (exterior column C1) triggers the collapse of the whole structure. This point is crucial, since OpenSees only considers uniaxial deformation behavior of materials in fiber elements. Therefore, a new constitutive model for torsion was added for the relevant transverse beam following Valipour et al (2010). The model is shown in figure 3. It is noted that the onset of torsional failure occurs at a torsion strain of 0.99E-4.

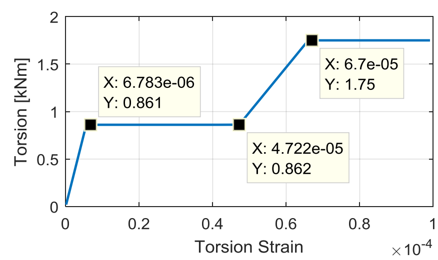

Figure 3. Constitutive model for torsion

The total mass of the model is 11.005kg. This weight is made up of selfweigth of the specimen (excluding the foundation) which is 3492kg and added wight. The latter is added by means of steel plates and some gadgets. The mass of the added wight put on the top of the columns is 6223kg and the mass spread out on floor diaphragm is 1290kg.

Finally, a nonlinear time history analysis was performed using the actual accelerations recorded in the shaking table during each seismic simulation (C100, C200, C300 and C350). The four seismic simulations were linked and run in a unique analysis in order to hold the damage caused by the ground motions upstream. The time-step increment used in both test and simulation was 0.005s.

4 RESULTS

The histories of lateral displacement in the direction of shaking, the energy input and the torsion moment in the transverse beam of the exterior plate-column subassemblage predicted by the numerical model are show in Figure 4 . All of them have been overlapped with the test results. It is worth nothing that they match each other reasonably well. Plus, similarly to the tests, the numerical model predicts the failure of the transverse beam during the seismic simulation C350.

5 CONCLUSION

A numerical model was developed using the software OpenSees to predict the seismic response measured during several shaking table tests conducted by the authors on a reinforced concrete waffle-flat plate structure. The numerical model was subjected to four seismic simulations of increasing amplitude. The response predicted numerically with this model was compared with test results and in general a satisfactory agreement was found. This agreement was particularly good in terms of the history of energy input to the structure and the prediction of the failure of the transverse beam.

ACKNOWLEDGEMENTS

This research work was funded by the Spanish Government (Ministerio de Economía y Competitivad) under project BIA2014-60093-R and by the European Union (Fonds Européen de Dévelopment Régional).

REFERENCES

[1] Fomento, M. (2008). Instrucción de Hormigón Estructural EHE-08. Madrid, Spain.
[2] Fomento, M. (2003). Parte general y edificación (NCSE-02). Real Decreto, 997. Madrid, Spain.
[3] Benavent-Climent A., Donaire-Avila J., Oliver-Saiz E. (2016). Shaking table tests of a reinforced concrete waffle–flat plate structure designed following modern codes: seismic performance and damage evaluation, Earthquake Engineering Structural Dynamics, 45:315–336
[4] Lu, X., Xie, L., Guan, H., Huang, Y., & Lu, X. (2015). A shear wall element for nonlinear seismic analysis of super-tall buildings using OpenSees. Finite Elements in Analysis and Design, 98, 14-25.
[5] Valipour, H. R., & Foster, S. J. (2010). Nonlinear reinforced concrete frame element with torsion. Engineering Structures, 32(4), 988-1002.

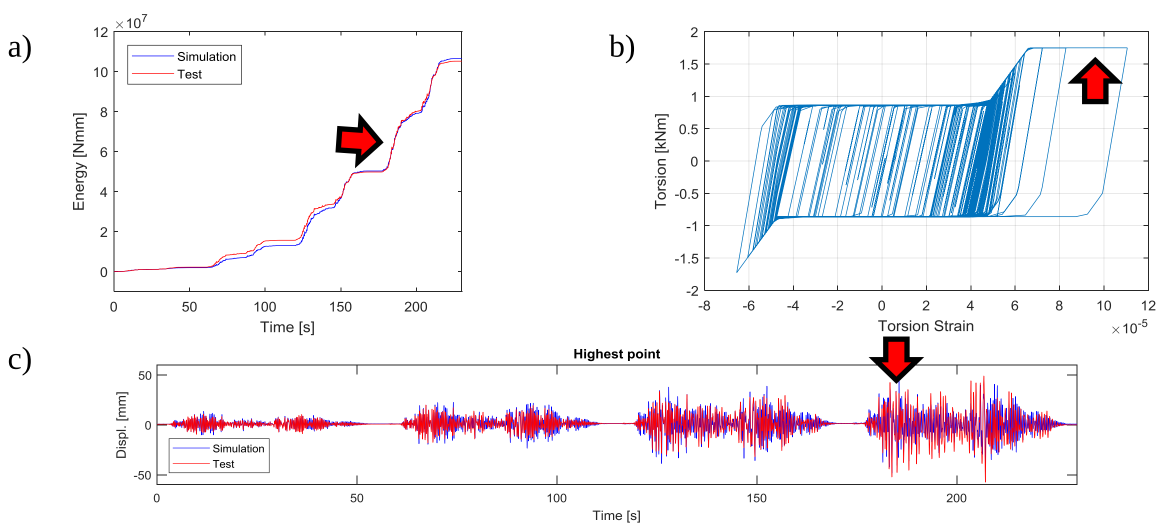

Figure 4. History of a)input energy, b) torsional moment in transverse beam and c) t displacement. Point of failure indicated with an arrow.

1st Conference on Structural Dynamics (DinEst 2018)
Madrid, 20-21 June

CHARACTERIZATION OF THE BEHAVIOR OF SEISMIC DAMPERS WITH SHAPE MEMORY ALLOYS

G. González-Sanz*, D. Galé-Lamuela*, A. Benavent-Climent*

* ETS Ingenieros Industriales
Universidad Politécnica de Madrid
28006 Madrid, Spain
e-mail: guillermo.gonzalez.sanz@upm.es

Abstract. Seismic dampers are devices specially designed to dissipate high amounts of energy in a stable way. The use of dampers allows to focus the energy demand imposed by an earthquake on very localized parts of the structure and reducing or nullifying the plastic deformation energy absorbed by the main structure responsible for supporting gravitational loads. Among the different materials used in the past for dissipating energy, Shape Memory Alloys are increasingly attracting the attention of the research community due to their superelasticity. The authors are working on new types of displacement-dependent dampers with recentering properties, that combine conventional steel with bars made of NiTi. The new dampers have been implemented in a $3x3x3m^3$ reinforced concrete structure and the response has been evaluated experimentally through dynamic tests conducted with the shaking table of the University of Granada (UGR). This paper presents preliminary static cyclic tests carried out in the Laboratory of Structures of the ETSII (UPM).

Key words: Earthquake Engineering, Hysteretic Damper, Shape Memory Alloy, Shaking-Table Tests, Laboratory Tests.

1 INTRODUCTION

Spain is located in a moderate seismicity zone, where the last earthquakes have revealed the vulnerability of many structures. Traditional earthquake-resistant design of structures allows, for economic reasons, significant damages that cannot be repaired. This philosophy implies a process of demolition and reconstruction in case of a severe earthquake, which is an unsustainable practice. Nowadays, this philosophy is not justifiable since new technologies of passive control can drastically limit the damage to the main structure and concentrate it on special easily replaceable elements after a seismic event. The current seismic engineering is oriented not only to avoid the loss of lives but to control the damage, within the paradigm that has been called the Performance Based Design.

The dynamic control of structures can be grouped into three areas: (i) base isolation, (ii) passive energy dissipation, and (iii) active control. It has been shown that base isolation is the best choice for most applications, but it is a very expensive technology and it is only justified for those of great importance. Active control systems are based on the use of actuators that apply forces to the structure in order to balance the hazardous excitation, thanks to real-time monitoring. Passive energy dissipation systems focus on enhancing the seismic response with the installation of devices integrated in the structural framework. These devices, called as dampers, represent an economically viable solution for a wide range of applications. Finally, hybrid control refers to a combined passive and active control systems. A review of the state-of-the-art and state-of-the-practice can be found in [1].

2 SEISMIC DAMPERS WITH SMAS

Seismic dampers are devices specially designed to dissipate high amounts of energy in a stable way. The use of dampers allows to focus the energy demand imposed by an earthquake on very localized parts of the structure and reducing or nullifying the plastic deformation energy absorbed by the main structure, responsible for supporting gravitational loads.

Dampers can be designed to work by several mechanisms, including metal yielding, phase transformation of metals, friction sliding, fluid orificing, and deformation of viscoelastic solids or liquids. The yielding of metals is one of the most popular mechanisms to dissipate energy, and several devices have been proposed. The phase transformation of metals has some interesting properties for the application on seismic engineering.

In this context, the research presented in this paper is part of a more extensive investigation aimed at developing new dampers with improved performance. The new damper combines the Tube-in-Tube Damper (TTD) developed by one of the authors [2] with a core bar made of NiTi alloys (SMA bar hereafter). On the one hand, the TTD exhibits a very stable hysteretic behavior with great energy dissipation in each cycle. On the other hand, the superelastic effect of the SMA bar provides recentering properties. The SMA bar can fully recover its shape after being subjected to large strains, up to 6-8%. This recentering property minimizes the plastic deformation of the main structure after a seismic event. Other benefits of the SMAs for seismic applications are: (i) they can dissipate some (limited) amount of energy in a hysteresis loop, (ii) the force transmitted to the structure is controlled by the stress plateau present in the material, (iii) for large lateral displacements the SMA bars exhibit a sudden increase of resistance that can be used to control the P-delta effects, and (iv) excellent resistance to corrosion and high fatigue resistance, remaining completely functional after an earthquake. [3]

The complete seismic damper (TTD + SMA) has the form of a conventional brace and it is intended to be installed in a framed structure as a standard diagonal bar, working with axial loads.

The cyclic behavior of the new damper can be idealized with two springs working in parallel. For this reason, the overall performance can be studied separately.

2.1 Tube-in-Tube Damper

The TTD is constructed by assembling two standard hollow structural rectangular sections of stainless steel, one into the other. In the walls of the outer tube a number of slits are cut leaving a number of strips between the slits The two tubes are joined by fillet and plug welds in specific points.

Under relative displacements of the ends of the brace damper in the direction of its axis, the strips behave as a series of fixed-ended beams and deform in double curvature. The tube-in-tube configuration and the overlapping length of one tube into the other increase the buckling capacity. Complete information and behavior prediction can be found in [2].

2.2 Shape Memory Alloy bar

The SMA bar have an almost equiatomic nickel-titanium (NiTi) composition and has been subjected to a heat treatment that guarantees superelastic properties. The NiTi bar is arranged inside the TTD, and the specially designed configuration of the plates and wedges ensure that, for alternative sense of the axial loads, the bar is always working in tension, and thus buckling is prevented. It has been also proven that the behavior of SMAs changes under the first repeated cycles but tends to stabilize [3,4].

3 STATIC CYCLIC TESTS

Several tests have been carried out in the Laboratory of Structures of the ETSII (UPM) with the aim of characterizing the behavior of both TTD and SMA bar separately. As earthquakes have a cyclic nature, the test protocol has been programed with repeated cyclic loading. The tests were performed with displacement control in quasi-static conditions.

Cycles of increasing amplitude were applied to the TTD (without the SMA bar), following the cyclic loading pattern proposed in [5] for seismic testing on structural components. The hysteretic curves obtained are shown in Figure 1. It can be seen that the TTD possess very stable cyclic behavior and great energy dissipation.

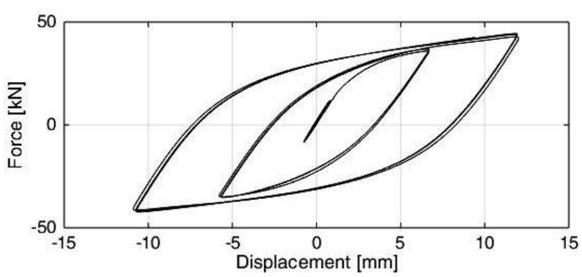

Figure 1: Hysteresis loops of the TTD tests.

The SMA bar was assembled inside the TTD damper and tested under cyclic loading. Figure 2 shows the axial load-displacement loops exhibited by the SMA bar (alone) when subjected to 10 cycles of constant amplitude.

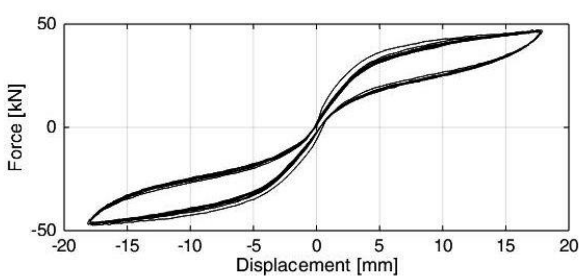

Figure 2: Hysteresis loops of the SMA bar tests.

As can be seen, the SMA bar develops stable loops with some (limited) energy dissipation and it is able to recover most of the deformation when the applied load is removed (recentering properties). Also, it is worth noting that for axial displacements (up to about 18mm) corresponding to lateral drifts of about 0.6%, the yielding plateau is almost flat.

4 SHAKING TABLE TESTS

The response of a 3x3x3m^3 reinforced concrete structure equipped with new seismic dampers that combine the TTD device with SMA bars has been experimentally evaluated by dynamic tests with the shaking table of the University of Granada (UGR).

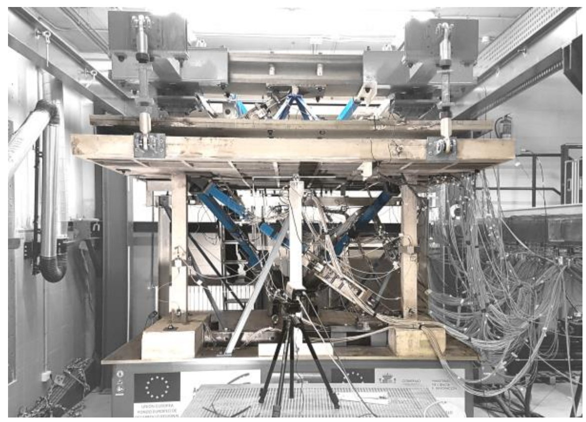

Figure 3: Specimen with dampers on the seismic table.

These tests confirmed that the new dampers dissipate most of the energy input by the earthquake and keep the main structure basically in elastic conditions (undamaged). Also, once the ground motion vanishes the remaining plastic deformations on the structure are negligible.

The combination of the TTD with the SMA results in a new device with high energy dissipation capacity (TTD damper) and recentering properties (SMA bar), that minimizes the remnant plastic deformations on the structure after the earthquake. Figure 4 shows the typical hysteresis loops underwent by the new dampers (TTD+SMA bar) during the dynamic shaking table tests. This behavior is consistent with previous results published in the literature [6].

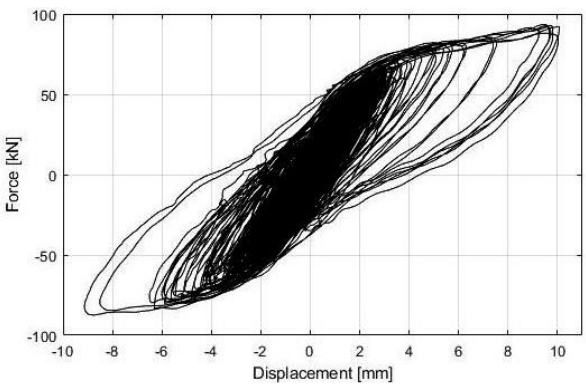

Figure 4: Hysteresis loops of the TTD+SMA bar tests.

During the shaking table tests the TTD suffered severe damage due to the cumulative plastic deformations, but the SMA bar remained in the elastic range, evidencing a high fatigue resistance and the possibility of being reutilized.

5 ONGOING STUDIES

This research is aimed at investigating the seismic behavior of a new damper which combines the energy dissipation of the steel yielding with the superelastic properties of NiTi alloys. Ongoing studies in the same line will attempt to propose a mathematical model that represents this behavior for its implementation in advanced numerical models. Another important issue under investigation is the life estimation of the complete damper, that is, the evaluation of the ultimate energy dissipation capacity.

6 CONCLUSIONS

- Passive control systems based on the use of displacement-dependent dampers are an efficient and economically viable solution for reducing the damage on a structure subjected to strong ground motions.
- Combining the high energy dissipation capacity of the steel under plastic deformations with the recentering properties of bars made of SMAs (among others) results in dampers with improved performance.

7 ACKNOWLEDGEMTS

The study and tests have been carried out within the research project JA PE2012 TEP12 2429 and the grant of the Spanish Government FPU16/03006.

REFERENCES

[1] Soong TT., Y Spencer J. *Supplemental energy dissipation: state-of-the-art and practice.* Engineering Structures, 2002; 24: 243-259.

[2] Benavent-Climent A. *A brace-type seismic damper based on yielding the walls of hollow structural sections.* Engineering Structures, 2010; 32: 1113-1122.

[3] Dolce M., Cardone D. *Mechanical behavior of shape memory alloys for seismic applications.* International Journal of Mechanical Sciences, 2001; 43: 2657-2677.

[4] DesRoches R., McCormick J., Delemont M. *Cyclic properties of superelastic shape memory alloys wires and bars.* Journal of Structural Engineering, 2004; Vol.130, Nº1 January.

[5] Helmut Krawinkler M. *Cyclic loading histories for seismic experimentation on structural components.* Earthquake Spectra, 1996; Vol.12, Nº1 February

[6] Valente C., Cardone D., Dolce M., Ponzo F. *MANSIDE: shaking table test of R/C frames with various passive control systems.* 12th World Conference on Earthquake Engineering, 2000.

1st Conference on Structural Dynamics (DinEst 2018)
Madrid, 20-21 June

SHAKING TABLE TESTING ON SEISMIC POUNDING OF A RC BUILDING STRUCTURE

A. Kharazian*, F. López Almansa*, A. Benavent Climent†, A. Gallego‡

* Universidad Politécnica de Cataluña
08034 Barcelona
e-mail: alireza.kharazian@upc.edu
ORCID: 0000-0003-2691-8875

† Universidad Politécnica de Madrid
28006 Madrid

‡ Universidad de Granada
18071 Granada

Abstract. This paper describes unidirectional shaking table tests on seismic pounding of a 3-D RC building structure. Two inputs were considered: a seismic accelerogram and a harmonic wave. The tested specimen is a one-and-a-half-story 2/5 scaled portion of a RC building structure consisting of waffle slabs and columns. The instrumentation consisted of strain gauges, displacement transducers, acoustic emission receivers, accelerometers, and video recording cameras. The experiments are simulated with SeismoStruct by using linear elements with concentrated plasticity; pounding is described with a concentrated Kelvin-Voigt model. The initial after-test observations showed some damage in the columns.

Key words: Shaking-Table Test; Seismic Pounding; RC Building Structure; Test Simulation.

1 INTRODUCTION

Impact between contiguous buildings under strong seismic events is a relevant issue since the huge forces that are generated during the collision significantly affect the dynamic behavior of the pounding buildings. On some occasions, the effect of impact might be beneficial, mainly in terms of inter-story drift; conversely, in many other situations, pounding is detrimental, particularly in terms of absolute acceleration. Collapses and structural and nonstructural damage of buildings due to seismic pounding have been reported. Although such collision can be avoided by adequately separating the involved buildings, and this gap is routinely required by the design codes, impact can anyway occur because of several reasons: sometimes code prescriptions are not fulfilled, some past codes did not oblige any such separation, and the seismicity can be underestimated. Therefore, seismic pounding of buildings is something to be taken into consideration.

Collision between adjoining buildings can be classified into two categories: slab-to-slab and slab-to-column (or slab-to-wall) impact; they correspond to aligned and unaligned slabs, respectively. The second type is by far more dangerous, since the impact of a rigid and massive slab on a column (or even on a wall) is most likely to lead to collapse. On the other hand, the first type is not free of danger, and is considerably more frequent, since adjoining buildings with unaligned slabs are regularly avoided. Moreover, the numerical simulation of slab-to-slab impact is highly challenging. Thus, this study focuses on seismic pounding of adjoining buildings with aligned slabs.

As outlined in the previous paragraph, collision between two building slabs is a complex phenomenon, because it involves stress traveling waves, high-frequency behavior, and significant local effects [1]. Although a number of pounding tests have been reported, they provide only limited information. Therefore, there is a strong need for additional testing. This research is oriented to fulfil this necessity.

2 EXPERIMENTS DESCRIPTION

This section describes the conducted tests. They consist in exciting the specimen in a single horizontal direction with a shaking table; as a result, the tested structure collides against a rigid steel structure.

Next four subsections deal with the laboratory, the RC structure, the sensors, and the shaking accelerograms, respectively.

2.1 Testing facility

The experiments were carried out on 26 January 2018 at the Structural Dynamics laboratory, University of Granada. These facilities are equipped with an uniaxial MTS shaking table; the table size is 3 m × 3 m.

2.2 Tested specimen

The tested specimen [2] corresponds to a portion of a RC building structure with waffle slabs; this structure is scaled with a factor 2/5. The structure was first designed to support only gravity loads; the live load is 2 kN/m^2 for the floors and 1 kN/m^2 for the roof. The characteristic value of the concrete compressive strength is f_{ck} = 25 MPa and steel yield point is f_{yk} =500 MPa. The waffle flat plates have a constant depth of 0.35 m, and the bottom part consists of a regular pattern of voids forming an orthogonal grid of 7 cm wide ribs separated 83 cm, and a solid zone around the columns. The cross section of the columns is 30 cm × 30 cm.

The tested portion consists of a rectangular fraction of the first floor slab (3.65 m × 3.02 m) together with three columns of the first floor (1.4 m high) and a segment (0.49 m high) of the second floor three ones. The aforementioned first story columns are clamped to the table, and the second story ones are hinged to a rigid steel external substructure. Steel blocks are attached at the top of the slab and at the top of half-columns of the second story to represent the gravity loads and to satisfy similitude requirements between prototype and test model. The weight of the test specimen (including the additional masses but excluding the foundation) was 109.1 kN. The slab pounded against a rigid steel buffer stop, being connected to a highly stiff steel structure; the initial separation (gap) was 20 mm.

Figure 1 displays an image and a sketch of the tested specimen.

2.3 Instrumentation

The test specimen was instrumented with strain gauges, displacement transducers (LVDTs and laser), acoustic emission receivers, accelerometers and video recording cameras. The strain gauges were connected to the longitudinal reinforcement bars of the slab and of the segments of the columns that are right under the slab. The displacement and acceleration transducers gaged the slab horizontal longitudinal motion. The acoustic sensors measured the concrete damage. Data were acquired continuously with a scan frequency of 200 Hz.

2.4 Seismic inputs

Two inputs were considered: (i) the SW component of the Calitri record of the Irpinia earthquake (23 November 1980), and (ii) a harmonic wave with 1 Hz period. Both inputs were scaled with different factors to generate pounding, while limiting the damage on the specimen. Figure 2 displays the Calitri accelerogram.

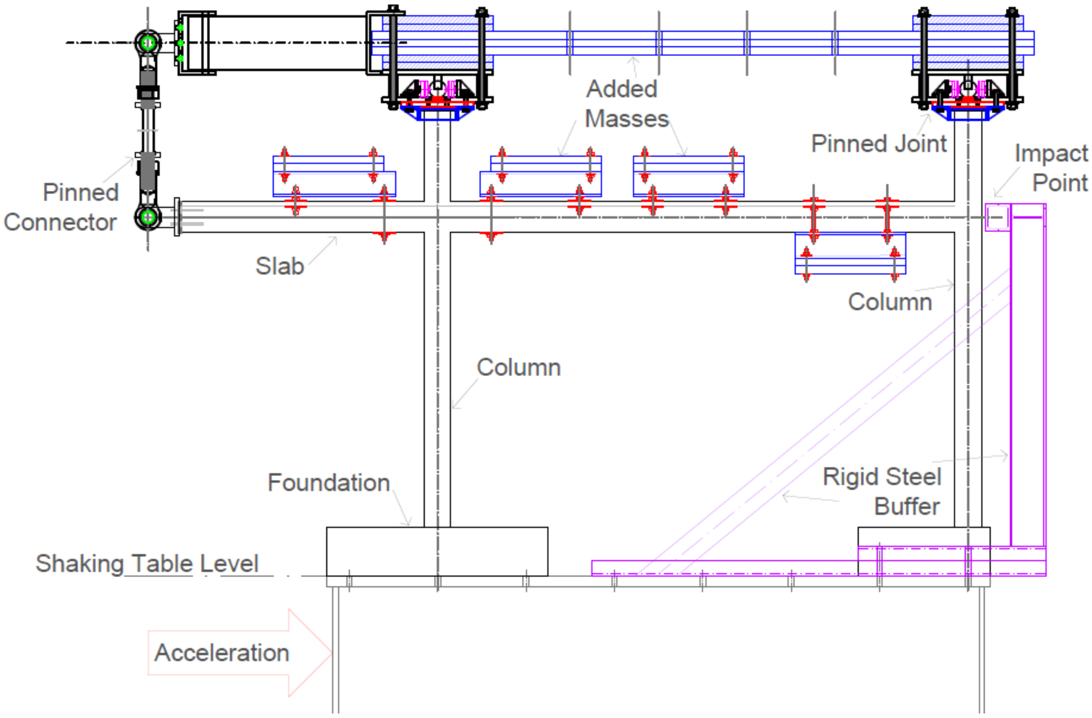

Figure 1: Tested RC building structure

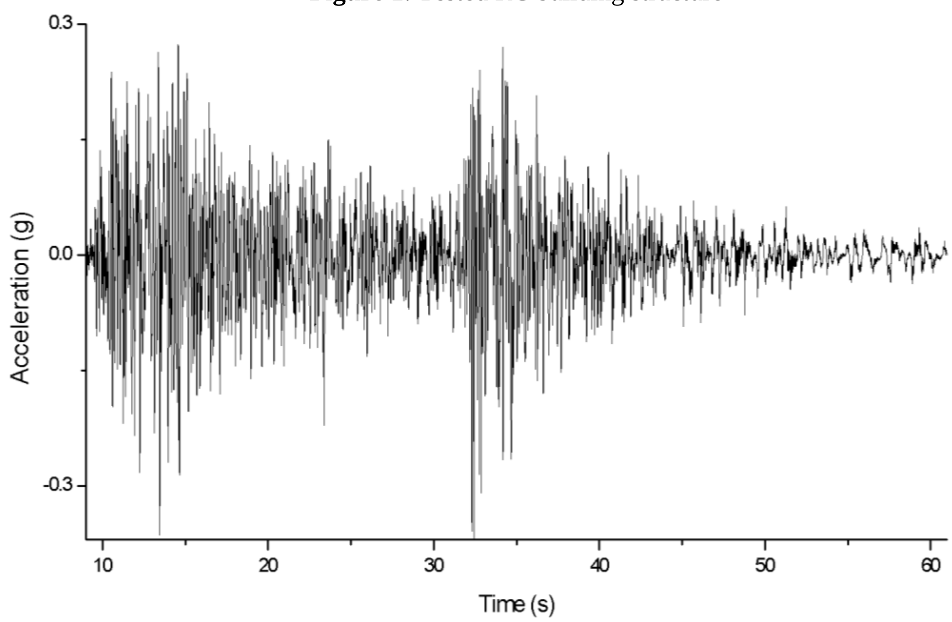

Figure 2: Scaled seismic accelerogram

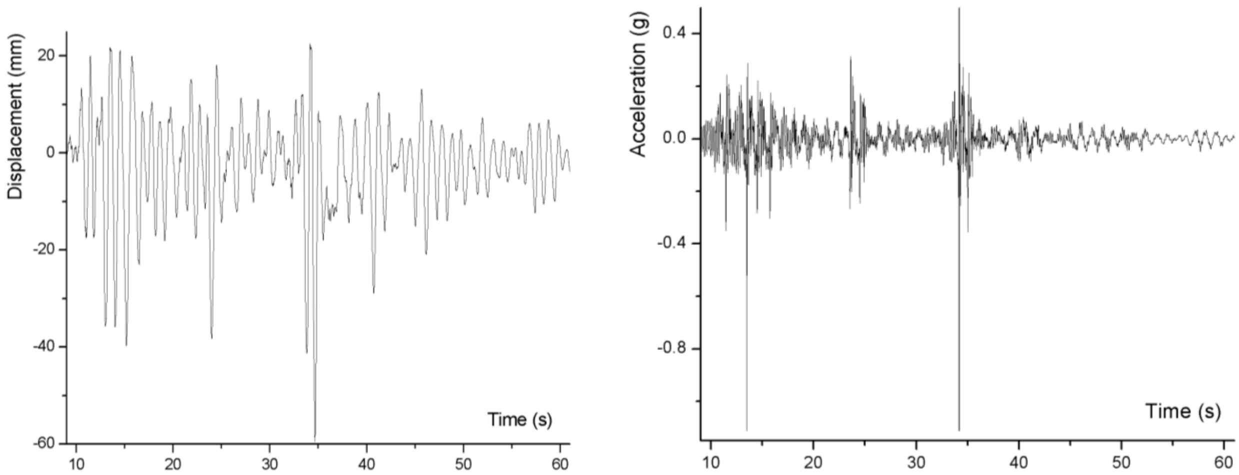

(a) Displacement (b) Acceleration

Figure 3: Preliminary experimental results of the slab time-history

3 EXPERIMENTAL RESULTS

Figure 3 displays preliminary experimental results; Figures 3.a and 3.b correspond to the slab displacement and the acceleration, respectively. Noticeably, the huge peaks in the acceleration correspond to the impact instants.

4 NUMERICAL SIMULATION

The experiments are simulated with SeismoStruct [3] by using concentrated plasticity. Pounding is described with a Kelvin-Voigt model [4].

5 CONCLUSIONS

This paper describes seismic pounding tests on a laboratory RC building structure with waffle slabs. Experiments are simulated with SeismoStruct and pounding is described with a Kelvin-Voigt model. Initial after test observations showed damage in the columns.

ACKNOWLEDGMENTS

This research work was funded by the Spanish Government (Ministerio de Economía y Competitidad) under projects BIA2014-60093-R and CGL2015-6591 and by the European Union (FEDR).

REFERENCES

[1] Kharazian A, Lopez-Almansa F. (2017). State-of-the-art of research on seismic pounding between buildings with aligned slabs. *Archives of Computational Methods in Engineering*. doi.org/10.1007/s11831-017-9242-3.

[2] Benavent-Climent A, Donaire-Ávila J, Oliver-Sáiz E. (2018). Seismic performance and damage evaluation of a waffle-flat plate structure with hysteretic dampers through shake-table tests. *Earthquake Engineering & Structural Dynamics*, **47**(5):1250-1269.

[3] SeismoSoft. (2017). A computer program for static and dynamic nonlinear analysis of framed structures. Available from URL www.Seismosoft.com.

[4] Kharazian A. (2017). Analysis of seismic pounding of moderate height RC buildings with aligned slabs. *Doctoral Dissertation, Technical University of Catalonia*.

1st. Conference on Structural Dynamics (DinEst 2018)
Madrid, 20–21 June

DYNAMIC MODELING OF FLUID-DRIVEN EARTHQUAKES IN POROELASTIC MEDIA

Pedro Pampillón, David Santillán, Juan Carlos Mosquera and Luis Cueto-Felgueroso

ETS Ingenieros de Caminos, Canales y Puertos
Universidad Politécnica de Madrid
28040 Madrid, Spain

e-mail: pedropampillonalonso@gmail.com; david.santillan@upm.es; juancarlos.mosquera@upm.es; luis.cueto@upm.es

Abstract. Earthquake ruptures in poroelastic media involve complex phenomena which stem from stick-slip frictional instabilities and hydromechanical couplings. Understanding inertia effects that control the rupture of induced earthquakes demands numerical simulations that couple fault poromechanics and rock poroelasticity including inertia. We analyze the effects of both poroelasticity and the viscous material properties on the characterization of injection-induced earthquakes. Our numerical model enjoys fully-coupled hydromechanical, frictional and dynamic features. We adopt a rate-and-state constitutive law for the fault and the Kelvin-Voigt model for the rock viscoelastic response.

We simulate the whole earthquake sequence, including interseismic and dynamic rupture phases, and quantify the differences in the rupture results when either the dynamic or the quasi-dynamic approaches are considered. The constitutive viscoelastic model relation for the solid domain adds a dissipative term that affects the overall response and lets us simulate the physical process of seismic wave attenuation. Moreover, viscous dissipation avoids spurious high-frequency oscillations during wave propagation. Including inertial terms enables the model to account for the incremental fluctuations of pore pressures and solid stresses during dynamic rupture, all of which may shed light on the mechanisms controlling dynamic triggering at nearby faults.

Key words: Induced seismicity, poroelasticity, dynamic modeling

1 INTRODUCTION

Induced seismicity has attracted great interest which stems from its engineering applications in many subsurface energy technologies and its social consequences. Some activities prone to trigger earthquakes are the disposal of waste water from oil and gas production into deep wells [14], the enhanced geothermal systems [4], the hydraulic fracturing [6] or the CO_2 sequestration [9]. Numerical simulations of the full earthquake sequence provide vital insight to understand the whole process [5]. Unfortunately, ignoring inertial effects may disturb simulations of the complete sequence [1, 10]. Here, we present numerical simulations of the whole earthquake sequence, including interseismic and dynamic rupture phases, of faults embedded in poroviscoelastic media. We quantify the differences in the rupture results when either the dynamic or the quasi-dynamic approaches are considered and study the effect of the viscosity of the rock.

2 MATHEMATICAL FORMULATION

We model rock as a poroelastic medium, governed by the quasi-static Biot equations for linear poroelasticity given by [3]:

$$\frac{1}{M}\frac{\partial p}{\partial t} + \alpha\frac{\partial \varepsilon_v}{\partial t} = \nabla \cdot \left(\frac{k}{\mu_f}\nabla p - \rho_f \mathbf{g}\right), \quad (1)$$

$$\nabla \cdot \sigma + \rho_b \mathbf{g} = \rho_b \ddot{\mathbf{u}}, \quad (2)$$

where $\mathbf{u}$ is the displacement field, α is the Biot coefficient, M is the Biot modulus, ε_v is the volumetric strain, $\varepsilon_v = \mathrm{tr}\,(\varepsilon)$, ε is the infinitesimal strain tensor, t is time, p is the pressure field, k is the intrinsic permeability of the porous medium, μ_f is the fluid dynamic viscosity, ρ_f is the fluid density, ρ_b is the bulk density, and σ is the total Cauchy stress tensor.

The effective stress tensor, σ', is slip into an inviscid part, σ'_{invis} plus a viscous one, σ'_{vis}:

$$\sigma' = \sigma'_{invis} + \sigma'_{vis}. \quad (3)$$

We adopt a Saint Venant–Kirchhoff hyperelastic material model for the inviscid part, and a Kelvin–Voigt model for the viscous part. The latter one reads:

$$\sigma'_{vis} = \frac{\eta_{kv}}{G}\dot{\sigma'}_{iso}, \quad (4)$$

where G is the Lamé shear modulus, η_{kv} is the viscous damping, $\dot{(\cdot)}$ denotes time derivative, and σ'_{iso} is the isochoric part of σ'.

We model the fault as a lower-dimensional object nearly impermeable. Shear stresses on the fault, τ, are limited by its strength, τ_f, defined as:

$$\tau_f = \begin{cases} \tau_c - \mu\sigma'_n + \xi V, & \sigma'_n < 0 \\ \tau_c, & \sigma'_n \geq 0 \end{cases} \quad (5)$$

where τ_c is the cohesive strength of the fault (hereafter $\tau_c \approx 0$), μ is the friction coefficient, ξ is the radiation damping factor used to prevent unbounded slip velocities if the mechanics is quasi-static [12], V is the slip velocity, and σ'_n is the effective contact pressure.

The friction coefficient follows the rate-and state-dependent law, given by [11, 13]:

$$\mu = \mu_0 + a\ln\left(\frac{V}{V_0}\right) + b\ln\left(\frac{V_0\theta}{D_c}\right). \quad (6)$$

μ_0 is the steady state friction coefficient at a slip rate $V = V_0$, a and b are friction parameters, θ is the state variable, and D_c is a characteristic slip length [7].

The evolution of the state variable is modeled by the Dirichlet aging law [13, 8], which captures the time-healing mechanism of contact surfaces and has the form [7, 2]:

$$\frac{d\theta}{dt} = 1 - \frac{V\theta}{D_c}. \quad (7)$$

2.1 Quasi-dynamic model

The quasi-dynamic model does not include inertia term on the equilibrium equation. Instead, the radiation damping term is included on the strength formulation. Moreover, viscous effects are also disregarded and the rock is then modeled as a Saint Venant–Kirchhoff hyperelastic material. The momentum balance equation follows then:

$$\nabla \cdot \sigma + \rho_b \mathbf{g} = 0, \quad (8)$$

and the fault strength:

$$\tau_f = \begin{cases} -\mu\sigma'_n + \xi V, & \sigma'_n < 0 \\ 0, & \sigma'_n \geq 0. \end{cases} \quad (9)$$

2.2 Dynamic model

The dynamic model accounts for inertia effects. The momentum balance equation reads:

$$\nabla \cdot \sigma + \rho_b \mathbf{g} = \rho_b \ddot{\mathbf{u}}. \quad (10)$$

Viscous effects are also considered and, consequently, both the inviscid and viscous parts of the effective stress tensor are accounted for. Lastly, the radiation damping term is then disregarded. The fault strength is then given by:

$$\tau_f = \begin{cases} -\mu\sigma'_n, & \sigma'_n < 0 \\ 0, & \sigma'_n \geq 0. \end{cases} \quad (11)$$

3 SIMULATION OF FLUID-INDUCED EARTHQUAKES

3.1 Model set-up

Our model is a trike-slip fault embedded in a two-dimensional domain (Fig. 1). The injection well is located 100 m away from the fault, and fluid is injected at a constant rate of 5500 ton/(m·year). The fault is 4000 m long, oriented at an angle of 30 degrees with respect to the x-axis, and centered in a 10 km square domain. The far-field regional stresses are $\sigma_x = 2\sigma_y = 10$ MPa applied respectively at the right and top boundaries, and the initial pore pressure is zero. The fault is stable for the initial state.

The permeability, porosity, solid density, Young modulus, and Poisson ratio of the rock are respectively $k = 10^{-14}$ m^2, $\phi = 0.1$, $\rho_s = 2500$ kg/m^3, E = 20 GPa, and ν=0.25. The fluid density, dynamic viscosity, and compressibility are: $\rho_f = 1000$ kg/m^3, $\mu_f = 0.001$ Pa·s, $\chi_f = 4 \cdot 10^{-10}$ Pa^{-1}. The Biot coefficient, α, is 1. Lastly, the parameters of the rate-and-state model are $\mu_0 = 0.6$, $a = 0.005$, $b = 0.02$, $D_c = 2 \cdot 10^{-4}$ m and $V_0 = 10^{-9}$ m/s. We assume plane strain conditions.

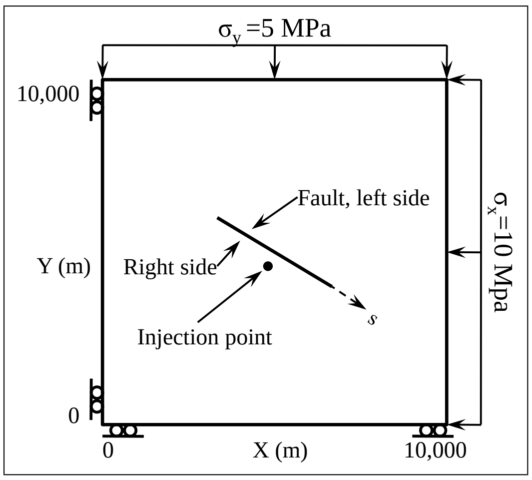

Figure 1: Scheme of the fault model.

3.2 The earthquake sequence

We model the whole earthquake sequence. We illustrate the cycles with the evolution of the accumulated slip (differential displacement of the sides of the fault) and the friction coefficient of the central point of the fault (Fig. 2). Initially, the fault is stable and the fluid injection stars at constant rate in time. The fluid injection increases the pore pressure, reducing the effective normal compression, and poroelastic effects induce deformations in the rock. The overall effect weakens the fault, leading to slip at approximately 1.05 days (Fig. 2a). The rupture phase is the sudden slip at approximately 1.05 days and it lasts less than a second. During this phase, elastic waves are radiated. Afterward, an interseismic phase occurs, where the fault is arrested. This period lasts about one day and is followed by a new rupture. During these evens, μ evolves governed by the rate-and state-dependent law (Fig. 2b).

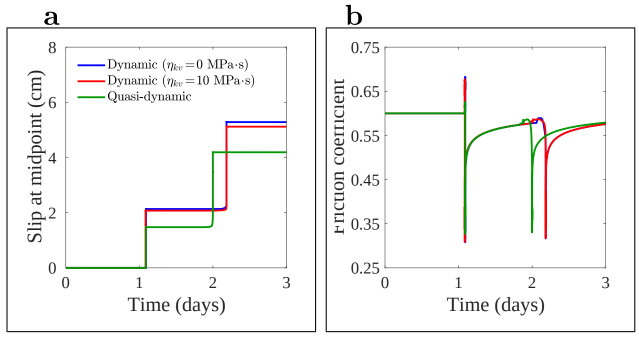

Figure 2: Comparison between quasi-dynamic model and viscoelastic dynamic models (for η_{kv} values of 0 and 10 MPa·s). (**a**) Evolution of the accumulated slip at the central point of the fault, and (**b**) evolution of the friction coefficient at the same point.

We include the evolution of the slip and μ for the quasi-dynamic model and two viscoelastic dynamic models with η_{kv} values of 0 and 10 MPa·s. The use of a quasi-dynamic simulation implies important differences as compared with a dynamic model. The first ruptures are similarly predicted, but deviations arise during the second one. The quasi-dynamic simulations provides lower rupture patch than the dynamic models. Moreover, the increase in the viscous damping in the dynamic models leads to slightly lower rupture patches.

3.3 Effect of viscoelasticity damping

The viscous damping simulates the physical process of small seismic wave attenuation. From a numerical point of view, it avoids spurious high-frequency oscillations due to dispersion errors. We characterize the impact of viscous damping though the attenuation of the radiated seismic waves (Fig. 3). Increasing values of η_{kv} results in dissipation of the acceleration, and eventually fading them out.

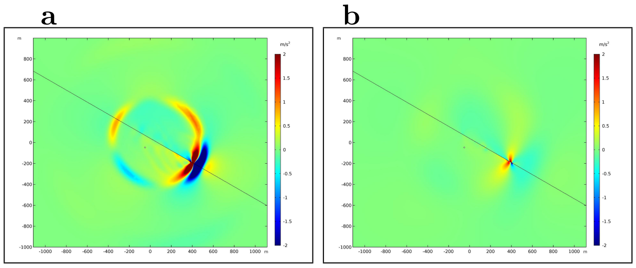

Figure 3: Acceleration fields during the first rupture for (**a**) $\eta_{kv} = 0$ and (**b**) $\eta_{kv} = 100$ MPa·s.

4 CONCLUSIONS

We have conducted two-dimensional simulations of earthquake sequences in a horizontal strike–slip fault. We describe frictional strength with the Dieterick–Ruina aging law, and we model rock as a poroelastic media. Earthquakes are driven by the injection of fluids. We have compared results from a dynamic model with those from a quasi-dynamic simulation.

5 ACKNOWLEDGMENTS

This research was supported by the Spanish Ministry of Economy and Competitiveness under grant CTM2014-54312-P. LCF also gratefully acknowledges funding from the Spanish Ministry of Economy and Competitiveness (grant RyC-2012-11704).

REFERENCES

[1] S. Barbot, N. Lapusta, and J.-P. Avouac. Under the Hood of the Earthquake Machine: Toward Predictive Modeling of the Seismic Cycle. *Science*, 336:707–710, 2012.

[2] N. M. Beeler, T. E. Tullis, M. L. Blanpied, and J. D. Weeks. Frictional behavior of large displacement experimental faults. *J. Geophys. Res.*, 21:8697–8715, 1996.

[3] M. A. Biot. General theory of three-dimensional consolidation. *Journal of Applied Physics*, 12(2):155–164, 1941.

[4] E. E. Brodsky and L. J. Lajoie. Anthropogenic Seismicity Rates and Operational Parameters at the Salton Sea Geothermal Field. *Science*, 341:543–546, 2013.

[5] L. Cueto-Felgueroso, D. Santillán, and J.C. Mosquera. Stick-slip dynamics of flow-induced seismicity on rate and state faults. *Geophysical Research Letters*, 44(9):4098–4106, 2017.

[6] K. Deng, Y. Liu, and R. M. Harrington. Poroelastic stress triggering of the December 2013 Crooked Lake, Alberta, induced seismicity sequence. *Geophys. Res. Lett.*, 43:8482–8491, 2016.

[7] J. H. Dieterich. Time-Dependent Friction and the Mechanics of Stick-Slip. *Pure Appl. Geophys.*, 116:790–806, 1978.

[8] J. H. Dieterich. Modeling of Rock Friction 1. Experimental Results and Constitutive Equations. *J. Geophys. Res.*, 84:2161–2168, 1979.

[9] R. Juanes, B. H. Hager, and H. J. Herzog. No geologic evidence that seismicity causes fault leakage that would render large-scale carbon capture and storage unsuccessful. *Proc. Natl. Acad. Sci. USA*, 109:E3623, 2012.

[10] H. Noda and N. Lapusta. Stable creeping fault segments can become destructive as a result of dynamic weakening. *Nature*, 493:518–521, 2013.

[11] J. R. Rice. Constitutive Relations for Fault Slip and Earthquake Instabilities. *Pure Appl. Geophys.*, 121:443–475, 1983.

[12] J. R. Rice. Spatio-temporal Complexity of Slip on a Fault. *J. Geophys. Res.*, 98:9885–9907, 1993.

[13] A. Ruina. Slip Instability and State Variable Friction Laws. *J. Geophys. Res.*, 88:10359–10370, 1983.

[14] M. Shirzaei, W. L. Ellsworth, K. F. Tiampo, P. J. González, and M. Manga. Surface uplift and time-dependent seismic hazard due to fluid injection in eastern Texas. *Science*, 353:1416–1419, 2016.

1st Conference on Structural Dynamics (DinEst 2018)
Madrid, 20-21 June

CONSTRUCTION OF ELASTIC SPECTRA FOR HIGH DAMPING

Jorge Conde-Conde*, Amadeo Benavent-Climent†

* ETS Arquitectura
Universidad Politécnica de Madrid
28040 Madrid, Spain
e-mail: jorge.conde@upm.es
ORCID: 0000-0002-5633-1170

†ETS Industriales
Universidad Politécnica de Madrid
28006 Madrid, Spain

Abstract. Construction of a site-specific elastic response spectrum is a well-defined and common procedure to describe earthquake action. Such a spectrum is usually defined for 5% damping ratio, which is a suitable value for most conventional buildings. A practical approach to consider high damping ratios in design is to build spectra by means of damping correction factors affecting 5% elastic response values. This paper discusses the adequacy of this approach and derives expressions for damping correction factors that are based upon and coherent with the Eurocode 8 elastic response spectrum.

Key words: High damping, damping coefficients, damping correction factors, elastic spectrum.

1 INTRODUCTION

Damping has a beneficial effect on the dynamic performance of conventional structures: an increase in damping results in a reduction of structural displacements, which in turn represents smaller internal forces associated with the dynamic excitation. From the point of view of energy balance, added damping reduces the demand on the structure by assuming a relevant part of the energy dissipation. Hysteretic mechanisms are greatly reduced or suppressed and therefore structural damage is diminished or even completely avoided.

Systems with Passive Energy Dissipation Devices (PEDs) will typically feature overall structural damping ratios higher than 10% in the first mode; higher modes will present higher damping ratios. Displacement-based design predicts the response of structures assimilating hysteretic behavior to damping. Damping values higher than 5% are thus frequent in practical design.

Damping correction factors

Codes generally define seismic action through elastic pseudo acceleration spectra for a 5% damping ratio. A convenient way to account for higher damping ratios is the simple scaling of spectral ordinates by means of a *damping correction factor* (DCF), η:

$$\eta = \frac{S_a(T,\xi)}{S_a(T,5\%)} \tag{1}$$

Where $S_a(T,\xi)$ is the elastic spectral acceleration for period T and viscous damping ratio, ξ, and $S_a(T,5\%)$ the elastic spectral acceleration for the same period and 5% viscous damping ratio.

From different independent studies [1-6], it can be concluded that DCFs are dependent on damping ratio, period and earthquake magnitude. The results are not so clear about source-to-site distance. DCFs seem to be only mildly dependent on site class. It is also clear that DCFs tend to unity as T tends to 0 (short period range), are nearly constant in the velocity region and increase to unity for long periods, although the rate of this increase is strongly dependent on magnitude and source-to-site distance (it converges faster to unity for smaller magnitudes and closer earthquakes).

Most studies refer the proposed values of DCFs to the 5%-damped elastic spectral response of a given earthquake, not to the design elastic spectrum. However, structures are designed for a code-defined elastic spectrum (not for a particular ground motion), therefore practical DCFs for design purposes should relate to the code-defined 5% elastic response spectrum:

$$\eta^C = \frac{S_a(T,\xi)}{S_e(T,5\%)} \tag{2}$$

Where $S_e(T,5\%)$ is the 5% code-defined spectral acceleration and superscript '*c*' stands for 'Code'. Because elastic spectra from actual accelerograms differ from elastic code-defined spectra, it is obvious that the two sets of factors are not coincident, although the trends detected in the previous studies apply to both.

Eurocode 8 (EN1998-1:2004) [7] defines the following expression for the DCFs:

$$\eta^C = \sqrt{\frac{10}{5+\xi}} \geq 0.55 \tag{3}$$

Where ξ is expressed as a percentage; the expression, proposed by Bommer *et al* (2000) [8], is valid for any damping ratio, but renders constant values over 28%. The oversimplified expression (3) presents some major drawbacks: i) it is independent of period; ii) it does not tend to unity as the period tends to 0 or to infinite (i.e. in the short or very long period range); iii) it does not account for high damping. The expression contradicts the findings in the different works cited above, is unsafe for the short- and long- period regions, and it might lead to the wrong conclusion that added damping is equally effective regardless of natural period.

2. DESCRIPTION OF STUDY

The main target of this study is to propose a simple modification for equation (3) to account for the different factors listed above. Because all factors external to the structure (magnitude, site-to-source distance, site class) are taken into account via spectrum definition and PGA, only period and damping ratio need to be considered explicitly in the proposed expression. Transition between spectral regions is included through T_C and T_D (site-class dependent periods defining the limits between acceleration, velocity and displacement regions). With these criteria and on the basis of the numerical analyses presented below, the following modification of the Eurocode formula is proposed:

$$\eta^* = \sqrt{\frac{10 + \dfrac{T_C(\xi-5)}{T_C+30T}}{5+\xi}} \tag{4a}$$

$$T \leq T_D : \eta^C = \eta^* \tag{4b}$$

$$T > T_D : \frac{1}{\eta^C} = 1 + \left(\frac{1}{\eta^*} - 1\right)\frac{T_D}{T} \tag{4c}$$

Expression (4) equals 1 for a 5% damping ratio and all periods; it converges to 1 for all damping ratios in very short and very long period regions.

The expression has been tested by a numerical study for a Single Degree of Freedom System (SDOF) with known properties (mass m, natural period T, viscous damping ratio ξ) subjected to several suites of recorded accelerograms using step-by-step time-history elastic analysis. The values of T ranged from T_B (class-site dependent period) to 4 s in 0.01 s increments. The damping ratio ξ ranged between 10% and 100% in 10% increments. Accelerograms were chosen from the European Strong Motion Database records [9], and subsequently scaled to match the 5% design elastic spectrum prescribed by Eurocode 8, using the scaling criterion defined in the same code. The criteria used to select the different sets are listed in Table 1, *Mw* being magnitude of the ground motion.

Table 1: Selection criteria of ground motion sets

Group	Number of registers	Mw	epicentral distance (km)	Site Class	Notes	Mean scale factor
SITE CLASS B (800 m/s ≥ v_{30} > 360 m/s)						
Ib	40	≥ 5.5	10-50	B		1.435
Ib1	40	≥ 5.0	10-20	B	Some registers in Ib repeated	1.616
Ib2	30	≥ 5.0	20-50	B	Some registers in Ib repeated	3.627
Ib3	40	≥ 5.0	10-50	B	Combination of registers in Ib1 and Ib2 but independent of Ib	3.462
Ib4	80	≥ 5.0	10-50	B	combination of Ib+Ib3	2.053
IIb	20	≥ 5.5	10-50	B	Reselection of Ib disregarding registers with extreme scale factors	1.277
IIb1	20	≥ 5.5	10-50	B	Reselection of Ib1 disregarding registers with extreme scale factors	1.152
IIb2	20	≥ 5.5	10-50	B	Reselection of Ib2 disregarding registers with extreme scale factors	1.705
IIb3	20	≥ 5.5	10-50	B	Reselection of Ib3 disregarding registers with extreme scale factors	1.259
IIb4	20	≥ 5.5	10-50	B	Reselection of Ib4 disregarding registers with extreme scale factors	1.152
SITE CLASS C (360 m/s ≥ v_{30} > 180 m/s)						
Ic	40	≥ 5.5	10-50	C		1.885
IIc	20	≥ 5.5	10-50	C	Reselection of Ic disregarding registers with extreme scale factors	1.440
SITE CLASS C (180 m/s ≥ v_{30})						
Id	10	≥ 5.5	10-50	D	Small number of registers available	1.742

Based on similarity of the group's mean 5% elastic spectrum to the Eurocode 8 spectrum, group Ib is considered to be the most representative for range T_C – 4 s. For this group, Figure 1 presents results DCFs at different values of ξ. For every case the actual value of η^C calculated for the group is compared with expression (4). Because DCFs are known to be only mildly dependent on site class, these results suffice to show that expression (4) is on the safe side. The plots show that the expression is more conservative for higher damping values. The region below T_C is unrepresentative and subsequently not plotted.

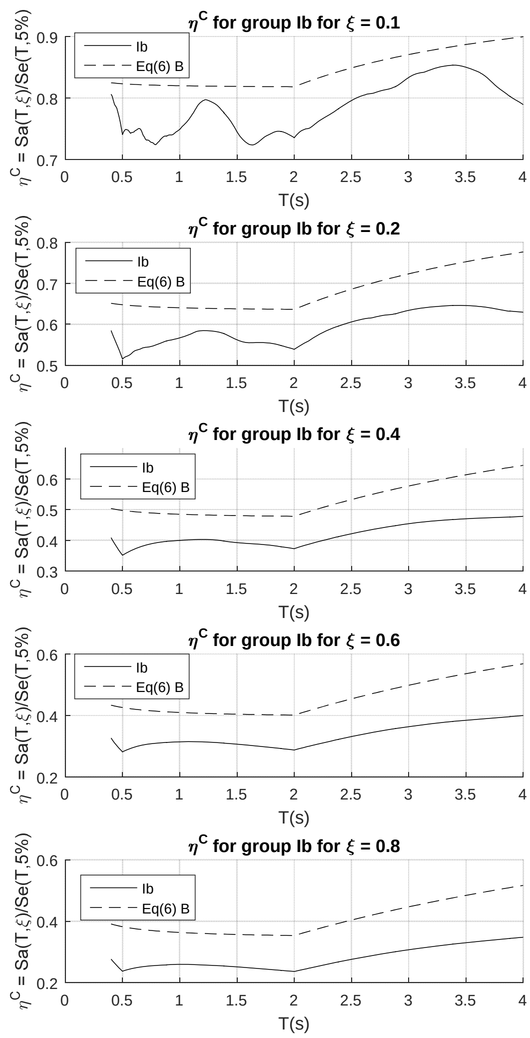

Figure 1: DCFs for groups Ib, IIc and Id, ξ = 10%, 20%, 40%, 60%, 80%.

3 CONCLUSIONS

- Damping Correction Factors (DCFs) when applied to the code 5%-damped elastic response spectrum, readily allow for construction of elastic spectra to different values of damping ratio.
- Eurocode 8 expression for DCFs is independent of period and therefore renders unsafe results in the short and long period ranges.
- A modification of the Eurocode expression is given in equation (4) to take into account conservatively the well-known influence of period. The proposed expression tends to unity for zero and infinite period. The expression has been checked through numerical study.

ACKNOWLEDGEMENTS

This research work was funded by the Spanish Government (Ministerio de Economía y Competitividad) under project BIA2014-60093-R and by the European Union (Fonds Européen de Dévelopment Régional).

REFERENCES

[1] Wu, J., & Hanson, R. D. (1989). Study of inelastic spectra with high damping. Journal of Structural Engineering, 115(6), 1412-1431.

[2] Ramirez O.M., Constantinou M.C., Kircher C.A., Whittaker, A.S., Johnson, M.W., Gomez J.D., Chrysostomou C.Z. (2001). Technical Report MCEER-00-0010. Development and Evaluation of Simplified Procedures for Analysis and Design of Buildings with Passive Energy Dissipation Systems. Revision 1. Multidisciplinary Center for Earthquake Engineering Research. University at Buffalo, New York.

[3] Lin, Y. Y., & Chang, K. C. (2004). Effects of site classes on damping reduction factors. Journal of Structural Engineering, 130(11), 1667-1675.

[4] Bommer, J. J., & Mendis, R. (2005). Scaling of spectral displacement ordinates with damping ratios. Earthquake Engineering & Structural Dynamics, 34(2), 145-165.

[5] Cameron, W. I., & Green, R. A. (2007). Damping correction factors for horizontal ground-motion response spectra. Bulletin of the Seismological Society of America, 97(3), 934-960.

[6] Rezaeian, S., Bozorgnia, Y., Idriss, I. M., Campbell, K., Abrahamson, N., & Silva, W. (2012). Spectral damping scaling factors for shallow crustal earthquakes in active tectonic regions (No. 2012/01). Pacific Earthquake Engineering Research Center.

[7] Standard, B. (2005). Eurocode 8: Design of structures for earthquake resistance—. Part, 1, 1998-1.

[8] Bommer, J. J., Elnashai, A. S., & Weir, A. G. (2000, January). Compatible acceleration and displacement spectra for seismic design codes. In Proceedings of the 12th World Conference on Earthquake Engineering (pp. 1-8).

[9] Ambraseys, N., Smit, P., Douglas, J., Margaris, B., Sigbjörnsson, R., Olafsson, S., ... & Costa, G. (2004). Internet site for European strong-motion data. Bollettino di geofisica teorica ed applicata, 45(3), 113-129.

1st. Conference on Structural Dynamics (DinEst 2018)
Madrid, 20–21 June

DYNAMIC SOIL-STRUCTURE INTERACTION IN AN OFFSHORE LATTICE TOWER

Alejandro E. Martínez-Castro*, **José M. Terrés Nícoli****, **Christian Mans**†

*ETS Ingenieros de Caminos, Canales y Puertos
Universidad de Granada
Avenida Fuentenueva sn, 18002 Granada, Spain

e-mail: amcastro@ugr.es
ORCID: 0000-0003-3023-1099

** Oritia & Boreas Wind Engineering
Calle Ojos del Salado 100, 18008 Granada, Spain
e-mail: terresnicoli@oritiayboreas.com

† Oritia & Boreas Wind Engineering
Calle Ojos del Salado 100, 18008 Granada, Spain
e-mail: mans@oritiayboreas.com

Abstract. The dynamic Soil-Structure Interaction (SSI) plays a major role in the characterization of an offshore structure, in which the foundation is gravity-based. In this work, an experience in the context of a steel lattice tower is reported. The computation of the dynamic stiffness is carried out by a three-dimensional boundary element model in the frequency domain. The soil is characterized as a multilayer viscoelastic half space, with an adequate consideration of water effects. A set of traction singular elements have been included in the model, in order to reduce mesh representation errors. The three dimensional Green function for the multilayered half space has been included. As a consequence, the only required mesh is the foundation contact surfaces. The complex dynamic stiffness matrices are computed in the frequency domain. The foundation is included in a global analysis model, based on modal analysis. The global dynamic model requires the representation of the interation effects in terms of coupled stiffness and damping matrices. Numerical results show that SSI is the cause of an important damping source, coming from the radiation condition at the soil. The SSI plays a major role in the verification of the fatigue limit state, for which an adequate damping evaluation is required.

Key words: Dynamic Soil-Structure Interaction, Offshore structures, Fatigue analysis, Boundary Element Method, Dynamic stiffness, Singular elements

1 INTRODUCTION

Soil-Structure Interaction (SSI) plays a major role in the design of structures subjected to dynamic effects. A recent review about SSI can be found in [5, 7]. In the context of offshore industry, the dynamic SSI causes important damping and stiffness effects, which must be considered in the evaluation of Ultimate and Service limit states. The verification of the Fatigue Limit state (FAT) is sensitive to stress-cycle reductions caused by different damping sources. Offshore standards [3] prescribe accurate analysis of the FAT limit state, providing recomendations about the SSI effect in foundations [2].

In the offshore industry, the use of Gravity Based Systems (GBS) as foundation is a common solution for wind turbines [1], and other related structures. In this paper, the SSI effect in the context of a lattice tower is reported. A similar study for wind turbines and piled foundation is reported in [6]. The present paper shows the analysis carried out in a project developed in 2014 for a meteorological mast. Figure 1 show a conceptual schema of the complete model: a concrete box, a pile, a deck, and a lattice tower are the main components.

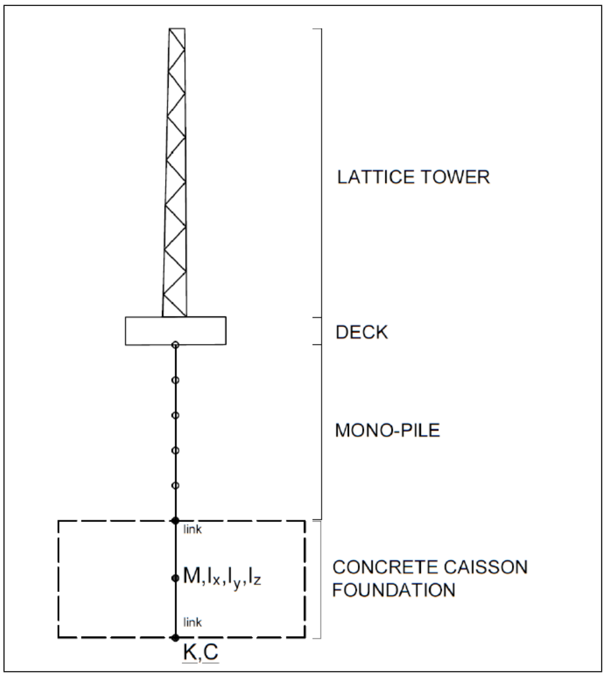

Figure 1: Conceptual model of the met mast

wave forces, considering the spatial and temporal correlation.

The foundation is linked through mass and damping matrices, computed by a set of independent SSI analyses, carried out with application of the Boundary Element Method (BEM). This substructuring approach leads to stiffness and damping effects computed by modal projection techniques. Additional damping was included, considering the different sources (structural, hydrodynamic, aerodynamic), at different water levels, wave height and wind speeds. The soil is considered as a multilayer half-space (Figure 2).

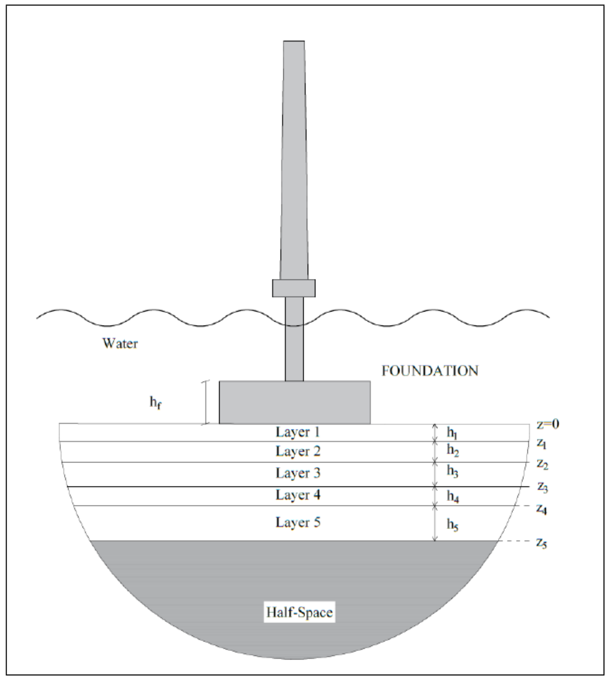

Figure 2: Coupled model with multilayered half-space

2 STRUCTURAL MODEL

A 3D structural model was developed (see a schema in Figure 1). Beam elements were used, with accurate representation of the local joint flexibilites in the lattice tower. The lattice tower is designed with circular hollow sections, with corrosion allowance included in the model through a 3mm thickness reduction. The analysis was carried out in the time domain, based on modal superposition. Time series were developed for wind and

3 BOUNDARY ELEMENT MODEL

The soil is represented as a viscoelastic multilayer half space. The BEM model is carried out with a fundamental solution in the frequency domain, in which the layers are included [8]. Figure 3 show the three-dimensional problem considered. By the use of the specific Green function, the only surface requiring a mesh is the base of the concrete caisson. The computations of the dynamic stifness matrices are carried out by 6 independent problems, in which the ridig-solid degrees of freedom of the foundation are prescribed with time-harmonic variation. The solution of the problem is obtained in terms of tractions at the contact surface, and the integration of such tractions gives the dynamic stifness matrices.

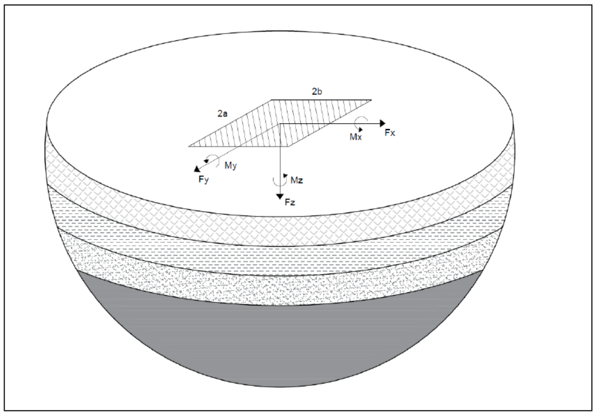

Figure 3: Layerd half-space and foundation

In the corners and edges of the fully-bonded contact surface, traction singularities were considered, according to the elasticity theory in sharp contacts, by use of traction singular elements [4]. The use of this kind of elements provides a minimal mesh with accurate results for the stifness componentes. Figure 4 shows a traction profile at the foundation surface obtined by this kind of elements for a particular stiffness component.

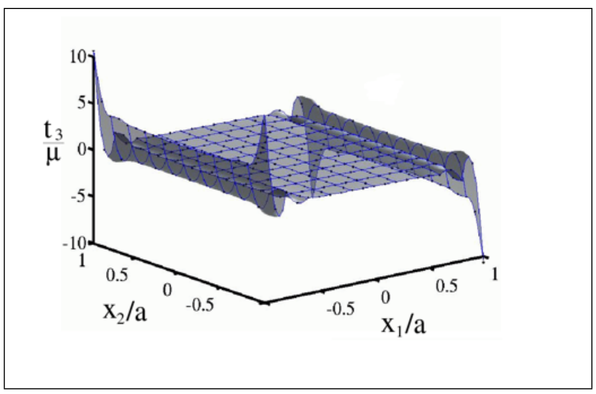

Figure 4: Singular traction elements in BEM

All the terms included in the stiffness matrices are complex-valued. Such values represents inertial, stiffness and damping effects caused by soil radiation. Additional hysteretic damping was considered by complex-valued material properties.

4 TIME-DOMAIN MODEL

The global model is analysed in the time-domain through modal superposition. The stiffness and damping effects from the SSI matrices are adapted by considering its calibration at the main frequency of the first vibration mode. The identification of the damping matrix $\mathbf{C}$ at the angular frequency ω is carried out by the identification of the real and imaginary parts of the dynamic stifness matrix $\mathbf{K}$.

$$\mathbf{K} = (\mathbf{K_r} + i\,\mathbf{K_i}) = (\mathbf{K_r} + i\,\omega\,\mathbf{C}) \tag{1}$$

in which i is the imaginary unit.

The matrix $\mathbf{C}$ can be computed as,

$$\mathbf{C} = \frac{1}{\omega}\,\mathbf{K_i} \tag{2}$$

The variability of soil parameters was considered by defining a set of layer profiles, considering the statistical distribution of the elastic properties and density.

5 VERIFICATION OF SSI EFFECT

In this section the SSI effect is shown by a free-vibration test. A soil profile is described in Table 1. In order to consider the water effect, the saturated density and cuasi-incompressible Poisson parameter is considered, according to literature ($\nu = 0.45$).

A free-vibration test is carried out. The axial force in a vertical steel member is monitored. Figure 4 shows two curves for the axial force. In both cases, constant modal damping $\zeta = 0.3\%$ is included, representative of the structural effects (welded and bolted unions). In addition, in one case, the SSI effect is included. The plot show an important axial force reduction when the SSI effect is included. This causes amplitude stress reductions, giving better results in the FAT limit state.

Table 1: Layer properties

Layer	h(m)	ρ_s (kg/m^3)	E(Mpa)
1	1.5	2200	34.8
2	3	1800	17.4
3	2	2100	58
4	3	2200	174
5	3	1800	43.5

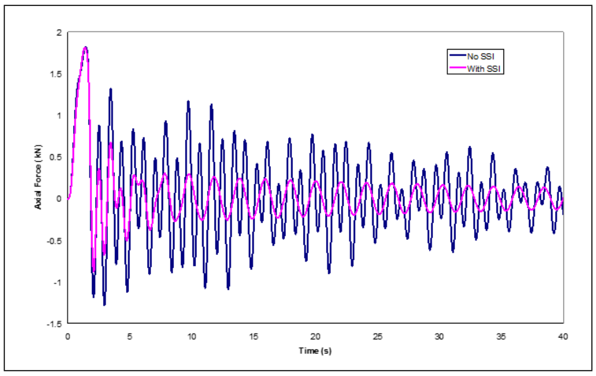

Figure 5: SSI effect in axial force of a steel member

6 CONCLUDING REMARKS

The SSI effect is an important damping source in the dynamic response of an offshore structure. In this work, an accurate characterization of the dynamic stiffness matrices is presented. The computation is carried out by an independent Boundary Element model. The combined use of a particular Green function for the layerd domain, and the use of traction singular elements, causes accurate and fast computations of the dynamic stiffness matrices. Included in the global model in the context of a real project, the SSI justified important stress reductions, which strongly affected the certification and verification process. In particular, the fatigue verifications were strongly affected by the SSI, with an adequate assessment of the lifetime in welded and bolted joints.

7 FIGURES

REFERENCES

[1] S. Bhattacharya and S. Adhikari. Experimental validation of soil–structure interaction of offshore wind turbines. *Soil Dynamics and Earthquake Engineering*, (31):805–816, 2011.

[2] CN-30.4. *Foundations*, DNV-GL edition, 1992.

[3] DNVGL-ST-0126. *Design of Offshore Wind Turbines structures*, DNV-GL edition, 2016.

[4] B. B. Guzina, R. Y.S. Pak, and A. E. Martínez-Castro. Singular boundary elements for three-dimensional elasticity problems. *Engineering Analysis with Boundary Elements*, 30(8):623 – 639, 2006.

[5] E. Kausel. Early history of soil–structure interaction. *Soil Dynamics and Earthquake Engineering*, 30(9):822 – 832, 2010. Special Issue in honour of Prof. Anestis Veletsos.

[6] G. M. Álamo, J. J. Aznárez, L. A. Padrón, A. E. Martínez-Castro, R. Gallego, and O. Maeso. Dynamic soil-structure interaction in offshore wind turbines on monopiles in layered seabed based on real data. *Ocean Engineering*, 156:14 – 24, 2018.

[7] M. Lou, H. Wang, X. Chen, and Y. Zhai. Structure–soil–structure interaction: Literature review. *Soil Dynamics and Earthquake Engineering*, 31(12):1724 – 1731, 2011.

[8] R. Y. S. Pak and B. B. Guzina. Three-Dimensional Green's Functions for a Multilayered Half-Space in Displacement Potentials . *Journal of Engineering Mechanics*, 128(4):449 – 461, 2002.

SECTION 7: Non-linear dynamics, dynamics of multibody systems, biomechanics, impact actions and explosions

1st. Conference on Structural Dynamics (DinEst 2018)
Madrid, 20–21 June

SYMMETRY-PRESERVING FORMULATION OF NONLINEAR CONSTRAINTS IN MULTIBODY DYNAMICS

Juan C. García Orden*

*ETS Ingenieros de Caminos, Canales y Puertos
Universidad Politécnica de Madrid
28040 Madrid, Spain

e-mail: juancarlos.garcia@upm.es
ORCID: 0000-000-2-9063-6584

Abstract.

Geometrical integrators are particular time-stepping schemes that have been successfully employed during the last decades in many applications, including multibody systems. One of them is the so-called Energy-Momentum (EM) scheme, that exhibits excellent stability and physical accuracy, but demanding a specific (consistent) formulation of constraints. In particular, EM penalty formulations are specially simple, based on the application of a discrete derivative of the constraint potential. However, this discrete derivative may take several forms, not all of them being consistent. In particular, when applied to constraint potentials endowed with certain symmetries (associated to the conservation of linear and angular momenta, found in many common practical joints), may produce numerical results that conserves the energy but violates the symmetries, thus obtaining unphysical motions.

The discrete derivative proposed in this work, while first introduced several years ago, overcomes this problem, mainly due to its particular implementation. Its discrete properties related with energy and symmetries are analyzed and several numerical results of practical multibody models will be presented.

Key words: Nonlinear Dynamics, Multibody, Constraints, Energy-Momentum, Symmetries

1 Introduction

A common feature of many multibody systems is the presence of joints that limit or couple the motion of the different parts of the system. A proper representation of these joints in the model is essential in order to obtain an accurate solution, usually through specialized numerical schemes, of their dynamical equations.

One category of such schemes is the so-called geometric integrators, that are designed to provide numerical solutions that exactly inherit basic features of the underlying time-continuous model. Some of these schemes, in the context of the dynamics of Hamiltonian systems, are the Energy-Momentum (EM) methods, that are second-order schemes that preserve the total energy in conservative mechanical problems and possible symmetries associated with the conservation of linear and angular momenta.

The concept of discrete derivative plays a central role in the systematic design of a EM method. Interestingly, its particular expression is not unique and accordingly several formulations have been proposed in the literature for our systems of interest. Nevertheless, not all of them reveal suitable for the EM formulation of completely general constraints and potential forces. Surprisingly, this fact seems to have been overlooked by many authors, and constitutes the main motivation of the developments presented in this paper.

2 Time-continuous model: energy conservation and symmetries

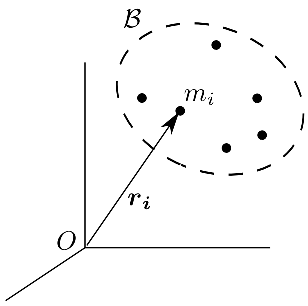

Let us consider a system $\mathcal{B}$ composed by N particles with masses $m_i, i = 1,..,N$, moving in the three-dimensional Euclidean space. The motion of this system at time $t \in [0,T]$ is described by the vectors $\mathbf{q}(t), \mathbf{p}(t) \in \mathbb{R}^{3\times N}$ that collects the cartesian inertial coordinates of their position and momentum vectors $\boldsymbol{r}_i(t), \boldsymbol{p}_i(t) = m_i\dot{\boldsymbol{r}}_i; i = 1,..,N$. What is more, lets us assume that there are no external forces and that the motion of the system is constrained by a general holonomic constraint function $\Phi : \mathbb{R}^{3\times N} \times [0,T] \to \mathbb{R}$, such that $\Phi(\mathbf{q},t) = 0$. The equations of motion are given by the index-3 DAE system:

$$\dot{\mathbf{q}} = \mathbf{M}^{-1}\mathbf{p} \quad \dot{\mathbf{p}} = -D_{\mathbf{q}}\Phi^{\mathrm{T}}\lambda \quad 0 = \Phi(\mathbf{q},t) \tag{1}$$

$\mathbf{M}$ being the mass matrix (diagonal), vector $D_{\mathbf{q}}\Phi = \partial\Phi/\partial\mathbf{q}$ and $\lambda \in \mathbb{R}$ a Lagrange multiplier. It is easy to prove that the energy of the system is constant provided the constraint does not depend explicitly on time (i.e., it is a scleronomic constraint), because in this case $\dot{\Phi} = D_{\mathbf{q}}\Phi\ \dot{\mathbf{q}} = D_{\mathbf{q}}\Phi\mathbf{M}^{-1}\mathbf{p}$.

On the other hand, Noether's theorem states that a mechanical system has a conservation law for each symmetry of its evolution equations [4]. In our system, these symmetries may be translational and rotational, and the corresponding conserved magnitudes would be the linear and angular momenta in O, defined respectively as:

$$\mathbf{L} = \sum_{i=1}^{N} \boldsymbol{p}_i = \mathbb{1}\mathbf{p} \quad , \quad \mathbf{J} = \sum_{i=1}^{N} \boldsymbol{r}_i \times \boldsymbol{p}_i = \mathbb{r}\mathbf{p} \tag{2}$$

$\mathbb{1}$ and $\mathbb{r}$ being the following $3\times 3N$ matrices:

$$\mathbb{1} = (\mathbf{1} \mid \mathbf{1} \mid ... \mid \mathbf{1}) \qquad , \qquad \mathbb{r} = (\hat{\mathbf{r}}_1 \mid \hat{\mathbf{r}}_2 \mid ... \mid \hat{\mathbf{r}}_N)$$

with $\mathbf{1}$ being the identity 3×3 matrix and $\hat{\mathbf{r}}_i$ denoting the 3×3 skew-symmetric matrix associated to vector $\mathbf{r}_i$. Differentiating (2), and considering the fact that $\dot{\mathbb{r}}\mathbf{p} = \mathbf{0}$, we obtain:

$$\dot{\mathbf{L}} = \mathbb{1}\dot{\mathbf{p}} = -\lambda\mathbb{1}D_{\mathbf{q}}\Phi^{\mathrm{T}} \qquad , \qquad \dot{\mathbf{J}} = \mathbb{r}\dot{\mathbf{p}} = -\lambda\mathbb{r}D_{\mathbf{q}}\Phi^{\mathrm{T}} \tag{3}$$

Equations (3) reveal the *orthogonality conditions* to be met by a constraint to conserve the linear and angular momenta:

$$\mathbb{1}D_{\mathbf{q}}\Phi^T = \mathbf{0} \qquad ; \qquad \mathbb{r}D_{\mathbf{q}}\Phi^T = \mathbf{0} \tag{4}$$

It is important to remark that these results are not altered by the use of a constraint enforcement method other than Lagrange multipliers', such as penalty or augmented Lagrangian.

3 EM formulation. Discrete energy conservation and symmetries

The proposed EM formulation is described by the following second-order time-stepping scheme, which at first glance can be interpreted as a modified implicit midpoint rule:

$$\mathbf{q}_{n+1} - \mathbf{q}_n = \frac{\Delta t}{2}\mathbf{M}^{-1}(\mathbf{p}_n + \mathbf{p}_{n+1}) \tag{5}$$

$$\mathbf{p}_{n+1} - \mathbf{p}_n = -\Delta t\lambda_{n+1}\mathsf{D}\Phi^{\mathrm{T}} \tag{6}$$

$$\Phi_{n+1} = 0 \tag{7}$$

$\mathbf{q}_n$ and $\mathbf{p}_n$ being the approximated values of $\mathbf{q}$ and $\mathbf{p}$ at $t_n \in [0,T]$ respectively, and $\Phi_n = \Phi(\mathbf{q}_n)$. The term $\mathsf{D}(\cdot)$, different from the standard continuous derivative denoted by $D(\cdot)$, is the *discrete derivative* operator. For a smooth function $f : \mathbb{R}^n \to \mathbb{R}$ with $n \geq 1$, the discrete derivative $\mathsf{D}f : \mathbb{R}^n \times \mathbb{R}^n \to \mathbb{R}^n$ is an operator that satisfies the following properties:

$$\text{Consistency: } \mathsf{D}f(\mathbf{x},\mathbf{y}) = Df\left(\frac{\mathbf{x}+\mathbf{y}}{2}\right) + \mathcal{O}(||\mathbf{y}-\mathbf{x}||) \tag{8}$$

$$\text{Directionality: } \mathsf{D}f(\mathbf{x},\mathbf{y})\ (\mathbf{y}-\mathbf{x}) = f(\mathbf{y}) - f(\mathbf{x}) \tag{9}$$

for any $\mathbf{x},\mathbf{y} \in \mathbb{R}^n$. Consistency ensures second order accuracy, while directionality is crucial to preserve discretely the energy, as will be seen next.

The discrete energy balance is null provided the directionality condition (9), that takes the form:

$$\mathsf{D}\Phi\ (\mathbf{q}_{n+1} - \mathbf{q}_n) = \Phi_{n+1} - \Phi_n \tag{10}$$

is satisfied

If the system has symmetries introduced by the action ψ of a Lie group G (in our case translations and/or proper rotations in $\mathbb{R}^3$), it is necessary to extend the previous discrete derivative concept defining the so-called *G-invariant discrete derivative* $\mathsf{D}^G(\cdot)$ that satisfies the consistency and directionality conditions (8), (9) and additionally the properties of equivariance and orthogonality:

$$\mathbb{1}\mathsf{D}^G\Phi^{\mathrm{T}} = \mathbf{0} \qquad , \qquad \mathbb{r}_{n+\frac{1}{2}}\mathsf{D}^G\Phi^{\mathrm{T}} = \mathbf{0} \tag{11}$$

It can be readly checked that the satisfaction of conditions (11) leads to the conservation of linear and angular momenta, which are the discrete momentum maps associated with the symmetries. Finally, observe the simillarity between the orthogonality conditions (4) and the second-order discrete counterparts (11).

4 Discrete derivatives

In this section we will discuss some particular expressions proposed in the literature over the years.

A. *Scaled midpoint gradient:*

$$\mathsf{D}f(\mathbf{x},\mathbf{y}) = \frac{f(\mathbf{y}) - f(\mathbf{x})}{Df\left(\frac{\mathbf{x}+\mathbf{y}}{2}\right)\cdot(\mathbf{y}-\mathbf{x})} Df\left(\frac{\mathbf{x}+\mathbf{y}}{2}\right) \tag{12}$$

This formula was first proposed by Chorin *et al.* [1] and later by Simó *et al.* [5] as a particular implementation of implicit EM algorithms based on projection.

B. *Collocation gradient:*

$$\mathsf{D}f(\mathbf{x},\mathbf{y}) = Df\left(\mathbf{x} + \beta(\mathbf{y}-\mathbf{x})\right) \tag{13}$$

$\beta \in [0,1]$ being a scalar such that the directionality condition (9) is satisfied.This formula was proposed by Simó *et al.* [5] as a particular implementation of implicit EM algorithms based on collocation.

C. *Corrected midpoint gradient:*

$$\mathsf{D}f(\mathbf{x},\mathbf{y}) = Df\left(\frac{\mathbf{x}+\mathbf{y}}{2}\right) + \frac{f(\mathbf{y}) - f(\mathbf{x}) - Df\left(\frac{\mathbf{x}+\mathbf{y}}{2}\right)\cdot(\mathbf{y}-\mathbf{x})}{||\mathbf{y}-\mathbf{x}||^2}(\mathbf{y}-\mathbf{x}) \tag{14}$$

Formula proposed by Gonzalez [2, 3] for both finite and infinite-dimensional problems.

D. *Partitioned discrete derivative.* It is also possible, using any of the previous formulas, to define a partitioned discrete derivative as a second-order approximation of a partial derivative. For all $\mathbf{v} \in \mathbb{R}^n$:

$$\mathsf{D}f(\mathbf{x},\mathbf{y})\mathbf{v} = \sum_{i=1}^{n} \mathsf{D}_i f(\mathbf{x},\mathbf{y})\ v_i = \sum_{i=1}^{n} \frac{1}{2}\left(\mathsf{D}f^i_{\mathbf{xy}}(x_i,y_i) + \mathsf{D}f^i_{\mathbf{yx}}(x_i,y_i)\right) v_i \tag{15}$$

$f^i_{\mathbf{xy}}$ and $f^i_{\mathbf{xy}}$ being the scalar functions defined as:

$$f^i_{\mathbf{xy}}(u) = f(x_1,..,x_{i-1},u,y_{i+1},...,y_n)$$
$$f^i_{\mathbf{yx}}(u) = f(y_1,..,y_{i-1},u,x_{i+1},...,x_n)$$

This formula is proposed by Gonzalez [2, 3].

Energy conservation. As explained in Section (3), consistency ensures second-order accuracy and directionality the conservation of energy. It is straightforward to check that all expressions A, B, C and D applied to the constraint function $\Phi(\mathbf{q})$ are second-order and satisfy the directionality condition (10), thus leading to second-order, energy-conserving formulations.

Preservation of symmetries The preservation of symmetries (linear and angular momenta) demands a G-invariant discrete derivative, satisfying the additional orthogonality conditions (11). The only formula that complies with all requirements is A, the scaled midpoint gradient. The proof of this claim is omitted due to lack of space, but it will be illustrated with one particular numerical example.

5 Example: alignment of three points

Let us consider three points with position vectors $\mathbf{r}_1, \mathbf{r}_2, \mathbf{r}_3$ collected in vector $\mathbf{q} \in \mathbb{R}^9$ forced to move aligned by the constraint function $\Phi(\mathbf{q}) = ||\boldsymbol{\Phi}||$, with $\boldsymbol{\Phi} = ||\mathbf{a}\times\mathbf{b}||$, $\mathbf{a} = \mathbf{r}_2 - \mathbf{r}_1$ and $\mathbf{b} = \mathbf{r}_3 - \mathbf{r}_2$. After some algebra, the following expression can be obtained for the constraint's derivative:

$$D\Phi^{\mathrm{T}} = \left(\frac{\mathrm{d}\boldsymbol{\Phi}}{\mathrm{d}\mathbf{q}}\right)^{\mathrm{T}} \left(\frac{\mathrm{d}\Phi}{\mathrm{d}\boldsymbol{\Phi}}\right)^{\mathrm{T}} = \left\{ \begin{array}{c} -\mathbf{b}\times\mathbf{n} \\ (\mathbf{a}+\mathbf{b})\times\mathbf{n} \\ -\mathbf{a}\times\mathbf{n} \end{array} \right\} \tag{16}$$

$$\text{with} \quad \mathbf{n} = \boldsymbol{\Phi}/\Phi \tag{17}$$

that fulfills the orthogonality conditions (4) at any instant $t \in [0, T]$:

$$\begin{aligned} \mathbb{1} D\Phi^{\mathrm{T}} &= -\mathbf{b}\times\mathbf{n} + (\mathbf{a}+\mathbf{b})\times\mathbf{n} - \mathbf{a}\times\mathbf{n} = \mathbf{0} \\ \mathbb{r} D\Phi^{\mathrm{T}} &= \left[\boldsymbol{r}_1^{\mathrm{T}}\boldsymbol{b} - \left(\boldsymbol{r}_2^{\mathrm{T}}(\boldsymbol{a}+\boldsymbol{b}\right) + \boldsymbol{r}_3^{\mathrm{T}}\boldsymbol{a}\right]\boldsymbol{n} \\ &= \left(-\boldsymbol{a}^{\mathrm{T}}\boldsymbol{b} + \boldsymbol{b}^{\mathrm{T}}\boldsymbol{a}\right)\boldsymbol{n} = \mathbf{0} \end{aligned}$$

Therefore, under the sole action of the constraint, total linear and angular momenta are conserved. This is an expected result since $D\Phi$ is proportional to the force vector, and the sum of internal forces and momenta is null.

Note that $\Phi(\mathbf{q})$ does not have any invariant being at most quadratic in $\mathbf{q}$, including the function Φ itself. Therefore we have the most general case presented in Section 4, and the only G-invariant discrete derivative satisfying the discrete orthogonality conditions is the scaled midpoint gradient (12):

$$\begin{aligned} \mathbb{1}\mathsf{D}\Phi^{\mathrm{T}} &= \gamma \mathbb{1} D\Phi^{\mathrm{T}}_{n+1/2} = \mathbf{0} \\ \mathbb{r}_{n+\frac{1}{2}}\mathsf{D}\Phi^{\mathrm{T}} &= \gamma \mathbb{r}_{n+\frac{1}{2}} D\Phi^{\mathrm{T}}_{n+1/2} = \mathbf{0} \end{aligned}$$

with $\gamma = \Delta\phi / D\Phi^{\mathrm{T}}_{n+1/2}\Delta\mathbf{q}$.

6 Conclusions

The use of a discrete derivative concept allows the systematic design of EM schemes, and several different formulas have been proposed in the literature over the years, all of them energy conserving. We have shown in this paper that some of them fail to define a scheme able to preserve linear and/or angular momentum in systems with constraints and/or potentials possessing symmetries. After a careful analysis only one of them, the scaled midpoint gradient, appears to comply with the requirements to produce a true EM scheme, at least for systems with finite-dimensional and linear configuration spaces. The results of some numerical experiments suggest that the scaled midpoint gradient could be indeed the optimal choice for defining stable and accurate EM schemes for solving the dynamics of constrained systems, such as those typically arising in multibody dynamics.

ACKNOWLEDGMENTS

Education, Culture and Sports Ministry of Spain supported this work under Project DPI2015-67667-C3-2-R. This support is gratefully acknowledged.

REFERENCES

[1] Alexandre J. Chorin, Thomas J.R. Hughes, Marjorie F. McCracken, and Jerrold E. Marsden. Product formulas and numerical algorithms. *Communications on Pure and Applied Mathematics*, 31:205–256, 1978.

[2] O. González. *Design and analysis of conserving integrators for nonlinear hamiltonian systems with symmetry.* PhD thesis, Stanford University Department of Mechanical Engineering, 1996.

[3] Oscar González. Time integration and discrete hamiltonian systems. *Journal of Nonlinear Science*, 6:449–467, 1996.

[4] J.E. Marsden and T.S. Ratiu. *Introduction to mechanics and symmetry.* Springer-Verlag, 1994.

[5] J.C. Simó, N. Tarnow, and K.K. Wong. Exact energy-momentum conserving algorithms and symplectic schemes for non-linear dynamics. *Computer methods in Applied Mechanics and Engineering*, 100:63–116, 1992.

SIMULATION STUDY OF THE INFLUENCE OF DESIGN PARAMETERS ON A VIBROCOMPACTION PROCESS

Javier González Carbajal*, **Daniel García-Vallejo*** **and Jaime Domínguez***

*ETS de Ingeniería
Universidad de Sevilla
41092 Sevilla, Spain

e-mail: dgvallejo@us.es
ORCID: 0000-0002-2319-2688

Abstract. Vibrating machines are extensively used as a mean to compact granular materials. This paper has been motivated by a particular manufacturing process, where a quartz-resin mixture is compacted by using the vibration produced by a set of unbalanced motors, together with a vacuum system. The compaction is conducted by means of several unbalanced electric motors, mounted on a piston with the dimensions of the slab surface. At the beginning of the vibrocompaction process, the piston descends onto the mixture and exerts a static pressure, due to its weight and to an air pressure applied on it. Then, the air pressure inside the mould is reduced by using a vacuum system, after which the motors are switched on. The vibration produced by the unbalanced motors is the main responsible for the compaction. During the motion of the system, there can be separations and impacts between the piston and the slab, which are generally beneficial for the compaction, as they produce very high peaks of compression forces. A nonlinear model is introduced which includes some of the main nonlinearities present in the real system: the nonideal interaction between the motors and the vibrating system, contact and impacts between mixture and piston (the platform upon which the motors are mounted) and also between the mixture and the supporting mould, and a nonlinear constitutive law for the mixture, which allows modelling the compaction itself. Solving the system of differential equations of such model, some insight into its nonlinear behaviour is obtained, with special interest in the influence of different factors on the final level of compaction achieved.

Key words: Vibrocompaction, non-linear vibrations, contacts/impacts.

1 INTRODUCTION

The vibrocompaction process of a quartz-resin mixture by using the vibration produced by a set of unbalanced motors is extremely complex from a physical point of view. A large number of factors -some of them being intrinsically nonlinear- influence the final result of the compaction:

- The quartz granulometry, the rheological properties of the resin and the mass ratio between quartz and resin affect the mechanical behaviour of the compacting mixture. This behaviour is necessarily nonlinear, since the mixture suffers irreversible deformation during compaction.

- The dynamic properties of the different elements of the machine -the piston, the conveyor belt supporting the mould, the elastomer between the foundation and the ground, etc. - may influence the vibrocompaction as well.

- The speed of the motors, their available power and the amount of unbalance are key parameters of the process.
- The final result of the compaction may also depend on the duration of the process.
- The spatial distribution of the vacuum channels influences the extraction of the air out of the mixture, thereby affecting the compaction.

In addition, when a structure is excited by one or more unbalanced motors, some particular nonlinear effects can take place due to the interaction itself between the exciter and the vibrating system [4, 3]. The motion of the unbalanced motor will be influenced by the response of the vibrating system, due to the inertia forces that the vibration produces on the unbalanced mass [3]. Then, rather than a known excitation acting on the vibrating system, what we generally have is a two-way coupling between the motions of the exciter and the structure. In the literature, this is called a nonideal excitation, and the associated nonlinear phenomena are usually referred to as The Sommerfeld effect [1]. Conversely, an excitation is said to be ideal if it remains unaffected by the vibrating response. After the works of Sommerfeld and Kononenko, many investigations have been conducted in order to better understand and predict the effect of nonideal excitations on vibrating systems. Most studies use averaging procedures to obtain approximate solutions to the equations of motion, Blekhman [2] proposed an alternative approach, based on the method of 'Direct Separation of Motions'. Balthazar et al. [1] published an extensive exposition of the state of the art concerning nonideal excitations. Considering the vibrocompacting machine for quartz agglomerates, it is reasonable to expect that nonlinear effects, produced by a nonideal coupling between the vibrating system and the unbalanced motors, are present in the system behaviour. The model presented in this paper will allow showing how these phenomena, associated to nonideality of the energy source, can affect the result of the compaction process.

2 DESCRIPTION OF THE MODEL

The quartz-resin mixture is represented in the model by a couple of masses attached to each other by a linear damper and a nonlinear spring, which models the compaction itself by allowing for permanent deformation when the spring is compressed. Then, the distance between both masses would represent the thickness of the compacting mixture. The mould is modelled as a rigid base, while the piston with the unbalanced motors is represented by a mass with a single unbalanced motor. The mixture is in contact -with separations and impacts allowed- with the mould at the bottom and with the piston at the top. The vacuum system is not included in the model. It should be noted that the model assumes the horizontal motion of the piston to be completely restrained, which makes unnecessary to include a couple of motors rotating in opposite directions.

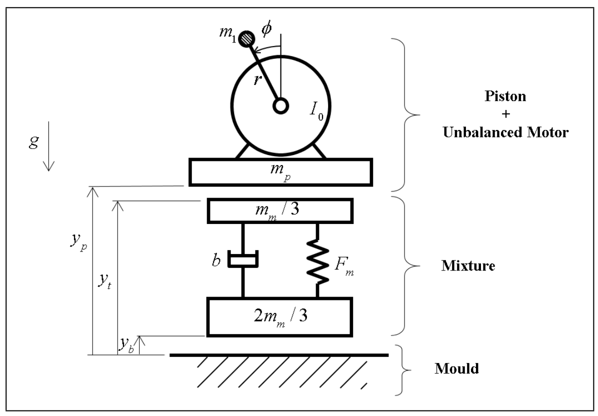

Figure 1: 4-DOF model of the vibrocompaction process.

As represented in Fig. 1, the model has 4 DOFs: y_b, y_t, y_p and ϕ, which correspond, respectively, to position of the bottom of the mixture, position of the top of the mixture, position of the piston and rotation of the motor. The parameters represented in Fig. 1 are as follows: m_m stands for the mass of the mixture, m_1 is the unbalanced mass, m_p is the mass of the piston and the motor, r is the eccentricity of the unbalance, I_o is the rotor inertia,

b is the damping coefficient, F_m is the force produced by the nonlinear spring and g is the gravity constant.

Notice that, based on the assumption of uniform deformation, which is suitable because the mass of the piston is much greater than that of the mixture, the total mass of the mixture is distributed in the proposed model in a particular way: one third corresponds to the upper mass and two thirds to the bottom mass. The driving torque provided by the motor minus the losses torque due to friction at the bearings and windage is assumed to be a linear function of the rotor speed:

$$L_m(\dot{\phi}) = A + D\dot{\phi}, \text{ with } A > 0,\ D < 0. \quad (1)$$

The equations of motion of the system can be obtained by equilibrium considerations as follows:

$$\begin{aligned}
&(m_p + m_1)\ddot{y}_p = m_1 r(\dot{\phi}^2 \cos\phi + \ddot{\phi}\sin\phi) + F_{ct} - (m_p + m_1)g\\
&(m_m/3)\ddot{y}_t + F_m + b(\dot{y}_t - \dot{y}_b) = -F_{ct} - (m_m/3)g\\
&(2m_m/3)\ddot{y}_b - F_m - b(\dot{y}_t - \dot{y}_b) = F_{cb} - (2m_m/3)g\\
&I\ddot{\phi} = L_m(\dot{\phi}) + m_1 r\sin\phi(\ddot{y}_p + g)
\end{aligned} \quad (2)$$

where $I = I_0 + m_1 r^2$ and F_{cb}, F_{ct} represent the normal contact force between mixture and mould and between mixture and piston, respectively. Clearly, the most challenging features of this model are the behaviour of the nonlinear spring and the computation of the contact forces. System (2), together with the definition of the spring force and the contact forces given in the following, constitutes the proposed model for the compacting machine. A Hunt and Crossley nonlinear contact model of the form $F_c = k_c\delta^n + b_c\delta^p\dot{\delta}^q$, is used, where it is standard to set $n = p$, $q = 1$. Note that the damping term depends on indentation, which is physically sound, since plastic regions are more likely to develop for larger contact deformations. Moreover, the contact force does not exhibit discontinuous changes at the impact and separation instants, thereby overcoming one of the main problems of the spring-dashpot model.

3 NUMERICAL RESULTS

In this section, system (2) is numerically solved. The chosen initial conditions for all the simulations correspond to the static equilibrium position of the system:

$$\begin{aligned}
&\phi(0) = \pi,\ \dot{\phi}(0) = 0,\ y_b(0) = d_b,\ \dot{y}_b(0) = 0,\\
&y_t(0) = d_b + L_D + d_{st},\ \dot{y}_t(0) = 0,\\
&y_p(0) = d_b + L_D + d_{st} + d_t,\ \dot{y}_p(0) = 0.
\end{aligned} \quad (3)$$

where d_t and d_b are the indentations at the top and bottom contacts, respectively, due to the weight of the elements above the contact. With this initial configuration, system (2) is solved, using embedded Runge-Kutta formulae of orders 4 and 5, for a simulation time t_f which varies between 30 s and 55 s. This total time includes three different stages in the simulation, of respective lengths t_1, t_2 and t_3 ($t_f = t_1 + t_2 + t_3$):

- During the first stage ($0 \le t < t_1$) parameter A is linearly increased from A_0 to A_f, with A_0 and A_f while slope D is kept constant. Then, the motor is being controlled as in Sommerfeld's experiment.
- At the second stage ($t_1 \le t < t_1+t_2$), parameter A is kept constant at its final value A_f. During this stage, the machine is expected to reach a stationary operating point.
- At time $t = t_1 + t_2$, the motor is switched off in order to let the system reach a compacted equilibrium position.

Clearly, once the motor is switched off, there is no driving torque on the rotor, and function $L_m(\dot{\phi})$ must only account for the resisting torque due to windage and friction at the bearings. This is modelled by replacing the motor characteristic with the following curve:

$$L_m(\dot{\phi}) = 0.2D\dot{\phi}, \text{ for } t_1 + t_2 \le t < t_f. \quad (4)$$

Hence it is being assumed that the slope of the resisting torque curve is 20% of the slope of the motor characteristic. Parameters t_2 and t_3 have been chosen as 15s for all the simulations, while t_1 will take different values depending on the case under study.

The proposed model is defined by 11 dimensional parameters

$$m_1,\ m_p,\ m_m,\ b,\ r,\ I_0,\ d_f,\ F_f,\ R_k,\ k_c,\ b_c \quad (5)$$

besides the two parameters associated to the motor control (A, D). For the simulation, the set of parameters (5) is chosen as m_1=20kg, m_m=240 kg, m_p= 1500 kg, r=0.1 m, I_0=0.84 kgm^2, b=4000 Ns/m, d_f=-0.1 m, F_f=-100 kN, R_k=0.1, $k_c = 3{\cdot}10^9$ N/m, $b_c = 9.5{\cdot}10^6$ Ns/m. Before the numerical resolution of the equations of motion, it is useful to obtain some previous information about the system. First, from the knowledge of parameters d_f, F_f and R_k, stiffnesses k_0 and k_f can be computed as:

$$k_0 = 1.82 \cdot 10^5\text{N/m},\ k_f = 1.82 \cdot 10^6\text{N/m}, \qquad (6)$$

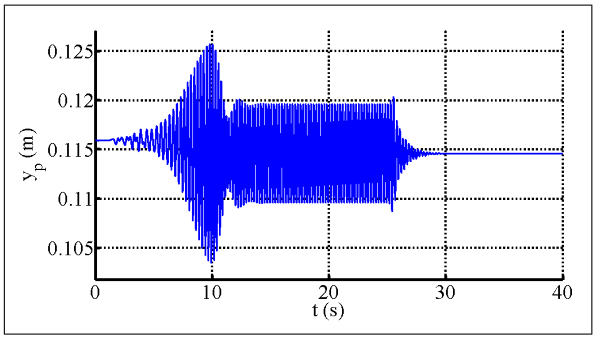

Figure 2: Piston displacement.

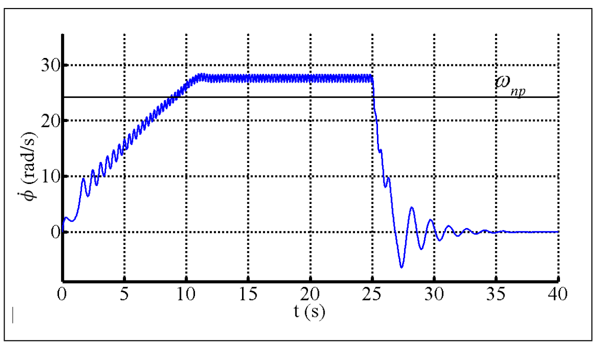

Figure 3: Rotor speed.

Then, the initial stiffness for the dynamic process can also be obtained, together with the static compaction:

$$k_{st} = 7.39 \cdot 10^5\text{N/m} \rightarrow y_{st} = 34.1\%. \qquad (7)$$

A numerical experiment is carried out now, where the motor control parameters are chosen as t_1=10 s, D=-5 Nms, A_0=20 Nm, A_f=140 Nm. The results of the simulation are represented in Fig. 2 and Fig. 3.

It is observed in Fig. 2 that, as the motor curve is displaced upwards between 0 and 10 s, the oscillation amplitude grows monotonically, until a point where a jump phenomenon is encountered. After the jump, the system clearly reaches a post resonant state of motion, as shown in Fig. 3, where ω_{np} represents the natural frequency of the system during the stationary motion of stage 2. The jump phenomenon encountered here clearly resembles the Sommerfeld effect. However, it might be somehow different to the general phenomenon since no clear slowing down in the increase of the rotor speed is observed in Fig. 3. This is probably due to the additional complexity of the vibrocompaction.

4 CONCLUSIONS

A novel nonlinear model for the vibrocompaction of quartz agglomeartes is proposed in this work. As far as the authors know, this is the first attempt to model this industrial process by using nonlinear systems analysis techniques, including both perturbation and averaging technics. Solving the equations of motion, the effect of different parameters of the process in the final level of compaction achieved is investigated.

REFERENCES

[1] J.M. Balthazar, D.T. Mook, H.I. Weber, B. R. A. Fenili, D. Belato, and J.L.P. Felix. An overview on non-ideal vibrations. *Meccanica*, 38:613–621, 2003.

[2] I.I. Blekhman. *Vibrational Mechanics-Nonlinear Dynamic Effects, General Approach.* Singapore, 2000.

[3] J. González-Carbajal and J. Domínguez. Limit cycles in nonlinear vibrating systems excited by a nonideal energy source with a large slope characteristic. *Nonlinear Dynamics*, 87(2):1377–1391, 2016.

[4] V.O. Kononenko. *Vibrating Systems with a limited power supply.* Illife, London, 1969.

1st. Conference on Structural Dynamics (DinEst 2018)
Madrid, 20–21 June

A NEW APPROACH BASED ON SPARSE MATRICES TO EFFICIENTLY SOLVE THE EQUATIONS ARISING FROM THE DYNAMIC SIMULATION OF MULTIBODY SYSTEMS

Antón, José A.*, **Cardenal, Jesús***

*Grupo de Dinámica de Vehículos
Universidad de A Coruña (Campus de Ferrol)
15403 Ferrol, Spain

e-mail: jose.augusto.anton@udc.es
ORCID: 0000-000-2-0504-7575

Abstract. This paper presents a new method to improve the efficiency in the solution of the dynamics of multibody systems with rigid elements both in open and closed chain forms. This improvement is achieved by means of a special reordering algorithm of the sparse matrices arising from the multibody constraint equations. In open-chain systems these matrices can be reordered to a block triangular form. In the closed-loop case these matrices can be reduced to a bordered block triangular form with very few columns in the border. This reorder effort led to a set of linear systems of equations that can be solved by means of block sparse matrices techniques.

In the first case (open-chain mechanisms) the proposed algorithm is able to perform an automatic reordering; for the mechanisms with closed chains a previous selection of some elements of the mechanism is performed in order to "broke down" the multibody system into open branches which yields to open-chain subsystems and therefore to an automatic reordering.

Mechanisms have been modelled using natural coordinates including some relative ones. The dynamic problem is solved with a global independent coordinates formulation and its corresponding coordinates partition. The dependent and independent coordinates are related to a velocity transformation making use of the matrix R.

In this work some examples solutions are presented, using the methods above mentioned, and also the improvements achieved in the efficiency and possible future developments.

Key words: Multibody System Dynamics, Computing Methods.

1 INTRODUCTION

Achieving real time in multibody system dynamic simulation has been a goal over the years [3].

To achieve this target, many authors focused on the numerical aspect of simulation, trying to get advantage from improvements in computer hardware, more efficient integration methods or best tuned algorithms, etc. [2]

Other authors put their effort on improving multibody system models to shorten the computational cost in the study of kinematic and dynamic problems. Among these efficient models it is worth mentioning the group of formulations that take advantage of the mechanism topology [5] and thus improve efficiency in the solution. As a counterpart, these methods, called topological, while more efficient than global ones, introduce an extra complexity in modelling and solving each mechanism.

The algorithm proposed in this work takes advantages both from the simplicity of global methods in the modelling side, and from the efficiency of topological ones, in the dynamic problem formulation. On the one hand, a global resolution method (simpler to implement than topological ones) is used and, on the other hand, the introduction of an appropriate reordering algorithm in the sparse matrices arising in the formulation, leads to a resolution whose efficiency resembles that of some topological formulations.

2 MULTIBODY DYNAMICS FORMULATION

As mentioned, the formulation presented on this work relies on a global method to model multibody systems.

Mechanisms are modelled using natural coordinates and including some relative ones. Multibody dynamics is solved with a global independent coordinates formulation and its corresponding coordinates partition. The dependent and independent coordinates are related to a velocity transformation through the use of matrix R [1].

$$\boldsymbol{\Phi}^d_{\mathbf{q}}\,\mathbf{R}^* = -\boldsymbol{\Phi}^i_{\mathbf{q}} \tag{1}$$

$$\boldsymbol{\Phi}^d_{\mathbf{q}}\,[\mathbf{Sb}] = -\boldsymbol{\Phi}_t \tag{2}$$

$$\boldsymbol{\Phi}^d_{\mathbf{q}}\,[\mathbf{Sc}] = -\dot{\boldsymbol{\Phi}}_{\mathbf{q}}\,\dot{\mathbf{q}} \quad -\dot{\boldsymbol{\Phi}}_t \tag{3}$$

In this context, the highest computational cost in the simulation of multibody dynamics corresponds to the solution of the linear systems shown in equations 1 - 3. Thus, any improvement in the solution efficiency of this linear systems will lead to an improvement in the whole simulation global efficiency.

In these systems the characteristic matrix is the Jacobian of the constraint equations ($\boldsymbol{\Phi}^d_{\mathbf{q}}$) in which only the dependent coordinates are considered. The size of this Jacobian matrix is related to the number of coordinates or constraints in multibody system model. In large systems it can be as much as 500 while in smaller ones is in the order of few tens. The key feature within this work is that this Jacobian is a sparse matrix, where the number of non-zero entries is less than 5% of the total in most complex mechanisms. As will be shown, a special tuned sparse matrix reordering algorithm takes advantage of Jacobian matrix structure to speed up the simulation.

3 PROPOSED ALGORITHM

The proposed algorithm rearrange Jacobian matrix elements to group them into a series of small square blocks located over the diagonal. There may also be any nonzero elements below the diagonal and in some cases a right few columns border of nonzero elements.

It can be stated that matrix $\boldsymbol{\Phi}^d_{\mathbf{q}}$ in equations 1 - 3 can always be reduced to the described *block diagonal form*, provided that coordinates and restrictions have been correctly ordered or numbered according to mechanism topology.

Once the leading matrix of any linear systems of equations has been reordered in such a way, its solution can be calculated recursively solving every small order system defined by diagonal blocks. This recursive solver is usually more efficient than any traditional factorization. Moreover, the smaller the right column border in the block diagonal form and the smaller the order of each block, faster is the recursive solver.

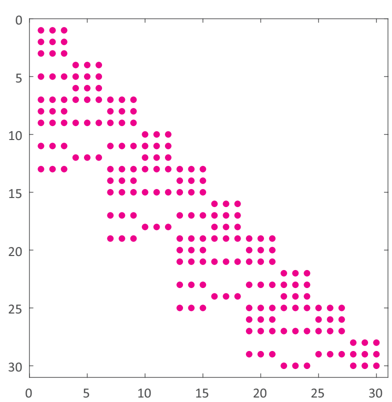

Figure 1: Open chain mechanism $\boldsymbol{\Phi}^d_{\mathbf{q}}$ matrix.

In the case of open chain mechanisms the Jacobian can be reduced to a *block-triangular form*, as depicted in figure 1. As can it be seen, it is a structure with blocks in the diagonal without any non-zero entry above diagonal.

When multibody system is a closed chain mechanisms, its Jacobian can be partially reordered into a block-triangular form, but some non-zero entries should be moved to form a right border columns. An example of this *bordered-block-triangular form*, is depicted in figure 2.

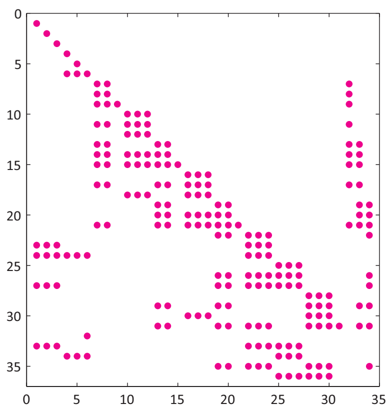

Figure 2: Closed chain mechanism $\mathbf{\Phi}_{\mathbf{q}}^{d}$ matrix.

The proposed reordering algorithm is based on the reordering method P^5 [4]. The P^5 aims to reduce the matrix into a bordered-block-triangular form. However, the algorithm not always minimizes the size of column border, to the point that in some cases, where the matrix could be completely reduced into a block-triangular form without any right border (such in the case of open chain multibody systems), the reordering process lead to a bordered-block-triangular form. The proposed modified version of P^5 algorithm is designed to overcome this drawback: in every case right column border size is minimized. Also, for efficiency purposes, maximum diagonal block dimensions are limited to 3×3.

Modified P^5 has been designed to perform matrix rearrangement in fully automatic mode. In current version there may be some cases (mainly when studying closed chain multibody systems) where the rearrangement needs some kind of preprocessor task to select which coordinates have to be moved to right border. These coordinates are selected in such a way that if their value were known the resulting system would be equivalent to an open chain mechanism. It is interesting to note the analogy between this way to solve the mechanism and that in topological methods: coordinates moved to right border are selected among kinematic pairs that should be *broken* in a topological method.

4 COMPARATIVE RESULTS

To show some comparative results the dynamic equilibrium problem of a four-wheel vehicle is presented. Vehicle model includes suspensions, steering mechanism and wheels. Figure 3 shows an schematic view of the complete system. Front suspension consist on a McPherson strut modelled by means of universal joints, bars and a slide. Rear suspension is of an independent multi-link type with five bi-articulated rods. Six solids and seven kinematic pairs are needed to model each side of this rear suspension. The steering mechanism has been integrated into the front suspension.

At the initial time, the vehicle is drop to the ground from a short heigh. Dynamic equations are integrated to simulate system behaviour for the next $10s$ following the contact with ground. The integration step size is $10^{-3}s$ and the simulation has been carried out on a PC with an Intel Core i7 processor at 2.7 GHz. In this manoeuvre there is no steering movement nor wheel rotation, resulting in a total of 10 degrees of freedom and 202 free coordinates. The multibody system model leads to 192 constraint equations. $\mathbf{\Phi}_{\mathbf{q}}^{d}$ is a square 192×192 matrix which its non-zero entries represents a 2.4% of total.

Figure 4 schematically depicts $\mathbf{\Phi}_{\mathbf{q}}^{d}$ matrix once it has been rearranged into bordered-block-triangular form by modified P^5 algorithm. Right non-zero border has 17 columns. Distribution of non-zero block elements over diagonal resembles that this multibody system is a compound of four subsystems (each suspensions).

For efficiency comparison, the systems of linear equations in expressions 1 and 3 have both been solved, using the proposed recursive method once Jacobian matrix has been reordered using modified P^5 strategy and also with the scientific public do-

	MA48	Modified P^5	%
$\mathbf{\Phi_q}$ partition	0.053 s	0.038 s	0.72
$\mathbf{R}$ evaluation (eq. 1)	3.233 s	2.548 s	0.79
$\mathbf{Sc}$ solution (eq. 3)	0.283 s	0.207 s	0.73
Total time	3.569 s	2.793 s	0.78

Table 1: CPU time using MA48 and modified P^5 solvers.

main sparse solver MA48 [6] that also implements a block form reordering strategy.

Table 1 summarizes comparative results. It shows computer elapsed times to perform $\mathbf{\Phi}^d_{\mathbf{q}}$ partition and to solve the systems of linear equations given by expressions 1 and 3. Modified P^5 is 22% faster than MA48 solver.

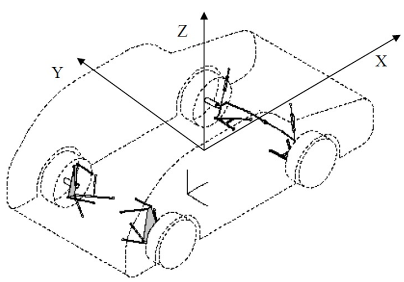

Figure 3: Automobile

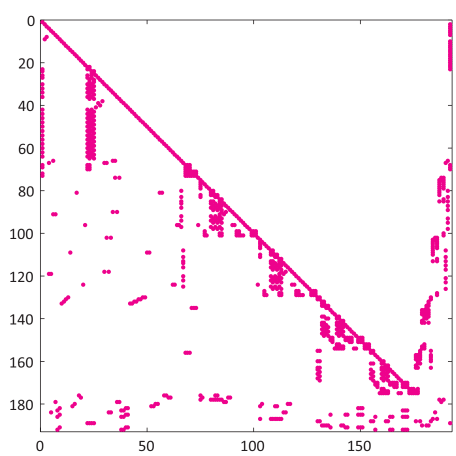

Figure 4: Automobile reordered $\mathbf{\Phi}^d_{\mathbf{q}}$ matrix.

5 CONCLUSIONS

This work presents in a very concise way a new algorithm to solve the systems of linear equations arising in multibody dynamic simulation. It is shown that proposed method behaves well compared to other general purpose sparse solver that fits the conditions of the problem. The modified P^5 reordering algorithm and its associated small block recursive solution outperforms MA48 for a 22% in terms of computational elapsed time.

REFERENCES

[1] José Augusto Antón Nacimiento. *Estrategias de reordenamiento de matrices huecas para el tratamiento óptimo de las ecuaciones de la dinámica de mecanismos.* PhD thesis, Universidade da Coruña, 2015.

[2] J. Cuadrado, J. Cardenal, and E. Bayo. Modeling and solution methods for efficient real-time simulation of multibody dynamics. *Multibody System Dynamics*, 1(3):259–280, 1997.

[3] J. Cuadrado and W. Schiehlen. Special issue: Real-time simulation and virtual reality applications of multibody systems. *Multibody System Dynamics*, 17(2-3), 2007.

[4] A. M. Erisman, R. G. Grimes, J. G. Lewis, and W. G. Poole, Jr. A Structurally Stable Modification of Hellerman Rarick's p4 Algorithm for Reordering Unsymmetric Sparse Matrices. *SIAM Journal on Numerical Analysis*, 22(2):369–385, April 1985.

[5] J. García Jalón, Álvarez E., de Ribera F., Rodríguez I., and Funes F. A fast and simple semi-recursive formulation for multi-rigid-body systems. In Ambrósio J.A., editor, *Advances in Computational Multibody Systems.*, volume 2 of *Computational Methods in Applied Sciences.* Springer, 2005.

[6] HSL. A collection of fortran codes for large-scale scientific computation.

Author index

Aenlle, M.L., 75
Alamo, G.M., 187
Alvarez Cabal, R., 20
Antón, J.A., 236
Arroyo, J., 79
Atorrasagasti-Villar, A., 172
Aznárez, J.J., 151, 178, 187, 195, 199

Barrera, C.A., 42
Barrios, E., 141
Basulto, D., 70
Becerra, J.A., 66
Benavent-Climent, A., 203, 207, 211, 219
Benito, B., 182
Bordón, J.D.R., 151
Brincker, R., 75
Bukovics, M., 79
Bustos, A., 88
Báez, M.F., 132

Calero-Moraga, M., 58
Callejas, A., 12
Calvo, J., 79
Cara, J., 2
Cardenal, J., 236
Carricondo Sánchez, E., 20
Castejón, C., 88
Cervera, J., 7, 182
Combescure, D., 191
Conde-Conde, J., 219
Connolly, D.P., 164
Cosido, Ó., 70
Cruz-Muñoz, F.J., 168
Cueto-Felgueroso, L., 215
Cuevas, R.G., 127

de la Concha, C.M., 83, 92
Deniz, J.C., 83
Domínguez, J., 232
Domínguez, V., 191
Díaz Heredia, E., 20
Díaz, I.M., 32, 42, 79, 83, 92, 96, 101, 105, 118, 127, 172
Díaz-Pavón, E., 20

Elejabarrieta, M.J., 28, 155
Embid, I., 92

Faris, I.H., 12
Fernández, J., 132
Fernández-Canteli, A., 75
Ferrer, B., 62
Fontán, A.N., 66
Fraile, A., 132

Gallego, A., 211
Gallego, R., 187
Galván, J.C., 199
Galvín, P., 109, 114, 164, 168
Galé-Lamuela, D., 203, 207
García Orden, J.C., 227
García-Macías, E., 123
García-Palacios, J.H., 32, 42, 79, 83, 92, 96, 101, 105, 118, 172
García-Prada, J.C., 88
García-Sánchez, F., 46
García-Vallejo, D., 232
Gaspar-Escribano, J.M., 182
Goicolea, J.M., 118, 141
Gonzalez-Sanz, G., 203, 207
González Carbajal, J., 232
González, C., 2
González-Gámez, N., 46

Hermanns, L., 132
Hernández, X., 28
Herrera, J., 178

Ibán, N., 38
Infantino, V., 38
Irazu, L., 28, 155
Iriondo, J., 28
Ismael, G., 50, 54, 160
Iturregui, C., 172

Jiménez-Alonso, J.F., 46, 58
Jurado-Camacho, D., 58

Kharazian, A., 211

Lacoma, L.M., 136
Lorenzana, A., 38
López Almansa, F., 211
López-Aenlle, M., 50, 54, 160
López-Mendoza, D., 164

Maeso, O., 151, 178, 187, 195, 199
Magdaleno, Á., 38

Mans, C., 223
Maqueda, L., 191
Marco, D., 66
Marinas-Sanz, G., 105
Marmo, R., 70
Martí, J., 136
Martín, A., 50
Martínez, F., 127, 136
Martínez-Castro, A.E., 123, 187, 223
Martínez-Rodrigo, M.D., 109, 114
Martínez-Valle, J.M., 16
Mas, D., 62
Melchor, J., 12
Mira, J.M., 2
Moliner, E., 109, 114
Morales, R.P., 50
Mosquera, J.C., 92, 215
Moya, L., 191

Naranjo-Pérez, J., 46
Navas, P., 142
Navas-Sánchez, L., 182
Nguyen, K., 118, 141, 172

Olalde, J., 191
Orta, B., 7

Padrón, L.A., 178, 187, 195, 199
Pampillón, P., 215
Pelayo, F., 50, 54, 75, 160
Pereira, E., 96, 101
Pereiro-Barceló, J., 147

Ramírez-Senent, J., 105
Rodríguez, J., 136
Rodríguez, P.M., 70
Romera, L.E., 66
Romero, A., 109, 114, 164, 168
Rubio, H., 88
Rueda, F., 191
Rus, G., 12
Ruíz, G., 142

Salcines, A., 70
San Segundo, S., 7
Santana, A., 195
Santillán, D., 215
Soria, J.M., 32, 42, 79, 83, 118, 172
Sáez, A., 46, 58

Tadeu, A., 168
Tena, M., 70
Terrés Nícoli, J.M., 223
Tortosa del Carpio, J., 24

Velarde, C., 118, 141

Wang, X., 32, 42, 83, 96, 101

Yu, R.C., 142

Zanuy, C., 32

EASD

IABSE
Spanish Group

SEMNI

Banco Caminos
banco privado